THÈSE

présentée à

L'UNIVERSITÉ DE BORDEAUX

École Doctorale des Sciences Chimiques

et

L'UNIVERSIDADE ESTADUAL PAULISTA

"JÚLIO DE MESQUITA FILHO"

Instituto de Química – *campus* Araraquara

par

Leonardo Vieira ALBINO

pour obtenir le titre de

DOCTEUR

Spécialité: Chimie ET Physico-chimie de la matière condensée

****

Synthèse et étude de verres à propriétés magnéto-optiques contenant des métaux de transition et des terres rares

****

Soutenue le 23 octobre 2023

Membres du jury **:**

M. NALIN Marcelo, Professor	Instituto de Química – Universidade Estadual Paulista « Júlio
de Mesquita Filho » *campus* Araraquara (IQ-UNESP)	– **Directeur de thèse**
M. CARDINAL Thierry, Docteur	Institut de Chimie de la Matière Condensée de Bordeaux –
Université de Bordeaux (ICMCB-UB)	– **Directeur de thèse**
M. DUCLERE Jean-René, Professor	Institut de Recherche sur les Céramiques – Université de
Limoges (IRCER-UL)	– **Rapporteur**
M. POIRIER Gael-Yves, Professor	Instituto de Ciência e Tecnologia – Universidade Federal de
Alfenas *campus* Poços de Caldas (ICT-UNIFAL-MG)	– **Rapporteur**
Mme GONÇALVES Rogéria Rocha, Professeure	Faculdade de Filosofia, Ciências e Letras de Ribeirão Preto -
Universidade de São Paulo (FFCLRP-USP)	– **Examinateur & Président du Jury**

Albino, Leonardo Vieira
A336s Síntese e estudo de vidros magneto-ópticos contendo metais de transição e terras raras / Leonardo Vieira Albino – Araraquara: [s.n.], 2023
203 p.: il.

Tese (doutorado) – Universidade Estadual Paulista, Instituto de Química
Orientador: Marcelo Nalin
Coorientador: Thierry Cardinal
Coorientador: Sidney José Lima Ribeiro

1. Vidro. 2. Magnetoptica. 3. Efeito de Faraday. 4. Metais de terras raras. 5. Manganês. I. Título.

Sistema de geração automática de fichas catalográficas da Unesp. Biblioteca do Instituto de Química, Araraquara. Dados fornecidos pelo autor(a).

Essa ficha não pode ser modificada

Leonardo Vieira Albino

Síntese e Estudo de Vidros Magneto-Ópticos contendo Metais de Transição e Terras Raras

Tese em cotutela apresentada ao Instituto de Química, Universidade Estadual Paulista "*Júlio de Mesquita Filho*" (IQ/UNESP) e Institut de Chimie de la Matière Condensée de Bordeaux, Université de Bordeaux (ICMCB/UB) para obtenção do título de Doutor em Química, especialidade em Físico-Química da Matéria Condensada

Orientador: Prof. Dr. Marcelo Nalin

Coorientador: Dr. Thierry Cardinal

Coorientador: Prof. Dr. Sidney José Lima Ribeiro

Araraquara

2023

Impacto potencial da pesquisa

Vidros com aplicações magneto-ópticas vem se tornando cada vez mais procurados por pesquisadores e empresas, sendo uma promessa significativa para vários avanços tecnológicos, com impactos potenciais que abrangem diversos setores. Em primeiro lugar, a exploração destes vidros pode impulsionar as tecnologias de comunicação. Os rotadores Faraday, dispositivos que giram a polarização da luz na presença de um campo magnético, são componentes integrais em sistemas de comunicação óptica. Ao melhorar as propriedades magneto-ópticas dos vidros, os pesquisadores podem abrir caminho para redes de comunicação óptica mais eficientes e rápidas. Isto poderia levar a melhores taxas de transmissão de dados, redução de perdas de sinal e aumento de largura de banda, atendendo à crescente demanda por comunicações mais rápidas e confiáveis. Também tem implicações profundas para o desenvolvimento de tecnologias de sensoriamento. As propriedades magneto-ópticas desses vidros podem ser aproveitadas na criação de sensores magnéticos/elétricos altamente sensíveis. Esses sensores podem encontrar aplicações em diversos campos, incluindo diagnósticos médicos, monitoramento ambiental e processos industriais. Atualmente vidros magneto-ópticos apresentam-se como um possível substituto dos monocristais utilizados comercialmente, devido as características isotrópicas, o processo de produção mais simples e a possibilidade de produção de fibras ópticas. Para esse fim, várias matrizes vítreas que suportem altas concentrações de terras-raras sem induzir cristalização vem sendo sintetizadas e estudadas. Vidros borogermanato vem se mostrando uma boa alternativa, porém os reagentes e a síntese desses vidros elevam o custo. Esta tese de doutorado teve como objetivo sintetizar a caracterizar diferentes sistemas vítreos mais baratos, um borotungstato contendo terras-raras e outro fosfato contendo manganês visando obter respostas magnéticas próximas aos monocristais e vidros germanato comerciais.

Potential research impact

Glasses with magneto-optical applications have become increasingly sought after by researchers and companies, holding significant promise for various technological advances, with potential impacts that span diverse sectors. Firstly, the exploration of these glasses can boost communication technologies. Faraday rotators, devices that rotate the polarization of light in the presence of a magnetic field, are integral components in optical communication systems. By improving the magneto-optical properties of glasses, researchers can pave the way for more efficient and faster optical communication networks. This could lead to better data transmission rates, reduced signal losses and increased bandwidth, addressing the ever-growing demand for faster and more reliable communication. Moreover, the research has profound implications for the development of advanced sensing technologies. The magneto-optical properties of these glasses can be used to create highly sensitive magnetic/electrical sensors. These sensors can find applications in a variety of fields, including medical diagnostics, environmental monitoring, and industrial processes. Currently, magneto-optical glasses are a possible replacement for commercially used monocrystals, due to their isotropic characteristics, the simpler production process and the possibility of producing optical fibers. To this end, several glass matrices that support high concentrations of rare earths without inducing crystallization have been synthesized and studied. Borogermanate glasses have proven to be a good alternative, but the reagents and synthesis of these glasses increase the cost. This doctoral thesis aimed to synthesize and characterize different cheaper glass systems, a borotungstate containing rare earths and another phosphate containing manganese, aiming to obtain magnetic responses close to commercial monocrystals and borogermanate glasses.

UNIVERSIDADE ESTADUAL PAULISTA

Câmpus de Araraquara

CERTIFICADO DE APROVAÇÃO

TÍTULO DA TESE: "Síntese e Estudo de Vidros Magneto-Ópticos contendo Metais de Transição e Terras Raras"

AUTOR: LEONARDO VIEIRA ALBINO
ORIENTADOR: MARCELO NALIN
COORIENTADOR: SIDNEY JOSE LIMA RIBEIRO
COORIENTADOR: THIERRY CARDINAL

Aprovado como parte das exigências para obtenção do Título de Doutor em Química, pela Comissão Examinadora:

Prof. Dr. MARCELO NALIN (Participaçao Presencial)
Departamento de Quimica Analitica, Fisico-Quimica e Inorganica / Instituto de Quimica - UNESP - Araraquara

Prof. Dr. THIERRY CARDINAL (Participaçao Virtual)
Institut de Chimie de la Matière Condensée de Bordeaux - UB - França

Prof. Dr. GAEL YVES POIRIER (Participaçao Presencial)
Instituto de Ciência e Tecnologia / Universidade Federal de Alfenas - UNIFAL - Poços de Caldas

Profa. Dra. ROGÉRIA ROCHA GONÇALVES (Participaçao Virtual)
Departamento de Química / Faculdade de Filosofia Ciências e Letras - USP - Ribeirão Preto

Prof. Dr. JEAN-RENÉ DUCLÉRE (Participaçao Virtual)
Institut de Recherche sur les Céramiques / Université de Limoges - França

Araraquara, 23 de outubro de 2023

Leonardo Vieira Albino; L. V. Albino; L. V. ALBINO

Occupation area

Major Area: Exact and Earth Sciences / Area: Chemistry / Subarea: Inorganic Chemistry.

Major Area: Exact and Earth Sciences / Area: Chemistry / Subarea: Materials Chemistry.

Major Area: Exact and Earth Sciences / Area: Chemistry / Subarea: Non-Crystalline Materials Chemistry.

Personal information

Birth date: January 21, 1994 - 29 years

Nationality: Brazilian.

Place of birth: Itapetininga, SP, Brazil.

Affiliation: Marcos Antônio Albino and Patrícia Maria Diniz Vieira Albino.

Marital status: single.

Occupation: PhD student.

Email: leonardoalbino63@gmail.com

Curriculo Lattes (in Portuguese): http://lattes.cnpq.br/0124534306474504

ORCID iD: https://orcid.org/0000-0003-0441-2371

Professional address

São Paulo State University (UNESP), Institute of Chemistry, Department of General and Inorganic Chemistry, Laboratório de Vidros Especiais (LaViE).

Av. Prof. Francisco Degni, 55

Jardim Quitandinha

14800060 - Araraquara, SP, Brazil

Telephone: +55 (16) 33019654

Academic education

PhD in Physico-Chimie de la Matière Condensée in progress. 2021 – in progress.
Institut de Chimie de la Matière Condensée de Bordeaux (ICMCB), UMR5026, CNRS, University of Bordeaux (UB) and Bordeaux INP.
Advisor: Dr. Thierry Cardinal
Scholarship: FUNGlass, received funding from the European Union's Horizon 2020 research and innovation programme under the Marie Skłodowska-Curie grant agreement No 823941.

PhD in Chemistry in progress (grade CAPES 7). 2018 – in progress
São Paulo State University (UNESP), Institute of Chemistry, Department of General and Inorganic Chemistry, Laboratório de Vidros Especiais (LaViE).
Title of thesis: Synthesis and Study of Magneto-Optic Glasses containing Transition Metals and Rare Earths.
Advisor: Prof. Dr. Marcelo Nalin.
Co-advisor: Prof. Dr. Sidney José Lima Ribeiro.
Scholarship: Coordenação de Apoio a Pesquisa no Ensino Superior (CAPES), Brazil.

Master in Chemistry (grade CAPES 7). 2016 - 2018
São Paulo State University (UNESP), Institute of Chemistry, Department of General and Inorganic Chemistry, Laboratório de Vidros Especiais (LaViE).
Title of dissertation: Study, Preparation and Application of Polymeric Optical Fibers using 3D Printing technology.
Advisor: Marcelo Nalin.
Scholarship: Coordination for the Improvement of Higher Education Personnel (CAPES), Brazil.

Bachelor in Chemistry. 2012 - 2015
São Paulo State University (UNESP), Institute of Chemistry, Department of General and Inorganic Chemistry, Laboratório de Vidros Especiais (LaViE).

Title of coursework completion: Luminescent Properties of Europium and Copper Doped PbO-GeO_2 Glass.
Advisor: Marcelo Nalin.
Scholarship: São Paulo Research Foundation (FAPESP), Brazil.

Technical/Professionalizing course in Chemistry. 2010 - 2011
Salles Gomes State Technical School (Paula Souza Center). Tatuí, Brazil.

Additional education

Minicourse Lanthanides: Chemistry, Luminescence and Applications, by Prof. Dr. Fernando Aparecido Sigoli. (Hours: 6). 46th Annual Meeting of the Brazilian Society of Chemistry (RASBQ). Águas de Lindóia - Brazil. (2023)

MOOC - Intégrité scientifique dans les métiers de la recherche. Université de Bordeaux. (2023)

French language course. Niveau B2 - Evening - Département d'Etudes de Français Langue Etrangère (DEFLE). (Hours: 50). Université Bordeaux-Montaigne, France. (2022)

2nd ICG-CGCRI Tutorial 2021 on Glass Science & Technology hosted by CSIR - Central Glass & Ceramic Research Institute, Kolkata - India, in association with International Commission on Glass, from 18th to 27th January - online (2021)

Pedagogical Training Workshop: Dialogues on University Teaching - PPD/FCF and Program for the Improvement and Support of Teaching in Higher Education (PAADES) - Campus (Hours: 8). São Paulo State University (UNESP), Brazil. (2019)

Pedagogical Training Workshop - Program for the Improvement and Support of Teaching in Higher Education (PAADES). (Hours: 22). São Paulo State University (UNESP), Brazil. (2018)

Introduction to 3D modeling of free software. (Hours: 15). Araraquara University (UNIARA), Brazil. (2016)

Next generation gene arrays: fresh new tools for. (Hours: 1). AFFYMETRIX BIOTECH LTDA, AB_FORN, Brazil. (2014)

Web of Science, EndNote e ResearcherID. Thomson Reuters Serviços Econômicos, THOMSON REUTERS, Brazil. (2014)

Forensic Medical Sciences. Courses and Events Renova, RENOVA CURSOS, Brazil. (2013)

Professional Experience

1. **Professor of Experimental Inorganic Chemistry** for the Chemical Engineering course (2019) by the Program for the Improvement and Support of Teaching in Higher Education (PAADES). São Paulo State University (UNESP), Institute of Chemistry, Araraquara, Brazil. (2019). 64h.
2. **Professor of General and Inorganic Chemistry I** for the Pharmacy-Biochemistry course (evening–2019) by the Program for the Improvement and Support of Teaching in Higher Education (PAADES). São Paulo State University (UNESP), Institute of Chemistry, Araraquara, Brazil. (2019). 64h.
3. **Intervention activity in the General Chemistry Laboratory** discipline for 1st year students of the Chemical Engineering course by the Special Topics discipline: Chemistry Teaching Practice - Theory and experiment. São Paulo State University (UNESP), Institute of Chemistry, Araraquara, Brazil. (2017). 180h.
4. **Teaching practice in Experimental Inorganic Chemistry** for Licentiate in chemistry students (2013) offered by the Coordination for the Improvement of Higher Education Personnel (CAPES) and Department of General and Inorganic Chemistry, São Paulo State University (UNESP), Institute of Chemistry, Araraquara, Brazil. (2017). 60h.
5. **Monitor of the General Physical Chemistry** discipline for Bachelor in chemistry (2013) offered by the Department of Physical Chemistry and Tutorial Education Program in Chemistry (PET-Química). São Paulo State University (UNESP), Institute of Chemistry, Araraquara, Brazil. (2013). 60h.
6. **Ministered short course Workshop: Origin,** during the XLIII Chemistry Week**.** São Paulo State University (UNESP), Institute of Chemistry, Araraquara, Brazil. (2013). 2h.

Languages

Portuguese

Comprehends Well, Speaks Well, Reads Well, Writes Well.

English

Comprehends Well, Speaks Well, Reads Well, Writes Reasonably.

French

Comprehends Well, Speaks Well, Reads Well, Writes Well. Niveau DELF B2.

Scientific production

Articles published in scientific journals

D. F. Franco, F. J. Caixeta, L. V. Albino, T. A. Lodi, J. R. Orives, E. O. Ghezzi, M. Nalin, **Terbium-doped transparent glass-ceramics containing $TbPO_4$ crystals: A promising material for photonic applications**. Opt. Mater. X. 20 (2023) 100272 https://doi.org/10.1016/j.omx.2023.100272

Presented works

1. Albino, L. V.; Cardinal, T.; Dussauze, M.; Adamietz, F.; Toulemonde, O.; Jubera, V.; Franco, D. F.; Nalin, M. "**Paramagnetic borotungstate glasses – a new magnetic-optical material**". 46 RASBQ. Águas de Lindóia - Brazil. (2023)
2. Ghezzi, E. O.; Albino, L. V.; Lodi, T. A.; Franco, D. F.; Nalin, M.; "**Synthesis and characterization of glasses for ultra-sensitive magneto-optical sensors**". 46 RASBQ. Águas de Lindóia - Brazil. (2023)
3. Albino, L. V.; Cardinal, T.; Dussauze, M.; Adamietz, F.; Toulemonde, O.; Jubera, V.; Franco, D. F.; Nalin, M. "**Estudos de vidros borotungstato com alta concentração de terras raras para aplicação fotônica**". Reunião Regional do Instituto Nacional de Ciência e Tecnologia de Fotônica (INFO). Ribeirão Preto - Brazil. (2023)
4. Albino, L. V.; Jubera, V.; Cardinal, T.; Toulemonde, O.; Dussauze, M.; Nalin, M. "**Structural, optical and magnetic properties of high rare earths ions containing Borotungstate glasses**". XX B-MRS Meeting, Foz do Iguaçu - Brazil. (2022)

5. Albino, L. V.; Dussauze, M.; Toulemonde, O.; Jubera, V.; Cardinal, T.; Nalin, M. "**Borotungstate glasses with a high concentration of rare earths for photonic application**". 26th International Congress on Glass (ICG2022). Berlin - Germany. (2022)

6. Albino, L. V.; Dussauze, M.; Danto, S.; Canioni, L.; Toulemonde, O.; Jubera, V.; Cardinal, T.; Nalin, M. "**Verre borotungstate d'ions de terres rares: Matériaux magnétiques pour la photonique**" 89e Congrès de l'Acfas. On-line. Oral presentation in french. 2022

7. Albino, L. V.; Dussauze, M.; Danto, S.; Canioni, L.; Toulemonde, O.; Jubera, V.; Cardinal, T.; Nalin, M. "**Magnetic materials for photonic applications: Borontungstate and rare earth ions glasses**". Physical Chemistry & Chemical Physics Workshop (PCCP-2022). Université de Bordeaux. Oral presentation in English. 2022

8. Roque, N. G.; Albino, L. V.; Marcondes, L. M.; Nalin, M. "**Obtenção do sistema vítreo SbPO4-ZnO-PbO-MnO e estudo das propriedades térmicas, ópticas e estruturais**". XXXII UNESP Scientific Initiation Congress (CIC-UNESP). On-line. (2020)

9. Roque, N. G.; Albino, L. V.; Marcondes, L. M.; Nalin, M. "**Synthesis of the SbPO4-ZnO-PbO-MnO magneto-luminescent glasses**". #LatinXChem Twitter Conference 2020. On-line. (2020)

10. Albino, L. V.; Nalin, M. "**Synthesis of transparent magneto-luminescent glass-ceramics with high concentrations of Tb^{3+}**". II Workshop National Institute of Photonics (INFo). Araraquara, Brazil. (2020)

11. Roque, N. G.; Albino, L. V.; Nalin, M. "**Synthesis of the SbPO4-ZnO-PbO-MnO magneto-luminescent glass**". II Workshop National Institute of Photonics (INFo). Araraquara, Brazil. (2020)

12. Roque, N. G.; Albino, L. V.; Nalin, M. "**Estudo das propriedades térmicas, ópticas e estruturais do sistema vítreo $SbPO_4$-ZnO-PbO em função da concentração de MnO**". XXXI UNESP Scientific Initiation Congress (CIC-UNESP). Araraquara, Brazil. (2019)

13. Ramos, R. G.; Albino, L. V.; Santagneli, S. H. "**Estudo da estrutura e propriedades de vidros boro-fosfato modificados com AlF_3**". XXXI UNESP Scientific Initiation Congress (CIC-UNESP). Araraquara, Brazil. (2019)

14. Sampaio, A. C. S.; Albino, L. V.; Nalin, M. "**Estudo das propriedades térmicas, ópticas e estruturais do sistema La_2O_3-B_2O_3-WO_3 dopados com Dy^{3+}, Tb^{3+} e Eu^{3+}**". XXXI UNESP Scientific Initiation Congress (CIC-UNESP). Araraquara, Brazil. (2019)

15. Sampaio, A. C. S.; Albino, L. V.; Nalin, M. "**Síntese de vidros boro-tungstato com alta concentração de lantânio**". XXX UNESP Scientific Initiation Congress (CIC-UNESP). Araraquara, Brazil. (2018)

16. Albino, L. V.; Nalin, M. "**Preparation of Polymeric Optical Fibers using 3D Printing technology and its application as sensors**". International Conference on Optical, Optoelectronic and Photonic Materials and Applications (ICOOPMA). Maresias, Brazil. (2018)

17. Albino, L. V.; Nalin, M. "**Preparação de Fibras Ópticas Poliméricas utilizando tecnologia de Impressão 3D**". 57° Brazilian Congress of Chemistry. Gramado, Brazil. (2017)

18. de Castro, G. B.; Porsani, G. F.; Albino, L. V.; Nalin, M. "**Multicore polymeric optical fiber obtained from preform with 3D printer**". XXVIII UNESP Scientific Initiation Congress (CIC-UNESP). Araraquara, Brazil. (2016)

19. Albino, L. V.; Silva, M. C. C.; Nalin, M. "**Estudo das propriedades luminescentes de vidros PbO-GeO_2 dopados com európio e cobre**". 38ª Annual Meeting of the Brazilian Chemical Society. Águas de Lindóia, Brazil. (2015)

20. Albino, L. V.; Silva, M. C. C.; Nalin, M. "**Estudo das propriedades ópticas dos vidros e vitrocerâmicas PbO-GeO_2 dopados com európio e cobre**". XXVII UNESP Scientific Initiation Congress (CIC-UNESP). Araraquara, Brazil. (2015)

21. dos Santos, I. F. M.; de Jesus, C. A. S.; Albino, L. V.; de Campos, G. P.; Faria, D. V.; Coco, J.; Teixeira, I. S.; Anhesine, N. B.; Rodrigues Júnior, J. R.; Tayar, S. P.; Lopes, M. N. "**Diagnóstico PET do curso de Bacharelado em Química do IQ/UNESP/CAr**". XVIII National Meeting of PET Groups (ENAPET). Recife, Brazil. (2013)

Participation in Events

Poster evaluation during **XXXII UNESP Scientific Initiation Congress (CIC-UNESP)**. On-line. (2020)

Presentation of "Photonic demonstration experiments: Photophone, Fiber optics and Preform; Total internal reflection; Infrared, red and green lasers" during **Science at School**. Araraquara, Brazil. (2019)

Poster evaluation during **XXXI UNESP Scientific Initiation Congress (CIC-UNESP)**. Araraquara, Brazil. (2019)

Poster evaluation during **XXX UNESP Scientific Initiation Congress (CIC-UNESP)**. Araraquara, Brazil. (2018)

Symposium in Commemoration of the International Year of Crystallography: Impact of Crystallography in Different Areas of Science, module I, diffraction and X-ray scattering. (2014)

Prizes

Best works in the poster session of the Materials Division: Ghezzi, E. O.; Albino, L. V.; Lodi, T. A.; Franco, D. F.; Nalin, M.; "**Synthesis and characterization of glasses for ultra-sensitive magneto-optical sensors**". 46 RASBQ. Águas de Lindóia - Brazil. (2023)

Dedication

Dedico este trabalho ao meu querido avô ***José Benedito*** *(1942–2020), homem que, mesmo sem pai, tornou-se o melhor pai e avô deste mundo, sendo uma das inúmeras vítimas da COVID-19.*

Agradecimentos – Acknowledgment – Remerciements

A jornada foi longa. Foram onze anos dedicados a viver o sonho de um jovem de 18 anos, feliz por ter passado no vestibular no curso e na cidade que queria. Não fazia ideia da proporção que me levaria no futuro. Não só conhecer e entender como a Ciência funciona e funciona, mas também contribuir para ela. Neste percurso, foram inúmeros os desafios, mas também inúmeros e agradáveis sucessos. Várias, inúmeras pessoas participaram direta ou indiretamente, para o bem ou para o mal, do meu crescimento científico, profissional e pessoal, o que me coloca numa situação difícil não só de nomeá-las todas, mas de garantir que sejam contempladas por esta simples menção.

Primeiramente quero agradecer a minha família. Minha âncora. Ao meu pai Marcos, minha mãe Patrícia, minha irmã Cristiane, que me amaram desde que nasci, me incentivaram a ser uma pessoa ética, forte, alegre e humana. Aos meus avós que também nunca desistiram de pensar, orar e fazer tudo ao seu alcance por mim. Aos meus tios, primos e todos os antepassados, que apesar da minha ausência da minha cidade natal, sempre me receberam com sorrisos, gargalhadas, preocupações e acolhimento, fortalecendo-me e enchendo-me de esperança.

Não posso deixar de comentar sobre a minha cidade natal, Itapetininga, a qual agradeço por ser a cidade natal de minha família e onde fiz amizades queridas que levarei comigo para toda a vida. Meu salve para vocês Bodão, Wandell, Sonoda, Tiaki, Paulinho e Bruno. Também gostaria de agradecer a meus professores do Ensino Médio, do Instituto Imaculada Conceição – Itapetininga, e do Curso Técnico em Química da Etec Sales Gomes – Tatuí, que me fizeram apaixonar pela Ciência e pela Química.

A minha amada República Diretoria, que me acolheu em fevereiro de 2012. Com certeza me ajudou a vencer minha timidez, me deixando um pouco mais responsável e maduro. Obrigado por aguentarem minhas loucuras e darem-me um nome. Um abraço especial para os diretores com quem convivi: Cafundó, Ariel, Jontex, Alfi, Gargamel, Al-Jazeera, Xaveco, Nissin, Fuinha, Bombinha, Dy, Zé, Conrado, Margarida, Jan, Rooney, Féélipe, Trepadeira, Matuta, Lalau, Vlad, Bilé, Pipico, Chicabom, DuPai, Hortência, Pupunha, R7, Moiado, Carinhoso, Lírio, Ragnar, Resgate, Bife e DogRagnar. DIRETORIAA ARRUL, ARRUL, ARRUL!!

Agradeço ao meu orientador Prof. Dr. Marcelo Nalin (Pre) pela oportunidade de trabalhar em seu laboratório, pelo apoio, pela inspiração, pela paciência e pelos ensinamentos em química, além da confiança depositada em mim nesses 10 anos.

A todos integrantes do Laboratório de Vidros Especiais e do Laboratório de Materiais Fotônicos, em especial ao Prof. Sidney, Prof. Douglas, Dra. Silvia, Prof. Edison, Lia, Juliane, Juliana, Samira, Nicole, Antonio Eduardo, Eduardo Ghezzi, Thiago, Adriana, Bea Freitas, Fábio, Léo e Vibra, pelo conhecimento compartilhado, pelas ajudas, ombros amigos e pelas divertidas discussões.

Aos funcionários e alunos do Instituto de Química, em especial os professores, por aumentar minha paixão por química no grau de querer futuramente lecionar numa

universidade. Também à técnica-administrativa Wennia, por todo auxílio durante a cotutela. Obrigado por essa chance que poucos no nosso país têm.

This study was financed in part by the Coordenação de Aperfeiçoamento de Pessoal de Nível Superior - Brasil (CAPES) - Finance Code 001 (grant 88887.571031/2020-00 and 88882.330082/2019-01).

I would also like to thank the FunGlass Project for funding, from the European Union's Horizon 2020 research and innovation program under the Marie Skłodowska-Curie (grant agreement 823941), to the Center for Research, Technology and Education in Vitreous Materials (FAPESP, grant 2013/07793-6) , French National Center for Scientific Research (CNRS), Bordeaux INP and National Council for Scientific and Technological Development (CNPq). Financing and support that allowed me to grow not only professionally, but also personally, socially and culturally.

Um agradecimento especial as minhas professoras de línguas, Carla, et surtout Islene, pour la tâche incroyable de m'aider à apprendre la langue française en peu de temps, m'aidant toujours, avec un professionnalisme et une volonté excellents. And Lenita, my English teacher, also for all her understanding, effort and help, for bringing out my dormant "English" and helping me with my greatest difficulties with patience, professionalism and good humor.

Aos meus grandes amigos que vou levar para toda a vida, Palmito, Maria, Cartola e Arroyos (Santiago) por todos os momentos alegres nessa caminhada.

E ao meu querido Fernando, que conheci no início do doc durante meu café com maçã, por todo companheirismo, amizade, força, conselhos, risadas, acolhimento e amor nos momentos fáceis e terríveis por toda essa minha jornada. Você é incrível!

Je n'ai pas pu m'empêcher de remercier tout particulièrement tout le monde en France. D'abord à mon directeur de thèse, M. Dr. Thierry Cardinal, pour l'opportunité de travailler dans son laboratoire, pour le soutien et pour les enseignements formidables et valables.

Je ne peux pas non plus oublier de remercier Dr. Marc Dussauze et Prof. Dr. Véronique Jubera, pour son amitié et aussi pour toute sa patience et ses enseignements durant mon séjour à Bordeaux et au-delà.

À l'Institut de Chimie de la Matière Condensée de Bordeaux (ICMCB) et à l'Institut des Sciences Moléculaires (ISM) et aux personnes que j'ai rencontrées dans ces laboratoires, pour toute l'aide et la structure. Je remercie les professionnels Sylvain Danto, Olivier Toulemonde, Patrick Rosa, Mattieu Duttine et Alexandre Fargues, Fred Adamietz, Vincent Rodriguez, Christian Aupetit et, en particulier, mes amis William, Gislene, Ana, Janete, Georges, Florian, Rayan, Fouad, Alizée, Louis, Sara, Mikko, Romain, Simon, Samar, Shashank, Alice, Julia, Lara, Clara, Simon, pour la convivialité à l'intérieur et à l'extérieur du laboratoire.

I hope I have reached as many people as possible. You were part of the construction of this work and of this person who speaks to you. No one can win alone!

If I have seen further it is by standing on the shoulders of Giants

Quando a educação não é libertadora, o sonho do oprimido é ser o opressor.

When education is not liberating, the dream of the oppressed is to be the oppressor.

Quand l'éducation n'est pas libératrice, le rêve de l'opprimé est d'être l'oppresseur.

Paulo Freire (1921–1997)

Citação atribuída a Paulo Freire no livro "*Começando bem, frases e pensamentos"*, de Carlos H. Biagolini (2009). A frase não está presente na obra "*Pedagogia do oprimido*", trata-se de um resumo das ideias do autor

Resumo

O estudo e preparação de novos materiais magneto-ópticos tem ganhado atenção significativa devido às suas potenciais aplicações em vários domínios tecnológicos. Vidros que suportam altas concentrações de íons paramagnéticos estão sendo muito procurados para esses fins, devido às propriedades inerentes que podem ser impostos aos vidros como alta janela de transmissão, altos índices de refração, fácil síntese e modelagem, todas propriedades interessantes para sistemas ópticos e inerente isotropia. Esta tese de doutorado investiga o domínio da ciência de materiais, investigando a síntese e ampla caracterização de dois sistemas vítreos, um borotungstato contendo primeiro térbio e posteriormente um estudo estendido a outros lantanídeos, e um sistema de fosfato de antimônio contendo manganês. O objetivo geral desta pesquisa é sintetizar materiais inovadores que possuam atributos magneto-ópticos elevados e interessantes, com ênfase específica em seu potencial utilidade em dispositivos que aproveitem o efeito Faraday. O estudo apresenta diferentes experimentos para determinar as características térmicas, ópticas, luminescentes, estruturais, magnéticas e magneto-ópticas dos sistemas propostos, garantindo um conhecimento aprofundado de diferentes técnicas, conceitos e métodos, importantes para aumentar o crescimento científico em química e físico-química de materiais não-cristalinos. Foram obtidos excelentes valores de constante de Curie, até 6.77 $emu.Oe^{-1}.mol^{-1}$, valores maiores que relatados na literatura, e constante de Verdet de 124 $rad.T^{-1}.m^{-1}$ 632.8 nm para amostra com 27.5 %mol de Tb_2O_3, comparáveis a vidros e monocristais comerciais, e -55.1 $rad.T^{-1}.m^{-1}$ para a amostra 30%mol de MnO, valores inéditos para esse tipo de rotador Faraday. Ao examinar o impacto de composições variadas nas propriedades estruturais, ópticas e magnéticas dos materiais resultantes, esta tese contribui para uma compreensão mais profunda da interação entre metais de transição, terras raras e o comportamento magneto-óptico de vidros. Além disso, a tese avalia a capacidade dessas composições de vidro em exibir rotação de Faraday. Os insights obtidos com essa pesquisa não apenas avançam no conhecimento fundamental sobre a influência desses íons paramagnéticos na resposta magneto-óptica, mas também abrem caminho para o design e a realização de novos materiais magneto-ópticos. Como resultado de investigação rigorosa, esta tese de doutorado contribui significativamente para a compreensão científica e desenvolvimento prático de materiais preparados para moldar a perspectiva de aplicações magneto-ópticas.

Résumé

L'étude et la préparation de nouveaux matériaux magnéto-optiques ont fait l'objet d'une attention particulière en raison de leurs applications potentielles dans divers domaines technologiques. Les verres qui supportent de fortes concentrations d'ions paramagnétiques sont largement recherchés à ces fins, en raison des propriétés inhérentes aux verres telles que l'isotropie, la fenêtre de transmission élevée, les indices de réfraction élevés, la synthèse et la modélisation faciles, toutes des propriétés intéressantes pour les systèmes optiques. Cette thèse de doctorat étudie le domaine de la science des matériaux avancés, en étudiant la synthèse et la caractérisation complète de deux systèmes vitreux, un borotungstate contenant d'abord du terbium et plus tard une étude étendue à d'autres lanthanides, et un système de phosphate d'antimoine contenant du manganèse. L'objectif global de cette recherche est de synthétiser des matériaux innovants qui ont des attributs magnéto-optiques élevés et intéressants, avec un accent particulier sur leur utilité potentielle dans les dispositifs qui tirent parti de l'effet Faraday. L'étude présente différentes expériences pour déterminer les caractéristiques thermiques, optiques, luminescentes, structurelles, magnétiques et magnéto-optiques des systèmes proposés, garantissant une connaissance approfondie des différentes techniques, concepts et méthodes, importants pour accroître la croissance scientifique en chimie et physique chimique des matériaux non cristallins. D'excellentes valeurs de constante de Curie ont été obtenues, jusqu'à 6,77 $emu.Oe^{-1}.mol^{-1}$, valeurs supérieures à celles rapportées dans la littérature, et une constante de Verdet de 124 $rad.T^{-1}.m^{-1}$ 632,8 nm pour un échantillon de 27,5 % mol de Tb_2O_3, comparable aux verres et monocristaux commerciaux, et -55,1 $rad.T^{-1}.m^{-1}$ pour l'échantillon à 30%mol MnO, des valeurs sans précédent pour ce type de rotateur de Faraday. En examinant l'impact de différentes compositions sur les propriétés structurelles, optiques et magnétiques des matériaux résultants, cette thèse contribue à une compréhension plus approfondie de l'interaction entre les métaux de transition, les terres rares et le comportement magnéto-optique des verres. De plus, la thèse évalue la capacité de ces compositions de verre à présenter une rotation de Faraday. Les connaissances acquises grâce à cette recherche font non seulement progresser les connaissances fondamentales sur l'influence de ces ions paramagnétiques sur la réponse magnéto-optique, mais ouvrent également la voie à la conception et à la réalisation de nouveaux matériaux magnéto-optiques. Fruit de recherches rigoureuses, cette thèse de doctorat contribue de manière significative à la compréhension scientifique et au développement pratique de matériaux prêts à façonner les perspectives d'applications magnéto-optiques.

Abstract

The study and preparation of new magneto-optical materials has gained significant attention due to their potential applications in various technological domains. Glasses that support high concentrations of paramagnetic ions are being widely sought after for these purposes, due to the inherent properties of glasses such as isotropy, high transmission window, high refractive indexes, easy synthesis and modelling, all interesting properties for optical systems. This doctoral thesis investigates the domain of advanced materials science, investigating the synthesis and comprehensive characterization of two glassy systems, a borotungstate containing first terbium and later an extended study to other lanthanides, and an antimony phosphate system containing manganese. The overall objective of this research is to synthesize innovative materials that have high and interesting magneto-optical attributes, with specific emphasis on their potential utility in devices that take advantage of the Faraday effect. The study presents different experiments to determine the thermal, optical, luminescent, structural, magnetic and magneto-optical characteristics of the proposed systems, guaranteeing an in-depth knowledge of different techniques, concepts and methods, important to increase the scientific growth in chemistry and chemical physics of non-crystalline materials. Excellent Curie constant values were obtained, up to 6.77 $emu.Oe^{-1}.mol^{-1}$, values higher than those reported in the literature, and Verdet constant of 124 $rad.T^{-1}.m^{-1}$ 632.8 nm for a sample with 27.5% mol of Tb_2O_3, comparable to commercial glasses and single crystals, and -55.1 $rad.T^{-1}.m^{-1}$ for the 30%mol MnO sample, unprecedented values for this type of Faraday rotator. By examining the impact of varying compositions on the structural, optical, and magnetic properties of the resulting materials, this thesis contributes to a deeper understanding of the interplay between transition metals, rare earths, and the magneto-optical behavior of glasses. Furthermore, the thesis evaluates the ability of these glass compositions to exhibit Faraday rotation. The insights gained from this research not only advance fundamental knowledge about the influence of these paramagnetic ions on magneto-optical response, but also pave the way for the design and realization of new magneto-optical materials. As a result of rigorous research, this doctoral thesis contributes significantly to the scientific understanding and practical development of materials poised to shape the prospect of magneto-optical applications.

List of Figures

List of Figures in Appendix

List of Tables

List of Equations

Summary

CHAPTER I – Introduction

Sixth Solvay Conference, whose theme was "*Le magnétisme*". Paris, 1930 [47].

Seated in front: Th. de Donder, P. Zeeman, P. Weiss, A. Sommerfeld, M. Curie, P. Langevin, A. Einstein, O. Richardson, B. Cabrera, N. Bohr, W. J. De Haas;

Standing: E. Herzen, E. Henriot, J. Verschaffelt, C. Manneback, A. Cotton, J. Errera, O. Stern, A. Piccard, W. Gerlach, C. Darwin, P. A. M. Dirac, H. Bauer, P. Kapitsa, L. Brillouin, H. A. Kramers, P. Debye, W. Pauli, J. Dorfman, J. H. Van Vleck, E. Fermi, W. Heisenberg.

Chapter I - Introduction

1. GLASSES

1.1. Brief history of the emergence of glassworking, glassmaking and photonic glasses.

Looking at vitreous materials, from the most common and trivial to the most technological niche, it's difficult to grasp the antiquity of the crafting and production of this category of materials. Glass is one of the oldest materials to have been processed by mankind. As natural materials, found in the environment, and due to their characteristics of easy handling, being able to form excellent sharp flakes for making knives, arrowheads and spears, natural glasses, especially obsidian, were used by hominids for making tools from at least 500,000 years ago, during the Lower Paleolithic, in what is now Kenya [1].

Our species, Homo sapiens, did not appear until 315,000 years ago, so the art of manipulating glass predates humanity. With the expansion of Homo sapiens and the exit from Africa to Eurasia (90,000 years ago), and the discovery of new sites containing obsidian, this material continued to be used. During the Mesolithic (20,000 - 12,000 years ago) and Neolithic (12,000 - 7,500 years ago) periods, obsidian became increasingly important due to its ability to form more complex tools, including finer and sharper points, needles, hooks, knives, implements, jewelry, and various other items[2–6].

Artificial glass, on the other hand, is a relatively modern development, though still surprisingly old. Archaeological evidence suggests that non-crystalline, glass-like materials called faience were used in ancient Egypt, Mesopotamia, and Syria well before the production of glass itself [7]. Egypt's favorable preservation environment means that most of the early, well-studied glassware is located there, although some may have been imported[8,9]. The earliest known glass objects, which were beads dating back 5500 years ago, were likely produced by accident during metal smelting or by the production of faience, a vitrified ceramic formed by mixing crystalline and non-crystalline phases, using a high-temperature firing process. Significantly, the emergence

of high-temperature furnaces capable of melting copper and bronze allowed for the production of faience.[10]

Around 2600 BC, there is evidence of the first human-made glass, which was still quite opaque due to the technology of the time. Glass preparation techniques spread and improved with the expansion of the Bronze Age and trade between Asia Minor, Africa and Europe. As a result, increasingly complex pieces were produced, which were cheaper, more transparent, and had better results, such as in terms of shape and color.[11,12]

Jumping ahead to the Roman domain of the Mediterranean, it was the Romans who became the first people to dominate the making of transparent glass. They perfected the blowing method, which involves using a metallic pipe and leaving the molten material forming a bubble while shaping it. Additionally, the Romans excelled in the production of stained glass. They were also the pioneers of the technique of producing colored stained glass for churches by adding salts during synthesis, which was highly explored in the Middle Ages to create glass of different colors. Furthermore, we must acknowledge the Lycurgus cup depicted in Figure 1 that exhibits a unique attribute of having two colors, one when viewed from the outside (reflection) and the other when viewed from the inside (transmission). Researchers were highly intrigued until a more in-depth evaluation using transmission electron microscopy revealed the presence of gold and silver nanoparticles in glass, in specific sizes and shapes. This was one of the initial demonstrations of control over crystal growth and nanotechnology. The Lycurgus cup, dating back to the 4th century, remains an enigma regarding the process used by the ancient Romans to manufacture it [13].

The glasswork produced by guilds in Venice and on the Murano islands was a notable attraction for the city-state in the Middle Ages. The addition of lead in the glass melting process alongside the development of high-temperature furnaces produced transparent glasses with a higher refractive index. This advance gave rise to the lenses in early modern telescopes and microscopes. From the 16th century onwards, handmade glass in Bavaria became famous for dominating these properties. The production was a state secret for the Bavarians. Michael Faraday was interested in synthesizing these

glasses (lead borosilicates) at the beginning of his career at the Royal Institution in London. We will discuss this in the next sections.

Figure 1. The Lycurgus Cup in reflected (a) and transmitted (b) light. Scene showing Lycurgus being enmeshed by Ambrosia, now transformed into a vine-shoot [The Trustees of the British Museum, Department of Prehistory and Europe, The British Museum. Height: 16.5 cm (with modern metal mounts), diameter: 13.2 cm][13].

The glass industry was a part of the Industrial Revolution. Synthetic and refined raw materials were used for the first time in the production of windows and inert packaging. However, the unpredictability and non-homogeneity on an industrial scale were still problematic. The high, consistently accurate and reproducible optical qualities in glasses resulted from the joint efforts of Otto Schott, Carl Zeiss, and Ernst Abbe. They founded one of the pioneer glass companies, Glastechnische Laboratorium Schott & Genossen (current Schott & Associates Glass Technology Laboratory) based in Jena, capitalizing on their specialized skills. There have been significant advancements in developing new glass materials since then. For instance, the discovery of lanthanum-doped glasses in the 1930s [14], the development of no oxygen–containing chalcogenide

glasses in the 1953[15], with high transparency in the near and mid-infrared (NIR and MIR), the first metallic glass in 1960[16], the first glass laser in 1961[17], and the discovery of fluoride glasses in 1974 by Jacques Lucas, Michel and Marcel Poulain[18].

One of the most pertinent studies conducted on photonic glasses was the report by Charles K. Kao published in 1966 which concluded that the primary issue concerning the production of optical fibers for telecommunication was inadequate material purity. He predicted that fibers created from highly pure materials would exhibit a loss lower than 0.3 dB/km[19]. Consequently, Kao's accomplishment earned him the Nobel Prize in Physics in 2009. By 1970, fiber optics degradation of as low as 20 dB/km at 632.8 nm had already been achieved by Corning. In 1979, the preform and fiber production processes were further refined, decreasing the value to 0.20 dB/km at 1550 nm. Currently, the minimum attenuation in mass-produced single-mode fiber is less than 0.17 dB/km[20]. Optical fibers enabled and still enable information and knowledge to travel across the planet at the speed of light, they are the backbone of the Internet and the key to today's global communications revolution. During the COVID-19 pandemic, we made extensive use of long-distance conferencing services powered by fiber optics, which kept us together during those difficult times.

Glasses are present from the windows to cell phone screens. From beverage bottles to vaccine flasks. Composites made from bioglass have improved health care through their ability to integrate with human bone. Glass panels support solar cells and provide clean energy. The development of glass optics and optoelectronics means the James Webb Space Telescope can study the first moments after the Big Bang and expand our understanding of the universe. Glass artists around the world have introduced humanity to this wonderful material, including its remarkable fabrication methods, its inherent beauty, and its ability to capture and display nature's full spectrum of colors[21,22].

For these and many other reasons, the UN General Council declared 2022 as the International Year of Glass. Throughout history, we define ages by the materials and movements that transformed civilization, such as the Stone Age, Bronze Age, Iron Age, which provided revolutions in the civilizations that experienced them. And, as well proposed by David L. Morse and Jeffrey W. Evenson, both researchers at Corning

Incorporated, we currently live in the "Age of Glass", due to all the social, cultural, and technological transformations associated with this class of material [23]. Welcome to the Glass Age!

1.2. Development of the definition of glasses.

Although glass has been used by humans for a long time, its definition has been the subject of several debates among scholars throughout history. One of the early pioneers in the study of glasses was the renowned physicist and chemist Michael Faraday (1791-1867), who defined them as follows:

> "Glass may be considered rather as a solution of different substances one in another, than as a strong chemical compound." Michael Faraday, 1830[24]

In the late 19th and early 20th centuries, Gustav Tammann (1861-1938) conducted experiments that proved the possibility of creating glasses from substances besides silica. To achieve ideal and homogeneous vitrification, it was essential to prevent the creation of crystalline nuclei, which leads to the expansion of macroscopic crystals. The possible vitrification process depends on the melting temperature of the material, the temperature for liquidus pouring, and/or tempering (a heat treatment used after glass formation to reduce post-quenching stress)[25]. After conducting these studies, glass definitions were formulated based on the viscosity of solids concept. This approach was necessary because, until then, glasses had only been prepared via the melting-quenching method, which involves rapidly cooling a molten substance. The viscosity criterion defines a solid as rigid material that doesn't flow when exposed to moderate forces. As a quantitative measure, a solid can be defined as a substance with a viscosity exceeding 10^{14} Pa.s.

> "Glass is non-crystalline, strongly supercooled melt inorganic product, which reaches a rigid condition by cooling, through a progressive increase in viscosity, without crystallization occurring." Gustav Tammann, 1925[26]

The emergence of techniques such as X-ray diffraction and the initial results from measuring glass samples[27–30] revealed that the structural organization of glasses resembles that of liquids more than crystalline solids. In 1932, William Houlder Zachariasen, a Norwegian-American researcher, published the well-known article *'The Atomic Arrangement in Glass'*, where he formulated his Random Network Theory (RNT) in glasses while studying their diffractograms. Zachariasen established the structural basis for the formation of glasses by melting-quenching and suggested that "*the atomic arrangement in glasses was characterized by an extended three-dimensional network, which lacked symmetry and periodicity*", and that "*interatomic forces were comparable to those of the corresponding crystal*". Additionally, the researcher notes that the presence or absence of periodicity and symmetry in a three-dimensional network distinguishes between a crystal and a glass.[31]

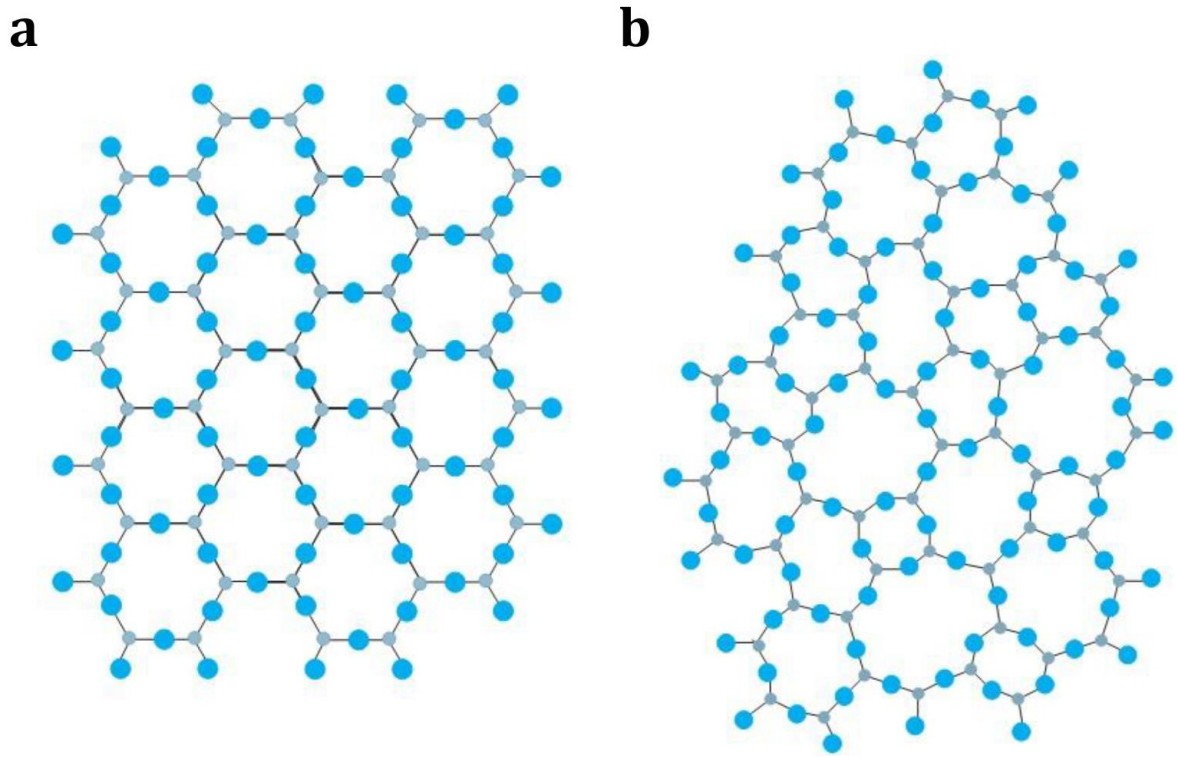

Figure 2. Two-dimensional schematic representation illustrating the difference between: (a) the symmetrical and periodic crystalline arrangement of a crystal of composition A_2O_3; (b) representation of the glass network of the same compound, in which the absence of symmetry and periodicity is characterized. (Adapted from [31])

Figure 2a shows the symmetric and periodic crystal arrangement of a crystal composition A_2O_3 in a two-dimensional format, while Figure 2b shows the glass network for the same compound, demonstrating the absence of symmetry and periodicity. This theory made the article a landmark in Glass Science. By combining Zachariasen's RNT and the contemporary concept of glass at the time of publication, we may arrive at the following definition:

> "Glasses are described as supercooled liquids or as solids, with absence of periodicity in the network, isotropic materials." William H. Zachariasen, 1932[31]

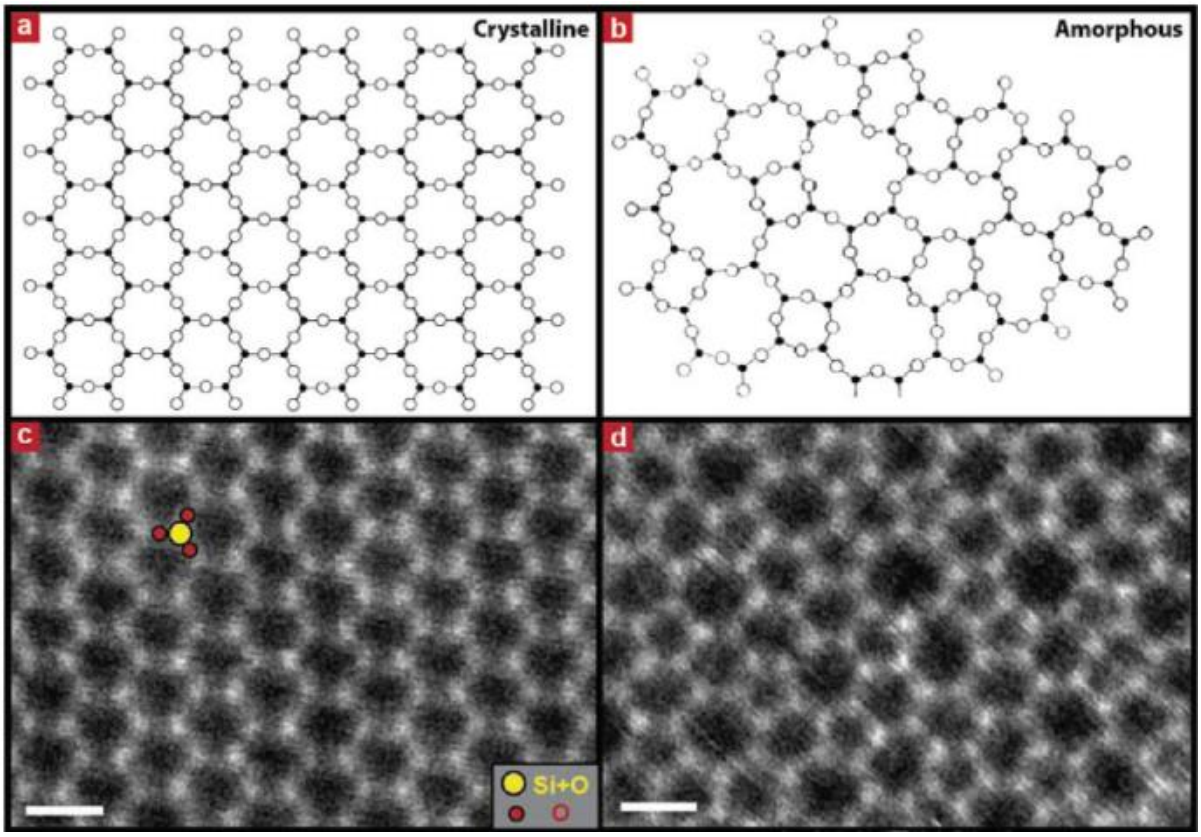

Figure 3. Atomic-resolution images of a 2D glass. (a,b) Zachariasen's models for a 2D crystal and a 2D amorphous glass. (c,d) Experimental TEM images of 2D crystalline and amorphous silica supported by graphene.[32]

In 2012, P. Y. Huang et al. [32] and M. Heyde et al. [33] demonstrated the atomic structure of a two-dimensional silica glass supported on graphene using

transmission electron microscopy (TEM), which emphasizes Zachariasen's accurate, insightful, and pioneering spirit. Transmission electron microscopy (TEM) experimental findings, as presented in Figure 3, closely resembled the picture proposed by Zachariasen 80 years earlier in 1932. The strong qualitative resemblance of these images to Zachariasen's model indicates that they show a 2D glass that approximately complies with the continuous random network model.

In the years following Zachariasen's publication, new definitions were proposed. These were based on the non-crystalline properties of glasses, their viscosity, and the glass transition. There are several definitions for glasses found in the literature:

> "Glass is an X-ray amorphous material that exhibits the glass transition. This being defined as that phenomenon in which a solid amorphous phase exhibits with changing temperature (heating) a more or less sudden change in its derivative thermodynamic properties such as heat capacity and expansion coefficient, from crystal-like to liquid-like value". J. Wong and C. Austen Angell, 1976[34]

> "Glasses are amorphous materials that do not have long-range translational order (periodicity), characteristic of a crystal, with glass being an amorphous solid that exhibits a glass transition." S. R. Elliott, 1989[35]

> "A glass is a non-crystalline solid exhibiting the glass transition phenomenon." J. Zarzycki, 1991[36]

> "Glass is an amorphous solid. A material is amorphous when it lacks long-distance order, that is, when there is no regularity in the arrangement of molecular constituents, on a scale larger than a few times the size of these groups. No distinction is made between the words vitreous and amorphous." R. H. Doremus, 1994[37]

However, these definitions are limited in several ways. The first one does not take into account glasses obtained by sol-gel or CVD (chemical vapor deposition). The second definition would emphasize that glasses can be formed from any composition - theoretically - whether it be inorganic, organic, biological, or metallic.

It is worth mentioning that until now, there has been no consensus on whether glasses are solids or supercooled liquids with such high viscosity that they appear solid but flow over time. This theory originated from the observation of ancient medieval stained glass in Europe. It was noted that the bottom of stained-glass windows were thicker than the top, implying the glass might have flowed over the centuries. The discussion culminated in an article entitled "*Do cathedral glasses flow?*" written by Edgar D. Zanotto [38]. Through viscosity measurements and calculations, they found that cathedrals' silica glasses would require 10^{32} years to flow significantly. This period is significantly longer than the current age of the Universe (13.8×10^9 years). The thicker base of stained glass was one of the challenges in producing flat glass during the medieval period. When placing the glass in the window, artisans favored positioning its thickest part downwards to prevent breakage.

> "Glass is an amorphous solid with complete absence of long-range order and periodicity, exhibiting a glass transition region. Any material, inorganic, organic or metal, formed by any technique, that exhibits a glass transition phenomenon is a glass." J. E. Shelby, 1997[39]

Gupta[40] proposed that a non-crystalline solid (characterized by the presence of a halo on the X-ray diffractogram without any identifiable peaks) can be divided, from a thermodynamic standpoint, into two different categories: glasses and amorphous solids. Non-crystalline solids refer to materials that possess an extended and random three-dimensional network, i.e., characterized by a lack of symmetry and translational periodicity. From a thermodynamic perspective, a non-crystalline solid is considered a glass when it undergoes the glass transition phenomenon. As a result, amorphous solids can be classified as non-crystalline solids that do not manifest the glass transition. New definitions have been suggested to support this new classification:

> "A glass is a non-crystalline solid, therefore, with absence of symmetry and translational periodicity, which exhibits the phenomenon of glass transition, and can be obtained from any inorganic, organic or metallic material and formed through any preparation technique." O. L. Alves, I. F. Gimenez and I. O. Mazali, 2001[41]

> "Glass is a solid having a non-crystalline structure, which continuously converts to a liquid upon heating." Arun K. Varshneya, 2012[42]

We finally arrived in 2017, when the researchers Edgar D. Zanotto and John C. Mauro published the article "*The glassy state of matter: Its definition and ultimate fate*"[43], in which they revised the old definitions and created a new, more comprehensive one, with a focus on both researchers in the field and the lay public:

> "Glass is a nonequilibrium, non-crystalline condensed state of matter that exhibits a glass transition. The structure of glasses is similar to that of their parent supercooled liquids (SCL), and they spontaneously relax toward the SCL state. Their ultimate fate, in the limit of infinite time, is to crystallize". Edgar D. Zanotto and John C. Mauro, 2017

Theoretically, any substance can be turned into glass, as long as we can cool it from a liquid or gaseous state at such a high rate that the atoms and molecules that make it up do not have enough time to arrange themselves into organized structures that are thermodynamically more stable. As Varshneya concludes, "*the kinetic theory of glass formation does not address the question as to what structural characteristics of substances encourage ready glass formation. It assumes that all substances can be brought into glassy state. The only question it addresses is what minimum cooling rate is required to avoid a perceptible degree of crystallization"*[42]. Each substance has its own properties, so the cooling rate can be very different from one substance to another. For example, for liquid water to turn into glass, the cooling rate must be 10^7 K . s^{-1},

while for silica this rate is 0.9×10^{-6} K . s^{-1}, which makes obtaining glasses of water more expensive and requires more specific techniques, in addition to limiting the size of the bulk, as there is a temperature gradient during the cooling process[44].

1.3. Glass formation from a melt.

Traditionally, conventional glasses are produced using the melting/quenching method. This method includes the melting of a mixture of initial materials, typically at high temperatures until they turn into a homogenous liquid. Then, the mixture is rapidly cooled to increase its viscosity and maintain its non-crystalline characteristic. The structures of the raw material of a glass are similar to a liquid when melted. As cooling occurs, and its viscosity increases, the molten material can follow different structural patterns based on the cooling rate used.

Figure 4 shows the volume-temperature (V-T) diagram for a glass-forming liquid. According to the diagram, starting from high to low temperatures, we have the *abc* path, which shows the natural path for crystal formation. When we reach the melting temperature (or melting point, freezing temperature) Tf, we have an abrupt change in volume (or enthalpy) and, finally, the crystal is formed, being the lowest energy level of the compound itself. However, it is possible to cool liquids at temperatures below Tf. This metastable condition is known as super cooled liquids (SCL). It is important to point out that as the temperature decreases, the viscosity of the SCL increases proportionally. If this cooling is faster, we have the *ade* path. The gradual increase in viscosity occurs until the SCL does not flow, forming the glass. The transition from the SCL to the glass is instituted when the viscosity reaches the value of 10^{14} Pa.s. The temperature at which this transition occurs is defined as the glass transition temperature (Tg). As observed in the *afg* path, if the cooling rate occurs more slowly, the viscosity increases in the same proportion, forming a different glassy phase, with a different Tg, density and enthalpy, starting from the same initial liquid.

The Tg represents the temperature range where structural relaxation starts (10^{14} Pa.s), transitioning from the glassy to the viscoelastic state. At this stage, certain properties such as viscosity, heat capacity, and thermal expansion begin to behave

differently than previously observed. Structural relaxation arises from unobstructed translational movements of chains relative to one another.

It is imperative to note that the V-T diagram is solely applicable to glasses created through melting-quenching. For instance, in the sol-gel process which achieves glasses from solutions at room temperature, and is a method unsuitable for V-T diagram application.

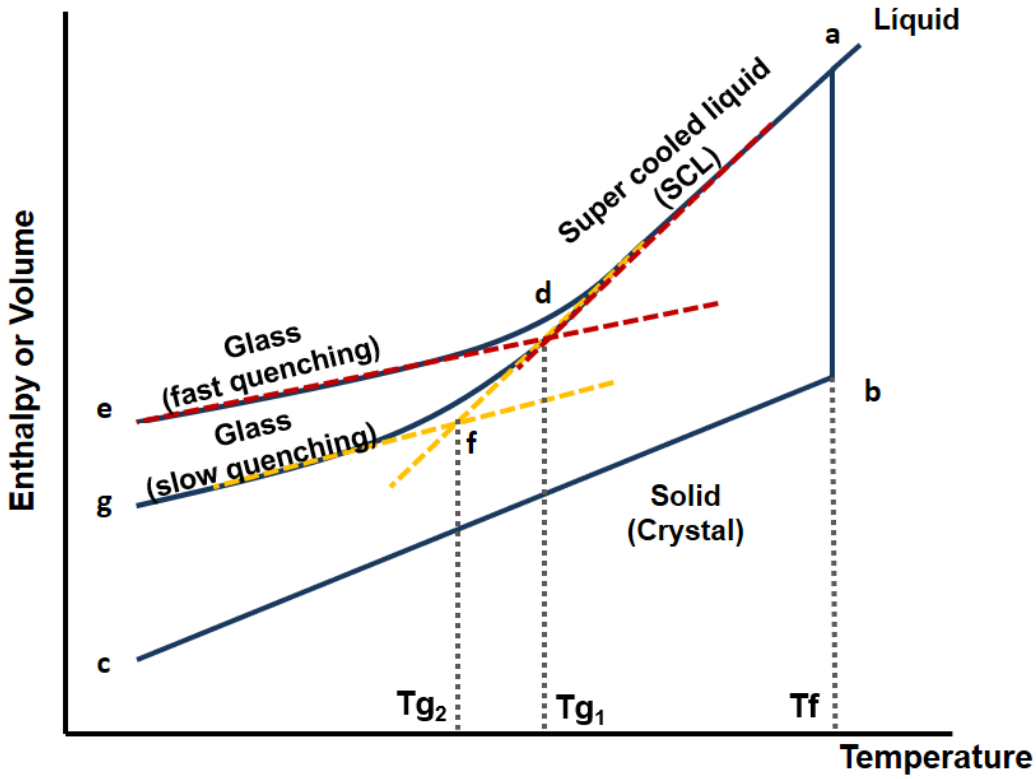

Figure 4. The volume-temperature diagram for a glass-forming liquid. *abc* path is related to the transition from a liquid to a conventional solid, with the transformation taking place at the melting point. *ade* path corresponds to a decrease in temperature and increase in viscosity of the liquid, becoming a supercooled liquid, and finally, with a sudden decrease in temperature and increase in viscosity, forming a glass. *afg* path corresponds to the same transformation, but with faster quenching. (Adapted from [43]).

2. MAGNETO-OPTICAL PROPERTIES

2.1 Brief history of magnetism and magneto-optical effect.

Magnetic phenomena have been present since the beginning of humanity. According to Roger Elliot: "*magnetism provides a particularly good example of the way in which the exact sciences have developed*"[45]. Magnetism was already known by the ancient Sumerians, Greeks, Chinese and America pre-Columbian people for millennia and interpreted it as magic. The name "*magnetic*" has its Greek origin, coming from the ferromagnetic stones extracted from the region of Magnesia, which became known as magnetites (from Greek μαγνῆτις [λίθος] - magnētis [lithos] - meaning "[stone] from Magnesia")[45,46].

During the Middle Ages, the Chinese developed the compass, a maritime instrument that was very relevant to the Chinese discoveries in the 15th century and the Iberian discoveries in the 16th and 17th centuries. In 1600, the Englishman William Gilbert (1544–1603) wrote *De Magnete, Magneticisque Corporibus, et de Magno Magnete Tellure* (On the Magnet and Magnetic Bodies, and on That Great Magnet the Earth), which is known to be the first scientific study on magnetism. In his work, Gilbert suggests that the Earth also operates as a large magnet [47].

In 1820, Hans-Christian Ørsted (1777-1851), a Danish physicist, observed that a defect occurred in a compass that was accidentally placed near his experiment while he was studying electricity and applied a current to metallic wires. This provided evidence that there was a physical relationship between electricity and magnetism. The unit of magnetic induction (Oe, oersted) in the centimeter-gram-second system (CGS) is named after Ørsted due to his contributions to the field of electromagnetism[47].

At the Royal Society in London, Humphry Davy (1778-1829) and William Hyde Wollaston (1766-1828) attempted to create an electric motor using magnets after learning of Ørsted's work, but it was Davy's student, Michael Faraday (1791-1867), who succeeded in creating the motor by using a steel magnet, a current-carrying wire, and a container of mercury as early as 1821. Faraday publicized his results in excitement without giving credit to Wollaston or Davy, causing controversy within the Royal Society. The controversy strained Faraday's relationship with his mentor Davy and possibly led to his assignment to other pursuits by the Royal Society. Faraday resumed his work on magnetism only after Davy's death years later[47,48].

In 1845, Faraday demonstrated that it was possible to change the plane of polarization of a beam of light when this beam passed through a specific medium (in this case, a glass containing PbO with a high refractive index) under a magnetic field application, parallel to the direction of light propagation. This effect became known as the Faraday effect, the first of the discovered magneto-optical effects[49,50]. Showing the relevance of this discovery, the Faraday effect proved that light is an electromagnetic radiation, mathematically demonstrated in 1864 by James Clerk Maxwell, unifying the theories of electricity, magnetism and light, which is summarized in the four famous equations that bear his name:

$$\oint \vec{E} \, . d\vec{A} = \frac{q}{\varepsilon_0} \qquad Gauss's\ Law \qquad (Eq.1)$$

$$\oint \vec{B} \, . d\vec{A} = 0 \qquad Gauss's\ law\ for\ magnetism \qquad (Eq.2)$$

$$\oint \vec{E} \, . d\vec{s} = -\frac{d\Phi_B}{dt} \qquad Faraday's\ law\ of\ induction \qquad (Eq.3)$$

$$\oint \vec{B} \, . d\vec{s} = \mu_0 \varepsilon_0 \frac{d\Phi_E}{dt} + \mu_0 i \qquad Ampère's\ circuital\ law \qquad (Eq.4)$$

where $\vec{E}$ is electric field, $\vec{B}$ is the magnetic field, $d\vec{A}$ is the differential surface vector, $d\vec{s}$ is the differential length vector, **q** is the charge, ε_0 is the vacuum electric permeability, μ_0 is the vacuum magnetic permeability, $d\Phi_B$ is the magnetic flux, $d\Phi_E$ is the electric flux, **dt** is the time and **i** the unit imaginary number[47].

In 1877, the Scottish physicist John Kerr (1824–1907) managed to change the polarization of a beam of light by reflection, under a magnetic field, which became known as the magneto-optical Kerr effect (MOKE)[51,52]. Over time, new magneto-optical effects were discovered and described, such as for example the Zeeman, Voigt, Cotton–Mouton and inverse Faraday effects[53–55]. From now on, we will focus on the magneto-optical Faraday effect, which will be explored in this work.

2.2. Magnetism in atoms and macroscopic magnetic properties of materials.

Magnetic susceptibility (χ) is a measure of the magnetizing strength of a material in an applied magnetic field. It is the ratio of the magnetization **M** (magnetic moment per unit volume) to the strength of the applied external magnetic field **B**, as shown in Eq. 5 below. This allows a simple classification of the response of most materials to an applied magnetic field: aligned with the magnetic field and being attracted by it, $\chi > 0$, called paramagnetic, or non-aligned with the magnetic field, being repelled, $\chi < 0$, called diamagnetic.

$$\chi = \frac{M}{B} \qquad (Eq. 5)$$

These magnetic properties are intrinsic to all matter and come from the filling of electrons in the valence layers, that is, from the total angular momentum of an atom (or ion, or molecule), resulting from the coupling of magnetic (mℓ) and spin (s) quanta number. For half-filled orbitals, the unpaired electrons line up with B and are attracted to it. As for orbitals with fully paired electrons, there is a resistance for these electrons to pair with the field, being repelled by it. This comes from the **Pauli exclusion principle** and the **Hund's rule of maximum multiplicity**. The Pauli Principle allowed each orbital to accommodate a maximum of 2 electrons at the same time, as long as they had opposite spin signals, which became known as paired electrons. According to this Principle, no two particles can have the same set of four quantum numbers in the same system. Hund's rule also facilitated the study of polyelectronic orbitals, proposing that the energy of a subshell is lowest when the orbitals are half-filled and, therefore, it is energetically preferable for atoms to be in their lowest energy state, the ground state. The Bohr–Van Leeuwen theorem proves that every sort of magnetism is impossible for electrons in classical physics, being totally dependent on states and quantum numbers.

It is important to note that most atoms have at least one filled orbital, so the sum of paramagnetic (χ_{para}) and diamagnetic (χ_{dia}) susceptibility is present in materials. Unlike paramagnetism, diamagnetism is a property of all atoms in a molecule. While paramagnetism is caused by the presence of unpaired electrons in the molecule, all electrons, whether paired or unpaired, induce diamagnetism. The conflict between

paramagnetism and diamagnetism defines the total (measured) magnetic susceptibility χ_{meas}, which is positive for paramagnetic materials and negative for diamagnetic materials. Diamagnetic effects are temperature independent and are naturally orders of magnitude smaller, ~ 10^{-6} emu.mol^{-1}, than paramagnetic effects, ~ 10^{-2} emu.mol^{-1}. Figure 5 shows the resulting molar magnetic susceptibility for each atom. It is possible to analyze that certain elements have dominant diamagnetic values, and, for others, dominant paramagnetic values. Fe, Co, and Ni atoms naturally have high χ values (1-10 emu.mol^{-1}), which promotes ferromagnetic effects.

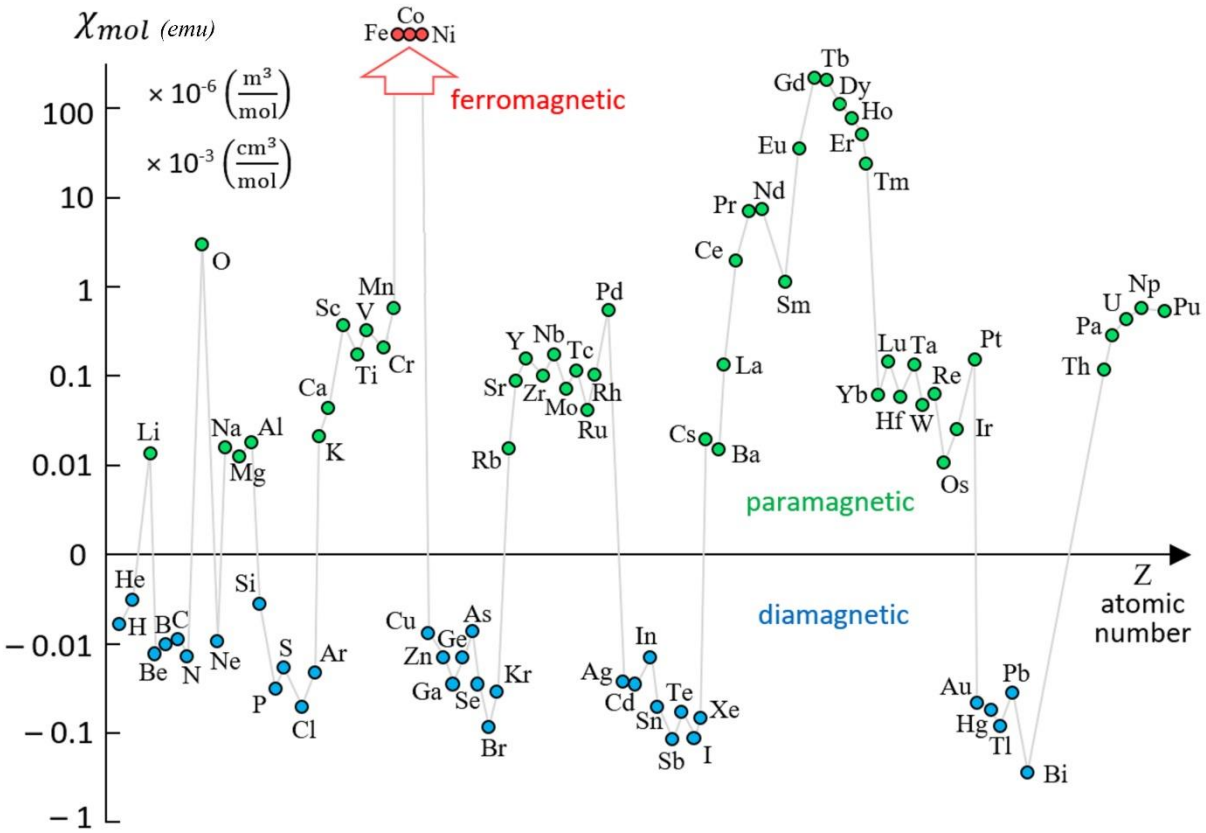

Figure 5. Variation of molar susceptibility for each atom. For some, the diamagnetic effect is dominant, mainly due to the filling of the valence orbitals. Negative values indicate that they are repelled by the external magnetic field, B. For others, the paramagnetic effect is the most relevant, due to the number of half-filled orbitals. Positive values show that they are attracted by B. Fe, Co and Ni atoms have naturally high susceptibility, promoting ferromagnetic characteristics [Figure from Stan Zurek, Magnetic susceptibility, Encyclopedia Magnetica].

The works of Paul Pascal[56–59] proposed that the diamagnetism of a molecule could be determined in an additive fashion using values for the diamagnetic susceptibility of every atom (χ_{Di}) and bond (λ_i) in the molecule, as show in Eq. 6

$$\chi_{dia} = \sum_i \chi_{Di} + \sum_i \lambda_i \qquad (Eq. 6)$$

Table 1 contain pre-determined χ_{dia} values for important groups of atoms or ions. These will be the values that will be used to determine the theoretical χ_{dia} of the glasses produced in this work and, from the χ_{meas}, determine the χ_{para}.

Table 1. Theoretical values of χ_{dia} for some ions[59].

Ion	O^{2-}	B^{3+}	W^{6+}	Tb^{3+}	Sb^{3+}
χ_{dia} (x 10^{-6} emu . mol^{-1})	-12	-0.2	-13	-19	-17
Ion	P^{5+}	Pb^{2+}	Zn^{2+}	Mn^{2+}	Mn^{3+}
χ_{dia} (x 10^{-6} emu . mol^{-1})	-1	-32	-15	-14	-10
Ion	Sm^{3+}	Eu^{3+}	Gd^{3+}	Dy^{3+}	Ho^{3+}
χ_{dia} (x 10^{-6} emu . mol^{-1})	-20	-20	-20	-19	-19

As stated earlier, paramagnetic effect arises from the interaction of B with the magnetic field of the unpaired electrons due to the coupling spin (S) and orbital angular momenta (L), the total angular momentum (J). Spin angular momentum is given by the product of the electron's spin quantum number and the Planck constant (h) divided by 2π, ħ. The spin quantum number can take on two possible values: +1/2 or -1/2, corresponding to the two possible orientations of the electron's spin, as show in Eq. 7.

$$\boldsymbol{S} = \left|\sum_{i=1}^{n} s_i\right| ; \qquad \boldsymbol{L} = \left|\sum_{i=1}^{n} l_i\right| ; \qquad \boldsymbol{J} = (\boldsymbol{L} + \boldsymbol{S}) \qquad (Eq. 7)$$

The orbital angular momentum (L) of an electron is given by the product of its orbital radius, its momentum, and the sine of the angle between its momentum vector and the radial vector pointing from the electron to the nucleus. This angular momentum can take on discrete values, determined by the principal quantum number (n), which is related to the shape of the electron's orbit. The possible values of l range from 0 to n-1, where n is the principal quantum number that specifies the energy level of the electron. The total angular momentum (J) is rise to several J –states, ranging $|L + S| \leq J \leq |L - S|$.

For paramagnetic effects, the magnetization M is directly proportional to an applied magnetic field B. However, if the material is heated, this proportionality is reduced. For a fixed field value, χ_{para} is inversely proportional to temperature, as shown in Eq. 8, called Curie's Law. The relation between χ and temperature was studied and postulated in the doctoral thesis of the French physicist Pierre Curie (1859–1906), entitled "*Propriétés magnétiques des corps à diverses temperatures" in 1895*[60].

$$\chi_{para} = \frac{M}{B} = \frac{C}{T} \qquad (Eq.8)$$

where T is temperature (K) and C is a material-specific Curie constant ($A.m^2.T^{-1}.mol^{-1}$).

Curie constant will depend on the J, which in turns depends on the atom (or ion, or molecule) ground state of each ion. Eq. (9) shows respectively those relations.

$$C = \frac{N_A {\mu_B}^2}{3\, k_B} . {\mu_{eff}}^2 = \mathbf{5/4} \, . \, {g_J}^2 [J(J+1)] \qquad Eq.(9)$$

in red, N_A is the Avogadro constant (6.022×10^{23} mol^{-1}), k_B is the Boltzmann constant (1.380×10^{-23} $J.K^{-1}$), μ_B is the electron's intrinsic magnetic moment, known as Bohr magneton ($e\hbar/2m_e = 9.274 \times 10^{-24}$ $A.m^2$). The ratio of these three constants is equal to the result **5/4** ($A.m^2.T^{-1}.mol^{-1}$) or **1/8** ($emu.Oe^{-1}.mol^{-1}$). the disordered state total magnetic moment, μ_{eff}, is dependent on J and the Landé g-factor, g_J, which is also a term dependent on the ground state of each ion, as shown in the Eq. (10).

$$g_J = 1 + \frac{J(J+1) + S(S+1) - L(L+1)}{2J(J+1)} \qquad Eq.\ (10)$$

It is possible to obtain the value of the Curie constant experimentally, observing the variation of the susceptibility varying the temperature, under a constant applied magnetic field. Figure 6a shows illustratively the variation of magnetic susceptibility with temperature, under constant B. χ_{dia} is not affected by temperature, but χ_{para} increases exponentially at T close to 0 K. Inset shown the inverse of susceptibility ($1/\chi_{para}$) versus temperature, varying linearity. The slope of this linear variation will be the value of the Curie constant. If the measured substance exhibits this linear behavior under $1/\chi_{para}$, it has paramagnetic interactions and follows Curie's law.

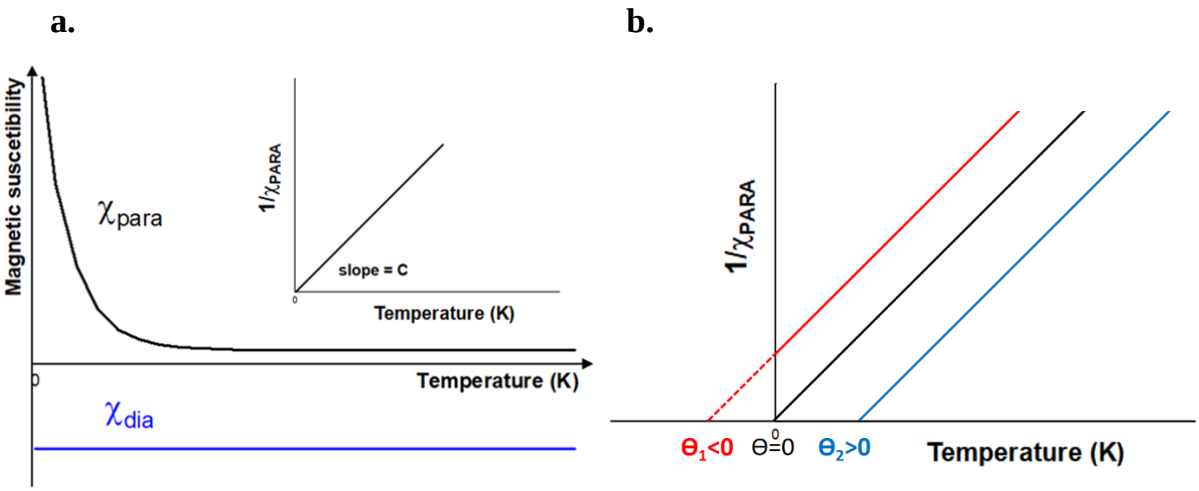

Figure 6. (a) Paramagnetic (black) and diamagnetic (blue) susceptibility versus temperature under constant applied magnetic field. Inset of shown the inverse of paramagnetic susceptibility versus temperature, varying linearity. (b) Curie's law deviation, with three different Weiss temperatures, $\theta < 0$, $\theta = 0$ and $\theta > 0$. [Adapted from [47]]

As observed in Figure 6b, some substances present a deviation in Curie's law. They still have the linear behavior for $1/\chi_{para}$, but the intercept is not exactly at 0 K, it can be before, or even after (using projection, since there are no values below 0 K). This effect occurs because there are interatomic interactions between moments, causing parallel or antiparallel spin alignments. This effect was added to Curie's law as the

correction constant θ (K), known as the Weiss Temperature, as shown in Eq. 11, the Curie–Weiss law, named in honor to Pierre-Ernest Weiss (1865–1940), who studied these effects[61].

$$\frac{1}{\chi_{para}} = \frac{1}{C}T + \left(-\frac{\theta}{T}\right) \qquad (Eq. 11)$$

For θ = 0 K, there are no interactions of interatomic spins and the equation becomes equal to Eq. 8. Now for, θ > 0 K, the spins are aligned parallel, causing low ferromagnetic interactions. If θ < 0 K, the spins are aligned antiparallel, causing low antiferromagnetic interactions. It is important to note that these interactions are insignificant compared to the paramagnetic effect and the ferromagnetism or antiferromagnetism effects have completely different behavior under the same conditions.

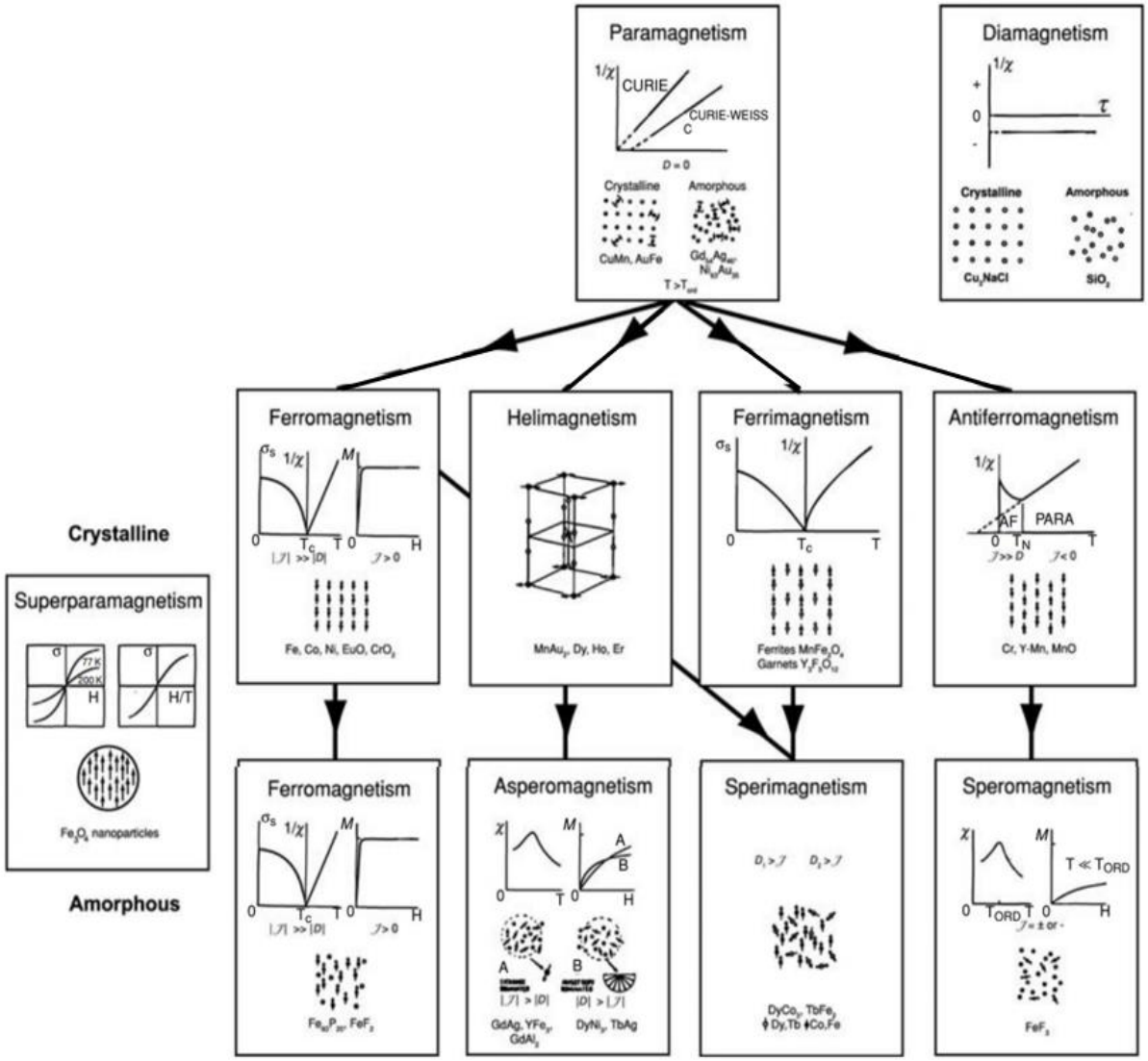

Figure 7. The magnetic family tree, showing the evolution of macro-magnetic properties, the behavior of magnetic susceptibility, the organization of spins and some examples of substances that have these effects, making clear the complexity of magnetic effects[47].

Now we can talk a little about the other magnetic effects. As seen in Figure 7, macroscopic magnetic effects arise from paramagnetism. It is present the names of the effects, the behavior of substances with this effect when we modify B or the temperature, drawings representing the ordering of spins, in addition to mentioning some compounds that present such effects. The most known are ferromagnetism, antiferromagnetism and ferrimagnetism, which differ in the way that the magnetic moments of atoms in a material are arranged.

Ferromagnetism is the most familiar type of magnetism, where the magnetic moments of the atoms are aligned parallel to each other within each domain, resulting in a net magnetic moment for the entire material. When an external magnetic field is applied, the magnetic domains become aligned with the field, leading to a strong attraction between the material and the magnetic field. They can be artificially magnetized applying a strong B for a period of time. It is observed in pure metals such as Fe, Ni and Co, as well as compounds such as Fe_3O_4 (found in magnetite) and $Nd_2Fe_{14}B$ (neodymium magnet).

Antiferromagnetism, on the other hand, is observed in certain materials such as chromium and manganese oxide. In antiferromagnetic materials, the magnetic moments of adjacent atoms are aligned in opposite directions, resulting in a net zero magnetic moment for the entire material. When an external magnetic field is applied, the magnetic moments become aligned with the field in a way that cancels out the overall magnetic moment of the material, leading to little or no attraction between the material and the magnetic field.

In ferrimagnetic materials, the magnetic moments of atoms in different sublattices are aligned parallel to each other, but the moments in different sublattices are oriented in opposite directions. This results in a net magnetic moment for the material, but it is smaller than in ferromagnetic materials. Ferrimagnetism is a complex phenomenon that arises from the competition between ferromagnetic and antiferromagnetic interactions within the material. This type of magnetism is observed in materials such as ferrites and garnets.

By raising the temperature of the substance, the ferromagnetic effect is lost, becoming the pure paramagnetic effect. The temperature at which this change occurs is called the Curie temperature, T_C (K). The same occurs for ferrimagnetic and antiferromagnetic substances. With increasing temperature, there is a transition from the effect in question to the paramagnetic effect. This temperature where the transformation of effects occurs is called the Néel temperature, T_N (K). Figure 8a illustrates the variation of magnetic susceptibility with temperature for hypothetical substances. Ferromagnetic and antiferromagnetic effects are present up to T_C and T_N, respectively. At higher temperatures, substances exhibit only the paramagnetic effect. Figure 8b. shows the

behavior of the same substances on a plot of the inverse of magnetic susceptibility versus temperature. Figure 8c. shows a representation of the spin alignments for these three substances, with parallel alignment in favor of the external field in for ferromagnets, antiparallel alignment, resulting in a null effect, for antiferromagnets, and an antiparallel alignment for ferrimagnets, but with differences in intensity between the spins (A > B) in the direction of external magnetic field, resulting in a non-zero effect, but smaller than for ferromagnets.

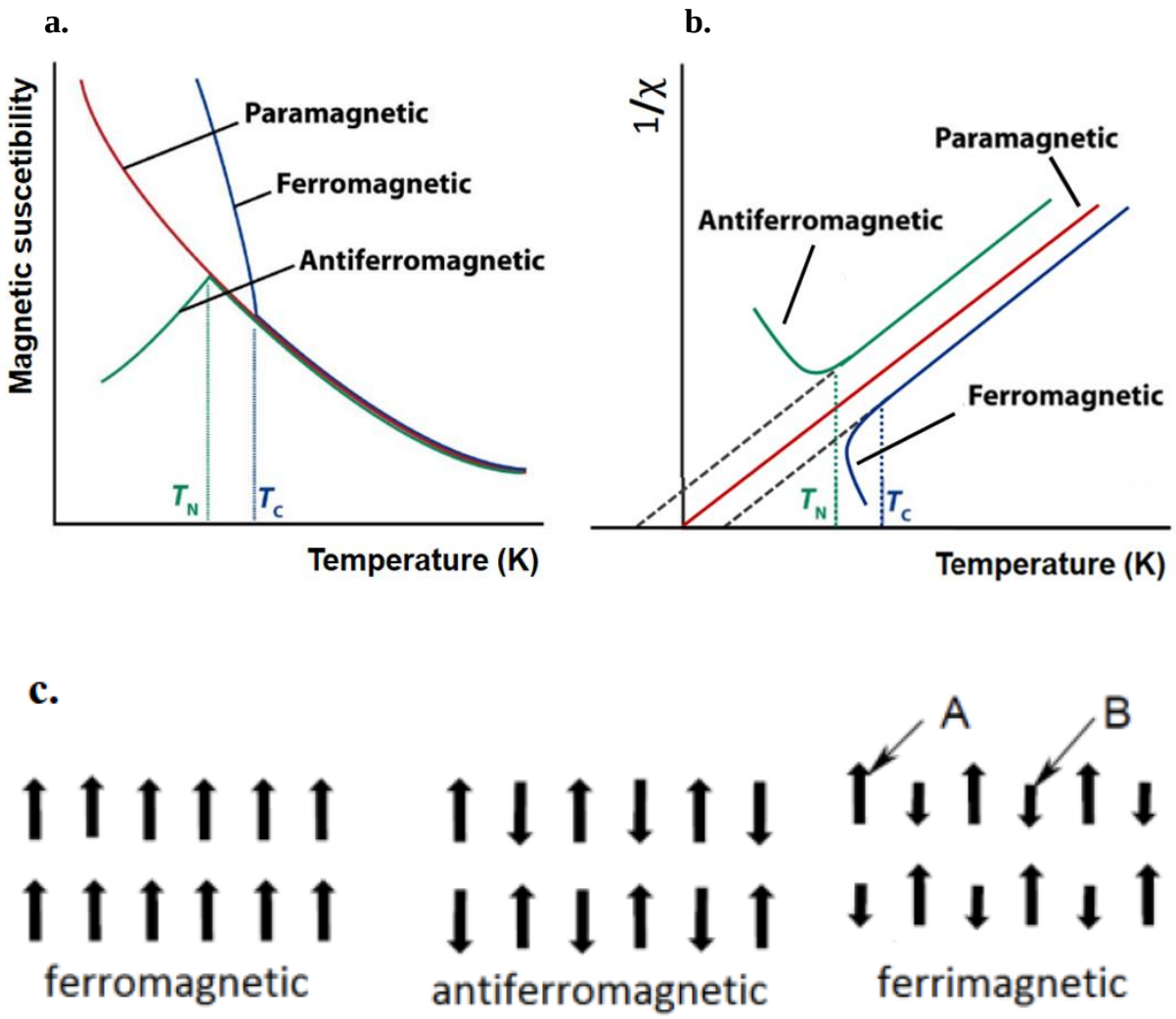

Figure 8. Behavior of (a) magnetic susceptibility and (b) of the inverse magnetic susceptibility for paramagnetic (red), ferromagnetic (blue) and antiferromagnetic (green) substances with temperature variation, under constant external magnetic field, showing T_C and T_N. (c) Representation of spin alignment for ferromagnetic (parallel alignment), antiferromagnetic

(antiparallel alignment) and ferrimagnetic (antiparallel alignment with differences in intensity A and B) substances. [Adapted from [47]

Helimagnetism effect occurs when, at certain temperatures, ferromagnetic layers couple ferromagnetically to the neighboring layers, but antiferromagnetically to the next-neighbour layers forming a helical spin structure. Examples of substances with this effect are FeGe (< 278 K), Tb (219-231 K) and β-MnO_2 (< 93 K)[47].

Superparamagnetism occurs in sufficiently small ferromagnetic or ferrimagnetic nanoparticles. The magnetization can randomly reverse direction under the influence of temperature (also called Néel temperature). In the absence of an external magnetic field, their magnetization appears to be zero on average. In this state, called superparamagnetism, an external magnetic field can magnetize the nanoparticles in a manner similar to that of a paramagnet. However, their magnetic susceptibility is much greater than that of paramagnets. An example is $ZnFe_2O_4$ nanoparticles[62,63].

When an antiferromagnetic response is observed for χ versus temperature curves, but the substance lacks a crystalline lattice, the effect is called speromagnetism or asperomagnetism. They are distinguished by the length scale over which the spin correlations reach zero. In a speromagnet, the average spin correlations are negative at nearest neighbor but tend to zero at some interatomic distances. In an asperomagnet, the correlations are ferromagnetic and tend towards zero on a larger scale. In sperimagnetism, there is an order in most of the spins when B is applied, but there is an offset of other spins close to those aligned to the field[47,64].

Finally, another observed effect is the Pauli paramagnetism. Restricted to metals, this effect occurs due to the delocalization of electrons due to the formation of the metallic band, the free-electron model, and there is a mixture of excited states that are not filled, regardless of temperature.

2.3 Principles of the magneto-optical Faraday effect.

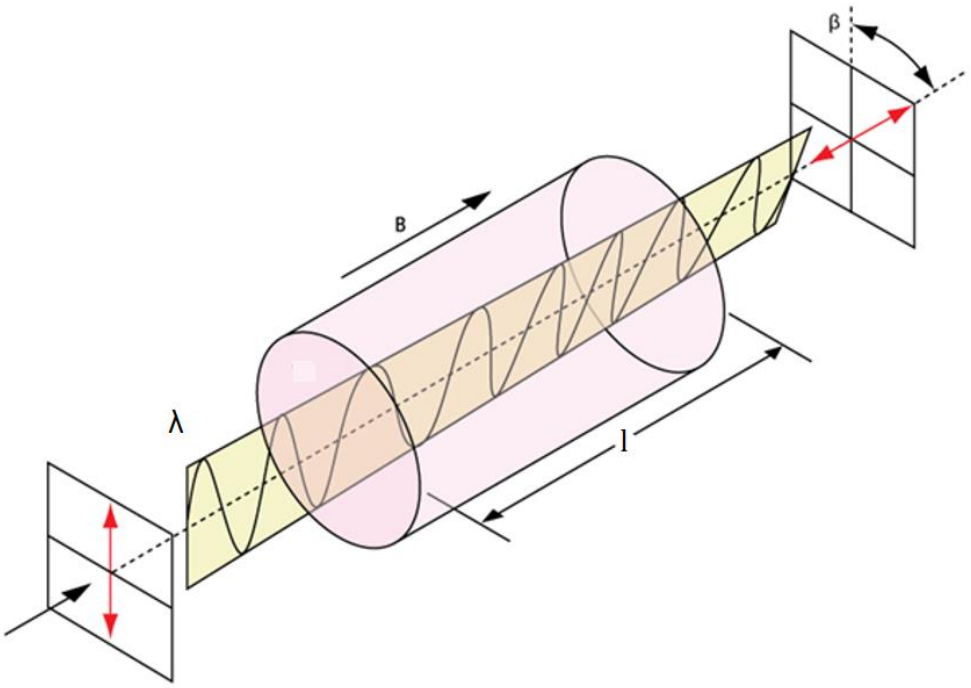

Figure 9. Schematic figure of a Faraday rotator. Polarizer light λ passes through the medium with optical path l, under the external magnetic field and constant B, causing a rotation of the plane of polarization of light, measured at angle β. [Extracted from ThorLabs – Faraday Rotators page. https://www.thorlabs.com/images/TabImages/Faraday_Rotator_Diagram_D1-780.gif]

As previously mentioned, and shown in Figure 9, the Faraday effect (or Faraday rotation) is a magneto-optical phenomenon (MOFE) which a change in the polarization plane of light occurs when passing through a medium, under the application of an external magnetic field, B. These conditions produce circular birefringence along B axis, resulting in a rotation of the polarization direction. The materials that have this effect are called Faraday rotators.

Already in Faraday's observations, in 1845, it was clear that the effect proportionally depended on some parameters such as the intensity of B, the size (l) and the index of refraction (n) of the transparent material. They have been summarized in Eq. 12 below.

$$\beta = V.B.l \qquad (Eq.12)$$

where β is the angle of rotation, and V an intrinsic constant of each material, dependent on the refractive index, called Verdet constant (min.Oe^{-1}.cm^{-1} or rad.T^{-1}.m^{-1}). B can occur clockwise, in this case the angle assumes a negative value, or counterclockwise, in this case assuming a positive value. Eq. 13 and 14 presents the dependencies of Verdet constant, that can be evaluated by constant presents diamagnetic (V_{dia}) and paramagnetic (V_{para}) contributions, respectively. If the resulting effect is diamagnetic, β will be positive. If the resultant is paramagnetic, the β will be negative.

$$V_{dia} = \left(\frac{e\nu}{m_e c}\right)\frac{dn}{d\nu} \qquad (Eq.13)$$

where e is the elementary charge (1.602176634 x 10^{-19} C), m_e is the mass of the electron (9.1093837015 x 10^{-31} kg), c is the speed of light (299792458 m.s^{-1}), ν is the frequency of the incident light, and dn/dν is the refractive index dispersion. This equation was derived by Antoine Henri Becquerel (1852-1908) on the basis of classical electromagnetic theory[65–67].

$$V_{para} = \left(\frac{4\pi^2 \mu_B \nu^2}{3Tchk_B}\right)\frac{N_I {\mu_{eff}}^2}{g}\sum_n \frac{C_n}{(\nu^2 - {\nu_n}^2)} \qquad (Eq.14)$$

where N_I is the number of paramagnetic species I per unit volume (I . cm^{-3}), C_n is related to the transition probabilities, ν_n is the transition frequencies. The Faraday effect is related to the inequality of the refractive indices of the left and right circularly polarized components into which the incident light is decomposed. The Verdet constant is dependent on the wave frequency and the internal resonance frequencies related to the transitions between electronic levels that are influenced differently by left and right circularly polarized waves, as well as on the associated transition probabilities. The Eq. 14 was studied and proposed by J. H. van Vleck and M. H. Hebb[68–70] and we can rearrange it as a function of χ_{para} using Eq. 8 and 9., forming Eq. 15, below.

$$V_{para} = \left(\frac{4\pi^2}{ch\mu_B N_A}\right)\frac{N_R v^2}{g}\chi_{para}\sum_n \frac{C_n}{(v^2 - {v_n}^2)} \qquad (Eq.15)$$

where $\frac{4\pi^2}{ch\mu_B N_A}$ is constant equal to 3.558 x 10^{25} mol.m.J^{-1}.A^{-1}, independent of medium or light. We can conclude that V_{para} is directly proportional on χ_{para} and its determination is extremely relevant for the study of paramagnet Faraday rotators, reaching higher Verdet constants and sensitivity orders of magnitude higher than diamagnetic Faraday rotators.

As seen in Eq. 13 and 15, the V is also dependent on the refractive index of the substance, due to the interaction of electromagnetic radiation with the molecular electric field. Therefore, larger, more polarizable atoms have greater interaction with electromagnetic radiation, with the electron cloud being more easily distorted. No wonder, the magneto-optical effect was discovered by chance by Faraday using a lead-borosilicate glass, where the presence of lead, a high polarizable atom, allowed the detection of the effect, despite being a glass with resulting diamagnetic susceptibility. The relationship between the V and the polarizability (α) can be better understood by means of the Eq. 16[20].

$$V = -\sum_n \frac{3I_n {\alpha_n}^2}{4{r_n}^6} \qquad (Eq.16)$$

where r_n is the distance between atoms and I_n is the ionization energy of which atom.

For MO materials, large angles of optical polarization rotation at wavelengths of interest as well as high optical transparency are generally required for use in photonic devices. This has been achieved by increasing the magnetic field intensity, increasing the path length in the material (like optical-fibers) or by developing new materials aimed at achieving higher V. Although any transparent materials under magnetic field exhibit some degree of Faraday rotation, only a few groups of substances can achieve large Faraday rotation angles and possess a high V for commercial applications in optics. Hence, the discovery of alternative high V materials for MO applications with inexpensive and abundant substances is a compelling technological opportunity for novel material innovation. Organic molecules containing aromatic

rings[71,72], polymers[73], and nanocomposite[74] have shown relevant results as MO materials in the visible and near infrared region, although the values are still low when compared to inorganic ones. Of these applications, the most commons are magnetic field sensors.

By far, the most frequent materials used in magneto-optical applications are single crystal materials based on inorganic garnets, as terbium gallium garnet (TGG), terbium aluminum garnet (TAG), rare earth iron garnets (RIGs), yttrium aluminum garnet (YAG), and other combinations of RE doped garnets, being commercially available, deployed in magneto-optical isolators and magnetic detection applications due to their high V, chemical stability and optical transparency in the region of interest. Garnets naturally have the general formula of $X_3Y_2(SiO_4)_3$, and synthetic garnets, mentioned above, were produced by replacing Si with Ga, Fe or Al. They are usually synthesized by Czochralski or Float Zone growth methods to produce high quality results without impurities or defects[75,76]. The V values for each single crystal is -134 $rad.T^{-1}.m^{-1}$ (TGG, at 632.8 nm), -174 $rad.T^{-1}.m^{-1}$ (TAG, at 632.8 nm), +5,86 $rad.T^{-1}.m^{-1}$ (YAG, at 632.8 nm), -232 $rad.T^{-1}.m^{-1}$ (YIG, at 1.86 μm)[77].

As previously seen Fe, Ni and Co have high paramagnetic susceptibilities, which allows them to be excellent ions to work in MO applications. However, the presence of these ions causes unwanted coloration in the material, having, in most cases, applications only in the infrared region. The second group of atoms with high paramagnetic susceptibility are the rare earths. Because they have many unpaired electrons in the 4f layer, as is the case with Tb, Gd, and because they do not have high absorptions in the visible, these ions are also used commercially.

One of the biggest difficulties of monocrystalline Faraday rotators is their production. The production of single crystals is extremely costly, as all material must be grown without impurities or defects, or the effect will be impaired. moreover, production is limited by the size of the piece, as it usually only reaches a few mm in thickness. And, of course, this reverts to the final price of the product. Searching for prices on Faraday rotators by *Thorlabs, Inc*., we will not find anything less than $600.00 on rotators smaller than 5 mm.

Seeking to overcome this, the study of glasses with magneto-optical applications has been an increasing focus in modern science. Glasses have a synthesis advantage, as the melt-quenching method only requires increasing the temperature of the precursor reagents until melting, homogenization and thermal quenching at a lower temperature. In addition, it is possible to manufacture pieces larger than 5 mm, the major limitation being the region forming the glass in question. If glass production is satisfactory, it is possible to produce an optical fiber from it, and even if the V is not as high as that of the monocrystalline Faraday rotators, the l of an optical fiber would be an extra gain (as already seen in Eq. 12). These promises of new materials have called the scientific community, as will be discussed in the next section.

2.4 State of the art of Faraday rotator glasses.

A web search was conducted on the Web of Science on October 20, 2023, using the terms *"Magneto-optical sensors*" and "*Magneto-optical glasses*", shown in Figures 10 and 11, respectively. The results showed a significant increase in publications and citations in recent years. The publication-citation records of 70-1400 and 47-1000 for the given date highlight the recent emergence, diversity, interest, and significance of these topics.

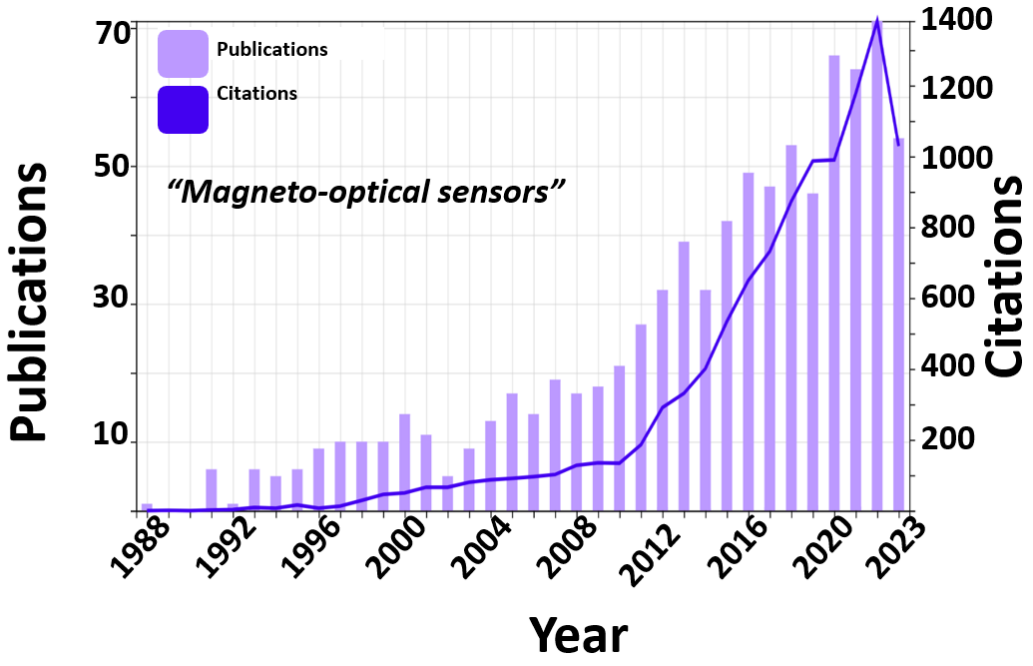

Figure 10. "*Magneto-optical sensors*" publications and citations made by Web of Science on October 20, 2023 [from Web of Science searching "*Magneto-optical sensors*"].

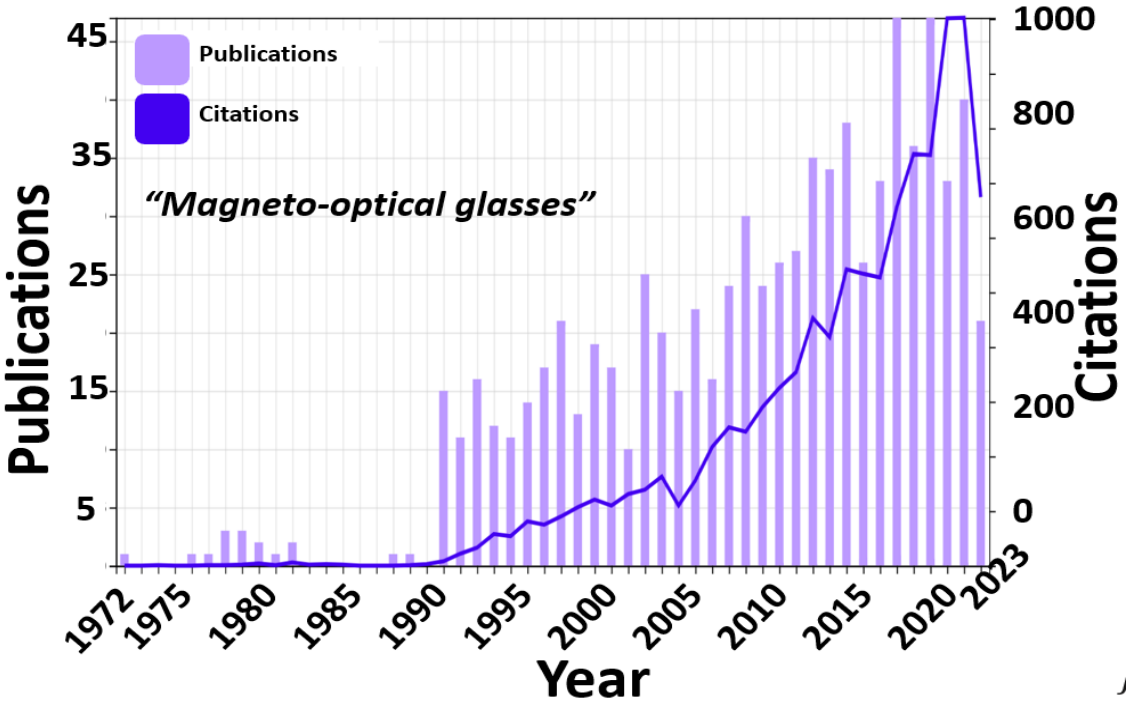

Figure 11. "*Magneto-optical glasses*" publications and citations made by Web of Science on April 14, 2023 [from Web of Science searching "*Magneto-optical glasses*"].

Several different applications can be mentioned, the main ones being magnetic and electrical sensors, normally made of a copper coil rotating around the MO material, with the coil connected to the electrical circuit. The polarization state of the light propagating in the material is rotated due to the Faraday effect generated by the current passing through the cable. Optical isolators are devices that allow light to pass through in one direction but block it in the opposite direction. There are crucial in many optical systems, such as laser systems, where it is essential to prevent reflections from interfering with the laser's operation. In this application, the MO material is used to rotate the plane of polarized light, which allows the light to pass through the isolator in one direction but blocks it in the opposite direction. Even the Laser Interferometer Gravitational-Wave Observatory (LIGO) used the magneto-optical properties of the TGG during the detection of gravitational waves in 2016[78–80].

MO materials are also used in optical modulators, which are devices that modulate the intensity or phase of light. In this application, the magneto-optical material is used to rotate the plane of polarized light, which changes the intensity or phase of the light passing through it. Optical modulators have several applications, including in fiber-optic communication systems, where they are used to modulate the light signals carrying information.

Another significant application of MO materials is in magnetic field sensors. These sensors are used in various applications, including navigation systems, geophysical exploration, and medical diagnosis. In this application, the magneto-optical material is used to detect and measure magnetic fields. When a magnetic field is applied to the material, it causes a rotation of the plane of polarized light, which can be detected and measured. Figure 12 shows the field values produced by natural events. The sensitivity values of the MO materials are also an important value to know and understand.

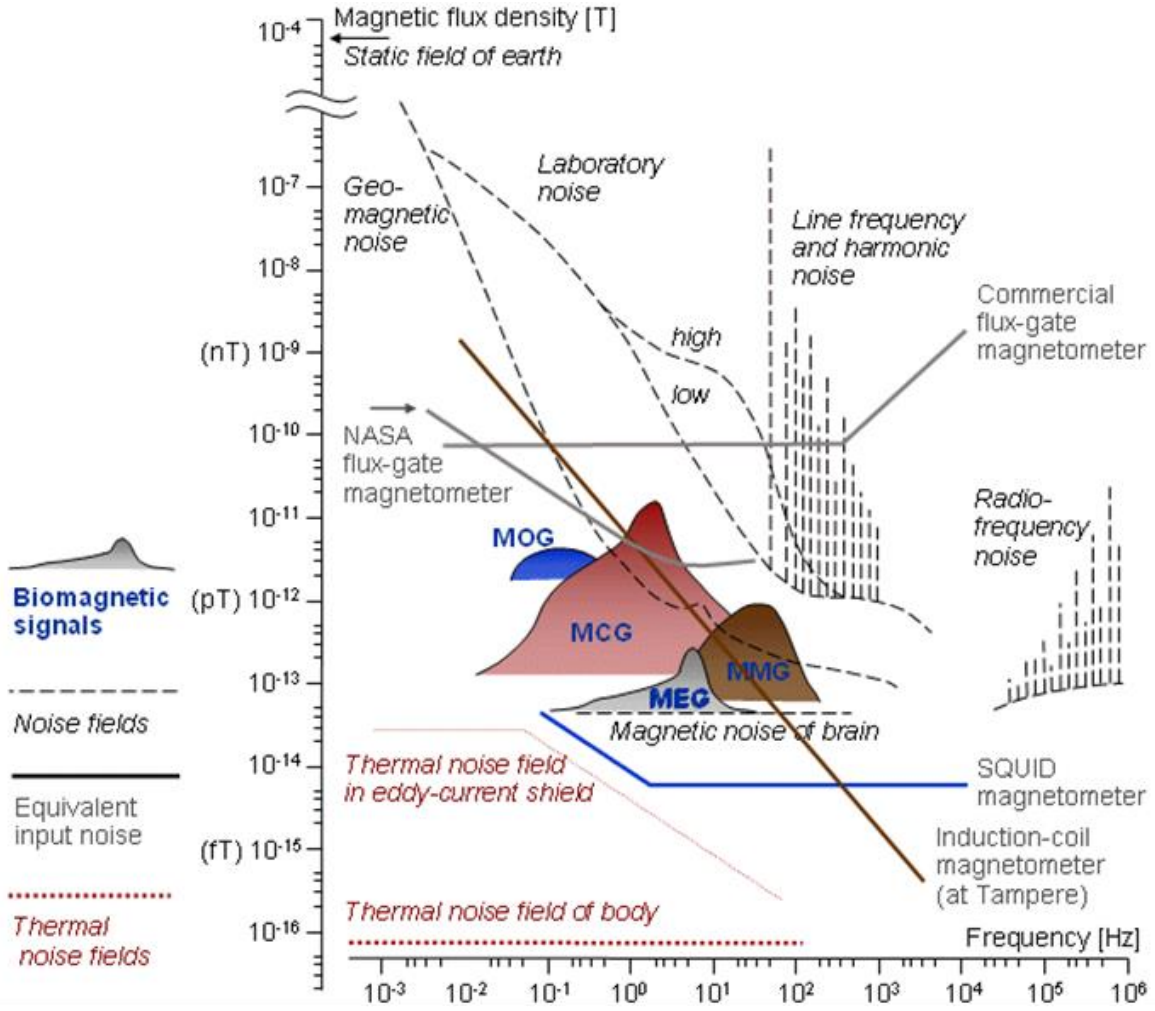

Figure 12. Magnetic signals produced by various sources[81].

Another recent spotlight was the improvement of the study of magnetism control using electric field in materials with high magnetic susceptibility, changing the population of charge carriers, paving the way for their use in spintronic integrated circuits with ultra-low energy consumption. Although studies use ferromagnetic carriers, paramagnetic materials also have their relevance, being an area still little studied[82–84].

The MO properties in glasses can be achieved by introducing paramagnetic ions, uniformly incorporated into solid glass matrices is the key to achieving large Faraday rotation through a transparent glassy material. These ions interact with the electromagnetic waves, causing the rotation of the plane of polarized light. The degree of rotation depends on the strength of the magnetic field and the concentration of the magnetic ions in the glass. The main approach to increase the green

constant is to increase the amount of these ions dissolved in the glass matrix, maintaining its optical properties in the region of interest. One of the first works focused on the production of glasses containing rare earths for MO applications is the works by Nicholas Borrelli[69], by the Corning Glass Works, and C. B. Rubinstein et al[85,86], by the Bell Telephone Laboratories, the three works published in 1964. His work demonstrated that the material's V depended directly on the concentration of RE ions formulated in the final glass. These works also revealed that the Tb^{3+} ion had the greatest magneto-optical effect, mainly due to its fundamental level and J.

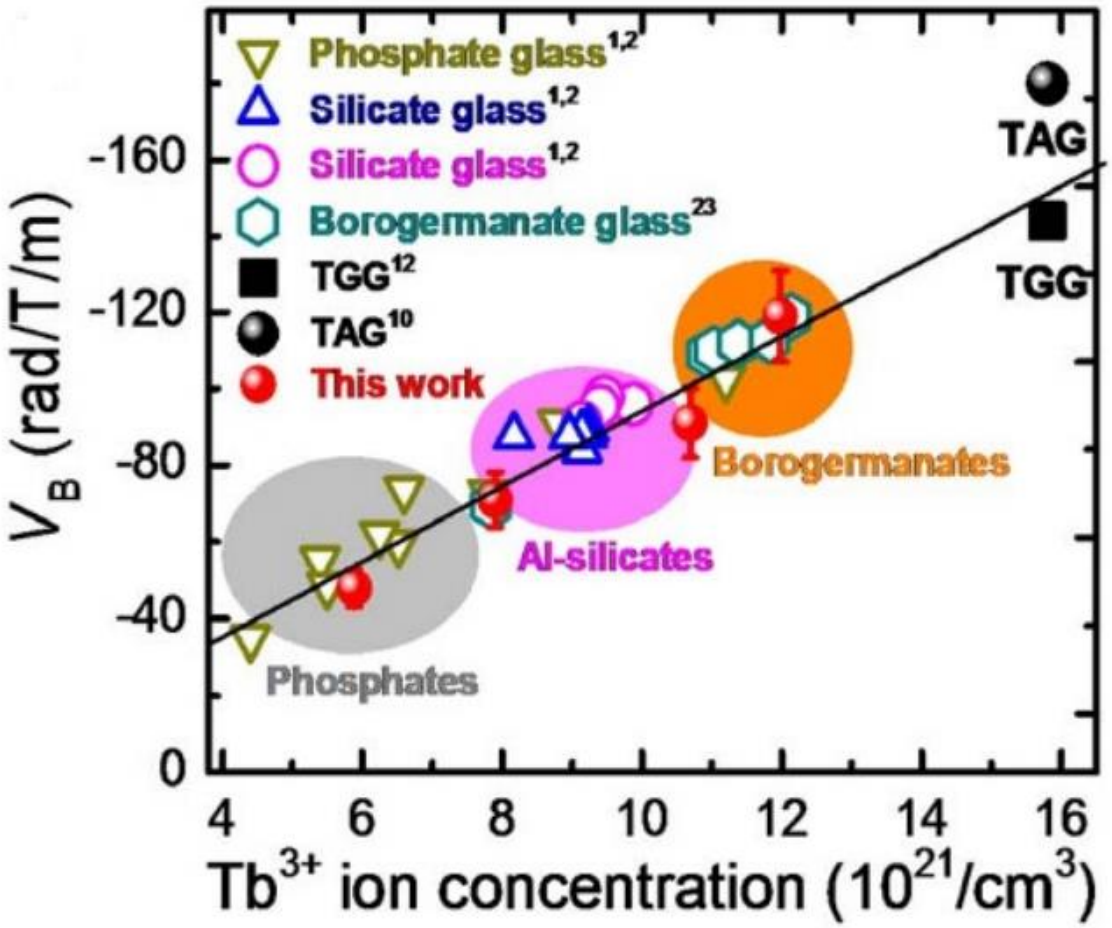

Figure 13. Dependence of V on Tb^{3+} ion concentration and comparison to other reported data glasses at a fixed wavelength of 632.8 nm [87].

M. Yamane and Y. Asahara[66], and G. Gao et al[87], produced a relation between the V of some terbium-contain glasses and different matrices by the concentration of Tb^{3+} ions per volume, at 632.8 nm. Figure 13 is taken from the article

by G. Gao. We observed that phosphate glasses have a lower capacity to dissolve Tb^{3+} ions, going through silicate and alumino-silicate glasses to borogermanate glasses, with the highest amounts of ions per volume even in so. Germanium also helps with higher V values because germanium is a polarizable atom, which increases the refractive index of the glass, which is directly proportional to V as seen earlier.

One of the disadvantages of germanate glasses is their high value (~ $1,600 / 100 g, ≥99.99% trace metals basis, by Sigma-Aldrich), which makes the final product more expensive, which leads us to study one of the systems in this work, changing the germanium for another polarizable atom.

In addition to the germanate glasses, borates[88,89], boro- and aluminosilicates[90–93], phosphates[94–96] glasses also have good solubility of lanthanides, but for good applications in photonics and magneto-optics it will be interesting that the chosen system presents 5 main characteristics: high paramagnetic ions concentration, high refractive index, low absorption coefficient (in the operational spectral region), high thermal stability against devitrification, in order to obtain large bulk samples and eventually optical fibers and a more affordable price than germanate glass.

Borotungstate glasses[97–102], fulfil these requirements, presenting high solubility of Ln_2O_3, high refractive index (1,6-1,9) due to the higher polarizability of tungsten atoms, besides to be transparent from the visible to near infrared, include the telecom region (1.55 μm). The price of tungsten is also lower than germanate (~ $180 / 100 g, powder, puriss., 99.9%, by Sigma-Aldrich), and the synthesis temperature is lower (1450 °C for borogermanate glasses and 1250 °C for borotungstate glasses). As stated in the review work by Mohamed Ataalla et al[98], the presence of tungsten in these glasses entails several other interesting characteristics that can be explored, mainly in sensing field, like gas, electric, humidity, light, temperature, high energy radiation sensors, which can lead to more characteristics interesting in the material in future discussions. In addition to WO_3 being a great modifier of the vitreous network, breaking the former chains and allowing greater stability for the vitreous phase. The glass system Ln_2O_3-B_2O_3-WO_3 (Ln = lanthanide trivalent ion) studied in this work has been

previously explored[103–110], mainly with high concentrations of La^{3+} and Gd^{3+} glasses.

In this work we will study in depth the Ln_2O_3-B_2O_3-WO_3 system for applications in magneto-optics, firstly with trivalent terbium ion (Ln^{3+} = Tb^{3+}), as this has the highest value of paramagnetic susceptibility of the lanthanides and low absorption in the visible region, making the best glass-forming region effective, improving the parameters of the synthesis process and, subsequently, applying it to other lanthanides.

On the other hand, we can choose to use transition metals (TM) to obtain Faraday rotators. This makes the process even cheaper, as lanthanide ions also have high market values. Fe, Co and Ni ions are already commercially used as Faraday rotators glasses, they have higher V even than glasses containing rare earths, but they are generally used in the infrared region, as they have high absorption in the visible region. In this sense, depending on the need for sensitivity and application, glasses with other TMs that present greater transparency in the visible region, can find specific niches in the market with much more affordable prices.

One of the proposals is the use of divalent manganese ion (Mn^{2+}) as active ion is convenient instead of Fe, Co and Ni, as it is the next ion with greater paramagnetic susceptibility. Mn^{2+} is also important due to the extreme sensitivity of its optical spectra in the nature of the host matrix and has been regularly used as a paramagnetic probe (for low grades) in glassy systems.

In glass matrices, manganese can be present in the form of Mn^{2+} or Mn^{3+} ions, that is, d^5 and d^4, respectively, occupying tetrahedral and/or octahedral sites depending on the chemical composition. Octahedral Mn^{2+} exhibits transparency in the visible window, being limited by the low-intensity prohibited absorption at 410 nm ($^6A_1(S) \rightarrow {}^4A_1$, $^4E(G)$) extending the optical window, compared to magneto-optical glasses containing Tb^{3+} (480 nm) . As far as magneto-optical properties are concerned, the use of Mn^{2+} is also interesting over all other TMs, as it is the only one that can be loaded in large amounts without compromising the optical absorption window in the visible or infrared. next.

For higher performance of MO material, we need high refractive index. In this sense, a glass composition based on antimony, a highly polarizable ion, which has higher refractive indices and is a well-known matrix for Mn^{2+} ions, was chosen.

Phosphate glasses generally have low optical dispersion (high Abbe number), large transmission window and high refractive index[111]. The presence of Pb also increases the refractive index of the glass, as already discussed. The addition of PbO and ZnO also lower the melting point of the glass because they are network modifiers, breaking the former interactions.

R. S. Manzan [112,113] and C. A. S. Lereno[114], which this work follows, prepared $SbPO_4$-PbO-ZnO glasses doped with Mn and Fe, conferring magnetic properties to them, due to the formation of a glass-ceramic, containing crystals with the ferromagnetic oxides of each mentioned metal. However, the magneto-optical applications of these glasses have not yet been studied, which leads us to this work in question. We had the participation of Scientific Initiation student, Nicole Gouveia Roque, with VUNESP Scholarship, an agreement between the Secretary of Education of the State of São Paulo-UNESP-VUNESP Foundation, who helped in the preparation and study of these glasses.

References in this chapter

[1] H. V. Merrick, F.H. Brown, Obsidian sources and patterns of source utilization in Kenya and northern Tanzania: some initial findings, African Archaeol. Rev. 2 (1984) 129–152. https://doi.org/10.1007/BF01117229.

[2] J.R. Cann, C. Renfrew, The Characterization of Obsidian and its application to the Mediterranean Region, Proc. Prehist. Soc. 30 (1964) 111–133. https://doi.org/https://doi.org/10.1017/S0079497X00015097.

[3] A. Yoshida, Y. Kudo, K. Shimada, J. Hashizume, A. Ono, Impact of landscape changes on obsidian exploitation since the Palaeolithic in the central highland of Japan, Veg. Hist. Archaeobot. 25 (2016) 45–55. https://doi.org/10.1007/s00334-015-0534-y.

[4] L.E. Morgan, P.R. Renne, R.E. Taylor, G. WoldeGabriel, Archaeological age constraints from extrusion ages of obsidian: Examples from the Middle Awash, Ethiopia, Quat. Geochronol. 4 (2009) 193–203. https://doi.org/10.1016/j.quageo.2009.01.001.

[5] B. Gratuze, Obsidian characterization by laser ablation ICP-MS and its application to prehistoric trade in the Mediterranean and the Near East: Sources and distribution of obsidian within the Aegean and Anatolia, J. Archaeol. Sci. 26 (1999) 869–881. https://doi.org/10.1006/jasc.1999.0459.

[6] J.M. Erlandson, T.C. Rick, T.J. Braje, M. Casperson, B. Culleton, B. Fulfrost, T. Garcia, D. a Guthrie, N. Jew, D.J. Kennett, M.L. Moss, L. Reeder, C. Skinner, J. Watts, L. Willis, Paleoindian Seafaring, Maritime Technologies, and Coastal Foraging on California's Channel Islands, Science (80-.). 331 (2011) 1181–1185. https://doi.org/10.1126/science.1201477.

[7] C. Wilke, The ancient origins of glass, Knowable Mag. (2021) 1–12. https://doi.org/10.1146/knowable-111721-1.

[8] A.J. Shortland, M.S. Tite, Raw materials of glass from Amarna and implications for the origins of Egyptian glass, Archaeometry. 42 (2000) 141–151. https://doi.org/10.1111/j.1475-4754.2000.tb00872.x.

[9] S. J, Who were the glassmakers? Status, theory and method in mid- second

millenium glass production., Oxford J. Archaeol. 26 (2007) 261–274. http://onlinelibrary.wiley.com/doi/10.1111/j.1468-0092.2007.00284.x/full.

[10] A. Shortland, L. Schachner, I. Freestone, M. Tite, Natron as a flux in the early vitreous materials industry: Sources, beginnings and reasons for decline, J. Archaeol. Sci. 33 (2006) 521–530. https://doi.org/10.1016/j.jas.2005.09.011.

[11] E. V. Sayre, R.W. Smith, Compositional Categories of Ancient Glass, Science (80-.). 133 (1961) 1824–1826.

[12] M.S. Walton, A. Shortland, S. Kirk, P. Degryse, Evidence for the trade of Mesopotamian and Egyptian glass to Mycenaean Greece, J. Archaeol. Sci. 36 (2009) 1496–1503. https://doi.org/10.1016/j.jas.2009.02.012.

[13] I. Freestone, N. Meeks, M. Sax, C. Higgitt, The Lycurgus Cup - A Roman nanotechnology, Gold Bull. 40 (2008) 270–277. https://doi.org/10.1007/BF03215599.

[14] G.W. Morey, Optical glasses, 2150694, 1936. https://doi.org/10.1038/209966a0.

[15] B.T. Kolomiets, Vitreous Semiconductors, Pliys. Stat. Sol. 7 (1964) 359–372.

[16] W. Klement, R.H. Willens, P. Duwez, Non-crystalline structure in solidifed gold-silicon alloy, Nature. 187 (1960) 869–870.

[17] E. Snitzer, Optical maser action of Nd^{+3} in a barium crown glass, Phys. Rev. Lett. 7 (1961) 444–446. https://doi.org/10.1103/PhysRevLett.7.444.

[18] M. Poulain, M. Poulain, J. Lucas, Verres fluores au tetrafluorure de zirconium proprietes optiques d'un verre dope au Nd^{3+}, Mater. Res. Bull. 10 (1975) 243–246.

[19] C.C. Kao, G.A. Hockham, Dielectric-fibre surface waveguides for optical frequencies, Proc. IEE. 113 (1966) 1151–1158. https://doi.org/10.1049/piee.1966.0189.

[20] W. Blanc, Y. Gyu Choi, X. Zhang, M. Nalin, K.A. Richardson, G.C. Righini, M. Ferrari, A. Jha, J. Massera, S. Jiang, J. Ballato, L. Petit, The past, present and future of photonic glasses: A review in homage to the United Nations International Year of glass 2022, Prog. Mater. Sci. 134 (2023) 101084. https://doi.org/10.1016/j.pmatsci.2023.101084.

[21] T. Bajarin, Why Glass Is Critical to the Future of Tech, Recode.Net. (2015)

http://www.recode.net/2015/12/14/11621456/why-glas.

[22] A. Durán;, J.M. Parker, Welcome to the Glass Age. Celebrating the United Nations International Year of Glass 2022, CSIC, 2022.

[23] D.L. Morse, J.W. Evenson, Welcome to the Glass Age, Int. J. Appl. Glas. Sci. 7 (2016) 409–412. https://doi.org/10.1111/ijag.12242.

[24] M. Faraday, I. The Bakerian Lecture.— On the manufacture of glass for optical purposes, Philos. Trans. R. Soc. London. 120 (1830) 1–57. https://doi.org/10.1098/rstl.1830.0002.

[25] G. Tammann, Ueber die Kristallisationsgeschwindigkeit, II. Z. Phys. Chem. 26 (1898) 307–316.

[26] G. Tammann, Glasses as supercooled liquids, J. Soc. Glas. Technol. 9 (1925) 166–185.

[27] W. L. Bragg, Atomic Structure of Minerals, J. Phys. Chem. 41 (1937) 1149–1150. https://doi.org/10.1021/j150386a017.

[28] J.T. Randall, H.P. Rooksby, B.S. Cooper, X-ray diffraction and the structure of vitreous silica, Z. Krist. 75 (1930) 196–214.

[29] R.W.G. Wyckoff, G.W. Morey, X-ray diffraction measurement of some soda-lime-silica glasses, J. Soc. Glas. Technol. 9 (1925) 265–267.

[30] A.A. Lebedev, The polymorphism and annealing of glass, Trans. Opt. Inst. Petrograd. 2 (1921) 1–20.

[31] W.H. Zachariasen, The Atomic arrangement in Glass, J. Am. Chem. Soc. 196 (1932) 3841–3851. https://doi.org/10.1021/ja01349a006.

[32] P.Y. Huang, S. Kurasch, A. Srivastava, V. Skakalova, J. Kotakoski, A. V. Krasheninnikov, R. Hovden, Q. Mao, J.C. Meyer, J. Smet, D.A. Muller, U. Kaiser, Direct Imaging the Atoms in a Two-Dimensional Silica Glass on Graphene, Microsc. Microanal. 18 (2012) 1496–1497. https://doi.org/10.1017/S1431927612009336.

[33] M. Heyde, S. Shaikhutdinov, H.J. Freund, Two-dimensional silica: Crystalline and vitreous, Chem. Phys. Lett. 550 (2012) 1–7. https://doi.org/10.1016/j.cplett.2012.08.063.

[34] J. Wong, C.A. Angell, Glass: structure by spectroscopy, University Microfilms,

1976.

[35] S. R. Elliott, Physics of amorphous materials, Essex: Lon, 1989.

[36] J. (Université de M.I. Zarzycki, Glasses and the Vitreous State, Cambridge University Press, 1991.

[37] R.H. Doremus, Glass Science, 2nd ed., Wiley-Interscience, 1994.

[38] E.D. Zanotto, Do cathedral glasses flow?, Am. J. Phys. 66 (1998) 392–395. https://doi.org/10.1119/1.19026.

[39] J.E. Shelby, Introduction to Glass Science and Technology, The Royal Society of Chemistry, 1997. https://doi.org/10.1039/9781847551160.

[40] P. K. Gupta, Non-crystalline solids: glasses and amorphous solids, J. Non-Cryst. Solids. 195 (1996) 158–164. https://doi.org/10.1016/0022-3093(95)00502-1.

[41] O.L. Alves, I. de F. Gimenez, I.O. Mazali, Vidros, Química Nov. Na Esc. Edição Esp (2001) 13–24.

[42] A.K. Varshneya, J.C. Mauro, Fundamentals of Inorganic Glasses, 3rd ed., Elsevier, 2019.

[43] E.D. Zanotto, J.C. Mauro, The glassy state of matter: Its definition and ultimate fate, J. Non. Cryst. Solids. 471 (2017) 490–495. https://doi.org/10.1016/j.jnoncrysol.2017.05.019.

[44] P.I.K. Onorato, D.R. Uhlmann, Nucleating heterogeneities and glass formation, J. Non-Cryst. Sol. 22 (1976) 367–378. https://doi.org/10.1016/0022-3093(76)90066-1.

[45] R. Elliott, The story of magnetism, Physica A. 384 (2007) 44–52.

[46] J. M. D. Coey, Magnetism in future, J. Magn. Magn. Mater. 226 (2001) 2107–2112.

[47] J.M.D. (Trinity C.D. Coey, Magnetism and Magnetic Materials, Cambridge University Press, Cambridge, 2010.

[48] G. Cantor, Michael Faraday: Sandemanian and Scientist, Palgrave Macmillan London, 1991. https://doi.org/https://doi.org/10.1007/978-1-349-13131-0.

[49] M. Faraday, I. Experimental researches in electricity.—Nineteenth series, Philos. Trans. R. Soc. London. 136 (1846) 1–20. https://doi.org/10.1098/rstl.1846.0001.

[50] M. Faraday, Faraday's Diary of Experimental Investigation, 1820-1862, 7 Vol.,

1936.

[51] J. Kerr, XLIII. On rotation of the plane of polarization by reflection from the pole of a magnet, Philos. Mag. 3 (1877) 321–343. https://doi.org/10.1080/14786447708639245.

[52] J. Kerr, XXIV. On reflection of polarized light from the equatorial surface of a magnet, Philos. Mag. 5 (1878) 161–177. https://doi.org/10.1080/14786447808639407.

[53] H. Ebert, Magneto-optical effects in transition metal systems, Reports Prog. Phys. 59 (1996) 1665–1735. https://doi.org/10.1088/0034-4885/59/12/003.

[54] M.J. Freiser, A Survey of Magneto-Optic Effects, IEEE Trans Mag. 4 (1968) 152–161.

[55] V. Rodriguez, D. Verreault, F. Adamietz, A. Kalafatis, All-Optical Measurements of the Verdet Constant in Achiral and Chiral Liquids: Toward All-Optical Magnetic Spectroscopies, 2022. https://doi.org/10.1021/acsphotonics.2c00720.

[56] P. Pascal, No Title, Ann. Chim. Phys. 19 (1910) 5.

[57] P. Pascal, No, Ann. Chim. Phys. 25 (1912) 289.

[58] P. Pascal, No Title, Ann. Chim. Phys. 28 (1913) 218.

[59] G.A. Bain, J.F. Berry, Diamagnetic corrections and Pascal's constants, J. Chem. Educ. 85 (2008) 532–536. https://doi.org/10.1021/ed085p532.

[60] Pierre Curie, Propriétés magnétiques des corps à diverses temperatures, Faculté des Sciences de Paris, 1895.

[61] P.-E. Weiss, G. Foëx, Le Magnétisme, 1926.

[62] R.S. Yadav, Anju, T. Jamatia, I. Kuřitka, J. Vilčáková, D. Škoda, P. Urbánek, M. Machovský, M. Masař, M. Urbánek, L. Kalina, J. Havlica, Superparamagnetic znfe2o4 nanoparticles-reduced graphene oxide-polyurethane resin based nanocomposites for electromagnetic interference shielding application, Nanomaterials. 11 (2021). https://doi.org/10.3390/nano11051112.

[63] V. Marghussian, Magnetic Properties of Nano-Glass Ceramics, in: V. Marghussian (Ed.), Nano-Glass Ceram., William Andrew Publishing, 2015: pp. 181–223. https://doi.org/10.1016/B978-0-323-35386-1.00004-9.

[64] M. Krnel, S. Vrtnik, A. Jelen, P. Koželj, Z. Jagličić, A. Meden, M. Feuerbacher,

J. Dolinšek, Speromagnetism and asperomagnetism as the ground states of the Tb-Dy-Ho-Er-Tm "ideal" high-entropy alloy, Intermetallics. 117 (2020). https://doi.org/10.1016/j.intermet.2019.106680.

[65] H. Yang, Z. Zhu, Magneto-optical glass mixed with Tb3+ ions: High Verdet constant and luminescence properties, J. Lumin. 231 (2021) 117804. https://doi.org/10.1016/j.jlumin.2020.117804.

[66] M. Yamane, Y. Asahara, Glasses for Photonics, Cambridge University Press, Cambridge, 2000.

[67] H. Becquerel, No Title, Compt. Rend. 125 (1897).

[68] J.H. Van Vleck, M.H. Hebb, On the paramagnetic rotation of tysonite, Phys. Rev. 46 (1934) 17–32. https://doi.org/10.1103/PhysRev.46.17.

[69] N.F. Borrelli, Faraday rotation in glasses, J. Chem. Phys. 41 (1964) 3289–3293. https://doi.org/10.1063/1.1725727.

[70] M. Valeanu, M. Sofronie, A.C. Galca, F. Tolea, M. Elisa, B. Sava, L. Boroica, V. Kuncser, The relationship between magnetism and magneto-optical effects in rare earth doped aluminophosphate glasses, J. Phys. D. Appl. Phys. 49 (2016). https://doi.org/10.1088/0022-3727/49/7/075001.

[71] O. Louant, V. Liégeois, T. Verbiest, A. Persoons, B. Champagne, Faraday Effect in Stacks of Aromatic Molecules, J. Phys. Chem. C. 121 (2017) 15348–15352. https://doi.org/10.1021/acs.jpcc.7b04177.

[72] S. Vandendriessche, S. Van Cleuvenbergen, P. Willot, G. Hennrich, M. Srebro, V.K. Valev, G. Koeckelberghs, K. Clays, J. Autschbach, T. Verbiest, Giant faraday rotation in mesogenic organic molecules, Chem. Mater. 25 (2013) 1139–1143. https://doi.org/10.1021/cm4004118.

[73] C.-K. Lim, M.J. Cho, A. Singh, Q. Li, W.J. Kim, H.S. Jee, K.L. Fillman, S.H. Carpenter, M.L. Neidig, A. Baev, M.T. Swihart, P.N. Prasad, Manipulating Magneto-Optic Properties of a Chiral Polymer by Doping with Stable Organic Biradicals, Nano Lett. 16 (2016) 5451–5455. https://doi.org/10.1021/acs.nanolett.6b01874.

[74] K.J. Carothers, N.P. Lyons, N.G. Pavlopoulos, K.S. Kang, T.M. Kochenderfer, A. Phan, L.N. Holmen, S.L. Jenkins, I.B. Shim, R.A. Norwood, J. Pyun, Polymer-

coated magnetic nanoparticles as ultrahigh verdet constant materials: Correlation of nanoparticle size with magnetic and magneto-optical properties, Chem. Mater. 33 (2021) 5010–5020. https://doi.org/10.1021/acs.chemmater.1c00808.

[75] S. Ganschow, D. Klimm, P. Reiche, R. Uecker, On the Crystallization of Terbium Aluminium Garnet, Cryst. Res. Technol. 34 (1999) 615–619.

[76] M. Geho, T. Sekijima, T. Fujii, Growth of terbium aluminum garnet ($Tb_3Al_5O_{12}$; TAG) single crystals by the hybrid laser floating zone machine, J. Cryst. Growth. 267 (2004) 188–193. https://doi.org/10.1016/j.jcrysgro.2004.03.068.

[77] D. Vojna, O. Slezák, A. Lucianetti, T. Mocek, Verdet constant of magneto-active materials developed for high-power Faraday devices, Appl. Sci. 9 (2019). https://doi.org/10.3390/app9153160.

[78] T.L.S. Collaboration, Advanced LIGO, Class. Quantum Gravity. 32 (2015). https://doi.org/10.1088/0264-9381/32/7/074001.

[79] O. V. Palashov, D.S. Zheleznov, A. V. Voitovich, V. V. Zelenogorsky, E.E. Kamenetsky, E.A. Khazanov, R.M. Martin, K.L. Dooley, L. Williams, A. Lucianetti, V. Quetschke, G. Mueller, D.H. Reitze, D.B. Tanner, E. Genin, B. Canuel, J. Marque, High-vacuum-compatible high-power Faraday isolators for gravitational-wave interferometers, J. Opt. Soc. Am. B. 29 (2012) 1784. https://doi.org/10.1364/josab.29.001784.

[80] The LIGO Scientific Collaboration, Observation of gravitational waves from a binary black hole merger, Phys. Rev. Lett. 116 (2016) 1–16. https://doi.org/10.1103/PhysRevLett.116.061102.

[81] J. Malmivuo, R. Plonsey, Theory of Biomagnetic Measurements, in: Bioelectromagn. Princ. Appl. Bioelectric Biomagn. Fields, Oxford University Press, 1995: pp. 325–363.

[82] F. Matsukura, Y. Tokura, H. Ohno, Control of magnetism by electric fields, Nat. Nanotechnol. 10 (2015) 209–220. https://doi.org/10.1038/nnano.2015.22.

[83] C. Song, Y. You, X. Chen, X. Zhou, Y. Wang, F. Pan, How to manipulate magnetic states of antiferromagnets, Nanotechnology. 29 (2018). https://doi.org/10.1088/1361-6528/aaa812.

[84] G. Assefa, Electric Field Controlled Itinerant Carrier Spin Polarization in

Ferromagnetic Semiconductors, Adv. Condens. Matter Phys. 2021 (2021). https://doi.org/10.1155/2021/6663876.

[85] C.B. Rubinstein, S.B. Berger, L.G. Van Uitert, W.A. Bonner, Faraday rotation of rare-earth (III) borate glasses, J. Appl. Phys. 35 (1964) 2338–2340. https://doi.org/10.1063/1.1702860.

[86] C.B. Rubinstein, L.G. Van Uitert, W.H. Grodkiewicz, Magneto-optical properties of rare earth (III) aluminum garnets, J. Appl. Phys. 35 (1964) 3069–3070. https://doi.org/10.1063/1.1713182.

[87] G. Gao, A. Winterstein-Beckmann, O. Surzhenko, C. Dubs, J. Dellith, M.A. Schmidt, L. Wondraczek, Faraday rotation and photoluminescence in heavily Tb3+-doped GeO_2-B_2O_3-Al_2O_3-Ga_2O_3 glasses for fiber-integrated magneto-optics, Sci. Rep. 5 (2015) 1–6. https://doi.org/10.1038/srep08942.

[88] M. Zagrai, M. Unguresan, S. Rada, J. Zhang, M. Pica, E. Culea, Local structure in gadolinium-lead-borate glasses and glass-ceramics, J. Non. Cryst. Solids. 546 (2020) 120259. https://doi.org/10.1016/j.jnoncrysol.2020.120259.

[89] S. Sasaki, A. Masuno, K. Ohara, Y. Yanaba, H. Inoue, Y. Watanabe, S. Kohara, Structural Origin of Additional Infrared Transparency and Enhanced Glass-Forming Ability in Rare-Earth-Rich Borate Glasses without B-O Networks, Inorg. Chem. 59 (2020) 13942–13951. https://doi.org/10.1021/acs.inorgchem.0c01567.

[90] H. Yin, Y. Gao, H. Guo, C. Wang, C. Yang, Effect of B_2O_3 Content and Microstructure on Verdet Constant of Tb_2O_3-Doped GBSG Magneto-Optical Glass, J. Phys. Chem. C. 122 (2018) 16894–16900. https://doi.org/10.1021/acs.jpcc.8b04989.

[91] H. Lin, H. Yang, L. Zhou, J. He, B. Liu, N. Li, C. Li, S. Li, W. Yang, X. Jiang, H. Liu, F. Zeng, Z. Su, Research on the physical and optical properties of Dy_{3+} doped 30 mol%Tb_2O_3–B_2O_3-GeO_2-PbO-SiO_2 magneto-optical glass with high verdet constant, J. Phys. Chem. Solids. 166 (2022) 110682. https://doi.org/10.1016/J.JPCS.2022.110682.

[92] S. Ju, J. Kim, K. Linganna, P.R. Watekar, S.G. Kang, B.H. Kim, S. Boo, Y. Lee, Y.H. An, C.J. Kim, W.T. Han, Temperature and vibration dependence of the faraday effect of Gd_2O_3 NPs-doped alumino-silicate glass optical fiber, Sensors

(Switzerland). 18 (2018) 1–13. https://doi.org/10.3390/s18040988.

[93] V.D. Dubrovin, X. Zhu, M. Mollaee, J. Zong, N. Peyghambarian, Highly Dy_2O_3 and Er_2O_3 doped boron-aluminosilicate glasses for magneto-optical devices operating at 2 μm, J. Non. Cryst. Solids. 569 (2021) 120986. https://doi.org/10.1016/J.JNONCRYSOL.2021.120986.

[94] M. Elisa, R. Stefan, I.C. Vasiliu, M.I. Rusu, B.A. Sava, L. Boroica, M. Sofronie, V. Kuncser, A.C. Galca, A. Beldiceanu, A. Volceanov, M. Eftimie, Thermal, structural, magnetic and magneto-optical properties of dysprosium-doped phosphate glass, J. Non. Cryst. Solids. 521 (2019) 119545. https://doi.org/10.1016/J.JNONCRYSOL.2019.119545.

[95] B. Bellanger, Y. Ledemi, Y. Messaddeq, Fluorophosphate Glasses with High Terbium Content for Magneto-optical Applications, J. Phys. Chem. C. 124 (2020) 5353–5362. https://doi.org/10.1021/acs.jpcc.9b11696.

[96] A. Babkina, E. Kulpina, Y. Sgibnev, Y. Fedorov, A. Starobor, O. Palashov, N. Nikonorov, A. Ignatiev, K. Zyryanova, K. Oreshkina, E. Zhizhin, D. Pudikov, Terbium concentration effect on magneto-optical properties of ternary phosphate glass, Opt. Mater. (Amst). 100 (2020) 109692. https://doi.org/10.1016/j.optmat.2020.109692.

[97] R.M. Abdelouhab, R. Braunstein, K. Bärner, Identification of tungstate complexes in lithium-tungstate-borate glasses by Raman spectroscopy, J. Non. Cryst. Solids. 108 (1989) 109–114. https://doi.org/10.1016/0022-3093(89)90338-4.

[98] M. Ataalla, A.S. Afify, M. Hassan, M. Abdallah, M. Milanova, H.Y. Aboul-Enein, A. Mohamed, Tungsten-based glasses for photochromic, electrochromic, gas sensors, and related applications: A review, J. Non. Cryst. Solids. 491 (2018) 43–54. https://doi.org/10.1016/j.jnoncrysol.2018.03.050.

[99] Y. Taki, K. Shinozaki, T. Honma, T. Komatsu, L. Aleksandrov, R. Iordanova, Coexistence of nano-scale phase separation and micro-scale surface crystallization in Gd_2O_3-WO_3-B_2O_3 glasses, J. Non. Cryst. Solids. 381 (2013) 17–22. https://doi.org/10.1016/j.jnoncrysol.2013.09.014.

[100] W. Rittisut, N. Wantana, Y. Ruangtaweep, P. Mool-am-kha, J. Padchasri, S.

Rujirawat, P. Manyum, R. Yimnirun, P. Kidkhunthod, A. Prasatkhetragarn, S. Kothan, H.J. Kim, J. Kaewkhao, Bright white light emission from (Gd^{3+} /Dy^{3+}) dual doped transparent lithium aluminum borate glasses for W- LED application, Opt. Mater. (Amst). 122 (2021) 111705. https://doi.org/10.1016/j.optmat.2021.111705.

[101] L. Aleksandrov, T. Komatsu, K. Shinozaki, T. Honma, R. Iordanova, Structure of MoO_3-WO_3-La_2O_3-B_2O_3 glasses and crystallization of $LaMo_{1-X}W_xBO_6$ solid solutions, J. Non. Cryst. Solids. 429 (2015) 171–177. https://doi.org/10.1016/j.jnoncrysol.2015.09.004.

[102] Y. Wang, T. Honma, T. Komatsu, Effects of WO_3 substitution on crystallization behavior and laser patterning in Gd_2O_3-MoO_3-B_2O_3 glasses, J. Non. Cryst. Solids. 383 (2014) 86–90. https://doi.org/10.1016/j.jnoncrysol.2013.04.016.

[103] N. Wantana, E. Kaewnuam, Y. Ruangtaweep, D. Valiev, S. Stepanov, K. Yamanoi, H.J. Kim, S. Kothan, J. Kaewkhao, Tunable orange, yellow and white emission of Pr^{3+}-doped tungsten gadolinium borate glasses, J. Non. Cryst. Solids. 554 (2021) 120603. https://doi.org/10.1016/j.jnoncrysol.2020.120603.

[104] N. Wantana, Y. Ruangtaweep, E. Kaewnuam, S.C. Kang, H.J. Kim, S. Kothan, J. Kaewkhao, Development of WO_3-Gd_2O_3- B_2O_3 high density glasses doped with Dy^{3+} for photonics and scintillation materials application, Solid State Sci. 101 (2020) 106135. https://doi.org/10.1016/j.solidstatesciences.2020.106135.

[105] N. Wantana, E. Kaewnuam, Y. Ruangtaweep, D. Valiev, S. Stepanov, K. Yamanoi, H.J. Kim, J. Kaewkhao, Radio, cathodo and photoluminescence investigations of high density WO_3-Gd_2O_3-B_2O_3 glass doped with Tb^{3+}, Radiat. Phys. Chem. 164 (2019) 108350. https://doi.org/10.1016/j.radphyschem.2019.108350.

[106] N. Wantana, E. Kaewnuam, Y. Ruangtaweep, P. Kidkhunthod, H.J. Kim, S. Kothan, J. Kaewkhao, High density tungsten gadolinium borate glasses doped with Eu^{3+} ion for photonic and scintillator applications, Radiat. Phys. Chem. 172 (2020) 108868. https://doi.org/10.1016/j.radphyschem.2020.108868.

[107] N. Wantana, E. Kaewnuam, H.J. Kim, S.C. Kang, Y. Ruangtaweep, S. Kothan, J. Kaewkhao, X-ray/proton and photoluminescence behaviors of Sm^{3+} doped high-

density tungsten gadolinium borate scintillating glass, J. Alloys Compd. 849 (2020) 156574. https://doi.org/10.1016/j.jallcom.2020.156574.

[108] R. Iordanova, M. Milanova, L. Aleksandrov, K. Shinozaki, T. Komatsu, Structural study of WO_3-La_2O_3-B_2O_3-Nb_2O_5 glasses, J. Non. Cryst. Solids. 543 (2020) 120132. https://doi.org/10.1016/j.jnoncrysol.2020.120132.

[109] M. Milanova, K.L. Kostov, R. Iordanova, L. Aleksandrov, A. Yordanova, T. Mineva, Local structure, connectivity and physical properties of glasses in the B_2O_3-Bi_2O_3-La_2O_3-WO_3 system, J. Non. Cryst. Solids. 516 (2019) 35–44. https://doi.org/10.1016/j.jnoncrysol.2019.04.028.

[110] L. Aleksandrov, T. Komatsu, R. Iordanova, Y. Dimitriev, Raman spectroscopic study of structure of $WO_3La_2O_3B_2O_3$ glasses with no color and crystallization of LaBWO6, Opt. Mater. (Amst). 34 (2011) 201–206. https://doi.org/10.1016/j.optmat.2011.08.002.

[111] A. Winterstein, H. Akamatsu, D. Möncke, K. Tanaka, M.A. Schmidt, L. Wondraczek, Magnetic and magneto-optical quenching in (Mn^{2+}, Sr^{2+}) metaphosphate glasses, Opt. Mater. Express. 3 (2013) 184. https://doi.org/10.1364/ome.3.000184.

[112] Renata Siqueira Manzan, Preparação de Vidros e Vitrocerâmicas no sistema $SbPO_4$ – PbO – ZnO dopados com manganês e ferro, UFSCar, 2014.

[113] R.S. Manzan, J.P. Donoso, C.J. Magon, I.D.A.A. Silva, C. Rüssel, M. Nalin, Optical and structural studies of Mn^{2+} doped $SbPO_4$-ZnO-PbO glasses, J. Braz. Chem. Soc. 26 (2015) 2607–2614. https://doi.org/10.5935/0103-5053.20150289.

[114] C.A.S. Lereno, Estudo da cristalização de vidros contendo Fe_2O_3 e sua influência nas propriedades ópticas e magneto-ópticas, IQ-UNESP, 2018.

Objectives of this work

The main objective of this work is to synthesize and characterize glasses with high concentration of paramagnetic ions focusing on the formation of magneto-optical materials.

In this sense, the goals that will allow the achievement of the central objectives were listed in the following order:

1. Study glasses based on the system WO_3-B_2O_3, aiming to obtain glasses with high concentration of lanthanide ions with magneto-optical properties.

2. Study systems based on $SbPO_4$ containing Mn^{2+} ions, aiming to measure and understand the magnetic and magneto-optical effects in this system.

3. Systematically characterize, and understand the thermal, structural, morphological, optical, luminescent, magnetic and magneto-optical properties of these materials, aiming applications in magneto-optical systems.

CHAPTER II – Experimental Techniques

Chapter II – Experimental Techniques

1. SYNTHESIS OF THE SAMPLES

1.1. Tb_2O_3-B_2O_3-WO_3 System

A study was carried out on the Tb_2O_3-B_2O_3-WO_3 system. Batches of 10 g of samples were prepared by the traditional melt-quenching technique, using chemical-grade tungsten oxide (WO_3, 99.8 % AlfaAesar), boric acid (H_3BO_3, 99.9995 % AlfaAesar Puratronic) and tetraterbium heptaoxide (Tb_4O_7, 99.99 % Fox-Chemicals GmbH). The calculation of the final composition considers the total conversion of Tb_4O_7 → $2Tb_2O_3$.

To obtain vitreous boron oxide, thermal dehydration of boric acid was performed at 500 °C for 30 min in an electric furnace, following the chemical reaction shown below in Eq. (17):

$$2H_3BO_{3(s)} \xrightarrow{\Delta} B_2O_{3(s)} + 3H_2O_{(g)} \qquad Eq.(17)$$

Then, the other compounds, previously homogenized, were placed into the Pt crucible together with B_2O_3 and melted in an electric furnace at 1250 °C for 1 h. After that, the furnace temperature is raised to 1350 °C for 10 min. The glasses were formed by quenching the liquid into a steel mold kept at 30 °C below Tg and left at this temperature for 6 h for annealing before being slowly cooled down (1 °C . min^{-1}) to room temperature to reduce residual mechanical stress.

Figure 14 represents the ternary diagram of the system, with green circles representing the glassy compositions and red squares representing the crystallized phases after quenching. We tried to synthesize glasses with the maximum possible amount of Tb_2O_3 and WO_3, in order to increase the content of paramagnetic ions and the refractive index, extremely important parameters for Faraday rotators. It is important to take into account that high concentrations of B_2O_3 can lead to hygroscopic glasses. The small forming region shows how unstable glasses in this proportion are. However, glasses with high concentrations of Tb_2O_3 were obtained.

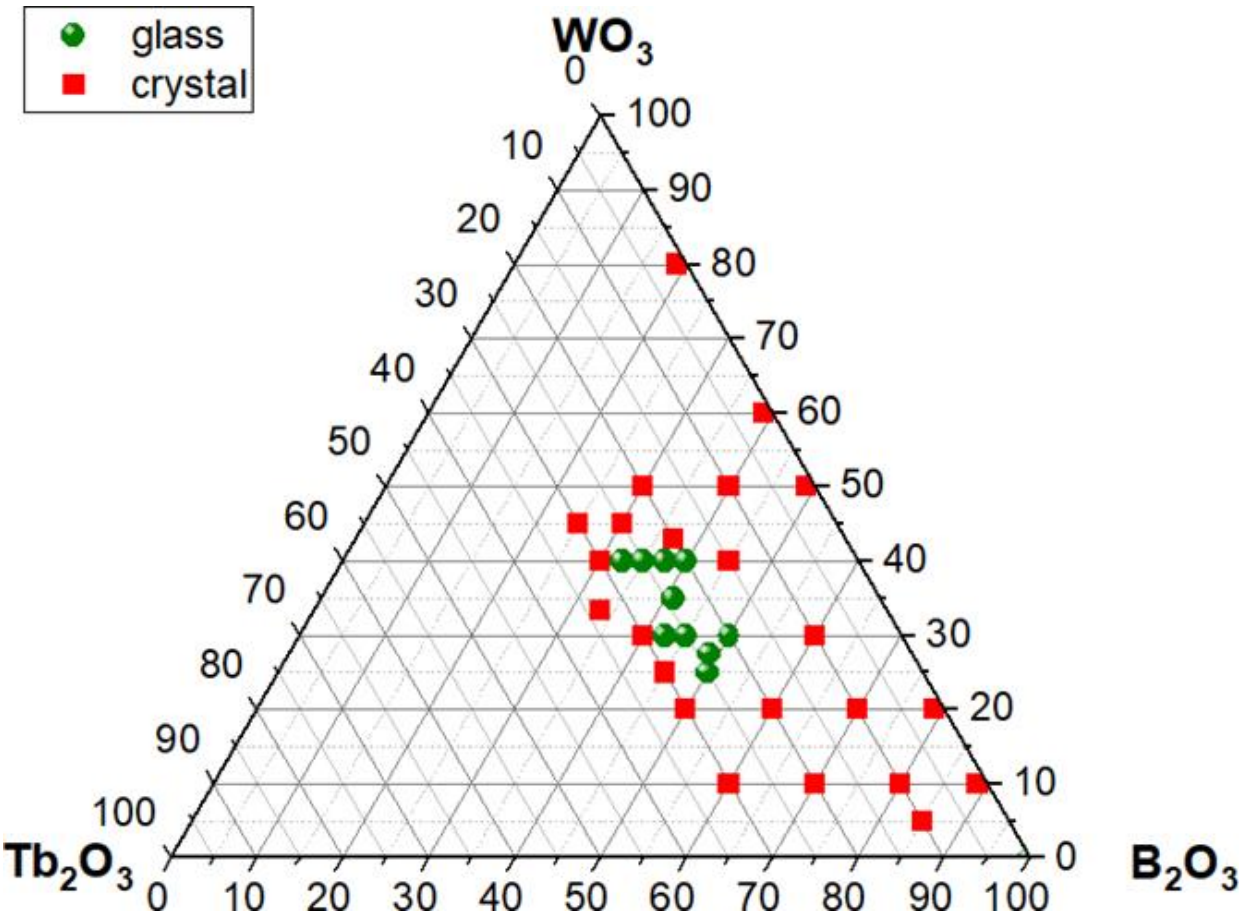

Figure 14. Ternary diagram of compositions in the Tb_2O_3-WO_3-B_2O_3 system. Green spheres correspond to glass samples and red square to crystallized compositions. The xTb_2O_3-(60-x)B_2O_3-40WO_3 (in mol %) series was chosen to study in this work. (Own authorship).

The ideal series that follows these prerequisites and will be studied in this work was xTb_2O_3-(60-x)B_2O_3-40WO_3, with x ranging from 20, 22.5, 25, 27.5 mol%. Samples with 15 and 30% were also synthesized, but spontaneous crystallization was observed after quenching. Using such fabrication procedure, certain samples underwent phase separation, indicating a small glass matrix-forming region.

It is worth mentioning that there were also attempts to synthesize the glass binary WO_3-B_2O_3, but without forming a glass phase. Figure 15 shows the WO_3-B_2O_3 phase diagram, based on the work of E. M. Levin[1], which highlight the difficulty of glass fabrication since liquids are immiscible over a large range of temperature . The WO_3-B_2O_3 vitreous system can be produced in small quantities (mg) using fast quenching[2].

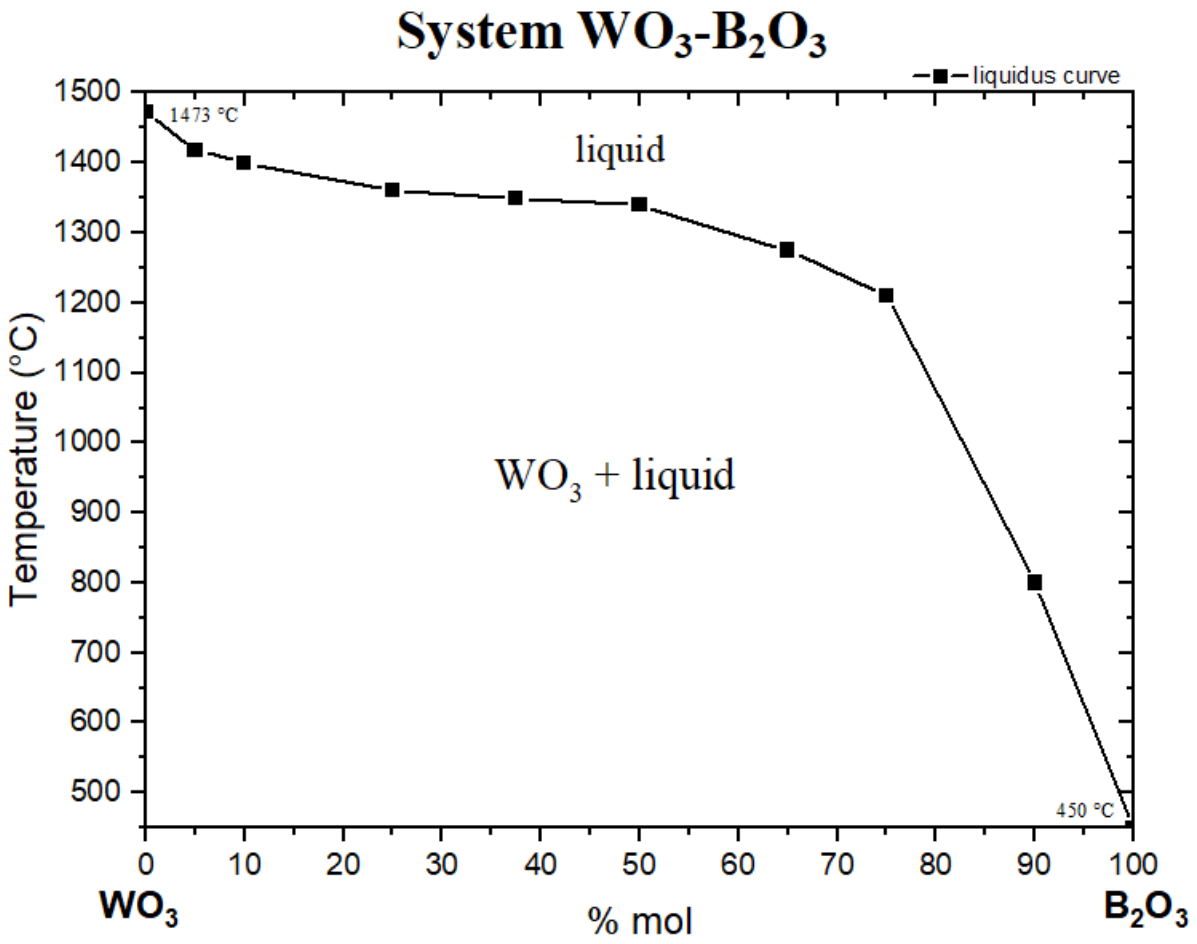

Figure 15. Binary phase diagram for the system WO_3-B_2O_3. [Adapted from [1]]

1.2. Ln_2O_3-B_2O_3-WO_3 System

For the study carried out with other lanthanides, the composition $25Tb_2O_3$-$35B_2O_3$-$40WO_3$, the most stable of the samples of the above-mentioned system, was used as a base. The same procedure was used, producing samples with 25 mol % of Nd_2O_3, Sm_2O_3, Eu_2O_3, Gd_2O_3, Dy_2O_3, Ho_2O_3, Er_2O_3 or Tm_2O_3 in addition to a sample with 12.5% Gd_2O_3 and 12.5% Tb_2O_3, all calculated to final mass of 10 g.

The pre-synthesis of H_3BO_3 was carried out in a Pt crucible, as shown in Eq. 1 and, after dehydration, the corresponding lanthanide masses and WO_3 were added. Melting occurred at 1250 °C and, after 1 h, the temperature was raised to 1350 °C, maintained for 10 min, to decrease the viscosity. Then, the liquid was quenched at 30 °C below Tg. The samples remained at this temperature for 6 h for thermal treatment to

reduce tensions in the glass and improves the mechanical properties and after it was left to reach the room temperature under cooling at 1 °C . min^{-1}.

Samples were cut and optically polished using sandpaper and polishing slurries for optical characterizations.

1.3. $SbPO_4$ synthesis

$SbPO_4$ was synthesized using Sb_2O_3 in H_3PO_4 medium by G. Alonzo et al method [3]. 95 mL of 85% H_3PO_4 was transferred to a 250 mL flask and then diluted in 1.5 L of deionized water. 21.5 g of Sb_2O_3 (Sigma-Aldrich, 99.9%) were weighed, placed in H_3PO_4 and left under constant agitation for four days. Soon after this period, agitation was stopped for 24 h so that the antimony orthophosphate could be decanted. After complete phase separation ($SbPO_4$(s)/supernatant), the process of replacing the supernatant with deionized water was started until the pH of the system reached neutrality (pH = 7.0).

The $SbPO_4$ was then dried in an oven at 150 °C for 3 days. Duly dried, it was macerated in an agate mortar and taken for thermal treatment in ovens. This thermal treatment consisted of using a heating ramp of 10 °C. min^{-1} with three temperature steps to convert $SbPO_4$ into its orthorhombic phase.

1- 200 °C – 2 h.
2- 400 °C – 4 h.
3- 550 °C – 6 h.

The final material was analyzed by Raman spectroscopy, with confirmation of the orthorhombic phase formation. The control of the $SbPO_4$ grade is very important, once the presence of Sb_2O_3, that has not been converted, can chemically attack the platinum crucible during glass melting.

1.4. $SbPO_4$-ZnO-PbO-MnO System

A series of glasses in the 100-x (70$SbPO_4$–10ZnO–20PbO) xMnO system, with x =0, 10, 20, 30 and 40 mol %, were prepared melt-quenching technique. ZnO (99.99% Aldrich), PbO (99.9% Sigma), $MnCl_2.4H_2O$ (99% Spectrum) and $SbPO_4$ reagents were weighed in the amounts relative to each composition, homogenized in a Speedmixer for 3 times of 1.5 min with 2000 rpm and transferred to a Pt crucible. First heated to 550 °C in an oven for dehydration of $MnCl_2.4H_2O$ and Cl_2 purging, then melted for 1 h at 1250-1400 °C, depending on the composition. Subsequently, the liquid was cooled in a preheated mold at 350 °C and left for annealing at this temperature for 5 h to reduce thermal stress. The samples were polished with SiC sandpaper to obtain optical quality for further characterization.

2. INSTRUMENTAL METHODS

2.1. Thermal analysis

Differential scanning calorimetry (DSC) is a thermal analysis technique in which the difference in energy delivered to the substance and a reference material as a function of temperature is measured while the substance and reference material are subjected to a controlled programming of temperature. According to the measurement method used, there are two modalities: with power compensation and with heat flow. Through these techniques, one can monitor the effects of heat associated with physical or chemical changes in the sample, such as phase transitions (melting, boiling, sublimation, freezing, inversions of crystalline structures) or reactions of dehydration, dissociation, decomposition, oxidation-reduction, etc. capable of causing heat changes. In general phase transitions, dehydrations, reductions and certain decomposition reactions produce endothermic effects, while crystallizations, oxidations, some decomposition reactions produce exothermic effects. This technique also allows studying second-order transitions involving entropy changes, of which the most common are glass transitions[4].

As previously discussed, the glass transition temperature is defined as the temperature region where, during heating, the passage of the vitreous material to the viscoelastic state occurs, and during cooling the passage of the supercooled liquid to the glass. This passage occurs at a viscosity of 10^{12} Pa.s, when the material begins to respond elastically to the applied force, without deforming elastically. Being a second-order thermodynamic transition, there is no heat transfer between the system and the environment, but a change in heat capacity and thermal expansion, which begin to manifest a different behavior from the pattern observed until then.

In this work, this technique was used to determine the characteristic temperatures of glasses (Tg, Tx, Tp and Tm). These temperatures are extremely important in the study of glass properties. Furthermore, this technique provides the parameter used to estimate the thermal stability of glasses, $\Delta T = Tx-Tg$, which means that the greater the difference, the more stable the glass is with increasing temperature, or in other words, the more difficult will be the crystallization of the glass. It is also a widely used parameter to estimate whether glass can be prepared as large pieces or even be pulled into fiber optics.

The DSC were carried out both at the *Departamento de Química Analítica, Físico-Química e Inorgânica* of the Institute of Chemistry (IQ) (UNESP / *campus Araraquara*), and at the *Institut de Chimie de la Matière Condensée de Bordeaux (ICMCB)*, UMR5026 of the CNRS, Université de Bordeaux and Bordeaux INP. At ICMCB, it was used Netzsch DSC Pegasus 404PC equipment, using small glass pieces (few mg) in a Pt pan at a heating rate of 10 °C. min^{-1} up to 900 °C under N_2 atmosphere with a precision of ± 3 °C for glass transition (Tg) and onset of crystallization (Tx). The reference used was an empty platinum pan. At IQ, it was used a Netzsch DSC 404 F3 Pegasus equipment, in the same conditions.

2.2. X-Ray Diffractometry

Another essential measure necessary for the study of glasses is X-ray diffraction, as it reveals whether the substance in question has monocrystalline, polycrystalline or non-crystalline phases. In XRD, a beam of X-rays is directed on the sample, and the scattered X-rays are collected with a detector. The detector records the

intensity and angle of the scattered X-rays. The angle of diffraction is determined by Bragg's law, which relates the wavelength of the X-rays, the angle of incidence, and the spacing between the planes of atoms in the material. By analyzing the diffraction pattern, the atomic or molecular structure of the sample can be determined. In the case of non-crystalline solids, like glass, the diffraction pattern is usually broad and diffuse because of the lack of long-range order.

XRD was carried out at ICMCB, collected on a PANalitycal X′pert PRO MPD diffractometer in Bragg−Brentano θ−θ geometry, equipped with a secondary monochromator and X′Celerator multi-strip detector. Each measurement was made within an angular range of 2θ = 8 − 80°. The Cu Kα radiation was generated at 45 kV and 40 mA (λ = 0.15418 nm).

2.3. Density measurements

The densities (ρ) of glasses were measured according to the Archimedes' principle using the buoyant force of diethylphthalate (DEP) as reference liquid, like Eq. 17.

$$\rho_{sample} = \rho_{DEP\,(T)} \frac{m_{air}}{m_{air} - m_{im}} \qquad (Eq.17)$$

The samples (a few square centimeters) are weighed precisely in the air (m_{air}) and then immersed in the liquid (m_{im}). The density of diethylphthalate is well known as a function of temperature (to within 0.25 °C). Thus, by checking the temperature, it is possible to determine the volume of liquid displaced during immersion and go back to the density of the sample. Changes in the temperature measurements remains the main source of errors for this technique, but the errors can be estimated as low as ± 5 x 10^{-3} g.cm^{-3}.

Measurements were performed at ICMCB, at room temperature, using a mercury thermometer Precision XT 220A analytical balance (error of ±0.0001 g). Each sample was measured five times, immersing and cleaning it properly after each immersion. Later, the mean and the standard deviation were calculated for each sample.

2.4. Fourier-transform infrared spectroscopy

Infrared spectroscopy exploits the fact that molecules absorb frequencies that are characteristic of their structure. These absorptions occur at resonant frequencies, that is, the frequency of the absorbed radiation corresponds to the vibrational frequency, corresponding molecular potential energy and the mass of the atoms involved. In order for a vibrational mode to be active in a sample, it must be associated with changes in the bond dipole moment. A permanent dipole is not necessary, as the rule requires only a change in dipole moment. As vibrational absorptions have low energy, nowadays IR spectroscopies made by interferometry are used, where the data are processed by Fourier transform (FTIR).

Measurements were collected using FTIR by specular reflectance, recorded from 275 to 4000 cm^{-1} at quasi-normal incidence (11°) on a Vertex 70 V Fourier transform spectrometer equipped with a Globar MIR type source, a DTGS detector and a beam splitter adapted to the MIR. Samples were used in bulk, with well-polished surfaces. All measurements were performed in vacuum at room temperature, with spectra been recorded from an average of 200 scans and resolution of 4 cm^{-1}. A gold mirror is used as a reference.

Measurements were made using specular reflectance, based on the principle that each sample has a refractive index that varies with the frequency of the light to which it is exposed and instead of examining the energy that is absorbed, we measure the energy that is reflected from the surface (the first few microns) of a sample. By examining frequency bands where the rate of change in the refractive index is high, correlations can be made about sample absorption.

A Kramers-Krönig inversion technique (KK transformation) then allows, from the specular reflection spectrum, to calculate the absorption coefficient spectrum. First, the measured reflectivity R(ν) is transformed to obtain the phase angle difference, β(ν), between reflected and incident wave:

$$\theta(\nu) = \frac{2\nu}{\pi} \int_0^\infty \frac{ln\, r(\nu')}{\nu^2 - \nu'} d\nu' \qquad (Eq.\,18)$$

where $(\nu) = (R(\nu))^{1/2}$, and the reflectivity coefficient is $re^{i\beta}$.

The above KK transformation was performed by utilizing the Brunker HIL program, after appropriate extrapolations of the reflectance data at $\nu \to 0$ and $\nu \to \infty$ (Bruker EXTPOLR program). Once the spectrum of $\beta(\nu)$ was calculated, then the real (n), and imaginary (k) parts of the refractive index were obtained on the basis of the Fresnel formulas:

$$n = \frac{1 - r^2}{1 + r^2 - 2r\cos\beta} \qquad (Eq.19)$$

$$k = \frac{2r\sin\beta}{1 + r^2 - 2r\cos\beta} \qquad (Eq.20)$$

Having determined the frequency dependent refractive index n, and the extinction coefficient k, the real and imaginary parts of the complex dielectric permittivity, ε’ and ε" respectively, can be obtained from the relations

$$\varepsilon' = n^2 - k^2 \qquad (Eq.21)$$

$$\varepsilon'' = 2nk \qquad (Eq.22)$$

The quality of the KK transformation (Eq. 18) is checked by comparing the experimental reflectance spectrum with that calculated by

$$R = \frac{(n-1)^2 + k^2}{(n+1)^2 + k^2} \qquad (Eq.23)$$

where n and k are those obtained from the KK analysis.

The optical and dielectric constants are then used to calculate the absorption coefficient (α), $\alpha = 4\pi\nu k = 2\pi\nu\varepsilon''/n$. This treatment have been performed to extract the real (n_0) and imaginary (k) parts of the refractive index n, using the relation $n = n_0 + ik$[5].

At IQ, measurements were made using attenuated total reflection method (ATR-FTIR). ATR uses a property of total internal reflection resulting in an evanescent wave. A beam of infrared light is passed through one diamond crystal in such a way that it reflects at least once out the internal surface in contact with the sample. This reflection forms the evanescent wave which extends into the sample. The measurements were performed in a BRUKER VERTEX 70 spectrophotometer, with a DLaTGS detector, made from 400 to 4000 cm^{-1}. Powder samples were used.

2.5. Raman scattering spectroscopy

Raman scattering spectroscopy is a vibrational spectroscopy that involves exciting the sample with light. The energy of the incident photons is too high to excite the modes of vibration; it is also too weak to excite electronic levels. Therefore, there is no absorption in Raman spectroscopy, being a phenomenon linked to light scattering. We say that excited levels are virtual levels.

There is a possibility that not all photons are reflected elastically (Rayleigh scattering occurs when the frequency of an incident photon is the same as the reflected photon) and some are reflected inelastically, with a small difference in energy relative to the vibrational levels of the substance. This inelastic scattering is orders of magnitude lower than Rayleigh scattering and is known as Raman scattering. If the reflected photon is of lower energy than the incident photon, it is called Raman-Stokes scattering (or simply Raman scattering), and if it is of higher energy, it is called anti-Stokes scattering, which is also much lower compared to Raman scattering. The energy diagram in Figure 16 represents these different energy levels and phenomena.

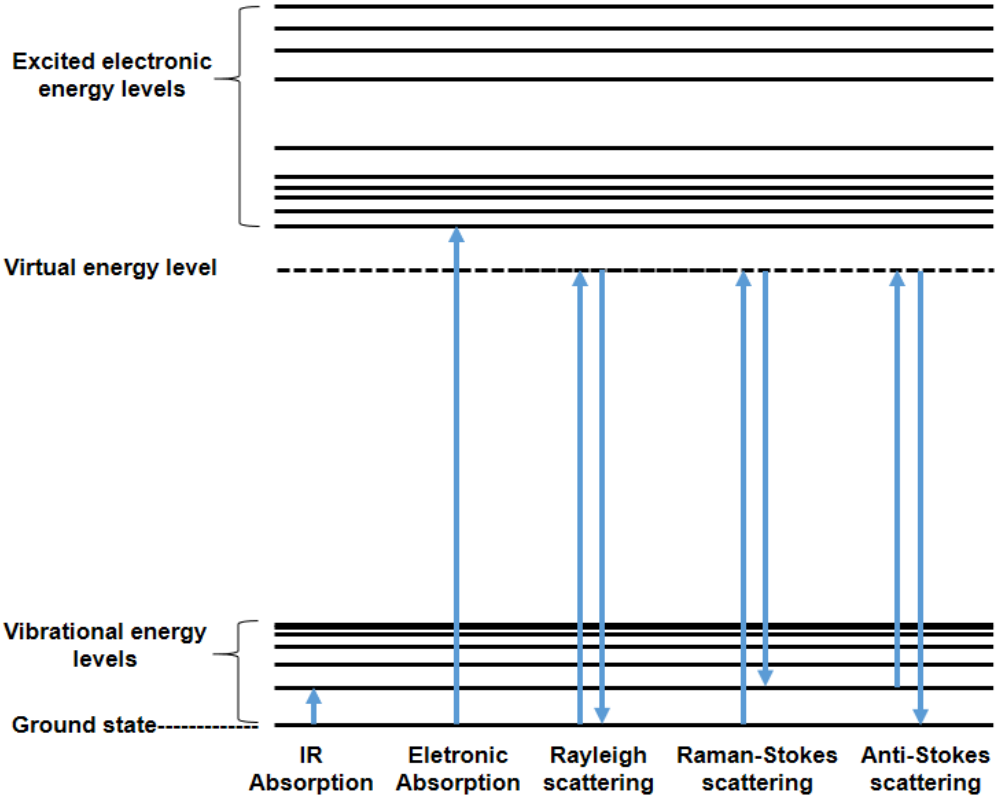

Figure 16. Energy diagram representing the principle of Raman scattering compared to Rayleigh scattering, anti-Stokes scattering, and electronic and IR absorption. (Own authorship).

Raman spectroscopy and IR spectroscopy are complementary. In fact, in Raman, the active modes are those for which the polarizability variation is different from zero. Thus, certain modes that are not active in IR, without changing the dipole moment, will be active in Raman and vice versa[6].

Raman scattering measurements were performed at IQ at room temperature using a LabRam HR spectrometer, Horiba-Jobin Yvon. The 632 nm line from an argon ion laser was focused on the samples by an optical microscope using a long work distance 50X objective. At ICMCB, measurements were performed at room temperature using XploRA PLUS (Horiba) spectrometer, with 532 nm and 785 nm, using 50X objective. Different wavelengths were used because some lanthanides can show luminescence under laser excitation. As the the luminescent emissions are much more intense than the scattering, the Raman spectra must be obtained using lasers that do not excite the rare earth absorption modes.

2.6. ^{11}B-Nuclear magnetic resonance

The ^{11}B-NMR method is based on the interaction between the nuclear spin of the boron atom and an external magnetic field. In the absence of a magnetic field, boron atoms have random orientations of their nuclear spins. However, when placed in a strong external magnetic field, the boron atoms align their nuclear spins in two energy levels, depending on their orientation with respect to the magnetic field.

When the boron atoms are irradiated with a radiofrequency pulse that matches the energy difference between the two nuclear spin levels, they can be excited to the higher energy level. The amount of energy required to excite the boron atoms depends on their local environment, which affects the strength of the external magnetic field experienced by each boron atom. Therefore, the resonance frequency of the boron atoms varies depending on the local environment and bonding of each boron atom in the glass.

In glasses, boron atoms can exist in various chemical environments, depending on their coordination number, the nature of their neighboring atoms, and the degree of polymerization of the glass network. For example, boron atoms can exist in three-, four-, or five-fold coordination, and their neighbors can be oxygen, tungsten or the rare earth. By analyzing the ^{11}B-NMR spectra of boron in glasses, it is possible to determine the chemical shifts and line shapes of the boron resonances, which provide information about the local bonding and environment of the boron atoms.

This technique was mainly used to help understand the structural part of glasses containing lanthanides, mainly as a complement to Raman and infrared spectroscopies. As the NMR technique is very sensitive to paramagnetic samples, glasses containing La_2O_3, mimicking different concentrations of other lanthanides, were used for this study.

2.7. UV-Visible-NIR Spectroscopy

UV-Visible-NIR spectroscopy is a technique that uses light in the ultraviolet (UV, 200 - 400 nm), visible (400-800 nm), and near-infrared (NIR, 800 - 3300 nm) regions of the electromagnetic spectrum to study the electronic and molecular structure of compounds. The principles are based on the fact that when a molecule

absorbs light, it undergoes a transition from a lower energy state to a higher energy state. The amount of energy absorbed depends on the molecular structure and the wavelength of light used. The amount of light absorbed by a molecule at a particular wavelength is proportional to the concentration of the absorbing entity in the sample, as well as to its molar absorptivity, at that wavelength. By measuring the intensity of incident and absorbed light for each wavelength, we can construct an absorption (or transmission) spectrum of the studied compound.

It is also interesting for us to know the transparency of the samples at 1550 nm, the main wavelength currently used in telecommunications. For applications in this field, it is necessary that the material presents considerable transparency in this wavelength, without absorptions characteristic of the components. Likewise, knowing the transparency of samples will be helpful to validate the possibility to use the glass as Faraday rotators.

Measurements were made using an Agilent Cary 5000 UV-Vis-NIR Spectrophotometer. Optically polished samples with ~1.0 mm thickness were used for the measurements.

2.8. Refractive index measurements

Refractive indices were measured using the Brewster angle method. Brewster's angle (θ_{B1}) is the angle of incidence at which light with a particular polarization is perfectly transmitted through a transparent surface, with no reflection. From the Snell-Descartes equation, follows the expression of this particular angle as a function of the indices n_1 (air = 1) and n_2 (sample). Thus, by knowing the value of the Brewster angle for a given wavelength, it is possible to find n_2.

$$\theta_{B1} = \arctan\left(\frac{n_2}{n_1}\right) \qquad Eq.25$$

To obtain this value, the sample is irradiated with polarized light, as shown in the scheme of Figure 17. Measurements were made for 4 different wavelengths, 532, 639, 785 and 925 nm, with an estimated error of 0.005.

The sample and detector are rotated automatically. Then, the angle of incidence is varied, with the reflectance data being analyzed by a computer.

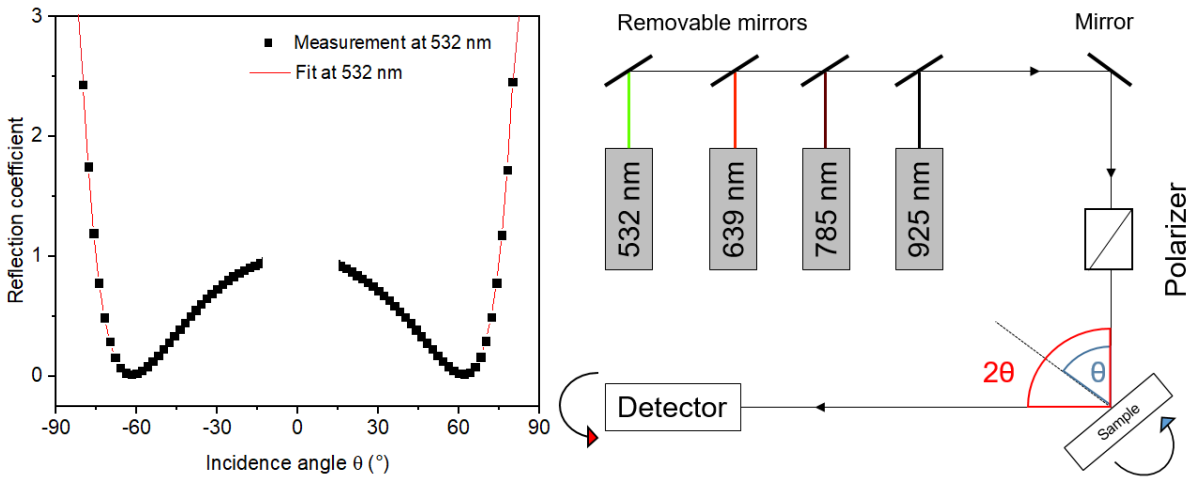

Figure 17. Experimental scheme for the refraction index measurement using the Brewster angle method. The graph on the side shows an example of the angular scan for the 25Tb40W sample at 532 nm. The red fit represents the adjustment of the parameters allowing the index to be extracted in the used wavelength. (Adapted from[7])

2.9. Fluorescence spectroscopy

Fluorescence spectroscopy is based on electronic excitation process using photons. During the photoluminescence process, light is shining on a sample where it is absorbed generating an excess of energy in the material, in an effect called photoexcitation. Photoexcitation causes the electrons in the material to undergo transitions to excited states with energies higher than those of the equilibrium states. When these electrons return to their equilibrium states, excess energy is emitted and may include the emission of light (radiative process) or not (non-radiative process). The energy of the emitted radiation is related to the difference between the two electronic states involved in the transition. The amount of light emitted depends on the relative contribution to the radiative process.

Photoluminescence measurements were made at room temperature using a Horiba Jobin Yvon Spectrofluorimeter, Model Fluorolog-3 FL3-122, front face, with powder samples, with the same amount filling the sample holder. Due to the high concentrations of emitting ions, mainly lanthanides, the quenching process was high,

making it impossible to identify luminescence with the naked eye. Therefore, for the emission spectra, larger apertures were used. For emission spectra 3-3-5 mm / 1-1-5 mm for entrance, exit and intermediate slit, respectively, with 0.3 s for accumulation time in a step of 0.5 nm. For excitation spectra, slits 1-1-7 / 2-2-7 mm, accumulation time of 0.3 s and step of 0.5 nm were used.

2.10. Magnetic susceptibility measurements

Magnetic susceptibility was collected at ICMCB using a superconducting quantum interference device (SQUID) with Quantum Design MPMS-7XL magnetometer in the temperature range of 5–150 K under 100 Oe (= 0.0001 T) in two different protocols for measuring, the ZFC and FC.

ZFC stands for "zero field cooled" and refers to a protocol in which the sample is first cooled down in the absence of any applied magnetic field. Then, a small magnetic field is applied, and the response of the sample to this field is measured as the temperature is increased. The ZFC curve represents the magnetic response of the sample as a function of temperature for increasing temperatures.

In protocol FC, field cooled, in which the sample is cooled down while an applied magnetic field is present. The field is then kept constant as the sample is warmed up, and the magnetic response of the sample is measured. The FC curve represents the magnetic response of the sample as a function of temperature for decreasing temperatures.

The key difference between the ZFC and FC measurements is the direction of the temperature sweep relative to the direction of the magnetic field. In the ZFC measurement, the magnetic field is applied after the sample has been cooled down, whereas in the FC measurement, the magnetic field is applied during the cooling process. The ZFC and FC curves can provide different information about the sample, depending on its magnetic properties. In general, the ZFC curve is sensitive to the presence of superparamagnetic or paramagnetic particles in the sample, which can become magnetized at low temperatures and then become disordered as the temperature is increased. The FC curve is sensitive to the presence of ferromagnetic or ferrimagnetic

particles in the sample, which can become magnetized and remain magnetized as the temperature is decreased.

However, it was observed that for all samples the ZFC and FC results presented the same behavior, indicating that there are no differences in the system.

2.11. Faraday effect measurements

The Faraday Effect was measured using a homemade optical bench at 632.8 nm. The He-Ne laser pass firstly by a polarizer then through the glass sample, which is inside a magnet, them through a second polarizer and finally reaches a detector. The measurement was done 5 times using a graduated polarizer with a precision of 2° (= 0.03491 rad). Faraday rotation angles (β) were measured at room temperature using an optical setup containing a magnet showing a static magnetic field of 0.15 T. The Faraday rotation setup was calibrated using a commercial terbium gallium garnet (TGG) single crystal with a length of 20 mm from EOT, with a Verdet constant value of -134 $rad.T^{-1}.m^{-1}$. Figure 18 shows the setup used in this work.

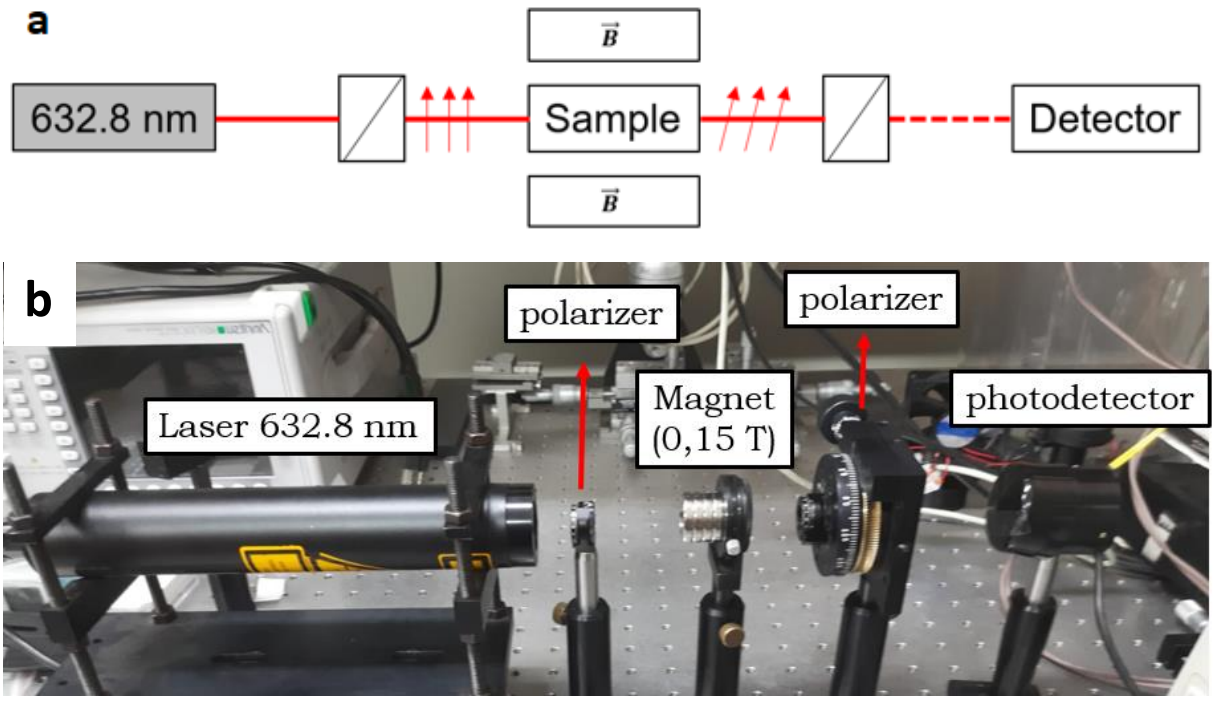

Figure 18. Scheme (a) and real apparatus (b) for Faraday effect measurements. Light from the 632.8 nm laser passes through the polarizer, then through the sample under the B field, which

causes a rotation on the axis of polarization of the light. This deflection is measured on the second polarizer. (Own authorship).

References in this chapter

[1] E.M. Levin, The System WO_3-B_2O_3, J. Am. Ceram. Soc. 48 (1965) 491–492. https://doi.org/10.1111/j.1151-2916.1965.tb14808.x.

[2] P.L. Baynton, H. Rawson, J.E. Stanworth, Glass based on the oxides of molybdenum, tungsten and uranium, Nature. 178 (1956) 910–911. https://doi.org/10.1038/178910a0.

[3] G. Alonzo, N. Bertazzi, P. Galli, M.A. Massucci, P. Patrono, F. Saiano, On the synthesis and characterization of layered antimony(III) phosphate and its interaction with moist ammonia and amines, Mater. Res. Bull. 33 (1998) 1221–1231. https://doi.org/10.1016/S0025-5408(98)00094-4.

[4] M. Ionashiro, Giolito - Princípios Básicos da Termogravimetria e Análise Térmica Diferencial/Calorimetria Exploratória Diferencial, GIZ Editorial, 2004.

[5] E.I. Kamitsos, A.P. Patsis, M.A. Karakassides, G.D. Chryssikos, Infrared reflectance spectra of lithium borate glasses, J. Non. Cryst. Solids. 126 (1990) 52–67. https://doi.org/10.1016/0022-3093(90)91023-K.

[6] O. Sala, Fundamentos da Espectroscopia Raman e no Infravermelho, 2nd ed., Editora UNESP, São Paulo, 2008.

[7] L. Karam, Structuration multi-échelle et multifonctionnelle de nouveaux matériaux vitreux pour la photonique intégrée, Université de Bordeaux, 2020.

CHAPTER III – Characterization and study of properties of the Tb_2O_3-B_2O_3-WO_3 System

Chapter III - Characterization and study of properties of the Tb_2O_3-B_2O_3-WO_3 System

1. Samples

As previously mentioned, the work will focus on the study of the series of samples containing the highest WO_3 and Tb_2O_3 mol % without crystallization. Therefore, we will focus on the xTb_2O_3-$(60-x)B_2O_3$-$40WO_3$ series. These most stable glassy samples were cut and polished for further optical characterizations, as seen in Figure 19. All samples show magnetic behavior, being attracted by commercial neodymium magnets (N42) at room temperature. Evidencing the high paramagnetic effect in these samples.

Figure 19. Samples xTb_2O_3-$(60-x)B_2O_3$-$40WO_3$ series, after cut and polishing, with their specific names. (Own authorship).

The acronyms, nominal compositions (xTb40W) and mol%, molar mass (M, g . mol^{-1}) of investigated samples are summarized in Table 2. The cationic percentage was also included for comparison purposes since glasses with this terbium concentration (> 25% Tb^{3+}) are not trivial to obtain. It is also indicated if there was phase separation during quenching. Samples 15Tb40W and 30Tb40W already had crystalline phase formation during pouring, showing the small glass-forming region for this system.

Table 2. Series of Tb-containing borotungstate glasses, showing name, nominal compositions (in mol % and cat mol %), molar mass (M) and if phase separation occurred during quenching.

Samples	Nominal compositions (mol %)			Nominal compositions (cat mol %)			M ($g \cdot mol^{-1}$)	Phase separation after melt-quenching
	Tb_2O_3	WO_3	B_2O_3	$TbO_{3/2}$	WO_3	$BO_{3/2}$		
15Tb40W	15	40	45	18.75	25	56.25	178.94	Yes
20Tb40W	20	40	40	25	25	50	193.75	No
22.5Tb40W	22.5	40	37.5	28.125	25	46.875	201.16	No
25Tb40W	25	40	35	31.25	25	43.75	208.56	No
27.5Tb40W	27.5	40	32.5	34.375	25	40.625	215.97	No
30Tb40W	30	40	30	37.5	25	37.5	223.38	Yes

(Own authorship).

The decrease in the concentration of B_2O_3, the main former of the vitreous network, decreases the stability of the network, inducing the formation of crystals more easily. At high concentrations of B_2O_3 the same occurs, with the formation of other crystalline phases.

2. XRD.

The formation of the vitreous phases was verified by the XRD, shown in Figure 20. The diffractograms reveal the presence of crystalline phases for samples 15Tb40W and 30Tb40W, indicating a low stability against devitrification for such compositions. The high concentration of Tb_2O_3 (> 27.5 mol %) favors the precipitation of a $TbBO_3$ phase (phase analogous to YBO_3, ICSD code - 27931)[1]. For concentrations below 15 mol %, polycrystalline precipitation occurs, characteristic of rare earth borates[2,3].

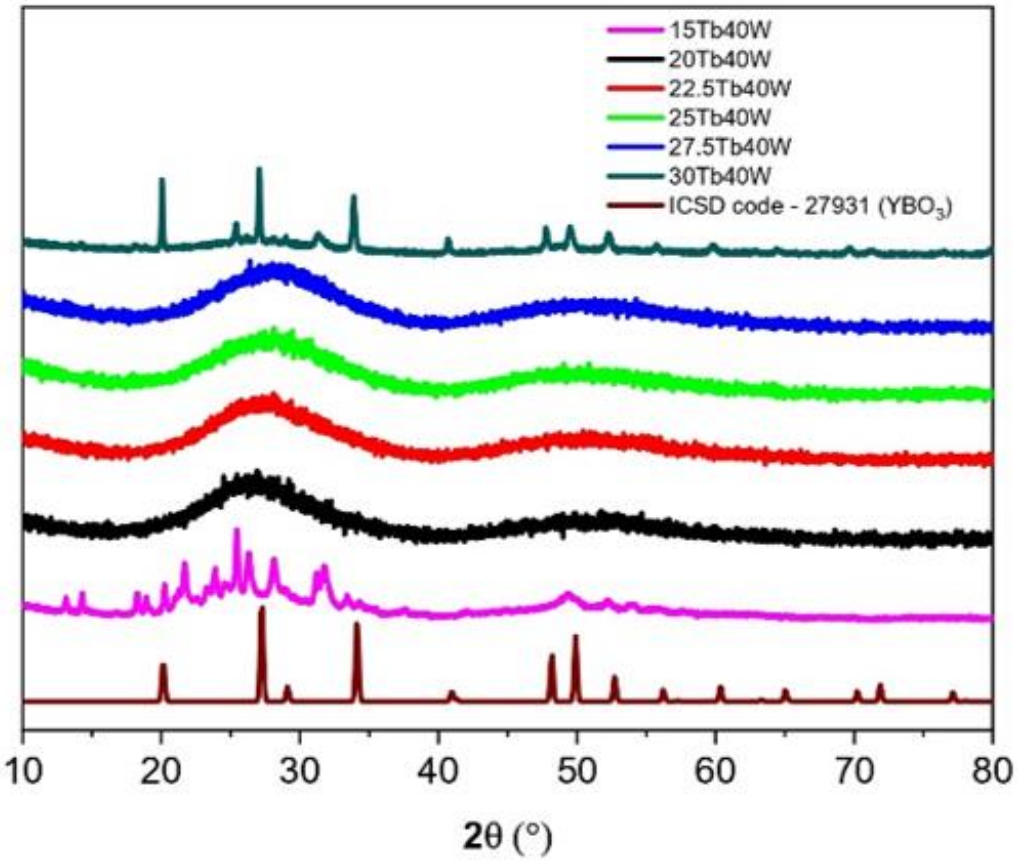

Figure 20. xTb40W samples diffractograms and YBO_3 analogous phase. (Own authorship).

As studied by E. M. Levin et al[2], there are several types of rare earth borates, depending on the proportion of boron, the ionic radius of the rare earth, the temperature of synthesis and, therefore, several factors interfere in these precipitations, forming polycrystalline phases as in the 15Tb40W sample.

On the other hand, samples 20Tb40W, 22.5Tb40W, 25Tb40W and 27.5Tb40W did not present such peaks, exhibiting the diffraction halos, characteristic of glassy materials.

3. Thermal analysis

Figure 21 a. and b. exhibits the DSC curves and Tg variation of the glass samples, respectively. The characteristic temperatures and thermal stability parameter values are show in Table 3. From Figure 21 b. one observes that the Tg increases as a

the content of terbium oxide increases and the boron oxide decreases, passing from 631 to 653 °C for samples containing 20Tb40W and 27.5Tb40W, respectively.

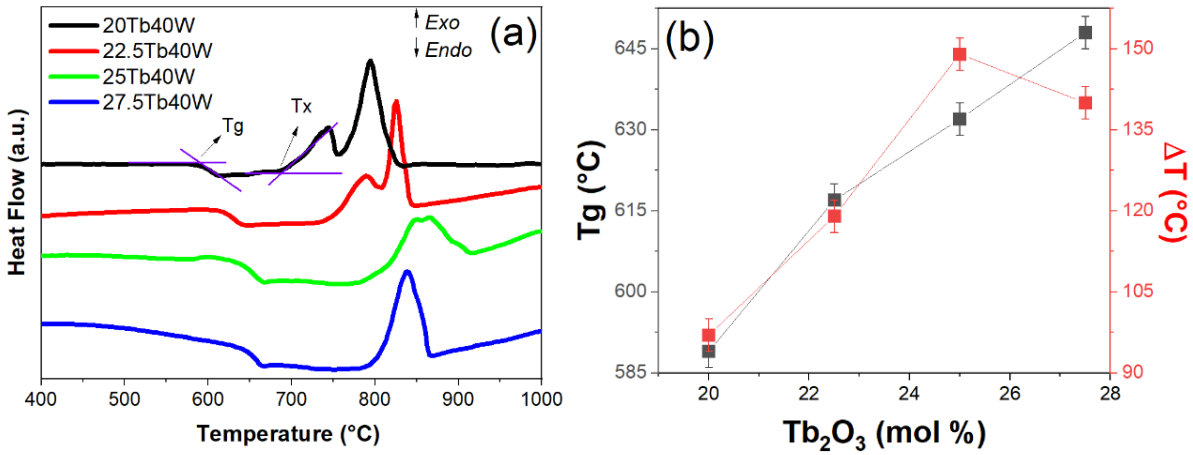

Figure 21. DSC curves (a), Tg and ΔT variation (b) for xTb40W samples. (Own authorship).

We can also observe that there are two crystallization peaks in the 20Tb40W and 25Tb40W samples, with the possible superposition of these phases in the other samples. This confirms that there is formation of different terbium borates in the crystallization process, as suggested in the XRD and in the previously mentioned works.

4. Density and Optical basicity

The characteristic temperatures, the densities (ρ), ion effective concentration (N_R, R = Tb^{3+}), theoretical optical basicity (Λ_{Th}) and short wavelength cut-off (λ_{UV}) for samples are resumed in Table 3.

Table 3. Thermal and physical properties of the glass samples: Tg (glass transition temperature), Tx (onset of the crystallization temperature), ΔT (thermal stability parameter), ρ (density), N_{Tb3+} (ion effective concentration), Λ_{Th} (theoretical optical basicity) and λ_{UV} (short wavelength cut-off).

Samples	**Tg** (±3 °C)	**Tx** (±3 °C)	**ΔT** (±3 °C)	**ρ** (±0.005 g.cm^{-3})	**N_{Tb}^{3+}** (10^{21} ion.cm^{-3})	**Λ_{th}**	**λ_{UV}** (nm)
20Tb40W	589	686	97	5.860	13.8	0.922	357

22.5Tb40W	617	736	119	5.904	14.5	0.927	377
25Tb40W	632	781	149	6.123	15.5	0.933	379
27.5Tb40W	648	788	140	6.629	17.2	0.938	388

(Own authorship).

One of the information that can be obtained using the density of the samples is the effective ionic terbium concentration (N_{Tb3+}), that is, the effective amount of trivalent lanthanide ions that entered the structure of the glass matrix and contributes to the magneto-optical effect. This ionic density is calculated using Eq. 24.

$$N_{Tb^{3+}}(ion.cm^{-3}) = \frac{2x\rho N_A}{M} \qquad (Eq.24)$$

where x is the mole fraction of Tb_2O_3, and N_A, ρ, M are, respectively, Avogadro constant, density, and molar mass for each composition.

Theoretical optical basicity (Λ_{th}) is obtained from the Lewis acid-base theory and electronic polarizability[4–6] and is often used to determine the ability to donate electrons from oxygen in a glass matrix. It is used to classify the covalent/ionic ratios of the glasses since its value is inversely proportional to covalency. Λ_{th} can be correlated with the structural properties, such as an increase in non-bridging oxygens (NBO) generated by the introduction of a modifier in the glassy matrix, or with the optical constants refractive indices, and Verdet constants, due to the change in the polarizability[4,6]. According to Duffy[6,7] and Liu et al[8], a lower value of Λ_{th} reflects a lower content of NBO, so lower oxidation numbers of positively charged cations in the glass composition are consequently preferred, while higher Λ_{th} is related to higher refractive indices. The expression Eq. 25, proposed by Duffy, allows us to calculate the optical basicity.

$$\Lambda_{th} = \sum x_i \Lambda_i \qquad (Eq.25)$$

where x_i is the mole fraction for one of the glass precursors and Λ_i the theoretical intrinsic optical basicity value of an individual glass precursor, which for B_2O_3, WO_3, Tb_2O_3, are respectively 0.425, 1.045 and 0.954[9,10].

The variation of the Λ_{th} as a function of the terbium oxide content is better shown in Figure 22. The Λth values increased as a function of the Tb_2O_3 concentration, passing from 0.922 to 0.938 from sample 20Tb40W to 27.5Tb40W, respectively. This can be understood as an increasing in the NBO units due to the higher concentration of Tb^{3+} ions in the glass network. The Tb^{3+} addition together with the decrease of the boron oxide content contribute to the depolymerization of the borotungstate network in the glass, which is better observed and discussed in the Raman and Infrared spectroscopy analysis section.

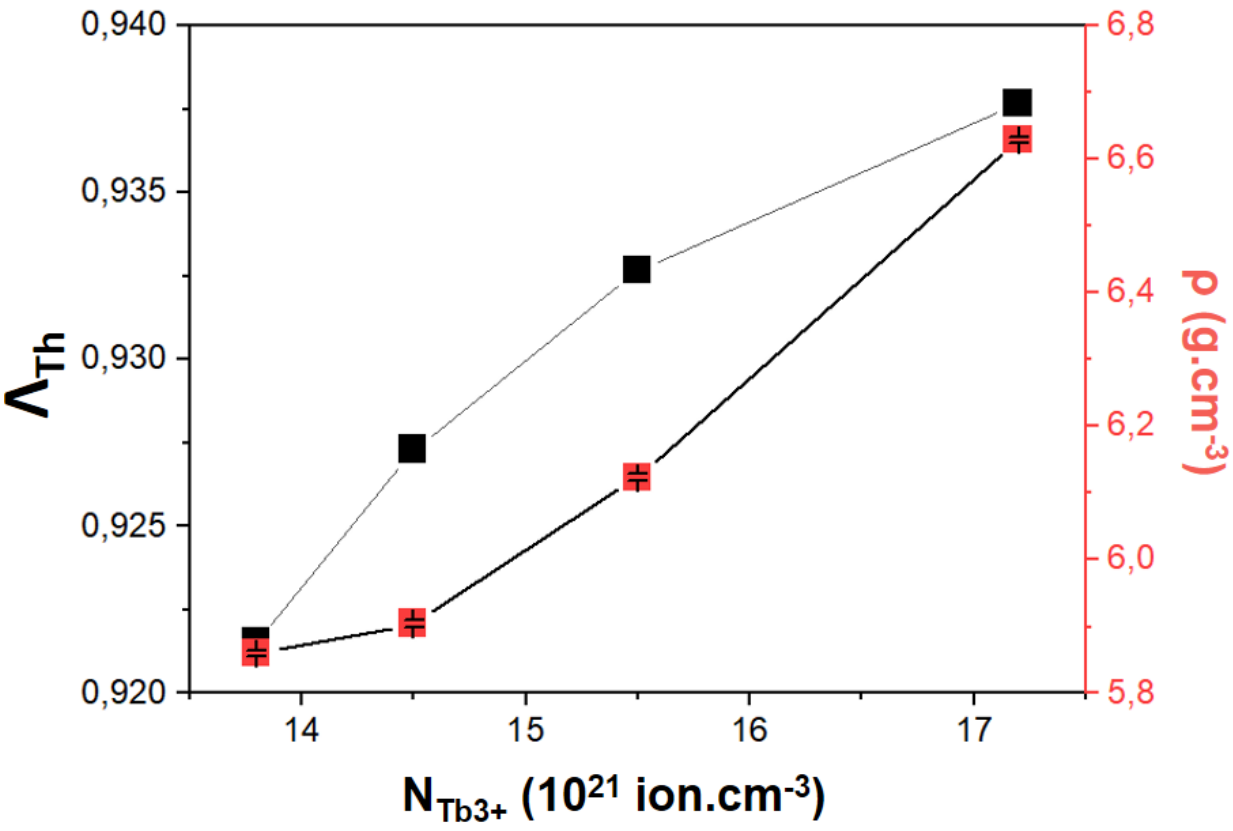

Figure 22. Theoretical optical basicity (Λ_{th}) and density (ρ) for the samples varying the Tb^{3+} ion effective concentration. (Own authorship).

One can notice that the density does not also evidence a linear evolution with the molar percent of terbium oxide. Both the evolution of the Tg and the density indicate that a structural evolution takes place when the Tb_2O_3 concentration increases.

5. Structural Analysis

Raman spectra of the samples xTb40W can be seen in Figure 23, with the respective bands attributions presented in Table 4. These Raman spectra are dominated by the tungsten associated modes at 350, 850 and 960 cm^{-1} as the polarizability of tungsten is much higher than that of boron. The boron structural units will be more easily determined by IR and ^{11}B- NMR. Figure 23 also shows the Raman spectrum of the sample 25La40W used for comparison purposes.

The Raman spectra show three main regions. At low frequencies (200-600 cm^{-1}), it is possible to identify a broad band centered at ~350 cm^{-1} that can be assigned to a coupling of vibrations, including bending modes of $[WO_6]^{6-}$ octahedral [11–14], with the stretching modes of Tb-O [18-20]. In the region between 600 and 1000 cm^{-1}, there is an envelope, corresponding to W-O stretching modes. The large band at 720 and 850 cm^{-1} contains mainly the contributions from tungsten species in a 3D network, respectively W-O-W symmetric and asymmetric stretching modes of the distorted $[WO_6]^{6-}$ octahedral in non-crystalline lattices, while the ~950 cm^{-1} band refers to stretching mode of $W\text{-}O^-$ having an ionic bonding with Tb^{3+}. The assignments of such bands have already been intensively discussed in the literature and they can be found in the following references [11–14,21,22]. According to Raman, there is a small variation in the relative intensity $\nu[W\text{-}O_t]^-$ / ν[W-O-W], regarding due to the increasing in the concentration of Tb^{3+} and consequent decreasing in B_2O_3. The higher concentration of $(WO_t)^-$ (~950 cm^{-1}) and consequently non-bridging oxygen (NBO), agrees with the data obtained for optical basicity.

As observed, the substitution of Tb^{3+} by La^{3+} does not seems to affect the structure of the glasses. It will be important, once NMR data cannot be obtained from terbium-containing glasses, due to its high paramagnetic behavior.

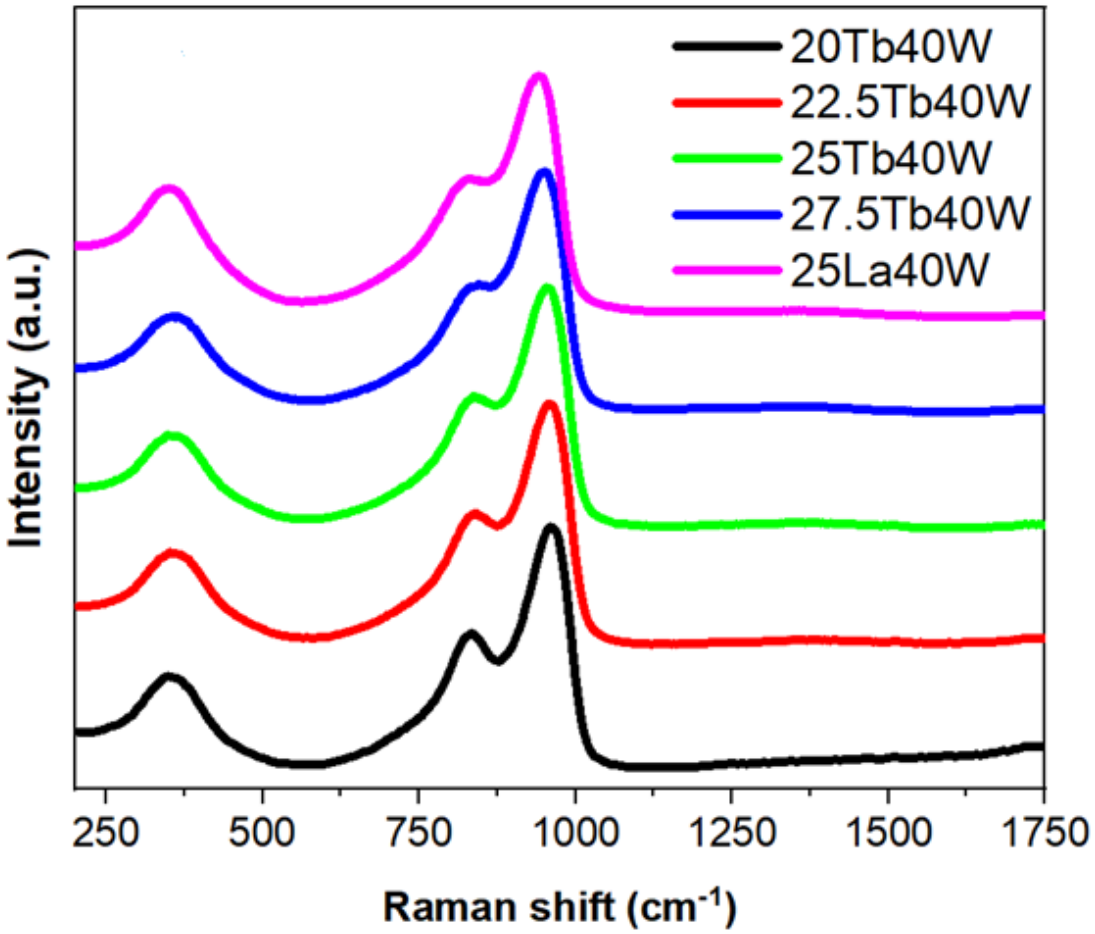

Figure 23. Raman scattering spectroscopy for the samples with different concentrations of Tb_2O_3, in addition to 25La40W sample, mimicking the 25Tb40W sample. (Own authorship).

Table 4. Band assignments of the main vibrational modes for the xTb40W glasses.

Band observed (cm^{-1})	**Raman**	**IR**	**Assignments**	**References**
350	Yes	X	Coupling of δ $[WO_6]^{6-}$ units and ν Tb-O modes	[11–14,18–20]
640-690	X	Yes	δ modes of BO_3 units	[16–19,23]
760	Yes	Yes	ν_s W-O-W of the distorted $[WO_6]^{6-}$ octahedral in non-crystalline lattices	[11–14,21,22]
840	Yes	Yes	ν_{as} W-O-W of the distorted $[WO_6]^{6-}$ octahedral in non-crystalline lattices	
950	Yes	Yes	ν $(W\text{-}O_t)^-$ of the distorted $[WO_6]^{6-}$ octahedral in non-crystalline lattices	
1060	X	Yes	ν B-O of tetrahedral $[BO_4]^-$ units	[16–19,23]

1200-1500	X	Yes	ν modes of pyroborate $[BØO_2]^{2-}$ and metaborate $[BØ_2O]^-$	

(Own authorship).

For a more accurate analysis of the contributions of boron environment in the structural part, we have combined IR spectroscopy and ^{11}B-NMR analysis. However, as indicated above, terbium containing glasses cannot be investigated using NMR due to the paramagnetic response of the terbium ions which affect the magnetic response. To bypass such limitation, a glass with substitution of terbium by lanthanum was prepared with the composition $25La_2O_3$–$40WO_3$–$35B_2O_3$ (25La40W) which is suitable for NMR characterizations. Infrared spectrum for the composition 25La40W is reported in Figure 6 b together with the spectra of others terbium-containing samples. It can be observed that there are few differences between the spectra, suggesting that the Tb/La substitution presents only few structural changes. It denotes that the substitution allows some combined IR -NMR structural characterizations.

Figure 24 shows the ^{11}B-NMR spectrum for sample 25La40W. ^{11}B MAS-NMR is able to provide the proportion of BO_4 and BO_3 with 34% of boron in tetrahedral sites and 66% in trigonal sites. Considering these results and the fact that the infrared response associated to boron in both lanthanum and terbium glasses are similar, one can assume that the 25Tb40W sample presents similar proportion of BO_4 and BO_3 than for 25La40W. The NMR spectrum indicates also two different trigonal and tetragonal sites. Regarding BO_4, on can observe that one site at δ_{iso} = 2.7 ppm is dominant. After signal decomposition, regarding the BO_3 sites, two different entities are observed at δ_{iso} = 16.9 ppm and δ_{iso} = 19.6 ppm. According to Stebbins et al. these two sites could correspond respectively to distorted trigonal site with one or two non-bridging oxygen. Note that the C_Q and η parameters obtained from the fitting of the NMR signal are also in accordance with the work of Stebbins et al.[70].

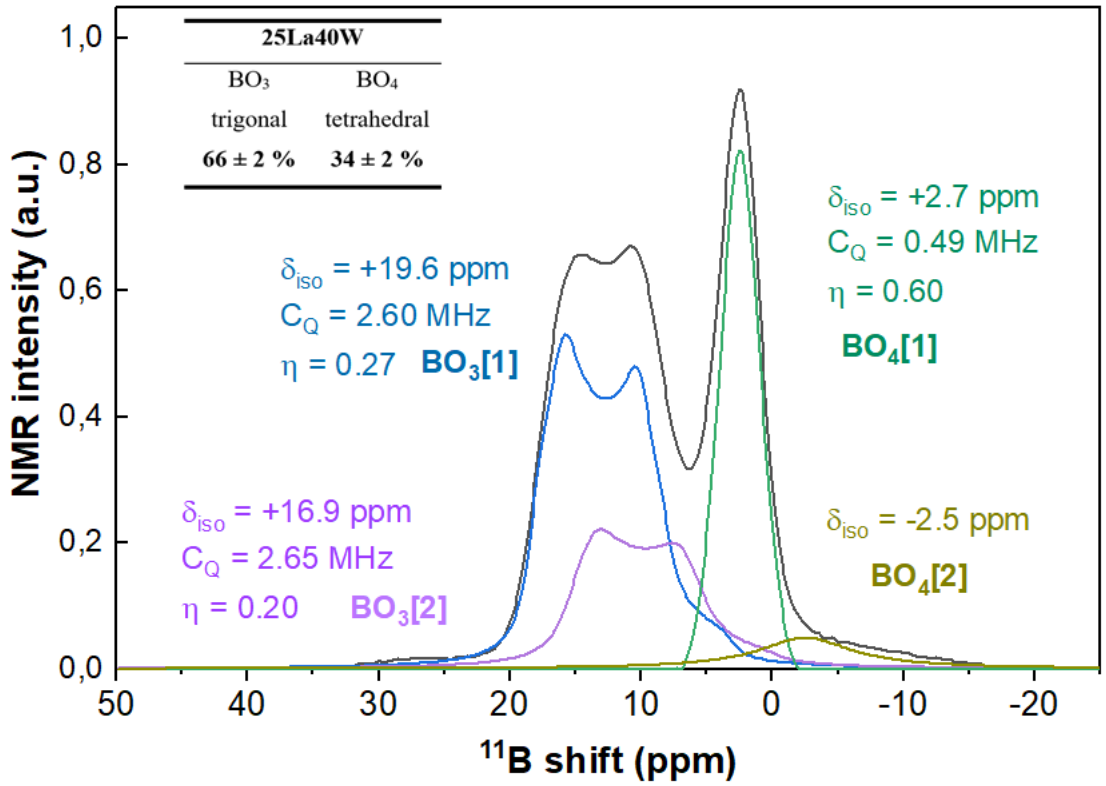

Figure 24. ^{11}B MAS-NMR for the sample 25La40W, mimetizing sample 25Tb40W. (Own authorship).

Focusing on the IR spectra, Figure 25, the band assignments around 640-690 cm^{-1}, can be assigned to bending vibrations of BO_3 units [16–19,23]. In the region between 760-840 cm^{-1}, attributed to ν_s and ν_{as} W-O-W from distorted $[WO_6]^{6-}$ octahedra, and shoulder in 960 cm^{-1} attributed to $_\nu(W\text{-}O_t)^-$ of the distorted $[WO_6]^{6-}$ octahedra [11–14,21,22]. At 1060 cm^{-1}, the characteristic stretching modes of BO_4 units arises followed by bands in the region from 1200-1500 cm^{-1} that can be attributed to the BO_3 triangular structural units, being formed by pyroborate $[B\text{Ø}O_2]^{2-}$ and metaborate $[B\text{Ø}_2O]^-$, respectively [16–19,23]. The broadening of the band at 1200-1500 cm^{-1} can be attributed to the perturbation caused by the Tb^{3+} ion, indicating a higher dispersion of ionic interaction occurring when interacting with these ions. The relative intensities of these bands are also higher, indicating an increasing in the amount of pyroborates and metaborates, comes from the need to stabilize the terbium ions by compensating its charge with NBO, which is also in agreement with the optical basicity data.

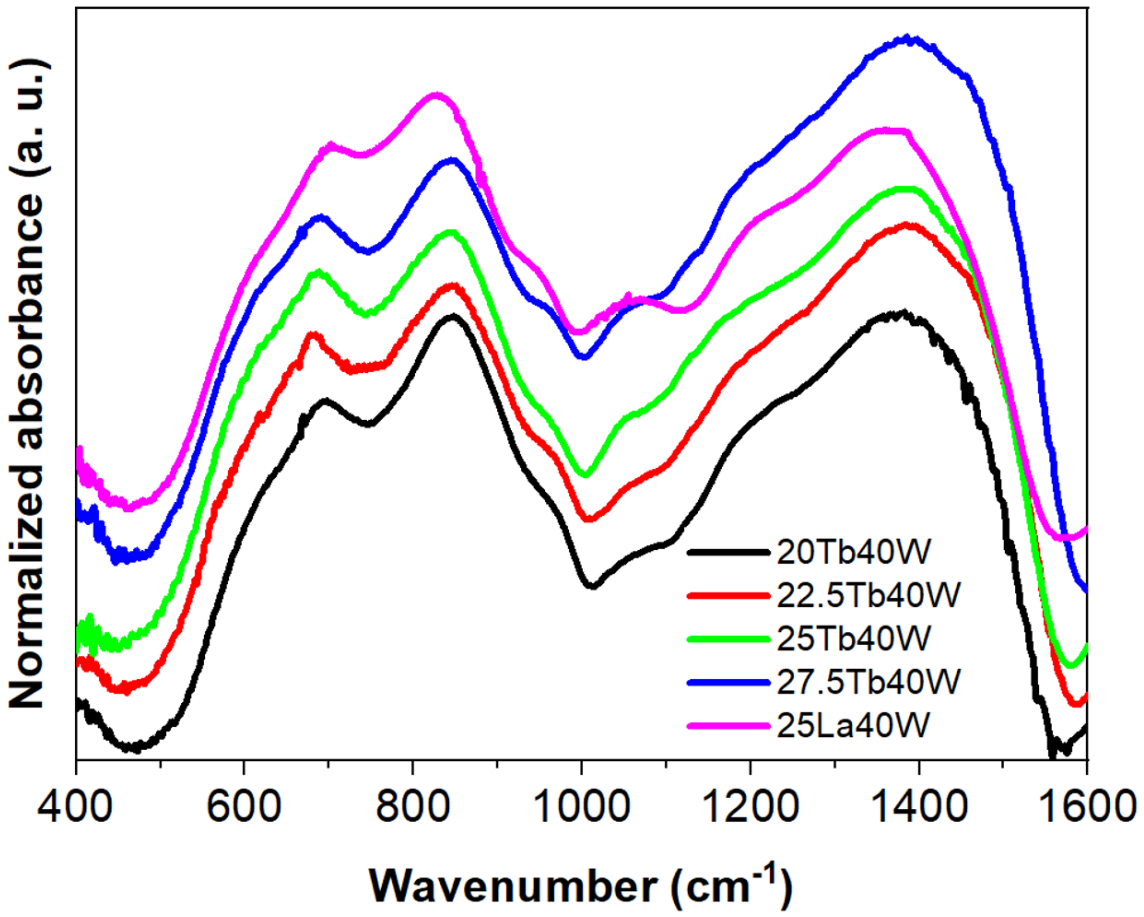

Figure 25. Normalized infrared absorption spectra, obtained by DRIFT, for xTb40W samples and 25La40W. (Own authorship).

The NMR, Raman and infrared spectroscopy analysis are in agreement and have highlighted the presence of both trigonal and tetrahedral negatively charged structural units of boron and tungsten bonding. It denotes the importance of both tungsten and borate network to facilitate the incorporation of high concentration of rare earth ions.

6. UV-Vis-NIR spectroscopies.

In Figures 26 and 27 are shown the absorption coefficient and transmittance spectra respectively of the terbium-containing samples, with the band gap energy values shown in Table 2. The absorption bands at 0.486, 1.9, 2.21, and 2.88 μm were assigned to the Tb^{3+} 4f–4f transitions from the $^7F_6$ ground state to the excited states

$^5D_4$, $^7F_{0,1,2}$, $^7F_3$, and $^7F_4$, respectively[4,25–29]. The other characteristic absorptions of the Tb^{3+} ion of wavelengths smaller than 486 nm do not appear as they have higher energies than the band gap of the glasses[4].

The short wavelength cut-off (λ_{UV}) also decreases from 357 to 388 nm for the 20Tb40W and 27.5Tb40W samples, respectively, as better observed in Figure 27, due to structural changes, as seen in the previous section. The infrared cut-off starts with the presence of a shoulder referring to an absorption band around 3.7 µm.

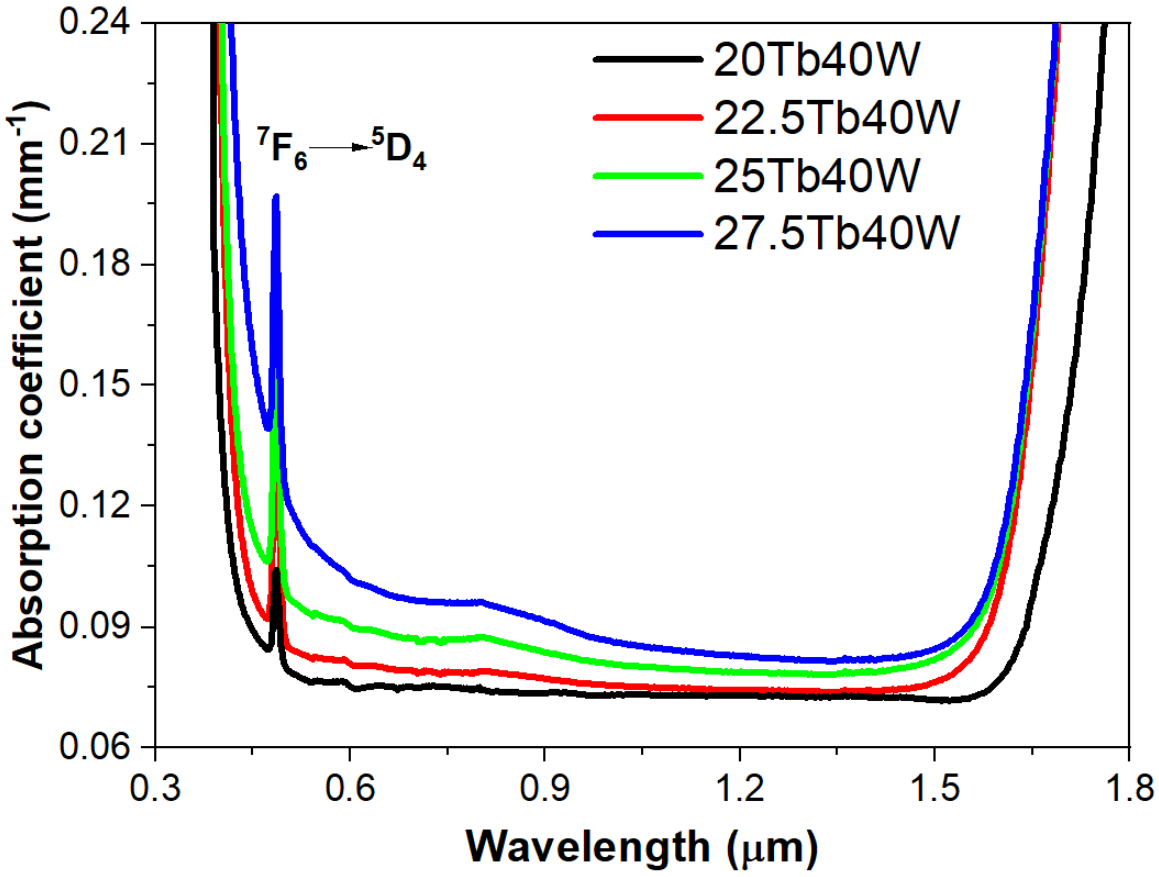

Figure 26. Absorption coefficient spectra of the xTb40W samples, with the respective absorption band. (Own authorship).

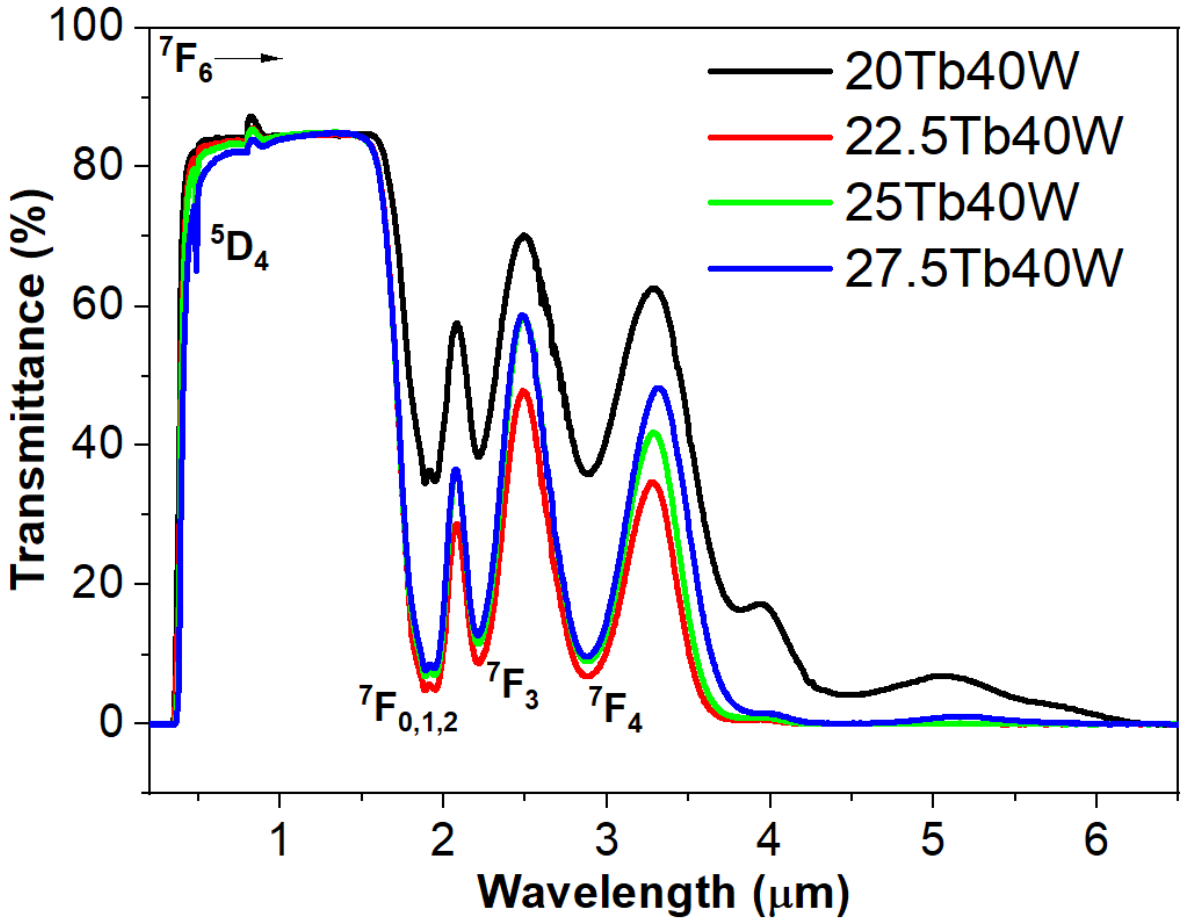

Figure 27. Transmittance spectra of the terbium-containing samples, with the respective absorption bands. (Own authorship).

From the transmission spectra it is possible to observe that the near infrared region, close to 1.55 μm, presents the higher transmission, indicating that such glasses can be used for devices operating in this specific wavelength, once the figure of merit (FOM) used for such devices is dependent on the absorption coefficient following the Eq. 26.

$$FOM = \frac{V}{\alpha_\lambda} \qquad (Eq. 26)$$

where V is the Verdet constant and α_λ is the absorption coefficient in a given wavelength. The discussion about the possible uses for construction of devices using such glasses will be given in the posterior section.

7. Refractive index.

As previously shown, knowing the refractive indices of glasses allows us to estimate high Verdet constants, in addition to the fact that high refractive indices (n) allow us to expand the applications of these glasses in photonics, such as fibers and waveguides. The n of the glasses from the visible to near-infrared regions, are shows in Figure 28. The maximum n obtained was 1.929±0.005 at 532 nm, for the sample 27.5Tb40W. As expected, the refractive index decreases for the samples containing lower Tb^{3+} contents, what also corroborates to the results of optical basicity. The refractive indexes were also obtained for other three wavelengths, as shown in Figure 29 and Table 5.

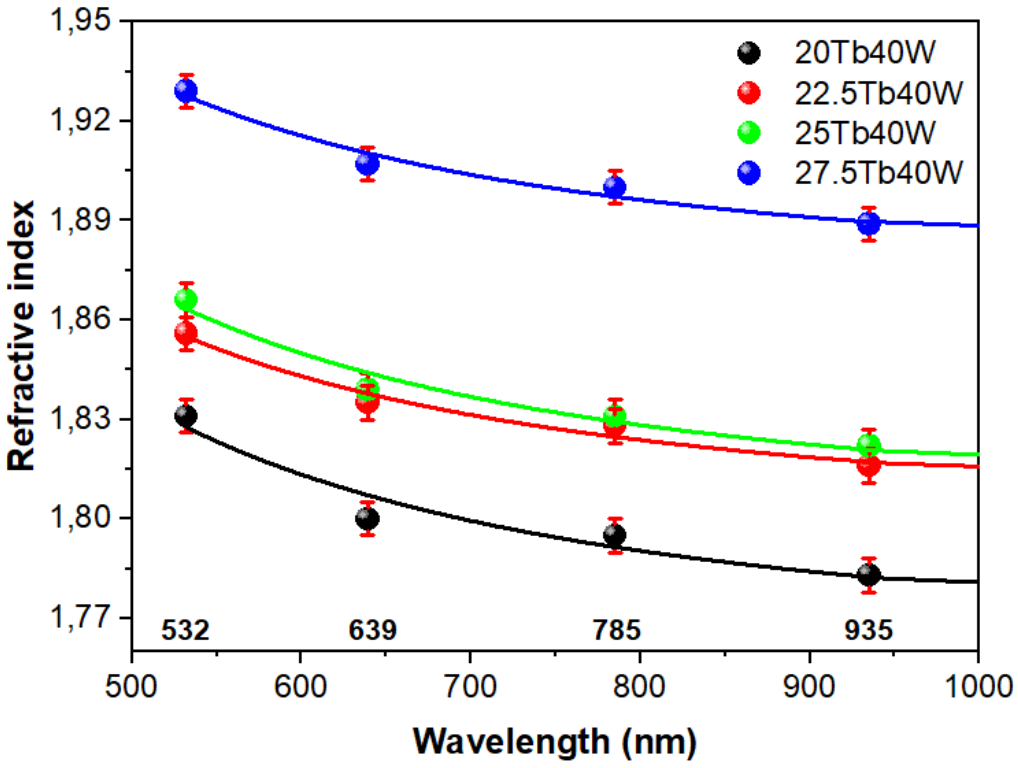

Figure 29. Refractive index for samples with different contents of Tb_2O_3 in the ternary system and Cauchy's Law for the witch sample. (Own authorship).

Table 5. Refractive indices for xTb40W samples, at wavelengths 532, 639, 785, 935 nm with ± 0.005 error. We obtained the refractive index for 1000 nm using Cauchy's Law.

Sample	Refractive index (n ± 0.005)				
	532 nm	639 nm	785 nm	935 nm	1000 nm
20Tb40W	1.831	1.800	1.795	1.783	1.780
22.5Tb40W	1.856	1.835	1.828	1.816	1.815
25Tb40W	1.866	1.839	1.831	1.822	1.820
27.5Tb40W	1.929	1.907	1.900	1.889	1.888

(Own authorship).

Using the experimentally measured values and Cauchy's Law [30,31], $n(\lambda) = A + B/\lambda^2$, we can fit and estimate the refractive index values for 1000 nm. Thus, the refractive index values at 1000 nm were measured and the results were 1.780, 1.815, 1.820 and 1.888 for 20Tb40W, 22.5Tb40W, 25Tb40W and 27.5Tb40W, respectively, with errors estimated in ±0.005. The values of refractive index for sample 25Tb40W don't fit well with the tendency of other samples, even if the calculated values of optical basicity and measured values of density have shown a good linear increasing tendency along with the increasing of the terbium content. These results were revisited and another sample was prepared and measured, however, the results were the same. This behavior is under investigation, but it was not yet well understood.

As expected, the refractive index increases with increasing the content of Tb_2O_3 and the decrease of the boron oxide content. As reported in the literature, the evolution of the refractive index is assigned to the higher polarizability of the Tb^{3+} ions.

8. Fluorescence spectroscopy.

Figures 29 and 30 show both the normalized photoexcitation (PLE) and the luminescence (PL) spectra for the samples containing terbium. The PLE peaks, corresponding to 4f- 4f transitions at $^7F_5$ level, are located at 487 ($^7F_6$), 379 ($^5D_3$ + $^5G_6$), 371 ($^5L_{10}$), 353 ($^5L_9$ + $^5D_2$ + $^5G_5$), 343 ($^5L_{5,8}$ + $^5G_3$) and 329 nm ($^5H_7$ + $^5D_1$). The broad peak in the range from 250 to 325 nm belongs to the charge transfer band (CTB) of O^{2-}

→ W^{6+} in $[WO_6]^{6-}$ group[32,33].

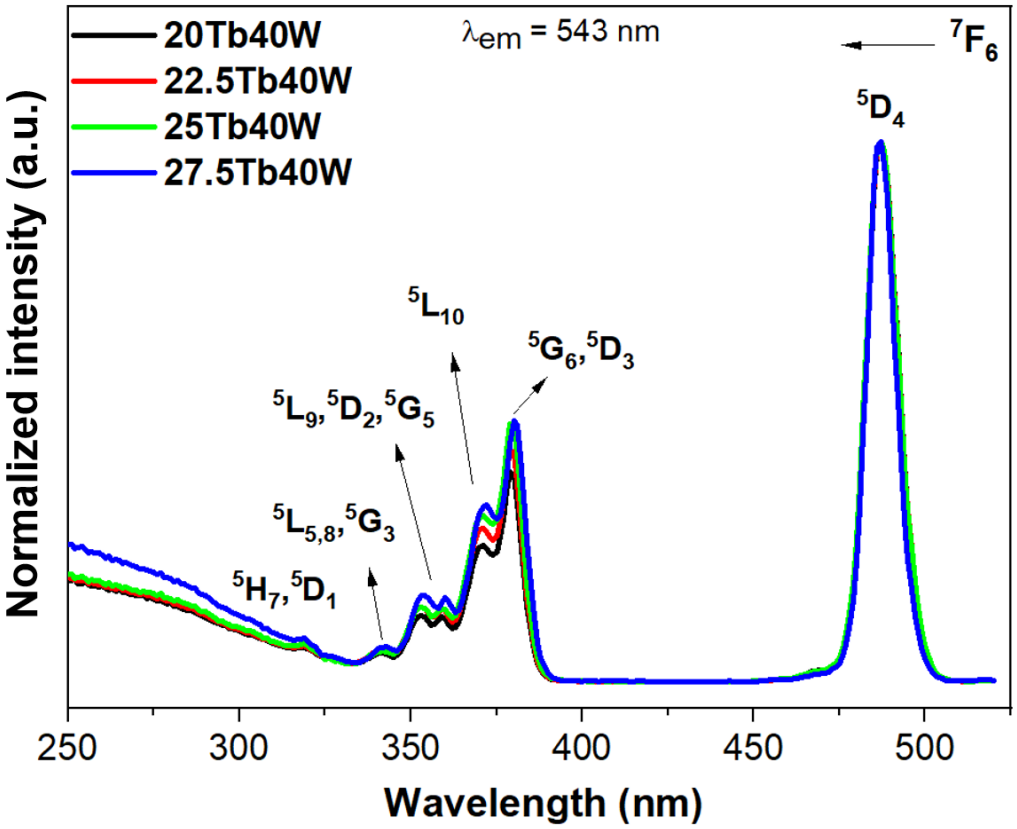

Figure 29. Normalized excitation spectra for the samples with different concentrations of Tb_2O_3, showing the 4f-4f transitions ($^7F_6$→) under λ_{em} = 543 nm. (Own authorship).

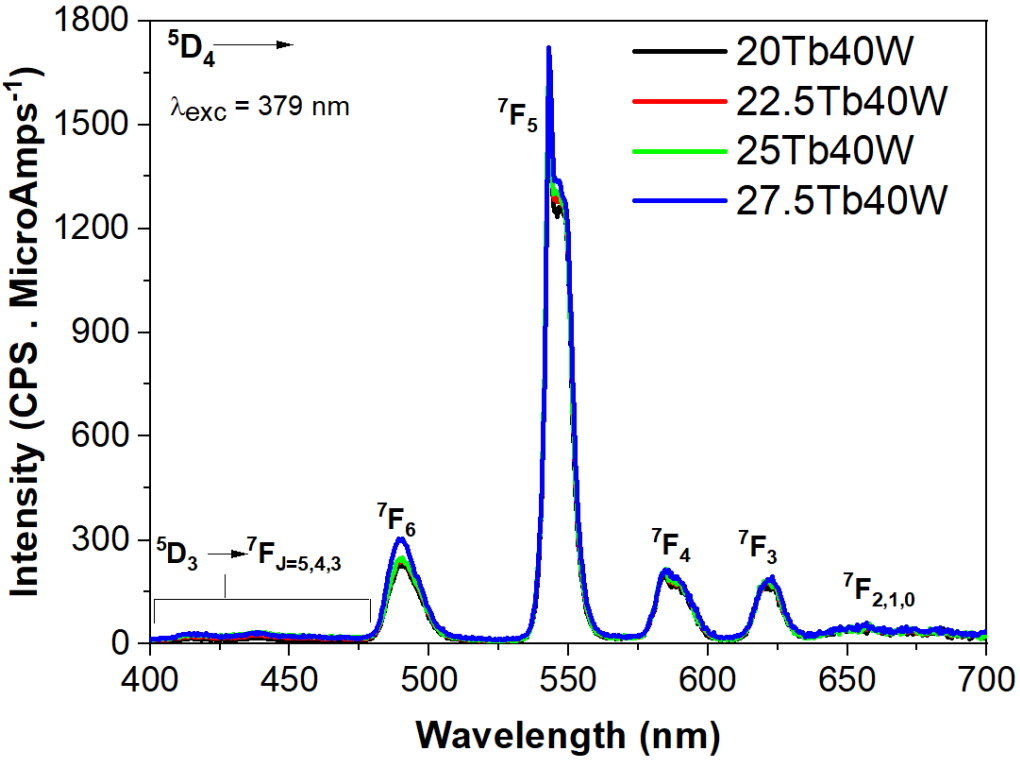

Figure 30. Emission spectra for xTb40W samples, showing the 4f- 4f ($^5D_4$ and $^5D_3$ →) transitions under λ_{exc} = 379 nm.

The PL peaks, corresponding to 4f-4f transitions with excitation in 379 nm, at 415 ($^5D_3$→$^5F_5$), 440 ($^5D_3$→$^5F_4$), 487 ($^5D_4$→$^7F_6$), 543 ($^5D_4$→$^7F_5$), 583 ($^5D_4$→$^7F_4$), 621 ($^5D_4$→$^7F_3$), 652 ($^5D_4$→$^7F_2$), 667 ($^5D_4$→$^7F_1$) and 679 nm ($^5D_4$ →$^7F_0$)[25–29]. The signal-to-noise intensity is low, allowing to identify transitions $^5D_3$→^7F_J and $^5D_4$→$^7F_{2,1,0}$, of relative low intensity.

It is observed that these samples present low luminescence intensities, not visible to the naked eyes, with few variations in intensities, indicating that the chemical environment for these Tb^{3+} concentrations does not show great differences, as revealed by the structural study. Low intensity is also characteristic of luminescence quenching effects, when high concentrations of the lanthanide ion allow the transfer of excitation energy between neighbors. For several glass systems, quenching can be observed above 3.0 % in mol of Tb^{3+} and, for this system, we have 20 - 27.5 % in mol of Tb_2O_3, extremely high concentrations to guarantee the paramagnetic effect in the matrix and, therefore, the quenching process was already expected.

Figure 31a shows the CIE 1931 chromaticity diagram, which uses the

emission spectrum of the samples to determine the final emitted color. From the Figure, we observed that the emitted colors are concentrated in the same region of the graph, with small variations between the dots, illustrating that the luminescence spectra do not change considerably as a function of the concentration of Tb^{3+} ions. The energy difference of the $^5D_3 \leftrightarrow {}^5D_4$ and $^7F_0 \leftrightarrow {}^7F_6$ levels is very close (~5700 cm^{-1}), which allows the cross-relaxation quenching process between neighboring Tb^{3+} to occur. Figure 31b illustrates the excitation process for Tb^{3+} ions, the $^5D_4 \rightarrow {}^7F_J$ emissions and the cross-relaxation energy transfer process between Tb^{3+} ions.

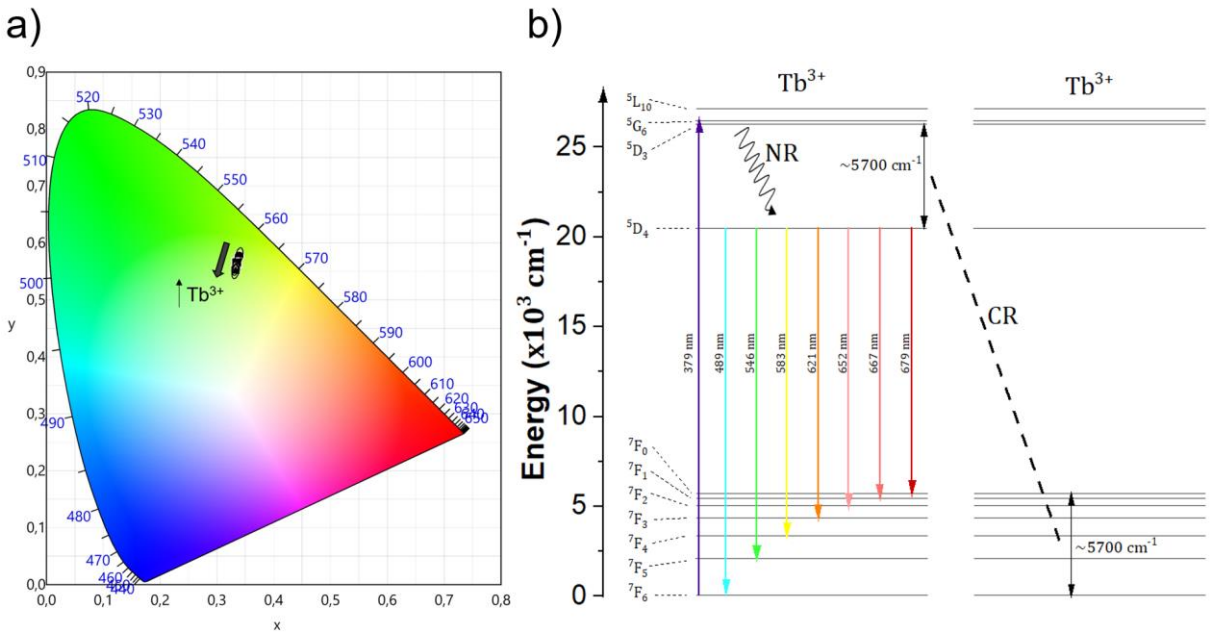

Figure 31. a. CIE 1931 chromaticity diagram for xTb40W samples under 379 nm excitation. **b.** Partial energy level diagram of Tb^{3+} illustrating the excitation $^7F_6 \rightarrow {}^5D_3 + {}^5G_6$, non-radiative decay (NR; $^5D_3 \rightarrow {}^5D_4$), emissions $^5D_4 \rightarrow {}^7F_J$, and cross-relaxation process (CR) between two neighboring Tb^{3+} ions.

9. Magnetic susceptibility

All samples were measured by ZFC and FC methods. Figure 32 shows the total susceptibility curves for the 25Tb40W sample, with no major variation, indicating that the environment remains the same for both methods. This is repeated for all other samples, whose graphs will not be shown here.

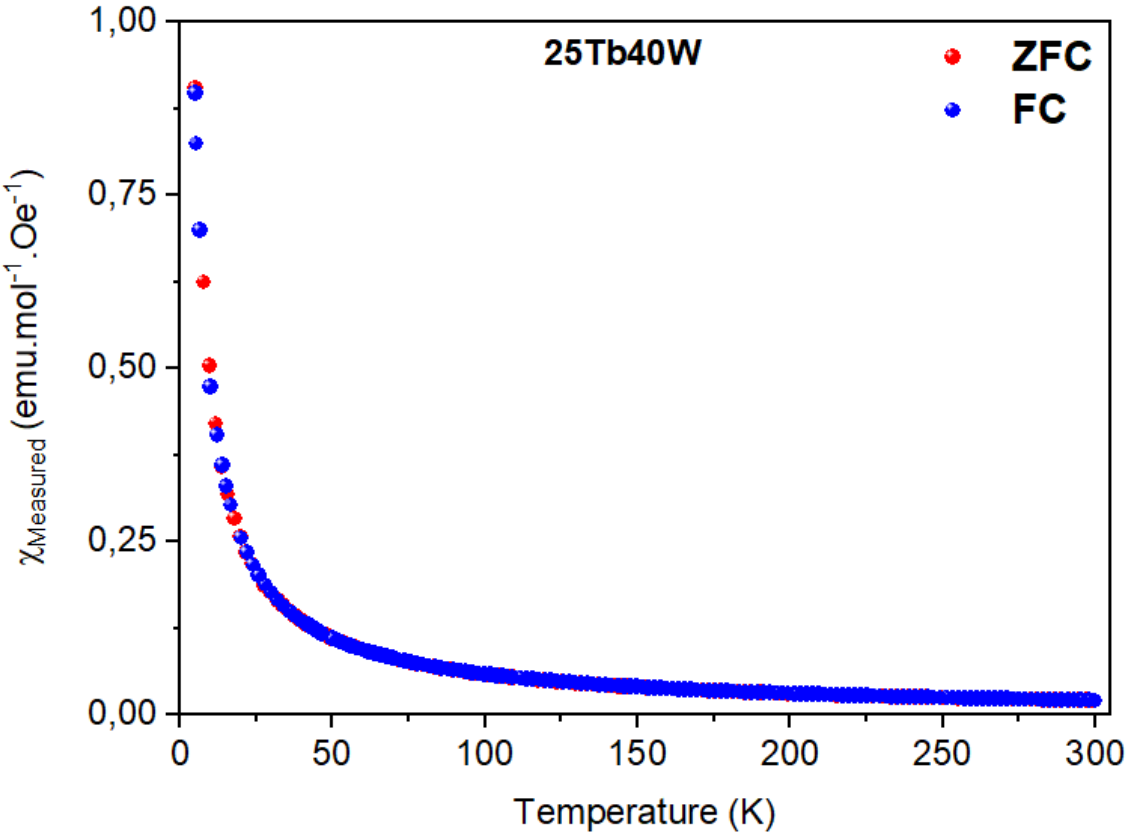

Figure 32. Measured magnetic susceptibility for the 25Tb40W sample, measured by zero field-cooled (ZFC) and field-cooled (FC) methods. (Own authorship).

The diamagnetic susceptibility (χ_{dia}) values, calculated using the values in Table 1, were extracted from the measured susceptibility data, leaving only the paramagnetic data (χ_{para}), which are shown in Figure 34. Figure Inset shows the inverse of χ_{para} ($1/\chi_{para}$) for all the samples. The linear behavior indicates that they all follow the Curie-Weiss Law (Eq. 11), showing paramagnetic behavior, and the Curie constant (C) and Weiss temperature (θ) values are shown in Table 6. C is obtained by the slope of the line and θ is obtained by intercepting the x axis. The Curie constant values are expressed in Oersted (Oe) and Tesla (T), as both units are well used in the literature.

The high values of the Curie constant reveal that the samples have high magnetic susceptibility. As discussed earlier, negative Weiss temperature values indicate that the spins are aligned antiparallel, causing low antiferromagnetic interactions.

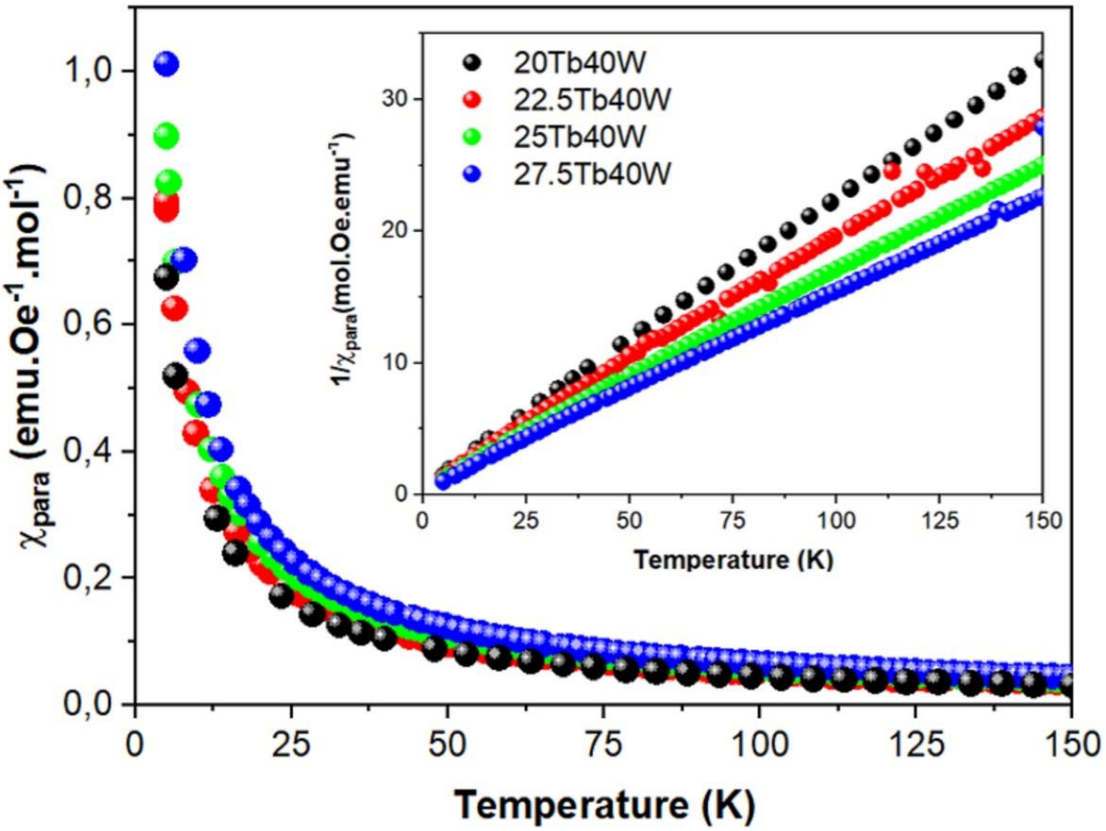

Figure 33. Temperature dependence of the paramagnetic molar susceptibility for all samples. Inset shown the inverse of susceptibility ($1/\chi_{para}$) versus temperature, varying linearity and follow the Curie-Weiss law. (Own authorship).

Table 6. theoretical diamagnetic susceptibility (χ_{dia}), Weiss temperature (θ), Curie constant (C) for two units (one in Oested, Oe, e other in Tesla, T) and probed Tb_2O_3 % mol for each sample. (Own authorship).

Samples	χ_{dia} **(x10^{-6} emu.mol^{-1})**	**θ (K)**	**C (emu . Oe^{-1} . mol^{-1})**	**[Tb_2O_3] (% mol)**		
				targeted	probed	error %
20Tb40W	-48.96	-4.28	4.68	20	19.79	1.04
22.5Tb40W	-49.90	-4.67	5.36	22.5	22.69	-0.82
25Tb40W	-50.84	-6.51	6.25	25	26.45	-5.78
27.5Tb40W	-51.78	-4.38	6.77	27.5	28.64	-4.15

As shown in Eq. 9 and 10, C can be calculated theoretically based on the values of J, L and S obtained at the fundamental level. For the Tb^{3+} ion we have the $^7F_6$ level, confirmed by the transmission and luminescence spectra. Carrying out the calculations, we obtain a g_J = 1.50, a μ_{eff} = 9.72 and a theoretical C of 11.81 emu.K.Oe^{-}

^{1}.mol^{-1}. Using this calculated C value and the measured C value, we can calculate the molar % of Tb^{3+} and Tb_2O_3 for each sample, which we can use as a probed to ascertain the paramagnetic ion concentration. From this study, we can determine the error rate by comparing the target and probed values of the Tb_2O_3 concentration. All these values are shown in Table 6.

Table 7 shows the values of the Curie constants and Weiss temperature of the glass samples in this article, comparing with the values obtained in the literature. The values obtained in this work show high susceptibility values when compared with the literature. The tellurite[34], iron-phosphate[35,36], iron-aluminoborate[37] and aluminosilicate[38] glasses presented comparable or higher values, but these glasses do not have good transparency in the visible region, restricting their range of applications for infrared MO devices.

The high values of Curie constant (C), refractive index (n) and ionic concentration per volume (N_{Tb3+}) support a high Verdet constant and are promising materials for Faraday rotation, which will be investigated in the next topic.

Table 7. Comparison between different Curie constant (C) values and Weiss temperature (θ) for samples from this work and examples from the literature.

Glass matrix	**Concentration paramagnetic species (% mol)**	**C (emu . Oe^{-1} . mol^{-1})**	**θ (K)**	**References**
Borotungstate	27.5% Tb_2O_3	6.77	-4.38	This work
	25% Tb_2O_3	6.25	-6.51	
	22.5% Tb_2O_3	5.36	-4.67	
	20% Tb_2O_3	4.68	-4.28	
Borogermanate	10% Tb_4O_7	4.29	-0.869	[39]
Borogermanate	20% Gd_2O_3	3.124	-1.56	[40]
Gallogermanate	25% Gd_2O_3	3.311	35.34	[41]
Aluminophosphate	9.52% Dy_2O_3	3.66	–	[42]
Iron tellurite	25% MnO_2	7.28	-5.098	[34]

Iron phosphate	43% Fe_2O_3 (wt%)	3.98	-54	[35]
Iron phosphate	57.1% FeO	4.82	-11.6	[36]
Iron aluminoborate	20% Gd_2O_3	8.2	-3.2	[37]
Aluminosilicate	11.8% Co	5.61125	-95	[38]
	12.3% Mn	6.0552	-194	
Boromolibdate	21.25% Gd_2O_3	1.672	-0.7	[43]

(Own authorship).

10. Magneto-optical measurements

Figure 34 presented the V values x Tb^{3+} ionic concentration (N_{Tb3+})[44–45] for some reference crystals [46–51] and several Tb-containing glasses. All values were obtained using lasers in the 630-650 nm range. As can be observed, the magneto-optical effect tends to increase linearly withincreasing of N_{Tb3+}.

Fluoride glasses[52] have the lowest N_{Tb3+} values, reflecting, proportionally, the smaller V. The values increase from phosphate glasses [45,53], passing for fluorophosphates glasses [45,47,52,54], aluminosilicate glasses [45,55–58], borate glasses [45,52,59,60] and borosilicates [57,61–63]. Currently, the glasses with the highest N_{Tb3+} and, consequently, Verdet constant, are borogermanate [4,39,44,64,65] and borogermanosilicate glasses [5,66–69]. The results obtained for the glasses studied in present work are shown as red squares. The Verdet constants obtained for samples 20Tb40W, 22.5Tb40W, 25Tb40W and 27.5Tb40W were -60, -67, -85 and -124 $rad.T^{-1}m^{-1}$, respectively.

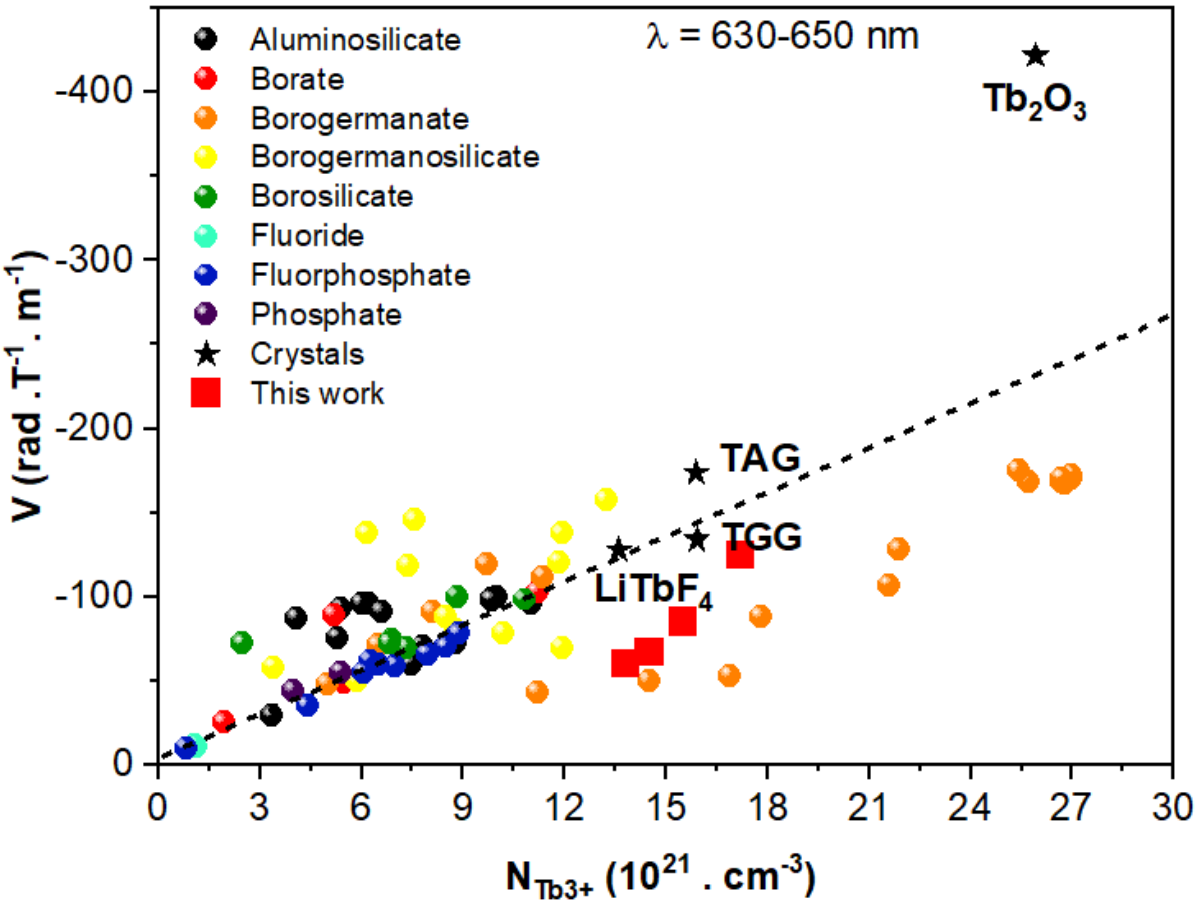

Figure 34. Variation of the Verdet constant by concentration of Tb^{3+} ions for the samples (red squares), some reference crystals (black stars) and different glass families (spheres): aluminosilicates (black), borates (red), borogermanates (orange), borogermanosilicates (yellow), borosilicates (green), fluorides (turquoise), fluorophosphates (blue) and phosphates glasses (purple). The dash line represent a fit of the data. (Own authorship).

Figure 35 shows the same graph V *versus* N_{Tb3+}, but focused only on the samples of this work, comparing them with crystals containing terbium used as commercial Faraday rotators. We can observe a tendency in the increase of V values with the increase of Tb^{3+} concentration, as expected. The value for the 27.5Tb40W sample was -124 $rad.T^{-1}.m^{-1}$, a very high value compared to borogermanate glasses and TGG, a reference single crystal. Even if the value is not identical, the possibility of forming glass bulks makes it possible to compensate for the difference in values, remembering that the Verdet constant depends on the optical path. In addition, the production process of these glasses needs a lower melting temperature and more cost-

effective preparation reagents, which allows a lower cost benefit for this system, when compared to borogermanate glasses.

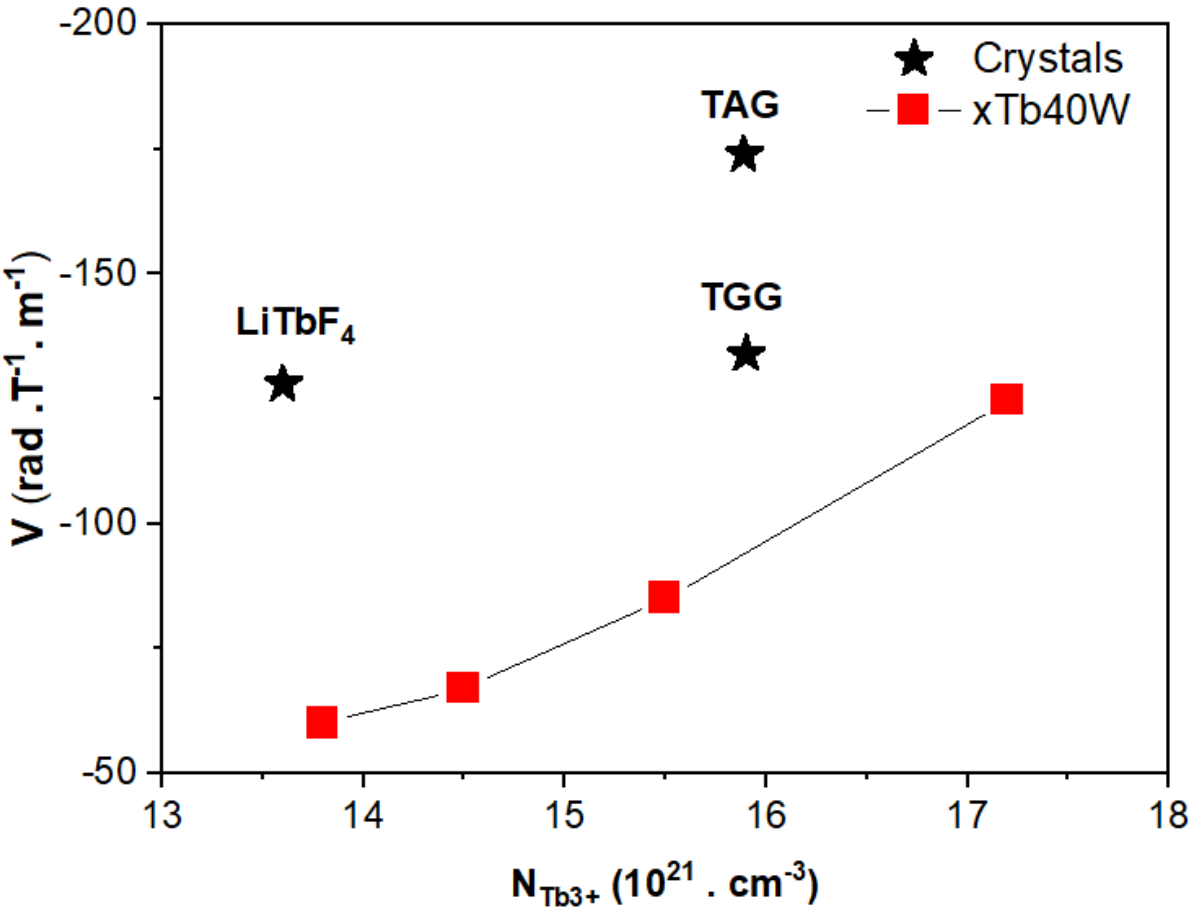

Figure 35. Behavior of the Verdet constant of the xTb40W samples (red squares) compared with commercially used crystals (black stars). (Own authorship).

11. Partial Conclusions of this Chapter.

With the end of this chapter and the study of the Tb_2O_3-B_2O_3-WO_3 vitreous system, we can conclude that the proposed objectives were achieved. Besides the glass forming region be small, high concentrations of rare earth were introduced into the borotungstate matrix. The addition of Tb_2O_3 increased the thermal stability (Tx-Tg) of the glasses while does not influenced significatively into the glass structure. Also, the rising content of Tb^{3+} has increased the optical basicity, density, magnetic susceptibility and refractive index of the samples, culminating in glasses with high Verdet constant,

compared to those of crystalline reference compound (TGG). Thus, it is important to highlight that the glass system herein studied has a very competitive price for large scale production, and may be used as faraday rotators and isolators devices.

References in this chapter

[1] R.E. Newnham, M.J. Redman, R.P. Santoro, Crystal Structure of Yttrium and Other Rare-Earth Borates, J. Am. Ceram. Soc. 46 (1963) 253–256. https://doi.org/10.1111/j.1151-2916.1963.tb11721.x.

[2] E.M. Levin, R.S. Roth, J.B. Martin, Polymorphism of ABOs Type Rare Earth Borates, Am. Mineral. 46 (1961) 1030–1055. http://www.minsocam.org/ammin/AM46/AM46_1030.pdf.

[3] V. Jubera, Etudes structurales et propriétés de luminescence de nouveaux composés des systèmes Li_2O-B_2O_3-Ln_2O_3 (Ln = terres rares), Université Sciences et Technologies - Bordeaux I, 2001.

[4] D.F. Franco, Y. Ledemi, W. Correr, S. Morency, C.R.M. Afonso, S.H. Messaddeq, Y. Messaddeq, M. Nalin, Magneto-optical borogermanate glasses and fibers containing Tb^{3+}, Sci. Rep. 11 (2021) 1–16. https://doi.org/10.1038/s41598-021-89375-1.

[5] H. Yang, Z. Zhu, Magneto-optical glass mixed with Tb^{3+} ions: High Verdet constant and luminescence properties, J. Lumin. 231 (2021) 117804. https://doi.org/10.1016/j.jlumin.2020.117804.

[6] J.A. Duffy, A review of optical basicity and its applications to oxidic systems, Geochim. Cosmochim. Acta. 57 (1993) 3961–3970. https://doi.org/10.1016/0016-7037(93)90346-X.

[7] J.A. Duffy, Optical basicity: A practical acid-base theory for oxides and oxyanions, J. Chem. Educ. 73 (1996) 1138–1142. https://doi.org/10.1021/ed073p1138.

[8] S. Liu, G. Zhao, W. Ruan, Z. Yao, T. Xie, J. Jin, H. Ying, J. Wang, G. Han, Reduction of Eu^{3+} to Eu^{2+} in aluminoborosilicate glasses prepared in air, J. Am. Ceram. Soc. 91 (2008) 2740–2742. https://doi.org/10.1111/j.1551-2916.2008.02496.x.

[9] V. Dimitrov, T. Komatsu, Classification of simple oxides: A polarizability approach, J. Solid State Chem. 163 (2002) 100–112. https://doi.org/10.1006/jssc.2001.9378.

[10] X. Zhao, X. Wang, H. Lin, Z. Wang, Electronic polarizability and optical basicity of lanthanide oxides, Phys. B Condens. Matter. 392 (2007) 132–136. https://doi.org/10.1016/j.physb.2006.11.015.

[11] L. Aleksandrov, T. Komatsu, R. Iordanova, Y. Dimitriev, Raman spectroscopic study of structure of $WO_3La_2O_3B_2O_3$ glasses with no color and crystallization of $LaBWO_6$, Opt. Mater. (Amst). 34 (2011) 201–206. https://doi.org/10.1016/j.optmat.2011.08.002.

[12] J.F.V.L. Munhoz, S.H. Santagneli, M. de Oliveira, A.C.M. Rodrigues, H. Eckert, M. Nalin, Glasses in the $NaPO_3$-WO_3-NaF ternary system: preparation, physical properties and structural studies, J. Non. Cryst. Solids. 505 (2019) 379–389. https://doi.org/10.1016/J.JNONCRYSOL.2018.10.043.

[13] G. Poirier, Y. Messaddeq, S.J.L. Ribeiro, M. Poulain, Structural study of tungstate fluorophosphate glasses by Raman and X-ray absorption spectroscopy, J. Solid State Chem. 178 (2005) 1533–1538. https://doi.org/10.1016/j.jssc.2004.10.032.

[14] A.K. Yadav, P. Singh, A Review of Structure of Oxide Glasses by Raman Spectroscopy, RSC Adv. 5 (2015) 67583–67609. https://doi.org/https://doi.org/10.1039/C5RA13043C.

[15] R.M. Abdelouhab, R. Braunstein, K. Bärner, Identification of tungstate complexes in lithium-tungstate-borate glasses by Raman spectroscopy, J. Non. Cryst. Solids. 108 (1989) 109–114. https://doi.org/10.1016/0022-3093(89)90338-4.

[16] E.I. Kamitsos, A.P. Patsis, M.A. Karakassides, G.D. Chryssikos, Infrared reflectance spectra of lithium borate glasses, J. Non. Cryst. Solids. 126 (1990) 52–67. https://doi.org/10.1016/0022-3093(90)91023-K.

[17] E.I. Kamitsos, A.P. Patsis, G.D. Chryssikos, Infrared reflectance investigation of alkali diborate glasses, J. Non. Cryst. Solids. 152 (1993) 246–257. https://doi.org/10.1016/0022-3093(93)90258-Y.

[18] S. Sasaki, A. Masuno, K. Ohara, Y. Yanaba, H. Inoue, Y. Watanabe, S. Kohara, Structural Origin of Additional Infrared Transparency and Enhanced Glass-Forming Ability in Rare-Earth-Rich Borate Glasses without B-O Networks, Inorg. Chem. 59 (2020) 13942–13951. https://doi.org/10.1021/acs.inorgchem.0c01567.

[19] B. Topper, N.S. Tagiara, A. Herrmann, E.I. Kamitsos, D. Möncke, Yttrium and rare-earth modified lithium orthoborates: Glass formation and vibrational activity, J. Non. Cryst. Solids. 575 (2022). https://doi.org/10.1016/j.jnoncrysol.2021.121152.

[20] C.P.E. Varsamis, N. Makris, C. Valvi, E.I. Kamitsos, Short-range structure, the role of bismuth and property-structure correlations in bismuth borate glasses, Phys. Chem. Chem. Phys. 23 (2021) 10006–10020. https://doi.org/10.1039/d1cp00301a.

[21] G. Poirier, M. Poulain, Y. Messaddeq, S.J.L. Ribeiro, New tungstate fluorophosphate glasses, J. Non. Cryst. Solids. 351 (2005) 293–298. https://doi.org/10.1016/j.jnoncrysol.2004.11.017.

[22] G. Poirier, F.C. Cassanjes, Y. Messaddeq, S.J.L. Ribeiro, A. Michalowicz, M. Poulain, Local order around tungsten atoms in tungstate fluorophosphate glasses by X-ray absorption spectroscopy, J. Non. Cryst. Solids. 351 (2005) 3644–3648. https://doi.org/10.1016/j.jnoncrysol.2005.08.038.

[23] C.P.E. Varsamis, N. Makris, C. Valvi, E.I. Kamitsos, Short-range structure, the role of bismuth and property-structure correlations in bismuth borate glasses, Phys. Chem. Chem. Phys. 23 (2021) 10006–10020. https://doi.org/10.1039/d1cp00301a.

[24] R. Iordanova, M. Milanova, L. Aleksandrov, K. Shinozaki, T. Komatsu, Structural study of WO_3-La_2O_3-B_2O_3-Nb_2O_5 glasses, J. Non. Cryst. Solids. 543 (2020) 120132. https://doi.org/10.1016/j.jnoncrysol.2020.120132.

[25] T. Yamashita, Y. Ohishi, Concentration and temperature effects on the spectroscopic properties of Tb^{3+} doped borosilicate glasses, J. Appl. Phys. 102 (2007). https://doi.org/10.1063/1.2821789.

[26] M. Kumar, A.S. Rao, Influence of Tb^{3+} ions concentration and temperature on lithium bismuth alumino borosilicate glasses for green photonic device applications, Opt. Mater. (Amst). 120 (2021) 111439. https://doi.org/10.1016/J.OPTMAT.2021.111439.

[27] T.A. Lodi, J.F.M. dos Santos, G. Galleani, L.G. Jacobsohn, T. Catunda, A.S.S. de Camargo, Promising Tb^{3+}-doped gallium tungsten-phosphate glass scintillator:

Spectroscopy, energy transfer and UV/X-ray sensing, J. Alloys Compd. 904 (2022) 164016. https://doi.org/10.1016/J.JALLCOM.2022.164016.

[28] P.S. Peijzel, A. Meijerink, R.T. Wegh, M.F. Reid, G.W. Burdick, A complete 4fn energy level diagram for all trivalent lanthanide ions, J. Solid State Chem. 178 (2005) 448–453. https://doi.org/10.1016/J.JSSC.2004.07.046.

[29] W.T. Carnall, P.R. Fields, K. Rajnak, Electronic Energy Levels of the Trivalent Lanthanide Aquo Ions. III. Tb^{3+} , J. Chem. Phys. 49 (1968) 4447–4449. https://doi.org/10.1063/1.1669895.

[30] L. Karam, F. Adamietz, V. Rodriguez, F. Bondu, A. Lepicard, T. Cardinal, E. Fargin, K. Richardson, M. Dussauze, The effect of the sodium content on the structure and the optical properties of thermally poled sodium and niobium borophosphate glasses, J. Appl. Phys. 128 (2020). https://doi.org/10.1063/5.0013383.

[31] J.E. Shelby, Introduction to Glass Science and Technology, The Royal Society of Chemistry, 1997. https://doi.org/10.1039/9781847551160.

[32] N. Wantana, E. Kaewnuam, Y. Ruangtaweep, D. Valiev, S. Stepanov, K. Yamanoi, H.J. Kim, J. Kaewkhao, Radio, cathodo and photoluminescence investigations of high density WO_3-Gd_2O_3-B_2O_3 glass doped with Tb^{3+}, Radiat. Phys. Chem. 164 (2019) 108350. https://doi.org/10.1016/j.radphyschem.2019.108350.

[33] N. Wantana, E. Kaewnuam, Y. Ruangtaweep, P. Kidkhunthod, H.J. Kim, S. Kothan, J. Kaewkhao, High density tungsten gadolinium borate glasses doped with Eu^{3+} ion for photonic and scintillator applications, Radiat. Phys. Chem. 172 (2020) 108868. https://doi.org/10.1016/j.radphyschem.2020.108868.

[34] Y.B. Saddeek, R. El Mallawany, I.S. Yahia, W. Dobrowolski, L. Kilanski, A. Avdonin, M. Arciszewska, Magnetic Properties of Some Tellurite Glasses, J. Supercond. Nov. Magn. 31 (2018) 3079–3084. https://doi.org/10.1007/s10948-018-4812-7.

[35] L. Pavič, M.P.F. Graca, Ž. Skoko, A. Moguš-Milankovič, M.A. Valente, Magnetic properties of iron phosphate glass and glass-ceramics, J. Am. Ceram. Soc. 97 (2014) 2517–2524. https://doi.org/10.1111/jace.12951.

[36] H. Akamatsu, K. Fujita, S. Murai, K. Tanaka, Magneto-optical properties of transparent divalent iron phosphate glasses, Appl. Phys. Lett. 92 (2008) 3–6. https://doi.org/10.1063/1.2952460.

[37] H. Akamatsu, J. Kawabata, K. Fujita, S. Murai, K. Tanaka, Magnetic properties of oxide glasses containing iron and rare-earth ions, Phys. Rev. B - Condens. Matter Mater. Phys. 84 (2011) 1–8. https://doi.org/10.1103/PhysRevB.84.144408.

[38] R.A. Verhelst, R.W. Kline, A.M. de Graaf, H.O. Hooper, Magnetic properties of cobalt and manganese aluminosilicate glasses, Phys. Rev. B. 11 (1975) 4427–4435.

[39] D.F. Franco, R.G. Fernandes, J.F. Felix, V.R. Mastelaro, H. Eckert, C.R.M. Afonso, Y. Messaddeq, S.H. Messaddeq, S. Morency, M. Nalin, Fundamental studies of magneto-optical borogermanate glasses and derived optical fibers containing Tb^{3+}, J. Mater. Res. Technol. 11 (2021) 312–327. https://doi.org/10.1016/j.jmrt.2021.01.010.

[40] R.G. Fernandes, D.F. Franco, V.R. Mastelaro, T. Cardinal, O. Toulemonde, M. Nalin, Thermal and structural modification in transparent and magnetic germanoborate glasses induced by Gd_2O_3, Ceram. Int. 46 (2020) 22079–22089. https://doi.org/10.1016/j.ceramint.2020.05.227.

[41] R. Zaiter, M. Dussauze, M. Nalin, E. Fargin, F. Adamietz, S. Danto, O. Toulemonde, T. Cardinal, Thermal and structural modification in transparent and magnetic gallogermanate glasses induced by Gd_2O_3, J. Alloys Compd. 912 (2022) 165181. https://doi.org/10.1016/j.jallcom.2022.165181.

[42] M. Elisa, R. Stefan, I.C. Vasiliu, M.I. Rusu, B.A. Sava, L. Boroica, M. Sofronie, V. Kuncser, A.C. Galca, A. Beldiceanu, A. Volceanov, M. Eftimie, Thermal, structural, magnetic and magneto-optical properties of dysprosium-doped phosphate glass, J. Non. Cryst. Solids. 521 (2019) 119545. https://doi.org/10.1016/j.jnoncrysol.2019.119545.

[43] F. Suzuki, T. Honma, Y. Doi, Y. Hinatsu, T. Komatsu, Magnetic properties and homogeneous distribution of Gd^{3+} ions in gadolinium molybdenum borate glass with high Gd_2O_3 content, Mater. Res. Bull. 47 (2012) 3403–3406.

https://doi.org/10.1016/j.materresbull.2012.07.015.

[44] G. Gao, A. Winterstein-Beckmann, O. Surzhenko, C. Dubs, J. Dellith, M.A. Schmidt, L. Wondraczek, Faraday rotation and photoluminescence in heavily Tb^{3+}-doped GeO_2-B_2O_3-Al_2O_3-Ga_2O_3 glasses for fiber-integrated magneto-optics, Sci. Rep. 5 (2015) 1–6. https://doi.org/10.1038/srep08942.

[45] M. Yamane, Y. Asahara, Glasses for Photonics, Cambridge University Press, Cambridge, 2000.

[46] P. Veber, M. Velázquez, G. Gadret, D. Rytz, M. Peltz, R. Decourt, Flux growth at 1230 °C of cubic Tb_2O_3 single crystals and characterization of their optical and magnetic properties, CrystEngComm. 17 (2015) 492–497. https://doi.org/10.1039/c4ce02006e.

[47] B. Bellanger, Y. Ledemi, Y. Messaddeq, Fluorophosphate Glasses with High Terbium Content for Magneto-optical Applications, J. Phys. Chem. C. 124 (2020) 5353–5362. https://doi.org/10.1021/acs.jpcc.9b11696.

[48] K.J. Carothers, R.A. Norwood, J. Pyun, High Verdet Constant Materials for Magneto-Optical Faraday Rotation: A Review, Chem. Mater. 34 (2022) 2531–2544. https://doi.org/10.1021/acs.chemmater.2c00158.

[49] C.B. Rubinstein, L.G. Van Uitert, W.H. Grodkiewicz, Magneto-optical properties of rare earth (III) aluminum garnets, J. Appl. Phys. 35 (1964) 3069–3070. https://doi.org/10.1063/1.1713182.

[50] D. Vojna, O. Slezák, A. Lucianetti, T. Mocek, Verdet constant of magneto-active materials developed for high-power Faraday devices, Appl. Sci. 9 (2019). https://doi.org/10.3390/app9153160.

[51] M.J. Weber, R. Morgret, S.Y. Leung, J.A. Griffin, D. Gabbe, A. Linz, Magneto-optical properties of KTb_3F_{10} and $LiTbF_4$ crystals, J. Appl. Phys. 49 (1978) 3464–3469. https://doi.org/10.1063/1.325255.

[52] J. Qiu, K. Tanaka, N. Sugimoto, K. Hirao, Faraday effect in Tb^{3+}-containing borate, fluoride and fluorophosphate glasses, J. Non. Cryst. Solids. 213–214 (1997) 193–198. https://doi.org/10.1016/S0022-3093(97)00101-4.

[53] A. Babkina, E. Kulpina, Y. Sgibnev, Y. Fedorov, A. Starobor, O. Palashov, N. Nikonorov, A. Ignatiev, K. Zyryanova, K. Oreshkina, E. Zhizhin, D. Pudikov,

Terbium concentration effect on magneto-optical properties of ternary phosphate glass, Opt. Mater. (Amst). 100 (2020) 109692. https://doi.org/10.1016/j.optmat.2020.109692.

[54] B. Bellanger, L. Audebert, Y. Ledemi, Y. Messaddeq, Superexchange Interaction Influence on the Faraday Effect in Terbium Fluorophosphate Glasses by Co-doping with Praseodymium, Dysprosium, and Holmium, J. Phys. Chem. C. 125 (2021) 17482–17492. https://doi.org/10.1021/acs.jpcc.1c04713.

[55] M.W. Shafer, J.C. Suits, Preparation and Faraday Rotation of Divalent Europium Glasses, J. Am. Ceram. Soc. 49 (1966) 261–264. https://doi.org/10.1111/j.1151-2916.1966.tb13253.x.

[56] M. Daybell, W.C. Overton, H.L. Laquer, The faraday effect at low temperatures in terbium alumina silicate glass, Appl. Phys. Lett. 11 (1967) 79–81. https://doi.org/10.1063/1.1755044.

[57] Y. Zhang, S. Murai, A. Maeno, H. Kaji, M. Shimizu, Y. Shimotsuma, Z. Ma, J. Qiu, K. Tanaka, Microstructure and Faraday effect of Tb_2O_3-Al_2O_3-SiO_2-B_2O_3 glasses for fiber-based magneto-optical applications, J. Am. Ceram. Soc. 105 (2022) 1198–1209. https://doi.org/10.1111/jace.18163.

[58] N.F. Borrelli, Faraday rotation in glasses, J. Chem. Phys. 41 (1964) 3289–3293. https://doi.org/10.1063/1.1725727.

[59] K. Tanaka, K. Hirao, N. Soga, Large Verdet Constant of 30Tb2O3·70B2O3 Glass, Jpn. J. Appl. Phys. 34 (1995) 4825–4826. https://doi.org/10.1143/JJAP.34.4825.

[60] C.B. Rubinstein, S.B. Berger, L.G. Van Uitert, W.A. Bonner, Faraday rotation of rare-earth (III) borate glasses, J. Appl. Phys. 35 (1964) 2338–2340. https://doi.org/10.1063/1.1702860.

[61] S.H. Yuan, X.Z. Shu, A new Faraday rotation glass with a large Verdet constant, J. Appl. Phys. 75 (1994) 6375–6377. https://doi.org/10.1063/1.355354.

[62] Y. Ding, K. Tanaka, L. Wondraczek, Mechanical Manipulation of a Fiber-Optical Microprobe Fabricated from Oxide Glasses with Magnetic Force Response, Adv. Photonics Res. 2 (2021) 2000100. https://doi.org/10.1002/adpr.202000100.

[63] M.A. Butler, E.L. Venturini, High frequency Faraday rotation in FR-5 glass, Appl. Opt. 26 (1987) 1581. https://doi.org/10.1364/ao.26.001581.

[64] L. Zhou, Z. Zhu, Study of magneto-optical properties of GeO_2-B_2O_3-P_2O_5-ZnO-Tb_2O_3 glass doped with different rare-earth ions, J. Non. Cryst. Solids. 576 (2022) 121241. https://doi.org/10.1016/j.jnoncrysol.2021.121241.

[65] V.I. Savinkov, V.N. Sigaev, N. V. Golubev, P.D. Sarkisov, A. V. Masalov, A.P. Sergeev, Borogermanate glasses with a high terbium oxide content, J. Non. Cryst. Solids. 356 (2010) 1655–1659. https://doi.org/10.1016/j.jnoncrysol.2010.06.011.

[66] H. Yin, Y. Gao, H. Guo, C. Wang, C. Yang, Effect of B_2O_3 Content and Microstructure on Verdet Constant of Tb_2O_3-Doped GBSG Magneto-Optical Glass, J. Phys. Chem. C. 122 (2018) 16894–16900. https://doi.org/10.1021/acs.jpcc.8b04989.

[67] H. Lin, B. Liu, L. Zhou, H. Yang, J. He, T. Zhang, H. Liu, X. Jiang, C. Li, S. Li, L. Liu, F. Zeng, Z. Su, Enhancements of magneto-optical properties of GeO_2-PbO-B_2O_3–SiO_2–P_2O_5 glass doped Tb^{3+} ion, Mater. Chem. Phys. 282 (2022). https://doi.org/10.1016/j.matchemphys.2022.125963.

[68] H. Guo, Y. Wang, Y. Gong, H. Yin, Z. Mo, Y. Tang, L. Chi, Optical band gap and photoluminescence in heavily Tb^{3+} doped GeO_2-B_2O_3-SiO_2-Ga_2O_3 magneto-optical glasses, J. Alloys Compd. 686 (2016) 635–640. https://doi.org/10.1016/j.jallcom.2016.06.074.

[69] Z.X. Mo, H.W. Guo, P. Liu, Y.D. Shen, D.N. Gao, Luminescence properties of magneto-optical glasses containing Tb^{3+} ions, J. Alloys Compd. 658 (2016) 967–972. https://doi.org/10.1016/j.jallcom.2015.10.236.

[70] J. F. Stebbins, P. Zhao, and S. Kroeker, "Non-bridging oxygens in borate glasses: Characterization by ^{11}B and ^{17}O MAS and $^{3}QMAS$ NMR," *Solid State Nucl. Magn. Reson.*, vol. 16, no. 1–2, pp. 9–19, 2000, doi: 10.1016/S0926-2040(00)00050-3.

CHAPTER IV - Characterization and study of properties of the Ln_2O_3-B_2O_3-WO_3 System

Chapter IV - Characterization and study of properties of the Ln_2O_3-B_2O_3-WO_3 System

1. Samples

As previously mentioned, we used as a basis for this chapter the composition 25Tb40W ($25Tb_2O_3$-$35B_2O_3$-$40WO_3$) from the previous chapter for the preparation of this series of glasses, changing the terbium oxide to Ln_2O_3 (Ln = Nd^{3+}, Sm^{3+}, Eu^{3+}, Gd^{3+}, Dy^{3+}, Ho^{3+}, Er^{3+}, Tm^{3+}) in order to understand the structural, optical, magnetic alterations that these ions of the same family give and modify in the glass composition. A sample containing $12.5Tb_2O_3$-$12.5Gd_2O_3$-$35B_2O_3$-$40WO_3$ was also synthesized under the same conditions for the same purpose. The choice of this 25Tb40W sample as the reference stemmed from the fact that it is the intermediate sample of the xTb40W system studied, its thermal stability is the best in the system and its structural part is better defined (by Raman, IR, and NMR of 25La40W). In all graphs presented where comparison occurs between the Ln^{3+} ions, the 25Tb40W sample will be considered.

The lanthanides consist of the fifteen elements of period six having atomic numbers 57 through 71, starting with the element lanthanum (La) after which they are named. The electron configuration of the f-block elements is interesting because there are parallels to be drawn here with electron configuration of the d-block elements - primarily the fact that the elements in both blocks are transitioning between two stable electronic configurations with respect to the filling of an inner electron shell. The noble gas configuration for the lanthanide elements, from lanthanum to lutetium, takes the following general form:

$[Xe]4f^{0-14}5d^{0-1}6s^2$;

The special spectroscopic properties of the trivalent ions arise from intraconfigurational f–f transitions inside their partially filled 4f shell, which is shielded by the outer filled 5s and 5p shells.

The transitions within the 4f shell are parity forbidden (Laport's selection rule) but, due to mixing of states with different parity from other orbitals, they are observed. This shielding is responsible for the main features of the lanthanide

luminescence, such as low molar absorption coefficients, narrow-line emission and long lifetimes of the excited states, ranging from microseconds to several milliseconds. Hence, although the absorption and emission of Ln^{3+} ions are only slightly affected by the environment, this small (10^3 cm^{-1}) crystal-field effect explains the emission features.

Due to the shielding effect, the lanthanide series elements exhibit the effect known as lanthanide contraction, where the nucleus offers a stronger electrostatic force on the 6s electrons in the outer layer, bringing them closer to the nucleus and decreasing the atomic radius. The chemical properties of the lanthanides are very similar to each other.

The prepared glasses are shown in Figure 37a. As shown in Figure 37b, some samples showed crystallization after quenching, precipitating a borate phase and suggesting a difference in solubility of the lanthanides for this specific system. Table 8 summarizes the acronyms, nominal compositions (25Ln40W), the mol% and the molar mass of investigated samples.

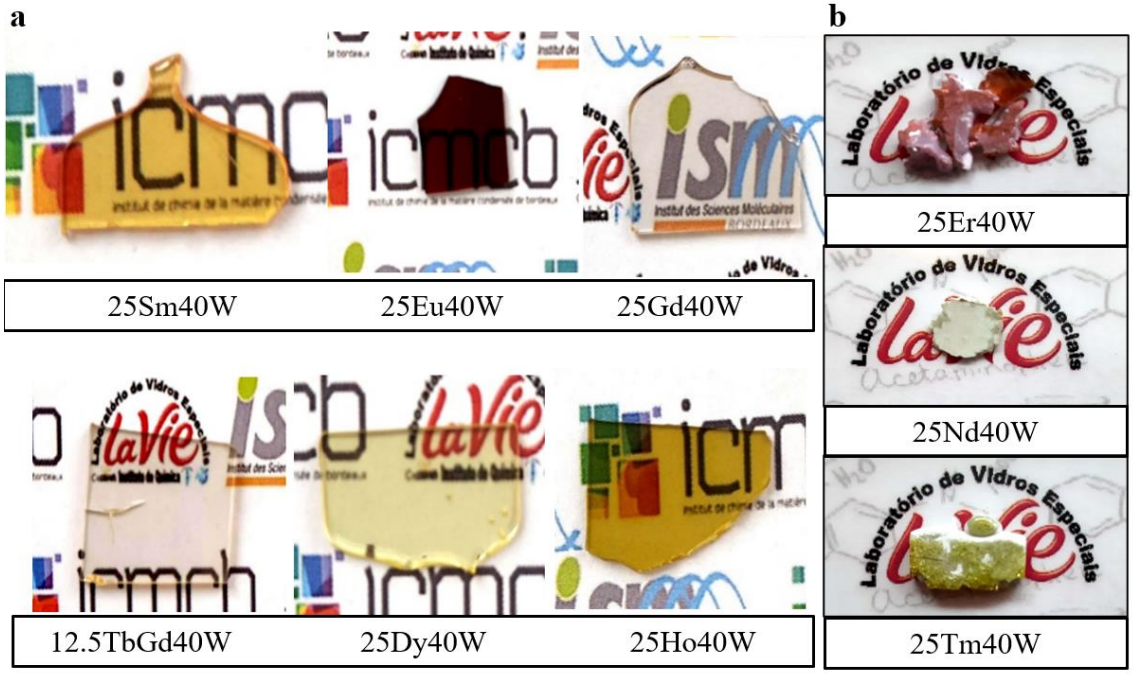

Figure 37. Samples for the $25Ln_2O_3$-$35B_2O_3$-$40WO_3$ system, where a. Ln = Sm, Eu, Gd, Dy, Ho, and a sample with $12.5Tb_2O_3$-$12.5Gd_2O_3$-$35B_2O_3$-$40WO_3$ and b. Ln = Er, Nd, Tm. (Own authorship).

Table 8. Series of Ln-contain borotungstate glasses, showing name, nominal compositions (% mol and % cat mol), molar mass (M) and if phase separation occurred during quenching.

Samples	Nominal compositions (% mol)			Nominal compositions (% cat mol)			M (g . mol^{-1})	Phase separation after melt-quenching
	Ln_2O_3	WO_3	B_2O_3	$LnO_{3/2}$	WO_3	$BO_{3/2}$		
25Nd40W	25	40	35	31.25	25	43.75	201.22	Yes
25Sm40W	25	40	35	31.25	25	43.75	204.28	No
25Eu40W	25	40	35	31.25	25	43.75	205.08	No
25Gd40W	25	40	35	31.25	25	43.75	207.72	No
25Dy40W	25	40	35	31.25	25	43.75	210.35	No
25Ho40W	25	40	35	31.25	25	43.75	211.57	No
25Er40W	25	40	35	31.25	25	43.75	212.73	Yes
25Tm40W	25	40	35	31.25	25	43.75	213.57	Yes
12.5TbGd40W	12.5+ 12.5	40	35	15.63+ 15.63	25	43.75	208.15	No

(Own authorship).

As observed, the radii of the lanthanides seems to play a role into the glass formation, for this specific composition. Thus the elements with lower ionic radii crystallizes after quenching at the same conditions of synthesis.

All samples showed paramagnetic response, at room temperature, when a magnet field (neodymium N42) was applied. Figure 38 presents a sequence of photos demonstrating this effect. This property comes from the high concentration of paramagnetic ions present in the samples.

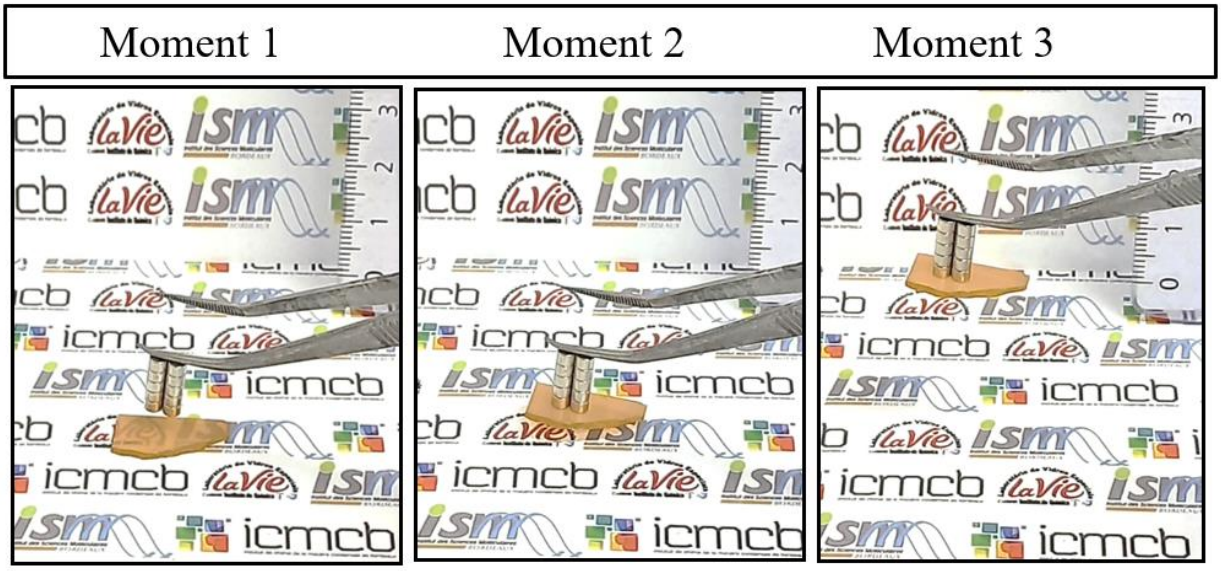

Figure 38. Photo sequence of the 25Ho40W sample being attracted by a neodymium magnet at room temperature. The high concentration of paramagnetic species imparts this effect to the samples. (Own authorship).

2. XRD

The vitreous phases were confirmed by the XRD analysis for 25Sm40W, 25Eu40W, 25Gd40W, 12.5TbGd40W, 25Dy40W and 25Ho40W samples, and the results are shown in Figure 39. The non-crystalline phase, characterized by the presence of the halo and the absence of crystallization peaks can be observed. However, the samples 25Nd40W, 25Er40W, 25Tm40W showed crystallization, already apparent during quenching. The precipitated phase contains at least one crystalline phase, identified as $LnBO_3$ (CIF - 1511089), hexagonal phase group P63/mmc, and is analogous to YBO_3, ICSD code - 27931[1]. 25Tb40W diffractogram was added for reference and comparison. The ionic radius of each lanthanide is also expressed in Figure 39.

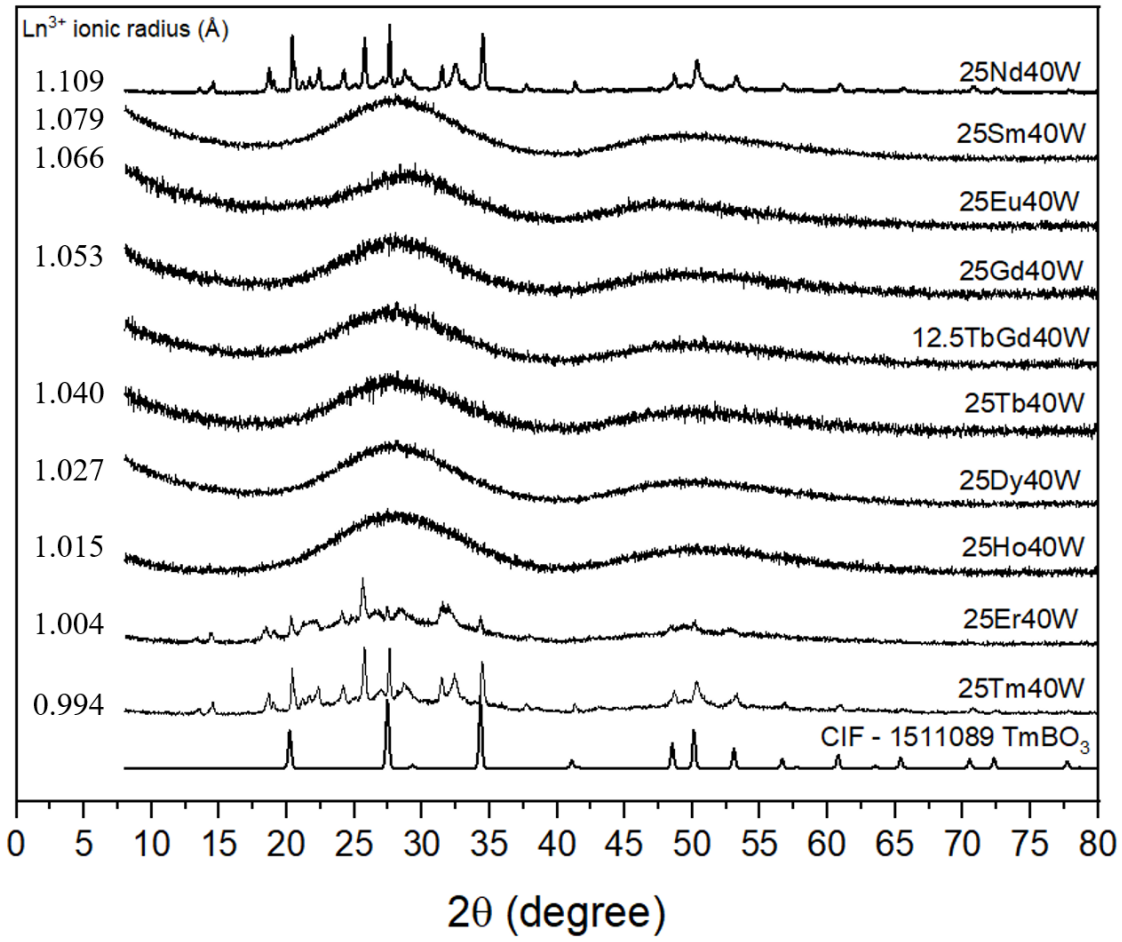

Figure 39. X-ray diffractograms for the 25Ln40W, Ln = Nd, Sm, Eu, Gd, Tb, Dy, Ho, Er or Tm samples, the ionic radius for the respective Ln^{3+} ion and the $TmBO_3$ standard, hexagonal phase group P63/mmc (CIF-1511089). (Own authorship).

As discussed in the previous section, the region of formation of the vitreous network is quite small., As studied by E. M. Levin et al[2], there are several types of rare earth based borates, depending on the proportion of boron, the ionic radius of the rare earth, temperature of synthesis and, therefore, can lead to form polycrystalline phases.

A variation of ~± 4% in the size of the Tb^{3+} ion (negative for Er^{3+} and Tm^{3+} and positive for Nd^{3+}) is enough to induce the precipitation of one or more borate phases, reinforcing that, for these synthesis conditions, the $25Ln_2O_3$-$35B_2O_3$-$40WO_3$ system is very unstable.

3. Thermal Analysis and density

Figure 40 reveals DSC curves for the 25Ln40W samples. We can see that some curves clearly show two crystallization events like the 25Sm40W, 25Tb40W and 12.5TbGd40W samples, while the others show a single, very broad crystallization peak, probably indicating that two crystallization events occurred. Table 9 presents the characteristic temperatures values and other information such as density (ρ), ion effective concentration (N_{Ln3+}), theoretical optical basicity (Λ_{Th}) and short wavelength cut-off (λ_{UV}).

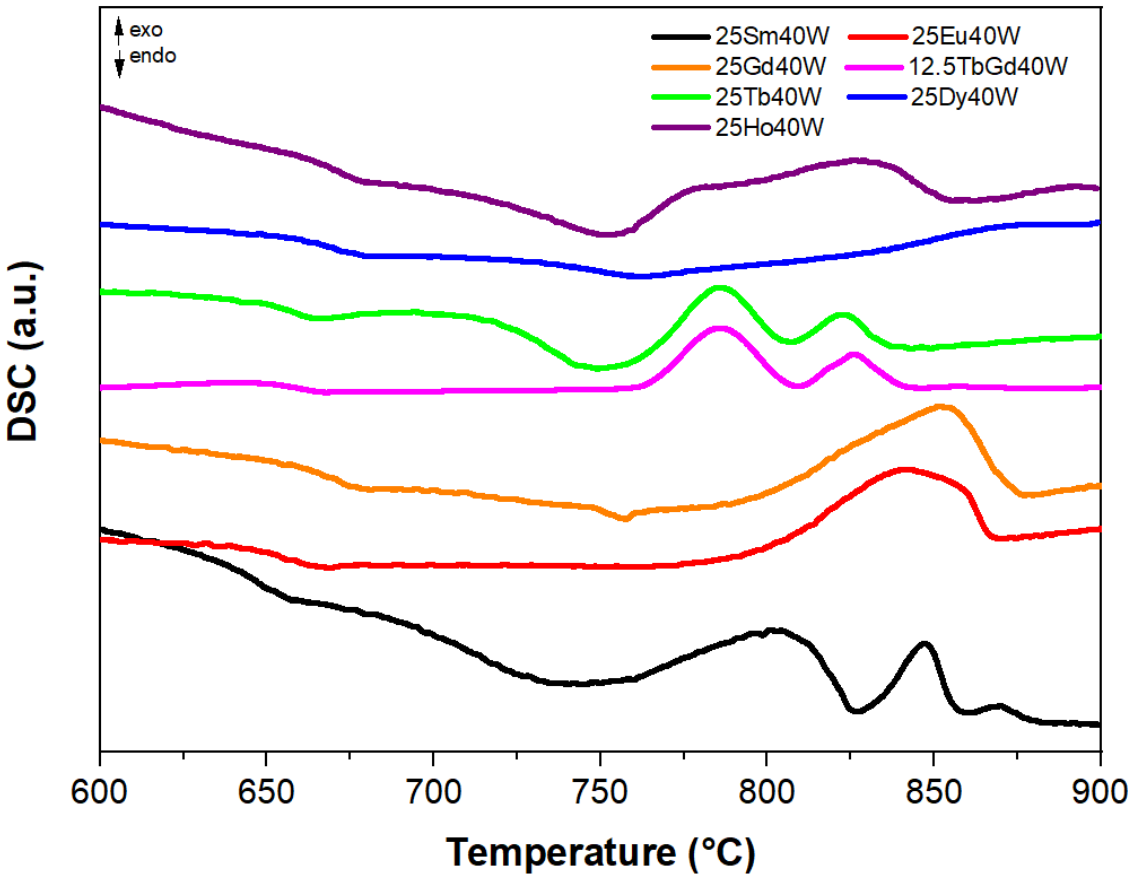

Figure 40. DSC curves for the 25Ln40W samples. (Own authorship).

Table 9. Thermal and physical properties of the glass samples: Tg (glass transition temperature), Tx (onset of the crystallization temperature), ΔT (thermal stability parameter), ρ (density), N_{Ln3+} (ion effective concentration), Λ_{Th} (theoretical optical basicity) and λ_{UV} (short wavelength cut-off).

Samples	Ionic	Tg	Tx	ΔT	ρ	N_{Ln3+}	Λ_{th}	λ_{UV}

	radius (Å)	(±3 °C)	(±3 °C)	(±3 °C)	(±0.005 g.cm^{-3})	(10^{21} ion.cm^{-3})		(nm)
25Sm40W	1.079	634	742	110	5.831	14.7	0.945	350
25Eu40W	1.066	643	780	137	6.074	15.3	0.942	531
25Gd40W	1.053	657	758	101	6.249	15.8	0.939	344
12.5TbGd40W	-	649	762	113	6.083	7.7	0.936	359
25Dy40W	1.027	655	763	108	6.192	15.7	0.929	346
25Ho40W	1.015	664	753	89	6.276	16.0	0.929	354

(Own authorship).

We can observe that the Tg tends to increase as the ionic radius of the lanthanide decreases. The thermal stability (ΔT) of all, except 25Ho40W, is close to 100±3 °C, which opens possibilities for controlled thermal treatment, seeking to precipitate a specific phase or prepare optical fibers by drawing, and it presents a variation that tends to increase as the ionic radius is greater. The variation in Tx might be caused by a variation in the structure of the crystallized phases. Figure 41 exemplifies and summarizes the evolution of Tg and ΔT with the variation of ionic radii of the lanthanides.

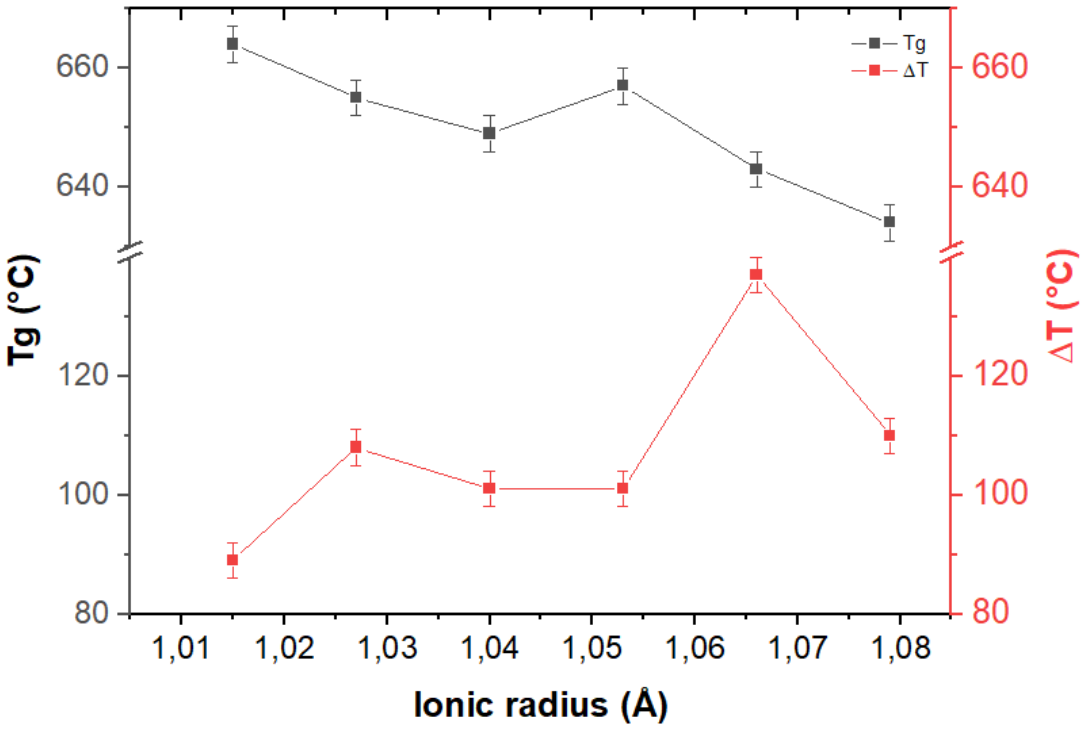

Figure 41. Tg and ΔT variation for each lanthanide ionic radius of 25Ln40W samples. (Own authorship).

4. Density and Optical basicity

As done in Chapter III, we can calculate the effective ionic concentration of Ln^{3+} ions (N_{Ln3+}) using the density of each sample and Eq. 24. Figure 42a. presents the N_{Ln3+} variation for the ionic radii of the studied lanthanides. Higher ionic concentrations show a higher susceptibility and Verdet constant response. The radius considered for the 12.5TbGd40W sample was the average of the Tb^{3+} and Gd^{3+} radii, since the concentration is half of each ion.

Despite having the same ionic concentration (25% Ln_2O_3), the calculation depends on the density that varies for each ion, as they have different atomic masses.

The theoretical optical basicity (Λ_{Th}) of the samples was calculated, using the Eq. 25. Λ_{Th} is used to determine the ability to donate electrons from oxygen in a glass matrix and the growth of the concentration of non-binding oxygens (NBO), which changes the polarizability of the material and positively influences the Verdet constant [3–5].

The theoretical intrinsic optical basicity value of an individual glass precursor (Λ_i), which for B_2O_3, WO_3, Tb_2O_3, Sm_2O_3, Eu_2O_3, Gd_2O_3, Dy_2O_3, Ho_2O_3 are respectively 0.425, 1.045, 0.954, 0.984, 0.976, 0.969, 0.945, and 0.945 [6,7]. The data are presented in Table 9 and in Figure 42b, which shows the variation of Λ_{Th} and density for each ionic radius of the studied lanthanides.

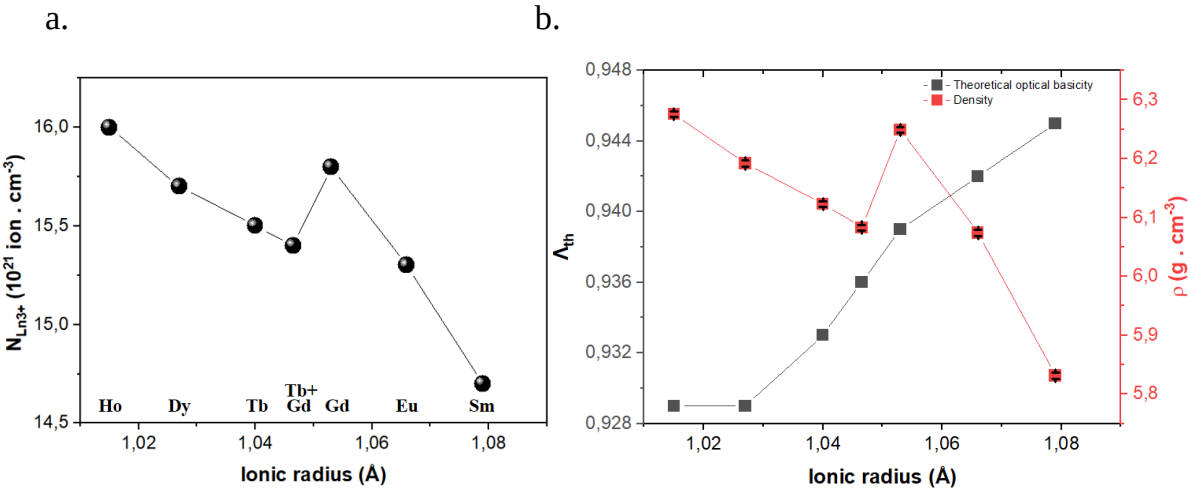

Figure 42. a) Variation of effective ionic concentration and b) theoretical optical basicity and density for 25Ln40W samples, compared by different ionic radii of Ln^{3+}. For the 12.5TbGd40W sample, the averages of the Tb^{3+} and Gd^{3+} radii were considered, as they represent half the concentration of each. (Own authorship).

5. Structural analysis

Figure 43 shows the Raman spectra for each glass sample and, can be observed that the bands do not suffer great variations and have the same regions assigned to the 25Tb40W sample, also included for comparison purposes, indicating a similar chemical environment. Table 10 summarizes the values of the described vibrational modes, by Raman and Infrared techniques.

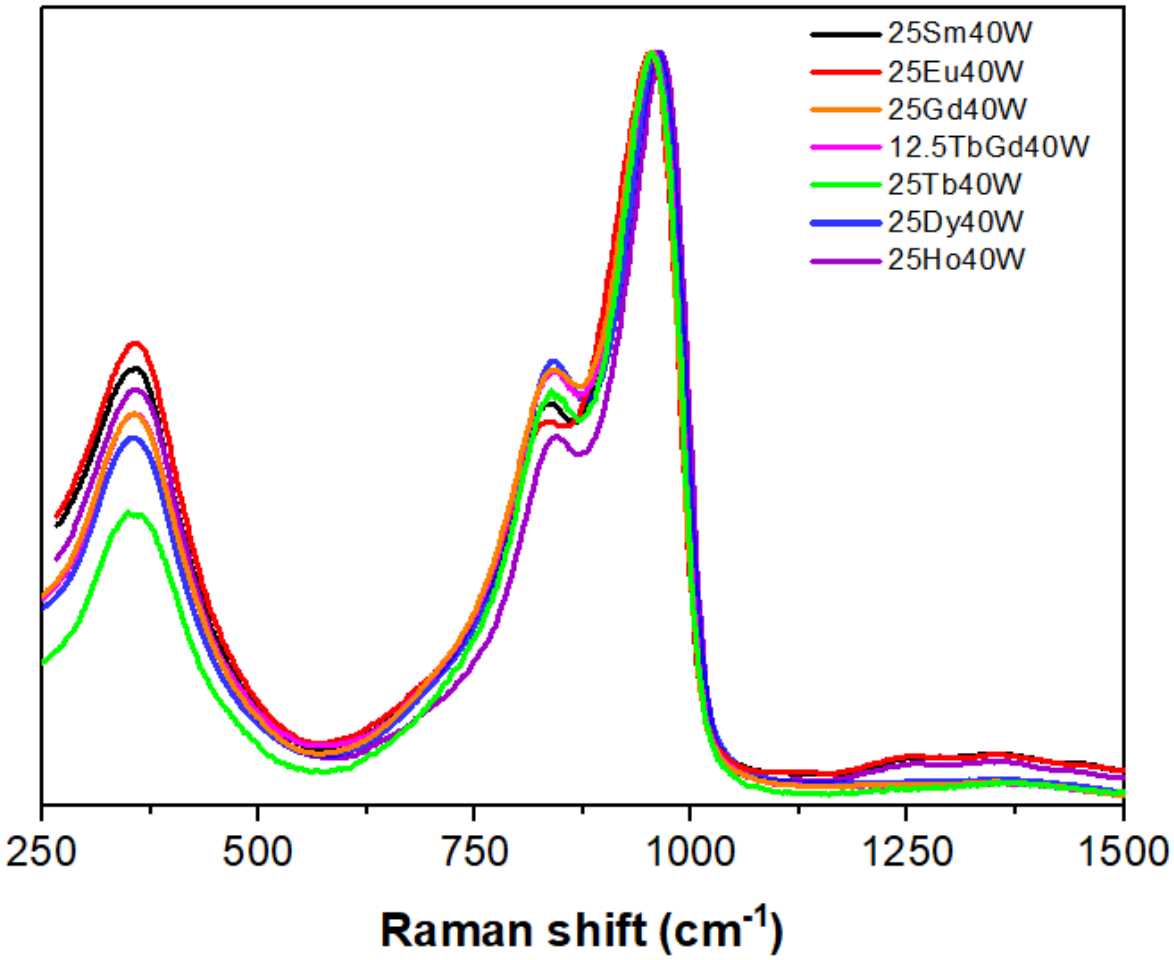

Figure 43. Raman spectra for each 25Ln40W sample. (Own authorship).

Using Raman scattering spectroscopy, at low frequencies (200-600 cm^{-1}) one can identify a broad band centered at ~350 cm^{-1}, related to the coupling of various vibrational modes, such as δ $[WO_6]^{6-}$ [8–10], δ B-O-B[11–13], and ν Ln-O[14]. In the region between 600-1000 cm^{-1}, as seen in the previous chapter, one can identify the bands related to the W-O-W stretching modes (ν_s at 720 cm^{-1} and ν_{as} at 840 cm^{-1}) and the ν $[W\text{-}O_t]^-$ terminal unit at 950 cm^{-1} [15,16]. At high frequencies (1000 - 1600 cm^{-1}), where the vibrational modes of the borate groups dominate, they are more easily identified by infrared spectroscopy.

Low significant variation occurs with the change of lanthanide ion. The band intensity at 840 cm^{-1} tends to be less intense for larger ions (Sm^{3+}, Eu^{3+}), indicating that larger ions need higher concentrations of $W\text{-}O_t]^-$. There is also a short shift of the 950 cm^{-1} band towards higher frequencies, which can also be attributed to the size of the lanthanide ion. This behaviour could be explained by the fact that bigger Ln ions tend

to be stabilized by nine oxygen atoms while lower ions need only 8, however, to prove such statement, a more detailed study would be necessary, as for example, using EXAFS, to confirm the coordination of each rare earth.

Figure 44 presents the normalized absorption coefficients for each 25Ln40W sample, with the absolute values presented in inset. The coefficients were obtained by specular reflectance infrared, with the data treated mathematically using the Kramers-Kroning transform[11,12].

Infrared spectra make it easy to interpret the borate portion of samples, although the attributions of the tungstate groups are also observed. The extended band centered at ~320 cm^{-1} can be attributed to overlapping contributions from various borates and tungstates units. The band at 650-720 cm^{-1} can be attributed to bending vibrations of various borate segments[11,12]. The most intense peak at 850 cm^{-1} and the band at ~950 cm^{-1}, which appears as a shoulder to the preceding band, can be attributed to tungsten modes, best discussed by Raman spectra[8–10,15,16].

At 1060 cm^{-1}, the characteristic stretching modes of BO_4 units. Finally, the localized widening band of 1100-1600 cm^{-1} is attributed to the BO_3 triangular structural units. being formed (pyroborate $[B\emptyset O_2]^{2-}$ and metaborate $[B\emptyset_2O]^-$, respectively) [11–14,19]. Due to the large size of Ln^{3+} ions, the presence of units and chains (such as orthoborates, metaborates and pyroborates) BO_3^{-3} is necessary to stabilize the presence of the ion in the glass matrix.

Table 10. Band assignments of the main vibrational modes in Raman and Infrared for the 25Ln40W glasses.

Band observed (cm^{-1})	**Raman**	**IR**	**Assignments**	**References**
350	Yes	Yes	Coupling of δ $[WO_6]^{6-}$, δ B-O-B units and ν Tb-O modes	[8–14]
650-720	X	Yes	δ modes of BO_3 units	[11,12]
760	Yes	Yes	ν_s W-O-W of the distorted $[WO_6]^{6-}$ octahedral in non-crystalline lattices	[8–10,15,16]

840	Yes	Yes	ν_{as} W-O-W of the distorted $[WO_6]^{6-}$ octahedral in non-crystalline lattices	
950	Yes	Yes	ν $(W\text{-}O_t)^-$ of the distorted $[WO_6]^{6-}$ octahedral in non-crystalline lattices	
1060	X	Yes	ν B-O of tetrahedral $[BO_4]^-$ units	[11–14,19]
1200-1500	X	Yes	ν modes of pyroborate $[B\text{Ø}O_2]^{2-}$ and metaborate $[B\text{Ø}_2O]^-$	

(Own authorship).

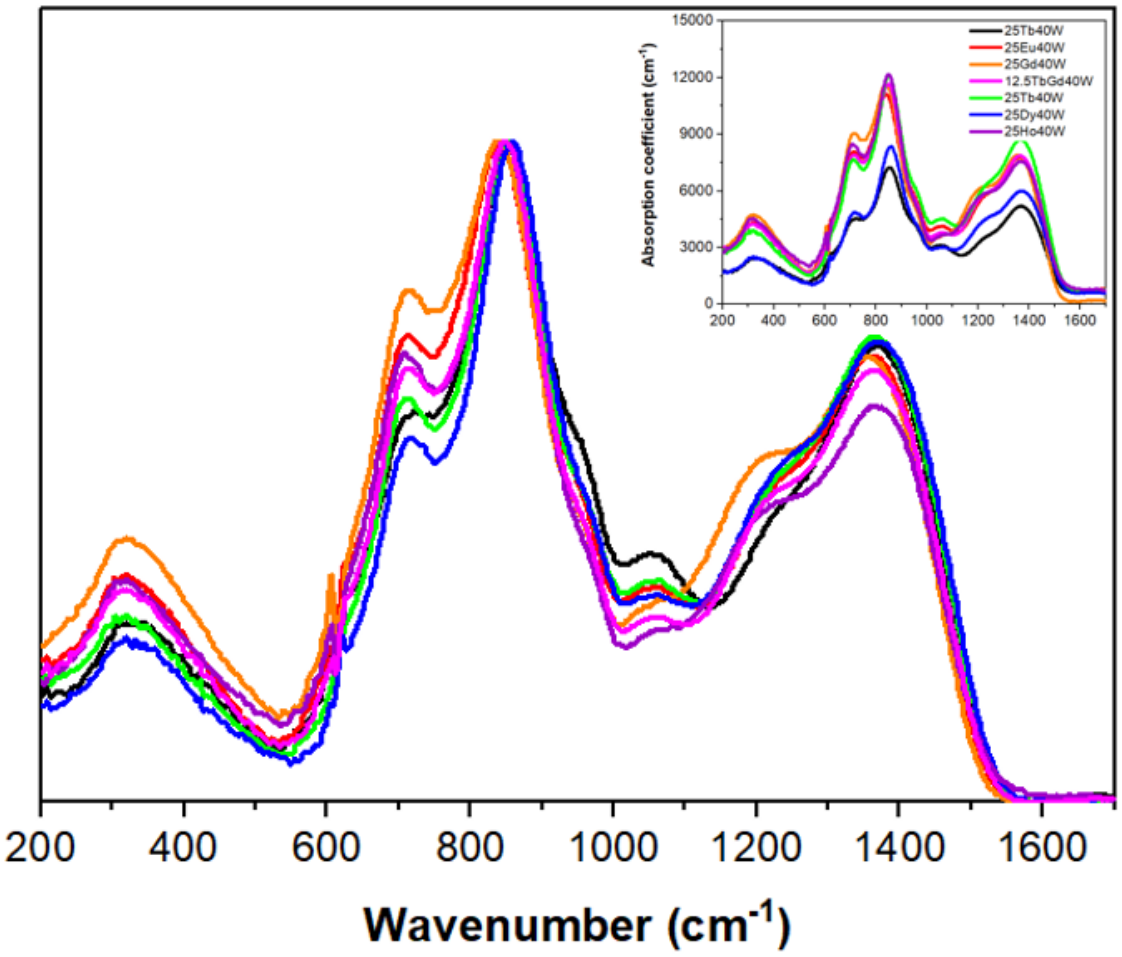

Figure 44. Normalized absorption coefficient for each sample 25Ln40W obtained Kramers-Kroning transform from infrared measurement by specular reflectance. The inset graph shows the absolute values for each sample. (Own authorship).

6. Optical analysis

Figure 45, 46 and 47 shows the 25Sm40W sample, transitions 4f-4f were assigned for the Sm^{3+} ion from the $^6H_{5/2}$ ground state, with absorption bands $^4H_{9/2}$ (0.344 µm), $(^4D + {}^6P)_{5/2}$ (0.361 µm), $^4L_{17/2}$ (0.374 µm), $^4(P_{5/2} + L_{13/2} + G_{11/2})$ (0.403 µm), $^4G_{9/2}$ (0.438 µm), $^4(G_{7/2} + M_{15/2} + I_{13/2})$ (0.477 µm), $^4F_{3/2}$ (0.527 µm), $^4G_{5/2}$ (0.562 µm), $^6F_{11/2}$ (0.944 µm), $^6F_{9/2}$ (1.08 µm), $^6F_{7/2}$ (1.24 µm), $^6F_{5/2}$ (1.41 µm), $^6F_{3/2}$ (1.49 µm), $^6H_{15/2}$ (1.53 µm), $^6F_{1/2}$ (1.59 µm), $^6H_{13/2}$ (1.97 µm), $^6H_{11/2}$ (2.60 µm) and $^6H_{9/2}$ (4.38 µm). The λ_{UV} was 350 nm for this sample[19]. Figures 46 and 47 feature a zoom of 0.2-0.8 µm and 0.8-1.75 µm, respectively, to observe the absorptions referring to the Sm^{3+} ion more clearly.

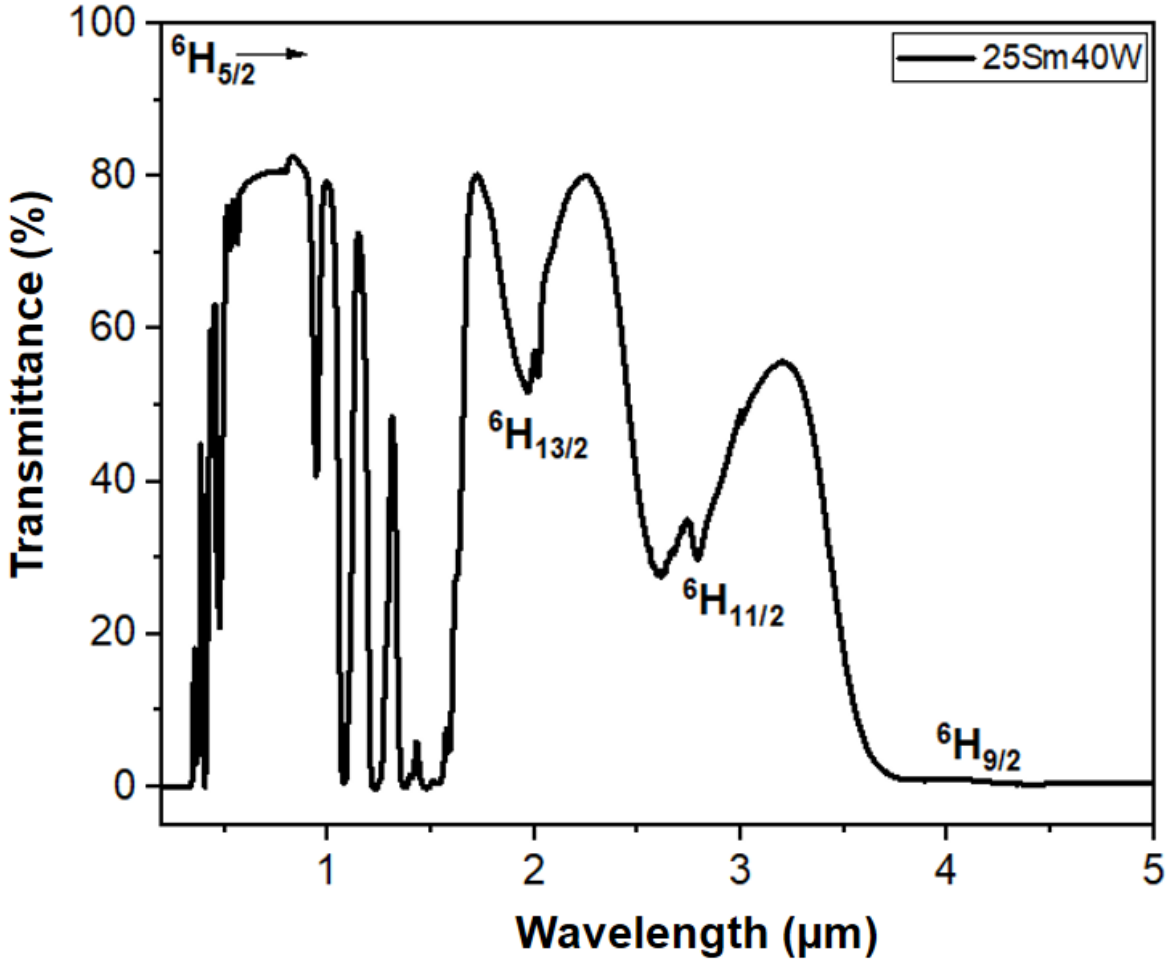

Figure 45. Transparency window for the 25Sm40W sample, with its main assignments starting from the ground state $^6H_{5/2}$. (Own authorship).

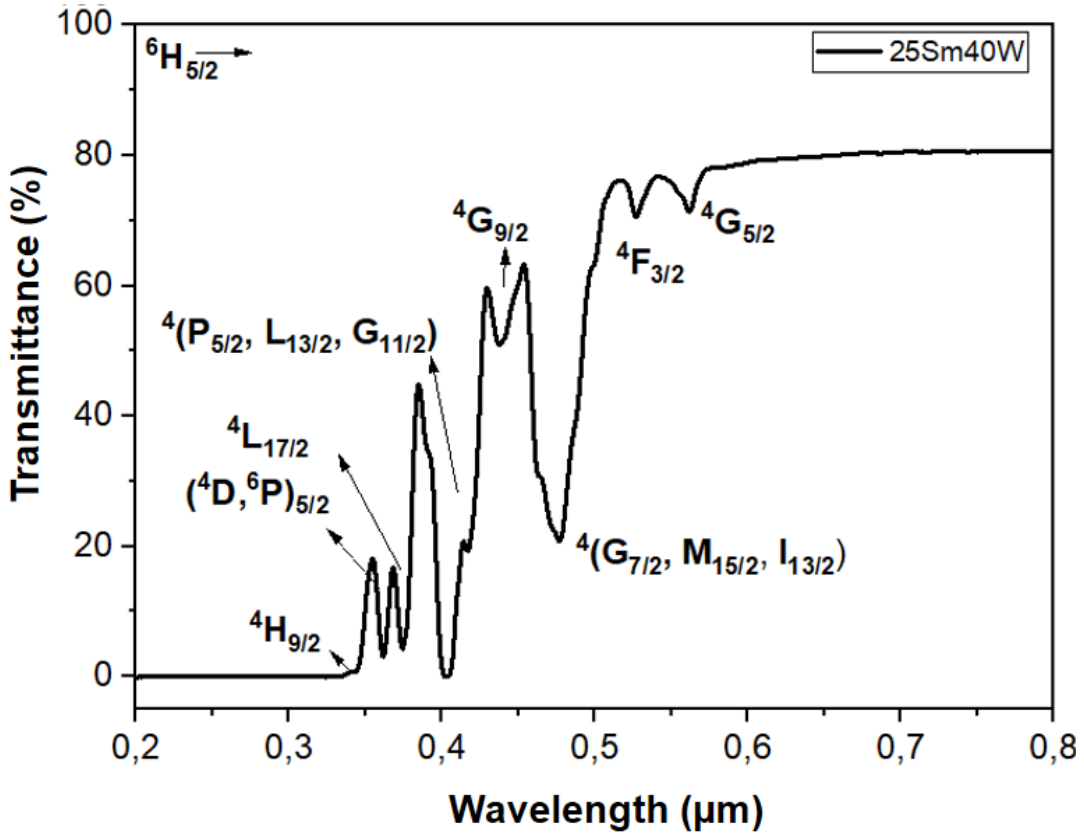

Figure 46. Zoom 0.2-0.8 μm transmittance spectra for the 25Sm40W sample, with its main assignments starting from the ground state $^6H_{5/2}$. (Own authorship).

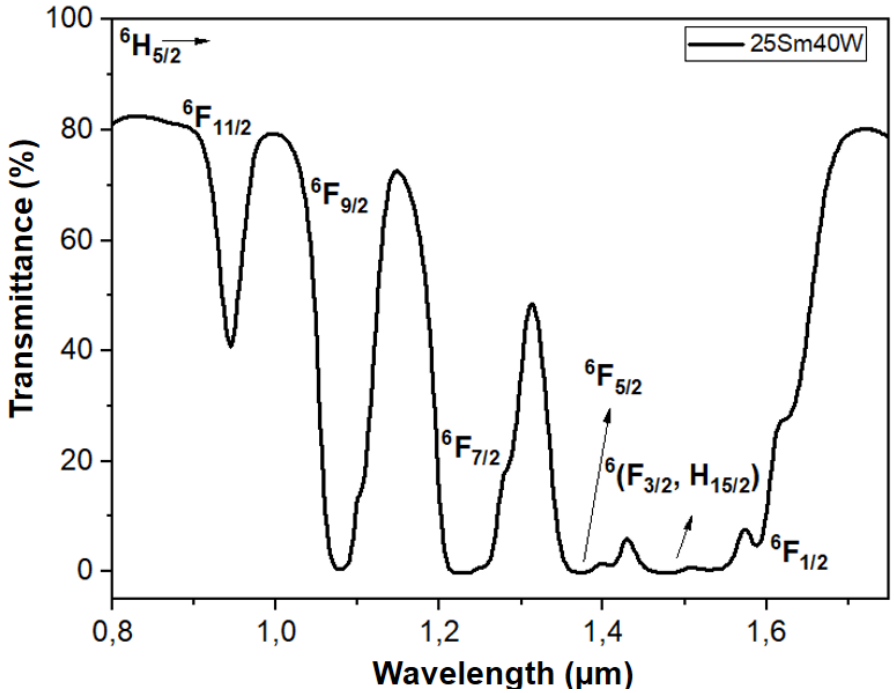

Figure 47. Zoom 0.8-1.75 μm transmittance spectra for the 25Sm40W sample, with its main assignments starting from the ground state $^6H_{5/2}$. (Own authorship).

Figure 48 shows the transmittance spectra for 25Eu40W sample. The λ_{UV} of the 25Eu40W sample was 531 nm, due to the high concentration of Eu^{3+}, verified by the 4f-4f transitions in the near infrared region, from the $^7F_0$ ground state we can observe the $^7F_6$ bands (2.09 µm), $^7F_5$ (2.57 µm) and $^7F_4$ (3.32 µm)[20,21]. There is an overlapping of the absorptions of shorter wavelengths, forming a broad absorption band in all visible.

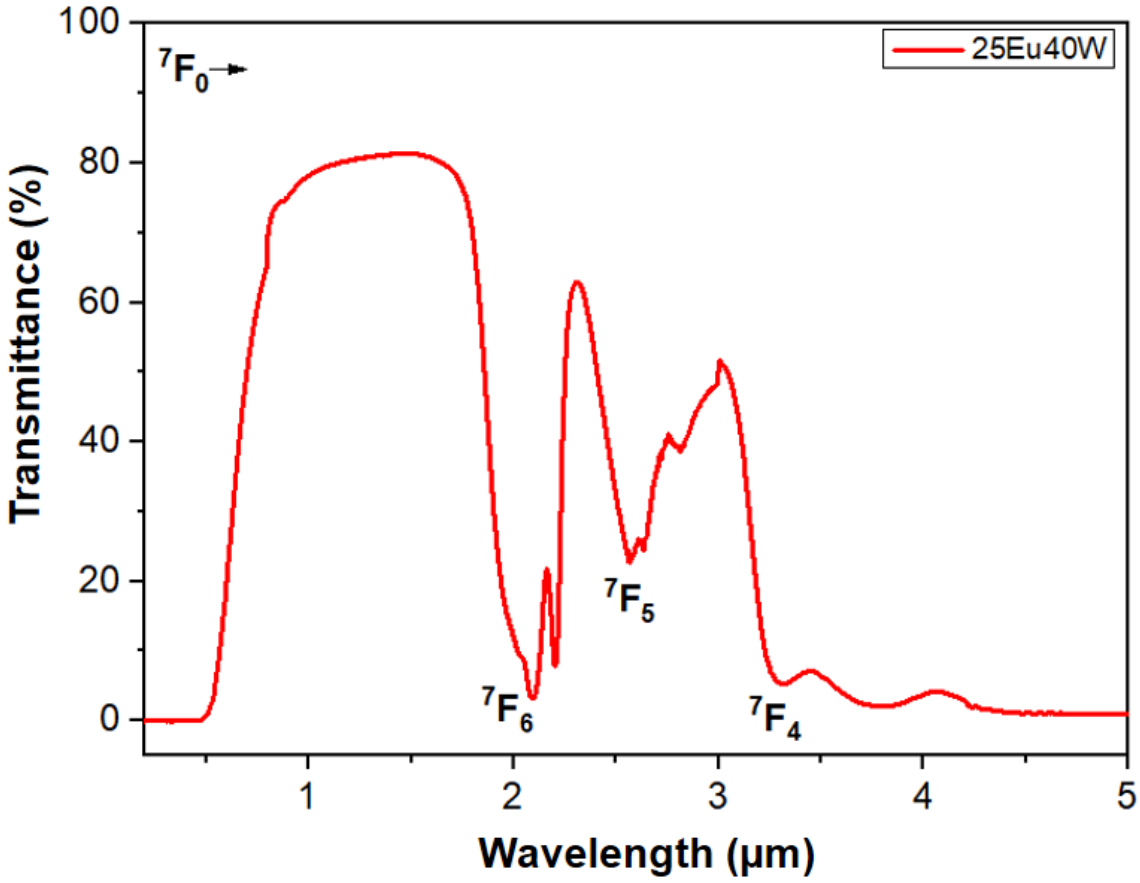

Figure 48. Transparency window for the 25Eu40W sample, with its main assignments starting from the ground state $^7F_0$. (Own authorship).

The 25Gd40W sample, showing in Figure 49, do not show a transition in the UV-Vis-NIR region, which corresponds to the Gd^{3+} ion. The λ_{UV} for this sample is 344 nm. The absorption band at 2840 nm can be considered due to the stretching vibration of hydrogen bonded OH− groups[22].

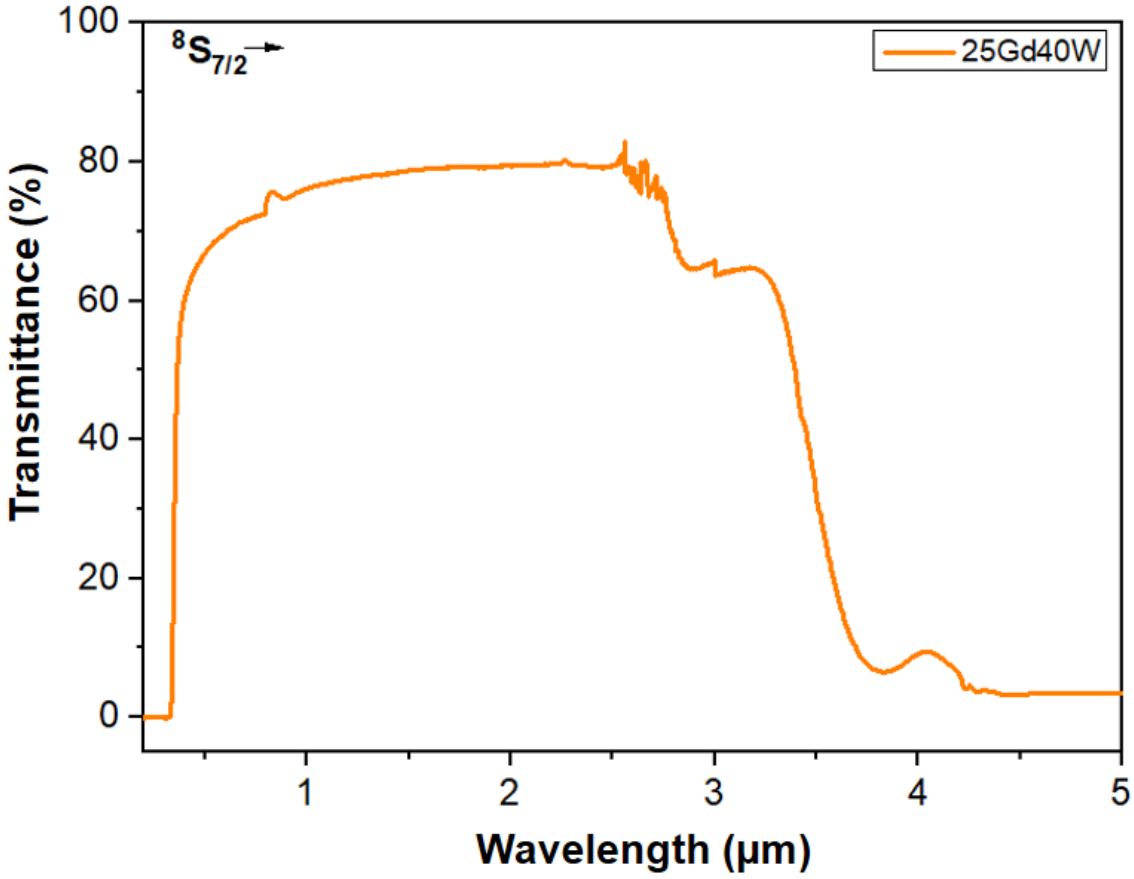

Figure 49. Transparency window for the 25Gd40W sample, with its main assignments starting from the ground state $^8S_{7/2}$. (Own authorship).

For the Tb sample, the absorption bands at 0.486, 1.89, 1.95, 2.21, and 2.88 μm were assigned to the Tb^{3+} 4f–4f transitions from the $^7F_6$ ground state to the excited states $^5D_4$, $^7F_{0,1,2}$, $^7F_3$, and $^7F_4$, respectively [23]. The same transitions were observed for the 12.5TbGd40W sample. The infrared cut-off starts with the presence of a shoulder referring to an absorption band around 3.7 μm and the multiphonon edge above 5.5 μm. For the 12.5TbGd40W sample, the λ_{UV} was 350 nm. The transmittance spectrum of the 12.5TbGd40W sample is shown in Figure 50. The spectrum of the 25Tb40W sample was taken as a reference.

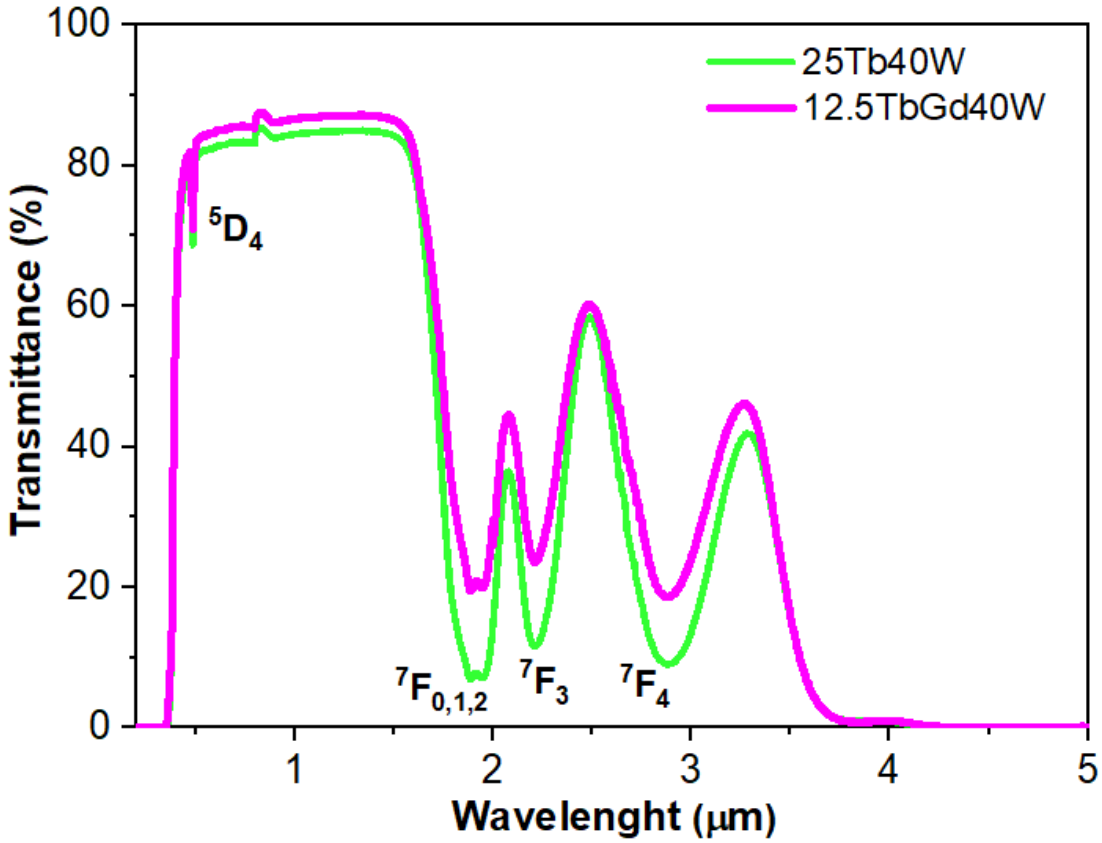

Figure 50. Transparency window for the 12.5TbGd40W sample, with its main assignments starting from the ground state $^7F_6$. 25Tb40W sample was taken as a reference. (Own authorship).

Dy^{3+} ion-specific 4f-4f transitions from the $^6H_{15/2}$ fundamental level were observed in the 25Dy40W sample, Figures 51, 52 and 53, at the respective wavelengths 0.351 μm ($^4I_{11/2}$), 0.365 μm ($^4M_{19/2}$), 0.387 μm ($^4F_{7/2}$), 0.426 μm ($^4G_{11/2}$), 0.452 μm ($^4I_{15/2}$), 0.472 μm ($^4F_{9/2}$), 0.730 μm ($^6F1/2$), 0.753 μm ($^6F_{3/2}$), 0.799 μm ($^6F_{5/2}$), 0.899 μm ($^6F_{7/2}$), 0.970 μm ($^6H_{5/2}$), 1.09 μm ($^6H_{7/2}$), 1.30 μm ($^6(F_{11/2} + H_{9/2})$), 1.72 μm ($^6H_{11/2}$) and 2.85 μm ($^6H_{13/2}$). The λ_{UV} was measured at 346 nm[19]. Figure 52 and 53 show a zoom in the 0.2-0.7 μm and 0.7-1.6 μm region, to improve the visualization of the respective Dy^{3+} levels.

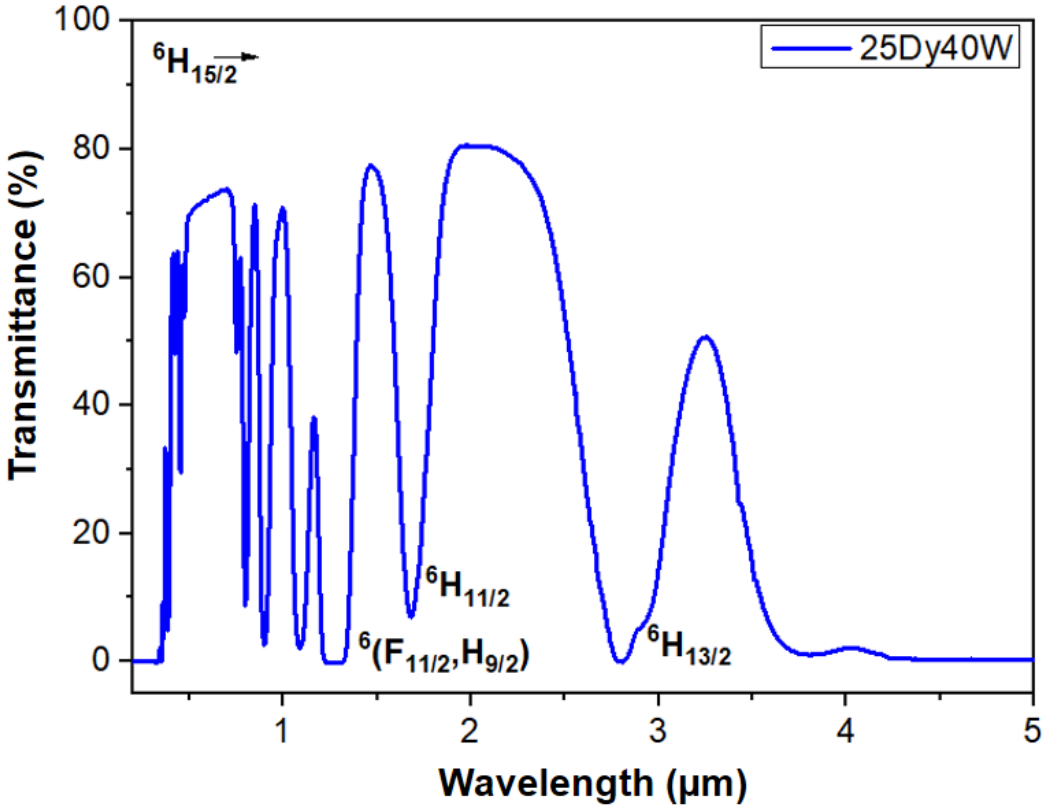

Figure 51. Transparency window for the 25Dy40W sample, with its main assignments starting from the ground state $^6H_{15/2}$. (Own authorship).

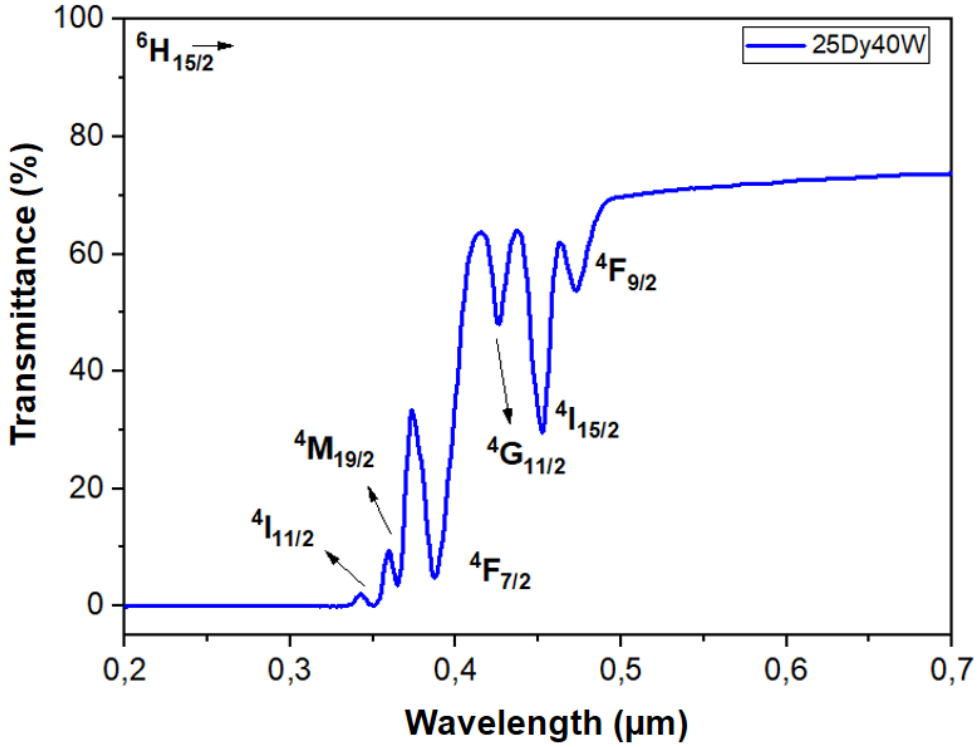

Figure 52. Zoom 0.2-0.7 μm transmittance spectra for the 25Dy40W sample, with its main assignments starting from the ground state $^6H_{15/2}$. (Own authorship).

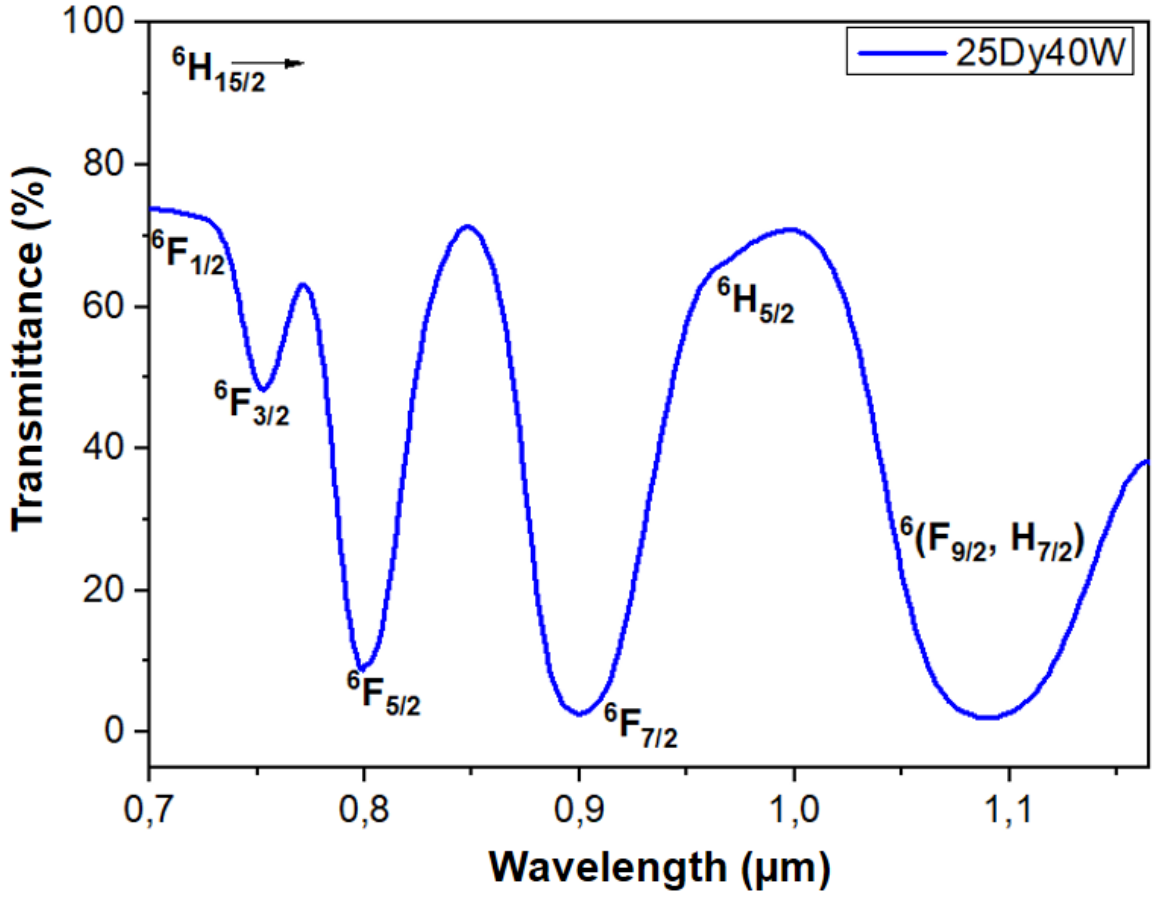

Figure 53. Zoom 0.7-1.6 μm transmittance spectra for the 25Dy40W sample, with its main assignments starting from the ground state $^6H_{15/2}$. (Own authorship).

Finally, for the 25Ho40W sample, showing in Figure 54 and 55, the respective transitions 4f-4f to the Ho^{3+} ion were observed, such as $^3L_9$ (0.343 μm), $(^5G,^3H)_5$ (0.362 μm), $^4G_5$ (0.385 μm), $(^5G,^3G)_5$ (0.417 μm), $^5F_{1,2}$ (0.469 μm), $^5F_3$ (0.486 μm), $^5S_2$+$^5F_4$ (0.539 μm), $^5F_5$ (0.643 μm), $^5I_4$ (0.748 μm), $^5I_5$ (0.890 μm), $^5I_6$ (1.115 μm) and $^5I_7$ (1.900 μm) from the fundamental level $^5I_8$. The λ_{UV} was 354 nm[19]. Figure 55 shows the region 0.2-0.85 μm, for a better identification of the Ho^{3+} ion transitions in this region. 25Ho40W sample also features the famous holmium effect, changing color depending on the light source. In daylight, it is a tannish yellow color. Under trichromatic light, it is a fiery orange red. This occurs due to absorptions in visible region of Ho^{3+}. This effect is shown an inset figure in Figure 54.

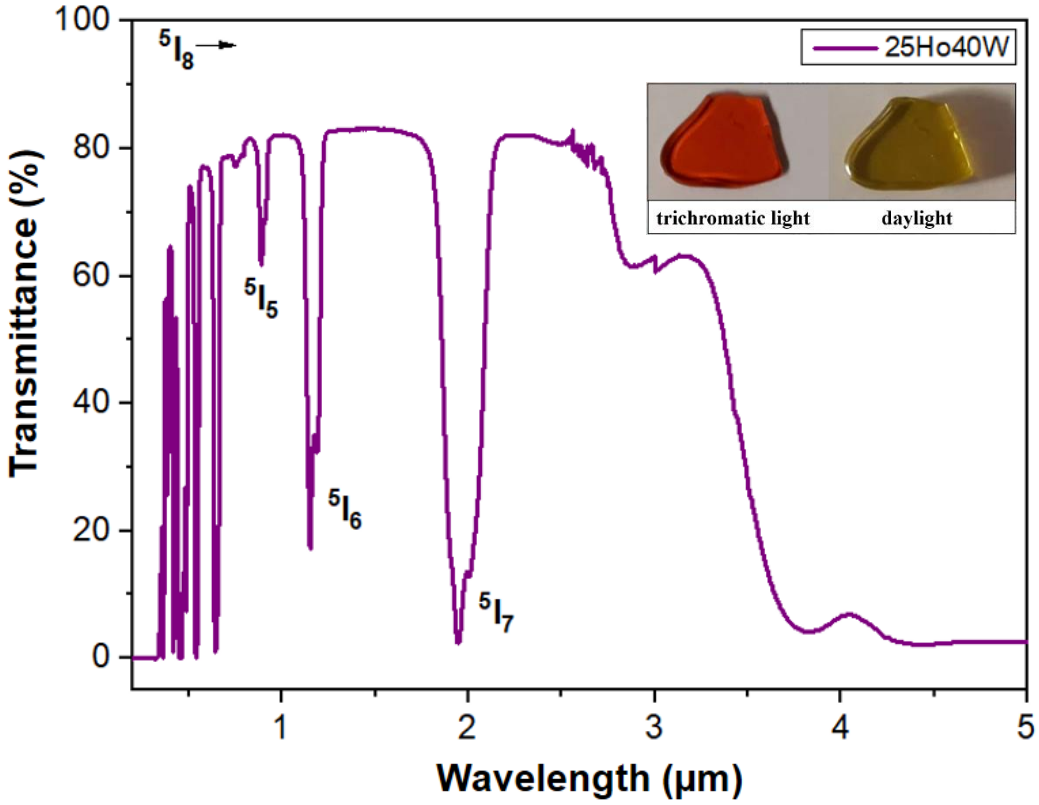

Figure 54. Transparency window for the 25Ho40W sample, with its main assignments starting from the ground state $^5I_8$. (Own authorship).

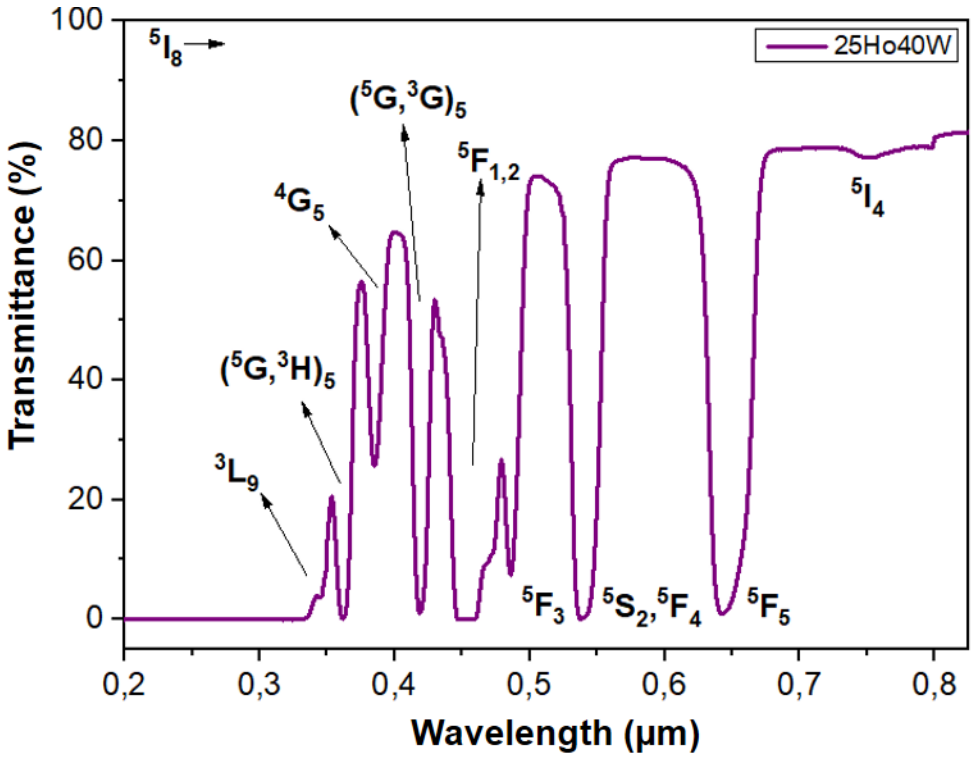

Figure 55. Zoom 0.2-85 μm transmittance spectra for the 25Ho40W sample, with its main assignments starting from the ground state $^5I_8$. (Own authorship).

7. Luminescence analysis

Figure 56 shows the PL spectra for the 25Sm40W sample, λ_{exc} = 404 nm, with the correspond to the 4f-4f Sm^{3+} transition, $^4G_{5/2}$ level to $^6H_{5/2}$, $^6H_{7/2}$, $^6H_{9/2}$ and $^6H_{11/2}$ levels at 564, 600, 646 and 707 nm, respectively[24].

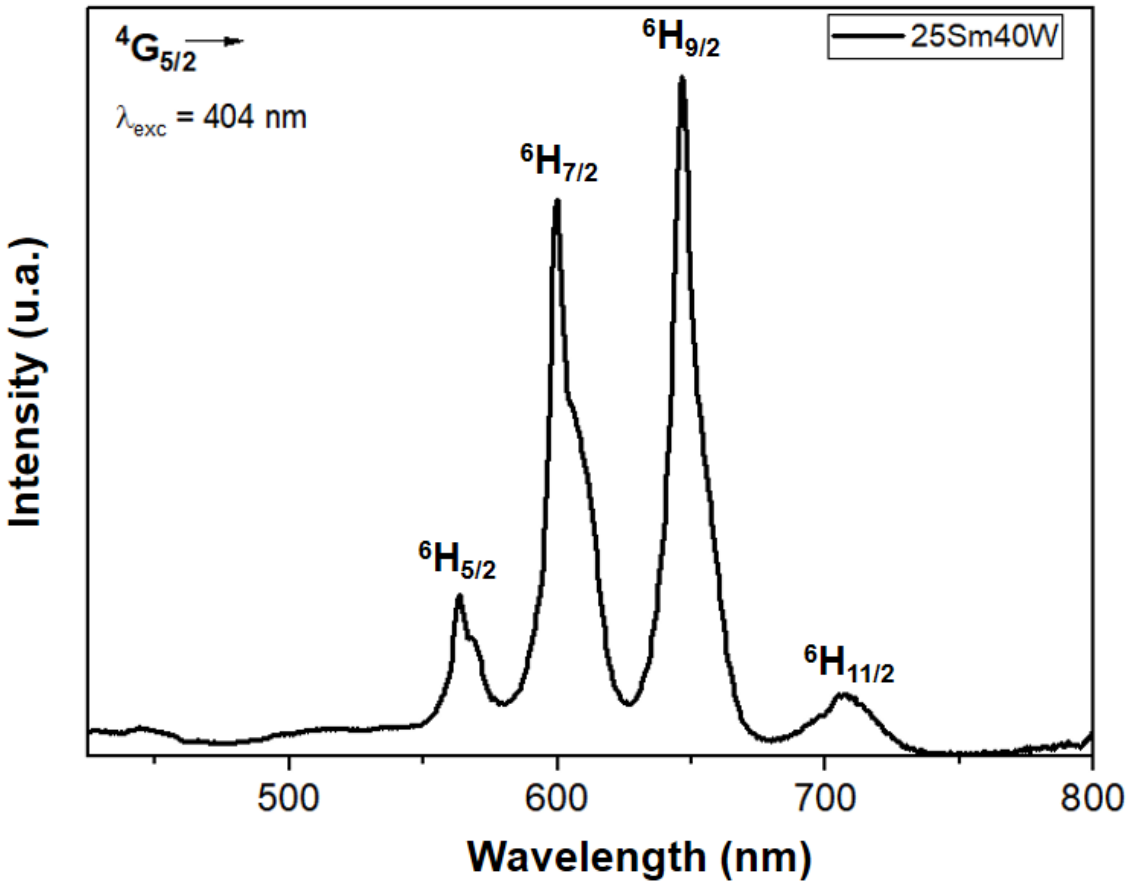

Figure 56. PL spectra for the Sm40W sample, showing the transitions from the excited level $^4G_{5/2}$ corresponding to the Sm^{3+} ion. λ_{exc} = 404 nm. (Own authorship).

For the sample 25Eu40W, showed at Figure 57, the emission spectra (λ_{exc} = 394 nm) displayed peaks, $^5D_0 \rightarrow 7F_0$ (579 nm), $^5D_0 \rightarrow ^7F_1$ (591 nm), $^5D_0 \rightarrow ^7F_2$ (613 nm), $^5D_0 \rightarrow ^7F_3$ (652 nm) and $^5D_0 \rightarrow ^7F_4$ (701 nm) also respectively transitions of Eu^{3+}[21].

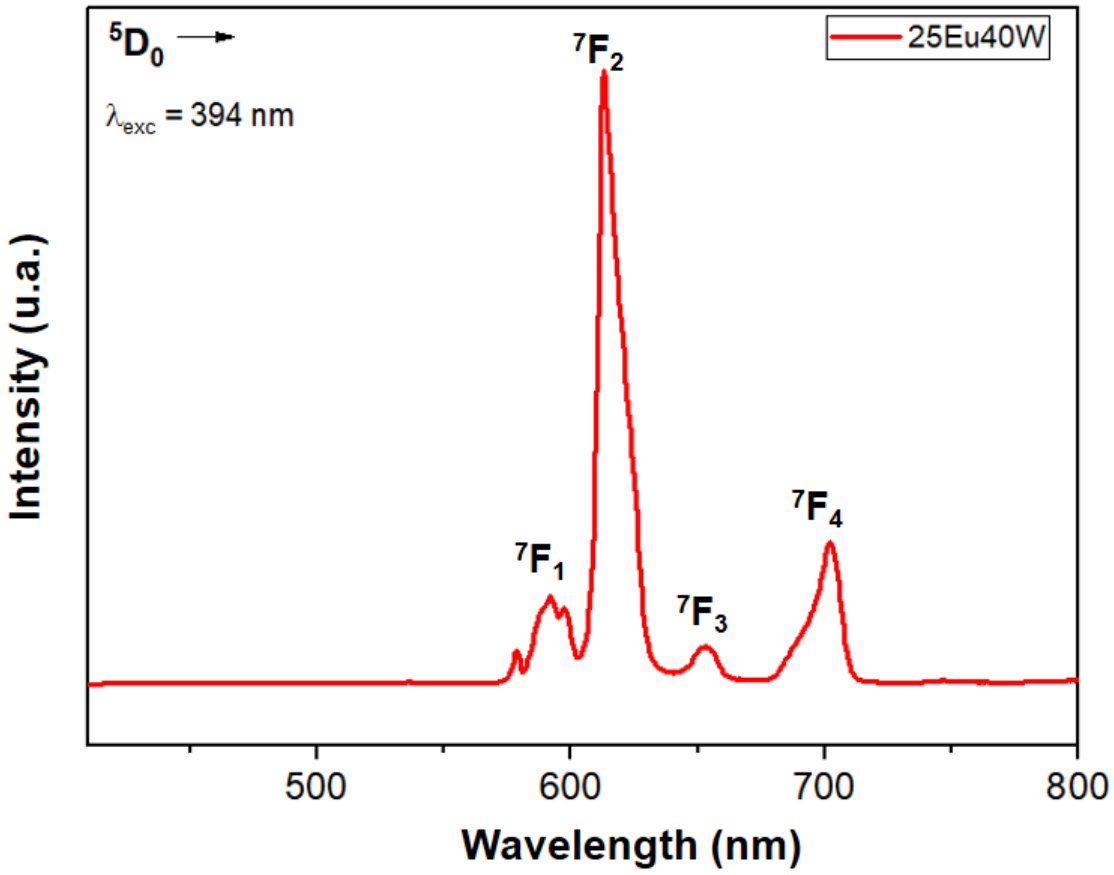

Figure 57. PL spectra for Eu40W sample, with the 4f-4f transitions from the excited level $^5D_0$, corresponding to the Eu^{3+} ion. λ_{exc} = 394 nm. (Own authorship).

Figure 58 shows the normalized photoluminescence (PL) spectra for the samples with Terbium, λ_{exc} = 379 nm, corresponding to 4f-4f transitions with excitation in 379 nm, at 415 ($^5D_3$→$^5F_5$), 440 ($^5D_3$→$^5F_4$), 487 ($^5D_4$→$^7F_6$), 543 ($^5D_4$→$^7F_5$), 583 ($^5D_4$→$^7F_4$), 621 ($^5D_4$→$^7F_3$), 652($^5D_4$→$^7F_2$), 667 ($^5D_4$→$^7F_1$) and 679 nm ($^5D_4$→$^7F_0$)[25,26].

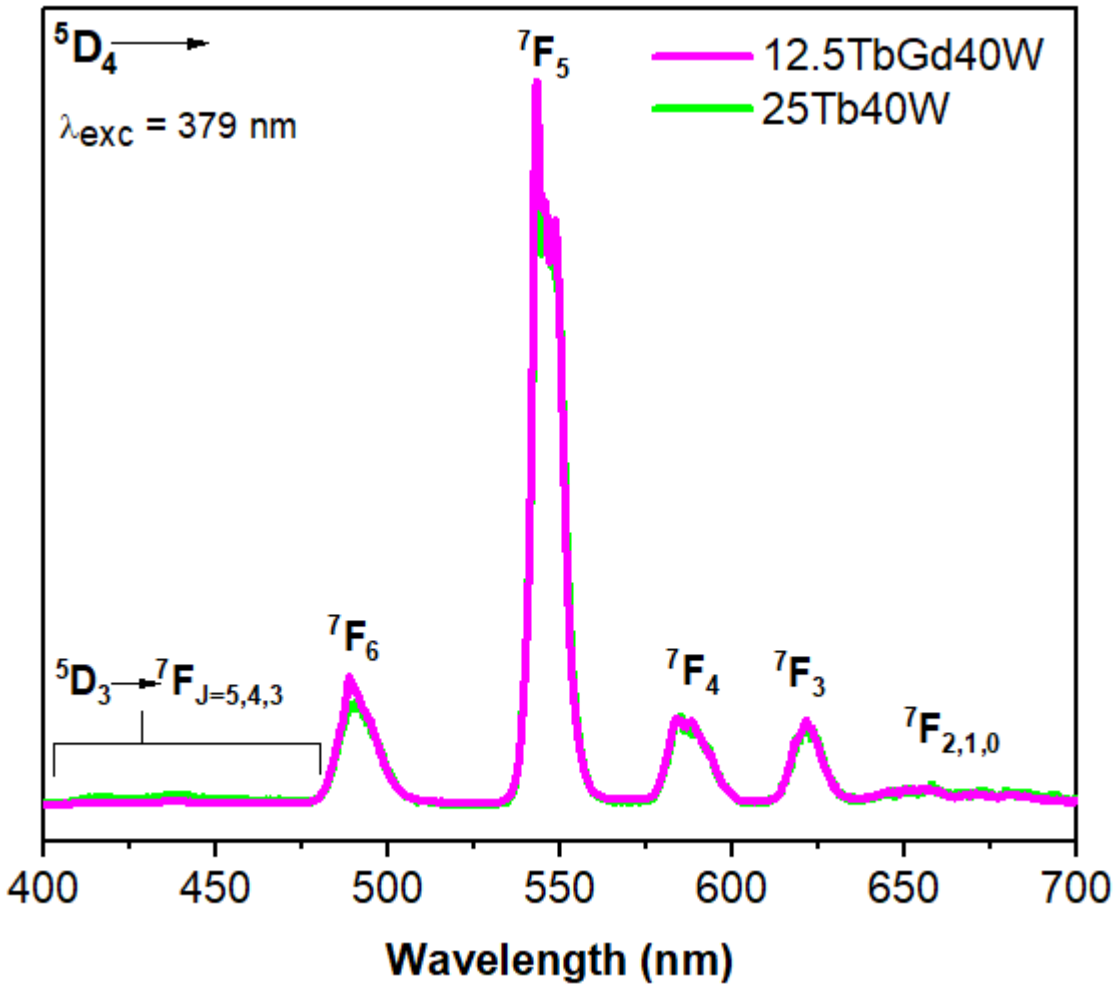

Figure 58. PL spectra for the 12.5TbGd40W sample, showing the transitions from the excited level $^5D_4$ corresponding to the Tb^{3+} ion. λ_{exc} = 379 nm. (Own authorship).

25Dy40W sample (λ_{exc} = 352 nm) Figure 59, many visible emission spectra perform the similar pattern of the main emission bands centering at 481 nm, 575 nm, 661 nm and 752 nm even under different excitation wavelengths. These bands attribute, respectively, to the Dy^{3+} transitions of $^4F_{9/2}$ to $^6H_{15/2}$, $^6H_{13/2}$, $^6H_{11/2}$ and $^6H_{9/2}$[27].

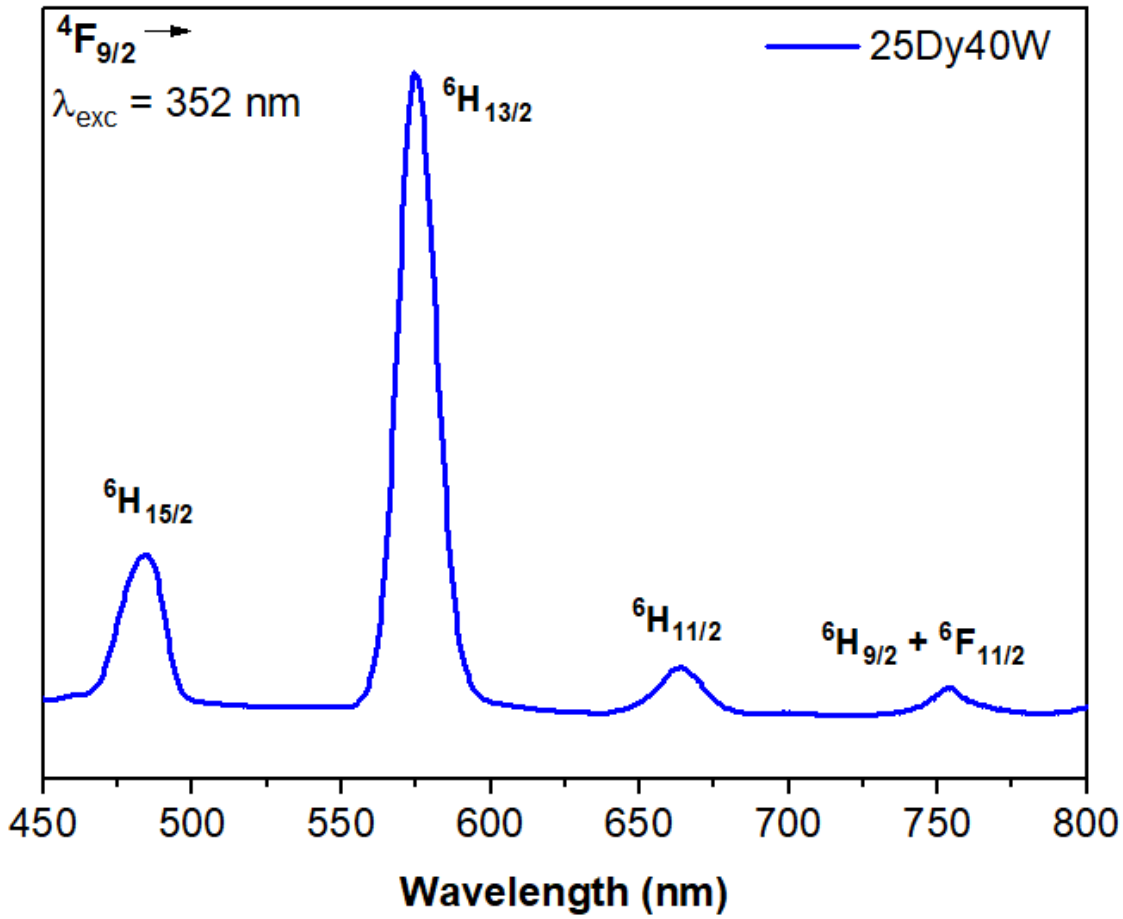

Figure 59. PL spectra for the 25Dy40W sample, showing the transitions from the excited level $^5F_{9/2}$ corresponding to the Dy^{3+} ion. λ_{exc} = 352 nm. (Own authorship).

Finally in Figure 60, the 25Ho40W sample presented the characteristic transitions 4f-4f for the Ho^{3+} ion, with the transitions 485, 541, 660, 756, 790, 982 and 1200 nm in PL spectra (λ_{exc} = 455 nm), can be assigned to $^5F_3 \rightarrow {}^5I_8$, $^5(F_4 + S_2) \rightarrow {}^5I_8$, $^5F_5 \rightarrow {}^5I_8$, $^5S_2 \rightarrow {}^5I_7$, $^5F_2 \rightarrow {}^5I_6$, $^5I_5 \rightarrow {}^5I_8$, $^5I_6 \rightarrow {}^5I_8$, respectively transitions[28]. Figure 57 shows an energy level diagram of Ln^{3+} ions.

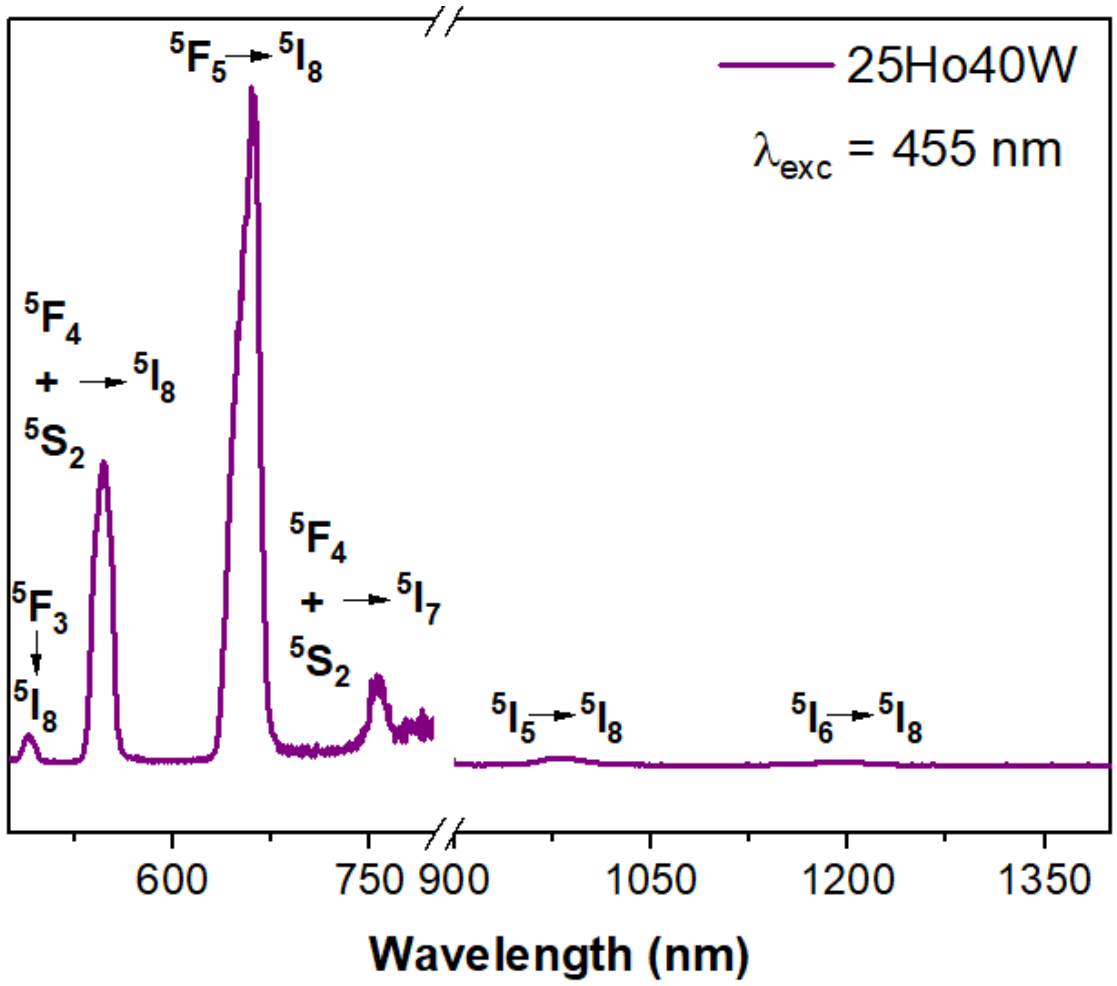

Figure 60. PL spectra for the 25Ho40W sample, showing the transitions corresponding to the Ho^{3+} ion. λ_{exc} = 455 nm. (Own authorship).

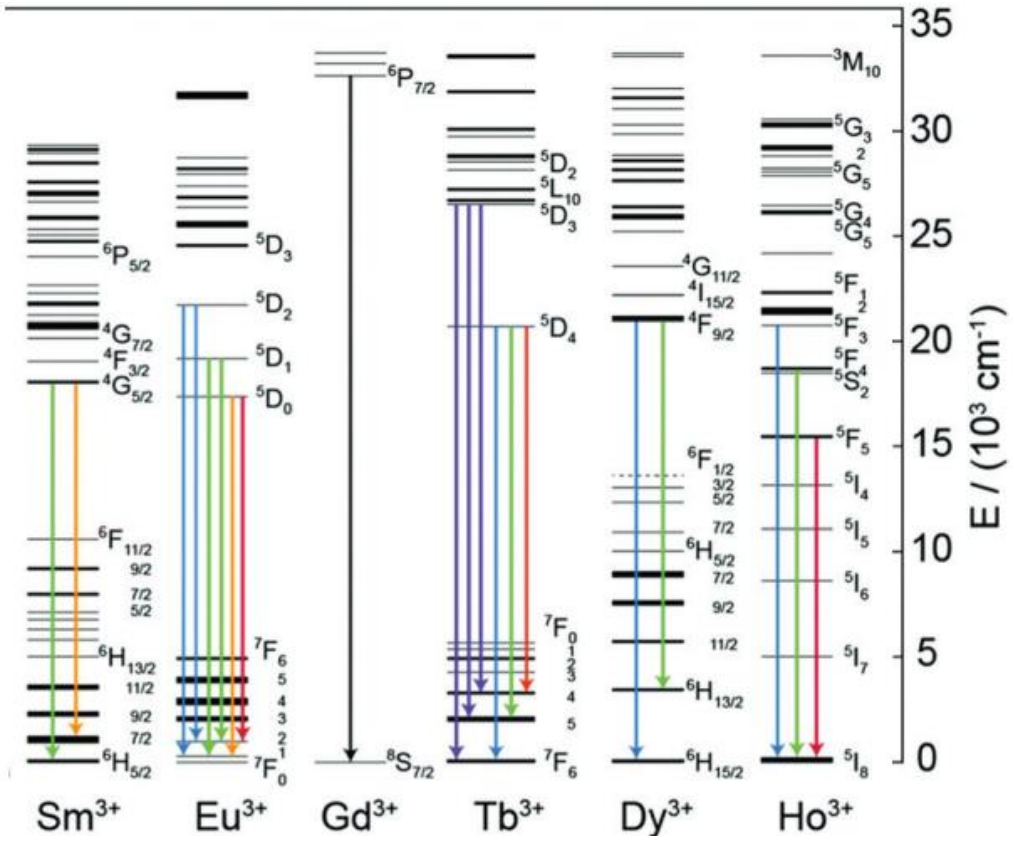

Figure 61. Partial energy level diagram of samples Ln^{3+} ions and the radiative transitions emissions [[29]].

8. Refractive index.

The refractive indices (n), from the visible to near-infrared regions, are shown in Figure 62 for samples containing the lanthanides ions studied here. The maximum n obtained was 1.904±0.005 at 532 nm, for the sample 12.5TbGd40W. The values are summarized on the Table 11. Due to the absorptions related to the respective ions, some measurements in the available lasers could not be carried out.

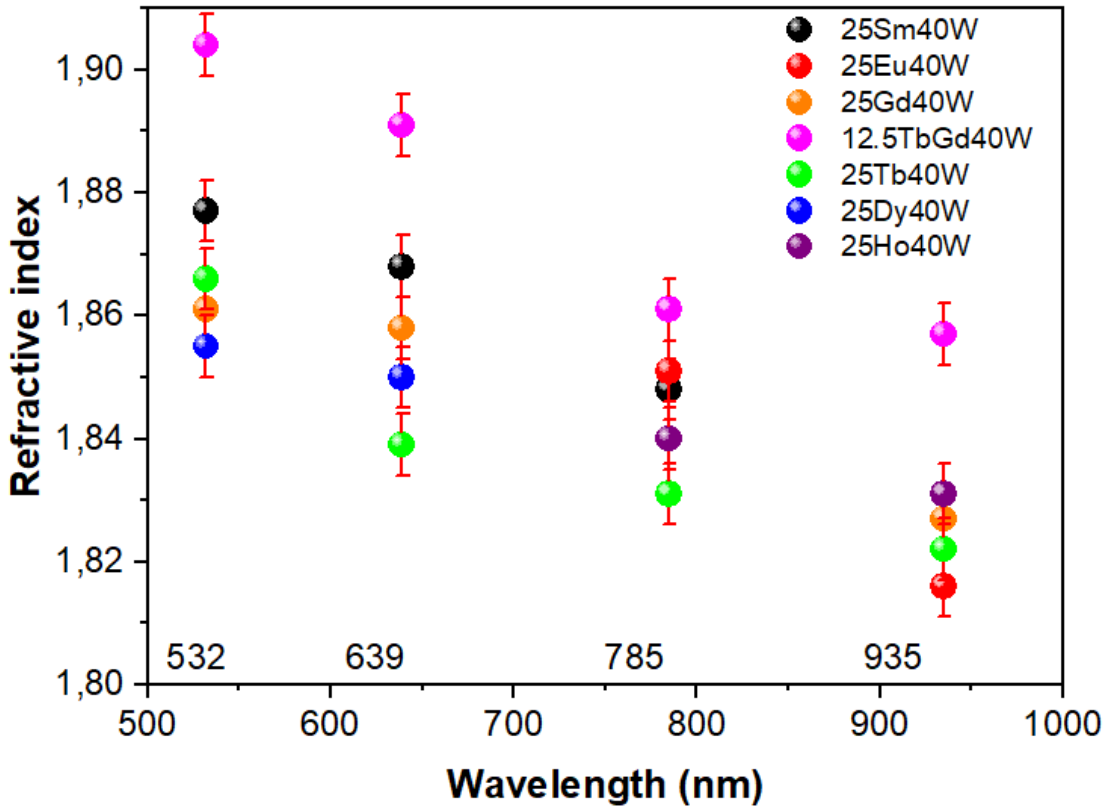

Figure 62. Refractive index for Ln trivalent ions glass samples. (Own authorship).

Table 11. Refractive index values for samples with different trivalent lanthanide ions for different laser wavelengths (error = ±0.005).

Sample	Refractive index (n ± 0.005)			
	532 nm	639 nm	785 nm	935 nm
25Sm40W	1.877	1.868	1.848	--
25Eu40W	--	--	1.851	1.816
25Gd40W	1.861	1.858	1.831	1.827
12.5TbGd40W	1.904	1.891	1.861	1.857
25Tb40W	1.866	1.839	1.831	1.822
25Dy40W	1.855	1.850	--	--
25Ho40W	--	--	1.840	1.831

(Own authorship).

9. Magnetic analysis

Figure 63 shows the magnetic variation of measured susceptibility (χ_M) by temperature, showing asymptotic aspect when the temperature tends to 0 K, characteristic behavior for paramagnetic materials. The measured susceptibility also corresponds to the sum of the diamagnetic and paramagnetic components. The

diamagnetic susceptibility (χ_{dia}) was calculated according to G. Bain and J. Berry[30] , and their results subtracted from the χM, leaving the values for paramagnetic susceptibility (χ_{para}).

Table 12 presents the values for the quantum numbers, the Curie constants, targeted, probed, and the % error of the Ln_2O_3 concentration, the Weiss temperature, and χ_{dia}, for each sample. The negative values of θ suggest passible antiparallel aligned spins i.e. that the molecular magnetic field (HM) opposes the applied magnetic field (H), causing misalignment of elementary moments with H and a tendency to decrease with χ_{para}.

The probes showed that the sample weighing, and synthesis error was considerably low and 25Gd40W, 25Tb40W, 25Dy40W and 25Ho40W samples showed high Curie constant values, showing that they are great candidates for magnetic applications.

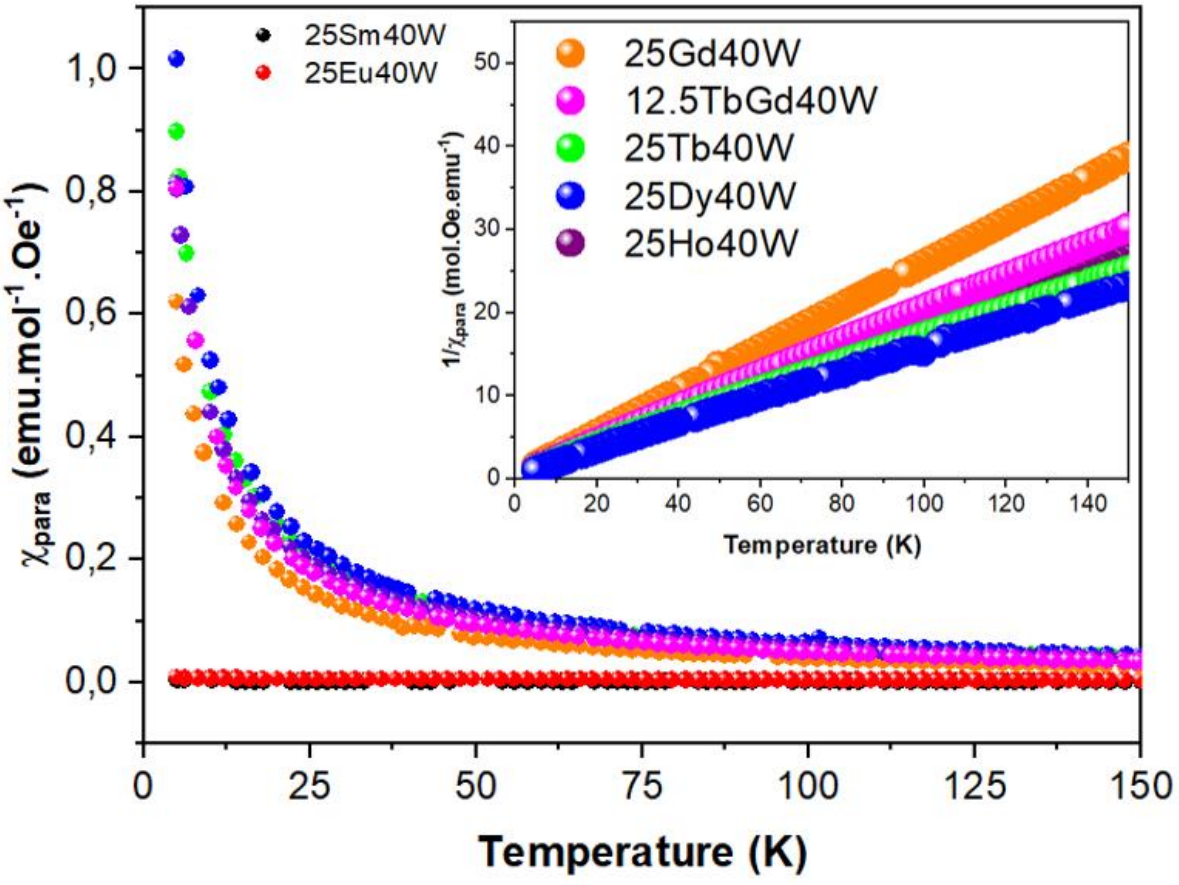

Figure 63. Temperature dependence of the paramagnetic molar susceptibility for all 25Ln40W glass samples. Inset shown the inverse of susceptibility ($1/\chi_{para}$) versus temperature, varying linearity and follow the Curie-Weiss law. (Own authorship).

Table 12. Fundamental level of Ln3+, spin angular momentum (S), orbital angular momentum (L), total angular momentum (J), diamagnetic susceptibility (χdia), Weiss temperature (θ), Curie constant (C) in two different units and Ln_2O_3 % mol for each 25Ln40W samples.

Sample	Fundamental level ion trivalent (Ln^{3+})	S	L	J	χ_{dia} (x 10^{-6} emu.mol^{-1})	θ (K)	C (emu.K.Oe.mol^{-1})	C (A.m^2.T^{-1}.mol^{-1})	[Ln_2O_3] %mol targeted	probed	% error
25Sm40W	$^6H_{5/2}$	5	5/2	5/2	-51.34	X	X	X	25	X	X
25Eu40W	$^7F_0$	3	3	0	-51.34	X	X	X	25	X	X
25Gd40W	$^8S_{7/2}$	0	7/2	7/2	-51.34	-1.54	3.90	39.04	25	24.79	0.85
12.5TbGd40W	*	*	*	*	-51.09	-3.04	5.03	50.32	12.5*	12.78*	-2.19
25Tb40W	$^7F_6$	3	3	6	-50.84	-6.51	6.25	62.64	25	26.45	-5.78
25Dy40W	$^6H_{15/2}$	5	5/2	15/2	-50.84	-4.11	6.58	65.82	25	23.23	7.62
25Ho40W	$^5I_8$	6	2	8	-50.84	-4.49	5.76	57.60	25	20.48	22.06

*: for the 12.5TbGd40W sample, the quantum number values of both Gd^{3+} and Tb^{3+} were considered, in addition to the 12.5 mol% concentration targeted for each Tb_2O_3 and Gd_2O_3. (Own authorship).

Due to the magnetic peculiarities of Europium and Samarium, resulting from their J = 0 for Eu^{3+} and Sm^{2+}, they do not follow Curie's Law, and it was not possible to determine their constants or their probe concentration[31,32].

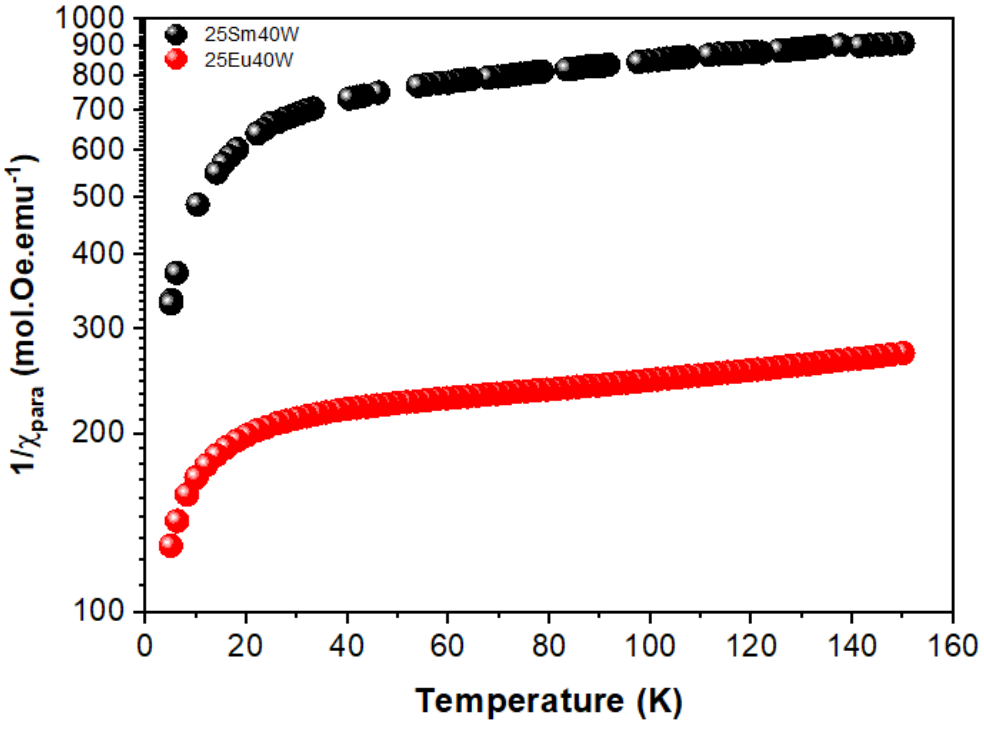

Figure 64. Inverse of susceptibility by temperature for the samples 25Sm40W and 25Eu40W.

10. Partial Conclusions of this Chapter.

The basic study of this vitreous system containing different lanthanides is interesting as it expands the knowledge about magneto-optical materials. In this chapter, glasses containing high concentrations of lanthanide ions were produced, mimicking the 25Tb40W composition of Chapter III.

Samples containing Nd, Tm and Er crystallizes during cooling, indicating a difference in solubility of these ions for this system under these preparation conditions, due to the difference in size between these ions compared to Tb. For samples containing Sm, Eu, Tb, Dy and Ho, XRD measurements confirmed the formation of the amorphous phase, while the glass transitions were verified by DSC analysis.

In the thermal analysis we can observe that Tg tends to decrease while the thermal stability parameter, ΔT, tends to increase, for smaller ionic radii (Sm→Ho). The density and effective concentration of Ln^{3+} ions also increase for smaller radii.

Going to the structural analysis, the Raman spectroscopy did not show major differences between these samples and 25Tb40W, indicating that the general structure of the glass barely changed with the presence of different lanthanide ions. Even the absorptivity, obtained by FTIR by specular reflectance, did not show great changes compared to the sample containing the Tb^{3+} ion.

Optical and luminescent analyzes revealed characteristic transitions for each ion, with transparency windows in the visible and the Near IR going up to 3000 nm depending on the glass composition. The measured refractive indices were greater than 1.8, making them excellent materials for photonic and magneto-optical applications.

Finally, the magnetic analysis showed that the target and probed concentrations are very close, with paramagnetic behavior, with a slight antiparallel alignment of the spins.

Magneto-optical measurements are being carried out to determine Verdet constant values.

References in this Chapter

[1] R.E. Newnham, M.J. Redman, R.P. Santoro, Crystal Structure of Yttrium and Other Rare-Earth Borates, J. Am. Ceram. Soc. 46 (1963) 253–256. https://doi.org/10.1111/j.1151-2916.1963.tb11721.x.

[2] E.M. Levin, R.S. Roth, J.B. Martin, Polymorphism of ABOs Type Rare Earth Borates, Am. Mineral. 46 (1961) 1030–1055.

[3] H. Yang, Z. Zhu, Magneto-optical glass mixed with Tb^{3+} ions: High Verdet constant and luminescence properties, J. Lumin. 231 (2021) 117804. https://doi.org/10.1016/j.jlumin.2020.117804.

[4] J.A. Duffy, A review of optical basicity and its applications to oxidic systems, Geochim. Cosmochim. Acta. 57 (1993) 3961–3970. https://doi.org/10.1016/0016-7037(93)90346-X.

[5] J.A. Duffy, Optical basicity: A practical acid-base theory for oxides and oxyanions, J. Chem. Educ. 73 (1996) 1138–1142. https://doi.org/10.1021/ed073p1138.

[6] X. Zhao, X. Wang, H. Lin, Z. Wang, Electronic polarizability and optical basicity of lanthanide oxides, Phys. B Condens. Matter. 392 (2007) 132–136. https://doi.org/10.1016/j.physb.2006.11.015.

[7] V. Dimitrov, T. Komatsu, Classification of simple oxides: A polarizability approach, J. Solid State Chem. 163 (2002) 100–112. https://doi.org/10.1006/jssc.2001.9378.

[8] L. Aleksandrov, T. Komatsu, R. Iordanova, Y. Dimitriev, Raman spectroscopic study of structure of $WO_3La_2O_3B_2O_3$ glasses with no color and crystallization of $LaBWO_6$, Opt. Mater. (Amst). 34 (2011) 201–206. https://doi.org/10.1016/j.optmat.2011.08.002.

[9] G. Poirier, Y. Messaddeq, S.J.L. Ribeiro, M. Poulain, Structural study of tungstate fluorophosphate glasses by Raman and X-ray absorption spectroscopy, J. Solid State Chem. 178 (2005) 1533–1538. https://doi.org/10.1016/j.jssc.2004.10.032.

[10] J.F.V.L. Munhoz, S.H. Santagneli, M. de Oliveira, A.C.M. Rodrigues, H. Eckert, M. Nalin, Glasses in the $NaPO_3$-WO_3-NaF ternary system: preparation, physical properties and structural studies, J. Non. Cryst. Solids. 505 (2019) 379–389. https://doi.org/10.1016/J.JNONCRYSOL.2018.10.043.

[11] G. Poirier, M. Poulain, Y. Messaddeq, S.J.L. Ribeiro, New tungstate fluorophosphate glasses, J. Non. Cryst. Solids. 351 (2005) 293–298. https://doi.org/10.1016/j.jnoncrysol.2004.11.017.

[12] G. Poirier, F.C. Cassanjes, Y. Messaddeq, S.J.L. Ribeiro, A. Michalowicz, M. Poulain, Local order around tungsten atoms in tungstate fluorophosphate glasses by X-ray absorption spectroscopy, J. Non. Cryst. Solids. 351 (2005) 3644–3648.

https://doi.org/10.1016/j.jnoncrysol.2005.08.038.

[13] A.K. Yadav, P. Singh, A Review of Structure of Oxide Glasses by Raman Spectroscopy, RSC Adv. 5 (2015) 67583–67609. https://doi.org/https://doi.org/10.1039/C5RA13043C.

[14] C.P.E. Varsamis, N. Makris, C. Valvi, E.I. Kamitsos, Short-range structure, the role of bismuth and property-structure correlations in bismuth borate glasses, Phys. Chem. Chem. Phys. 23 (2021) 10006–10020. https://doi.org/10.1039/d1cp00301a.

[15] E.I. Kamitsos, A.P. Patsis, M.A. Karakassides, G.D. Chryssikos, Infrared reflectance spectra of lithium borate glasses, J. Non. Cryst. Solids. 126 (1990) 52–67. https://doi.org/10.1016/0022-3093(90)91023-K.

[16] E.I. Kamitsos, A.P. Patsis, G.D. Chryssikos, Infrared reflectance investigation of alkali diborate glasses, J. Non. Cryst. Solids. 152 (1993) 246–257. https://doi.org/10.1016/0022-3093(93)90258-Y.

[17] B. Topper, N.S. Tagiara, A. Herrmann, E.I. Kamitsos, D. Möncke, Yttrium and rare-earth modified lithium orthoborates: Glass formation and vibrational activity, J. Non. Cryst. Solids. 575 (2022). https://doi.org/10.1016/j.jnoncrysol.2021.121152.

[18] S. Sasaki, A. Masuno, K. Ohara, Y. Yanaba, H. Inoue, Y. Watanabe, S. Kohara, Structural Origin of Additional Infrared Transparency and Enhanced Glass-Forming Ability in Rare-Earth-Rich Borate Glasses without B-O Networks, Inorg. Chem. 59 (2020) 13942–13951. https://doi.org/10.1021/acs.inorgchem.0c01567.

[19] W.T. Carnall, P.R. Fields, K. Rajnak, Electronic Energy Levels of the Trivalent Lanthanide Aquo Ions. I. Pr^{3+}, Nd^{3+}, Pm^{3+}, Sm^{3+}, Dy^{3+}, Ho^{3+}, Er^{3+}, and Tm^{3+}, J. Chem. Phys. 49 (1968) 18–21.

[20] W.T. Carnall, P.R. Fields, K. Rajnak, Electronic Energy Levels of the Trivalent Lanthanide Aquo Ions. IV. Eu^{3+}, J. Chem. Phys. 49 (1968) 18–21.

[21] K. Binnemans, Interpretation of europium(III) spectra, Coord. Chem. Rev. 295 (2015) 1–45. https://doi.org/10.1016/j.ccr.2015.02.015.

[22] A.K. Mandal, R. Sen, Optimization of melting parameters and minimizing OH content in SiO_2-B_2O_3-Na_2O-BaO glass system in microwave heating, Int. J. Appl. Glas. Sci. 10 (2019) 83–91. https://doi.org/10.1111/ijag.12439.

[23] W.T. Carnall, P.R. Fields, K. Rajnak, Electronic Energy Levels of the Trivalent Lanthanide Aquo Ions. III. Tb^{3+} , J. Chem. Phys. 49 (1968) 4447–4449. https://doi.org/10.1063/1.1669895.

[24] M. Shoaib, G. Rooh, R. Rajaramakrishna, N. Chanthima, H.J. Kim, S. Tuscharoen, J. Kaewkhao, Physical and luminescence properties of samarium doped oxide and oxyfluoride phosphate glasses, Mater. Chem. Phys. 229 (2019) 514–522. https://doi.org/10.1016/j.matchemphys.2019.03.016.

[25] D.F. Franco, R.G. Fernandes, J.F. Felix, V.R. Mastelaro, H. Eckert, C.R.M. Afonso, Y. Messaddeq, S.H. Messaddeq, S. Morency, M. Nalin, Fundamental studies of magneto-optical borogermanate glasses and derived optical fibers containing Tb^{3+}, J. Mater. Res. Technol. 11 (2021) 312–327. https://doi.org/10.1016/j.jmrt.2021.01.010.

[26] T.A. Lodi, J.F.M. dos Santos, G. Galleani, L.G. Jacobsohn, T. Catunda, A.S.S. de Camargo, Promising Tb^{3+}-doped gallium tungsten-phosphate glass scintillator: Spectroscopy, energy transfer and UV/X-ray sensing, J. Alloys Compd. 904 (2022) 164016. https://doi.org/10.1016/j.jallcom.2022.164016.

[27] V. Himamaheswara Rao, P. Syam Prasad, M. Mohan Babu, P. Venkateswara Rao, T. Satyanarayana, S. Luís F., N. Veeraiah, Spectroscopic studies of Dy^{3+} ion doped tellurite glasses for solid state lasers and white LEDs, Spectrochim. Acta - Part A Mol. Biomol. Spectrosc. 188 (2018) 516–524. https://doi.org/10.1016/j.saa.2017.07.013.

[28] E.W. Barrera, M.C. Pujol, J.J. Carvajal, X. Mateos, R. Solé, J. Massons, A. Speghini, M. Bettinelli, C. Cascales, M. Aguiló, F. Díaz, White light upconversion in Yb-sensitized (Tm, Ho)-doped $KLu(WO_4)_2$ nanocrystals: The effect of Eu incorporation, Phys. Chem. Chem. Phys. 16 (2014) 1679–1686. https://doi.org/10.1039/c3cp53847h.

[29] M. Safdar, A. Ghazy, M. Lastusaari, M. Karppinen, Lanthanide-based inorganic-organic hybrid materials for photon-upconversion, J. Mater. Chem. C. 8 (2020) 6946–6965. https://doi.org/10.1039/d0tc01216e.

[30] G.A. Bain, J.F. Berry, Diamagnetic corrections and Pascal's constants, J. Chem. Educ. 85 (2008) 532–536. https://doi.org/10.1021/ed085p532.

[31] B. S. Hopkins, Europium, a Rare Member of the Rare Earth Group, (1934) 49–56.

[32] S. Mugiraneza, A.M. Hallas, Tutorial: a beginner's guide to interpreting magnetic susceptibility data with the Curie-Weiss law, Commun. Phys. 5 (2022). https://doi.org/10.1038/s42005-022-00853-y.

CHAPTER V – Characterization and study of properties of the $SbPO_4$-ZnO-PbO-MnO System

Chapter V - Study of the structural and magnetic properties of the $SbPO_4$–ZnO-PbO–MnO System

1. Samples

The Table 13 summarizes the chemical compositions studied in the chapter, as well as the molar mass and characteristic temperatures. Samples with Mn are yellow to yellow-orange colored as observed in Figure 65. Changes in coloration comes specially from the conversion of Mn^{2+} to Mn^{3+}, which will be discussed below. The cationic compositions were not added since the Mn/O ratio is 1:1. The sample with 40 mol % (SZP40Mn) presented crystalline phase precipitation during thermal quenching of MnO and, therefore, it will not be further discussed in this work.

Table 13. Chemical compositions and characteristic temperatures of the glasses studied in this work. The thermal stability parameter (ΔT) and the refractive index (λlaser = 532 nm) of the samples are also shown.

Acronym	**Nominal compositions (mol %)**				***M*** ***(g.mol^{-1})***	***Tg*** **(±3 ºC)**	***Tx*** **(±3 ºC)**	***Tp*** **(±3 ºC)**	**ΔT (±3 ºC)**
	$SbPO_4$	***ZnO***	***PbO***	***MnO***					
SZP0Mn	70	10	20	0	204.49	371	482	576	111
SZP10Mn	63	9	18	10	191.14	387	523	590	136
SZP20Mn	56	8	16	20	177.78	410	553	591	143
SZP30Mn	49	7	14	30	164.43	432	552	594	120
SZP40Mn	42	6	12	40	151.07	-	-	-	-

(Own authorship).

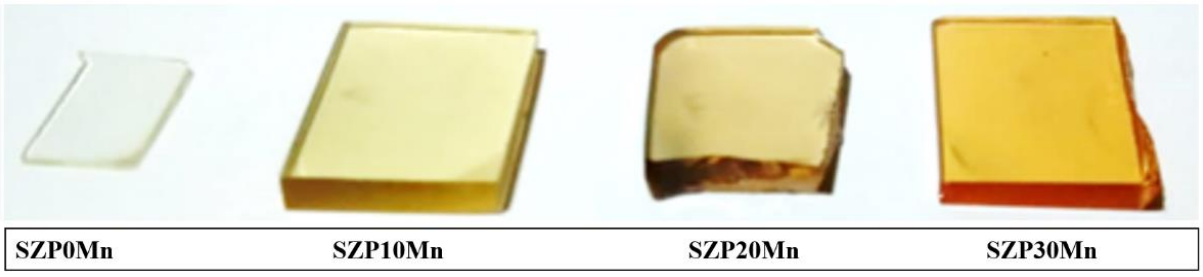

Figure 65. Photography of the glasses containing MnO studied in this work. (Own authorship).

An interesting property of such glasses is the fact that they are attracted by a magnet. This effect comes from the high paramagnetic moment of Mn^{2+} ions and this property will be discussed in more details in the optical section. In Figure 66 it is shown a sequence of photographs where it is possible to see that after the contact with the Nd-based magnet the glass remains attached to it been supported up to 5 and 10 cm above the surface. In the Figure, the sample used was the SZP30Mn, but the effect can be observed with all samples containing manganese. The attraction increases as a function of the MnO content. The reference sample SZP0Mn is not attracted by the magnet.

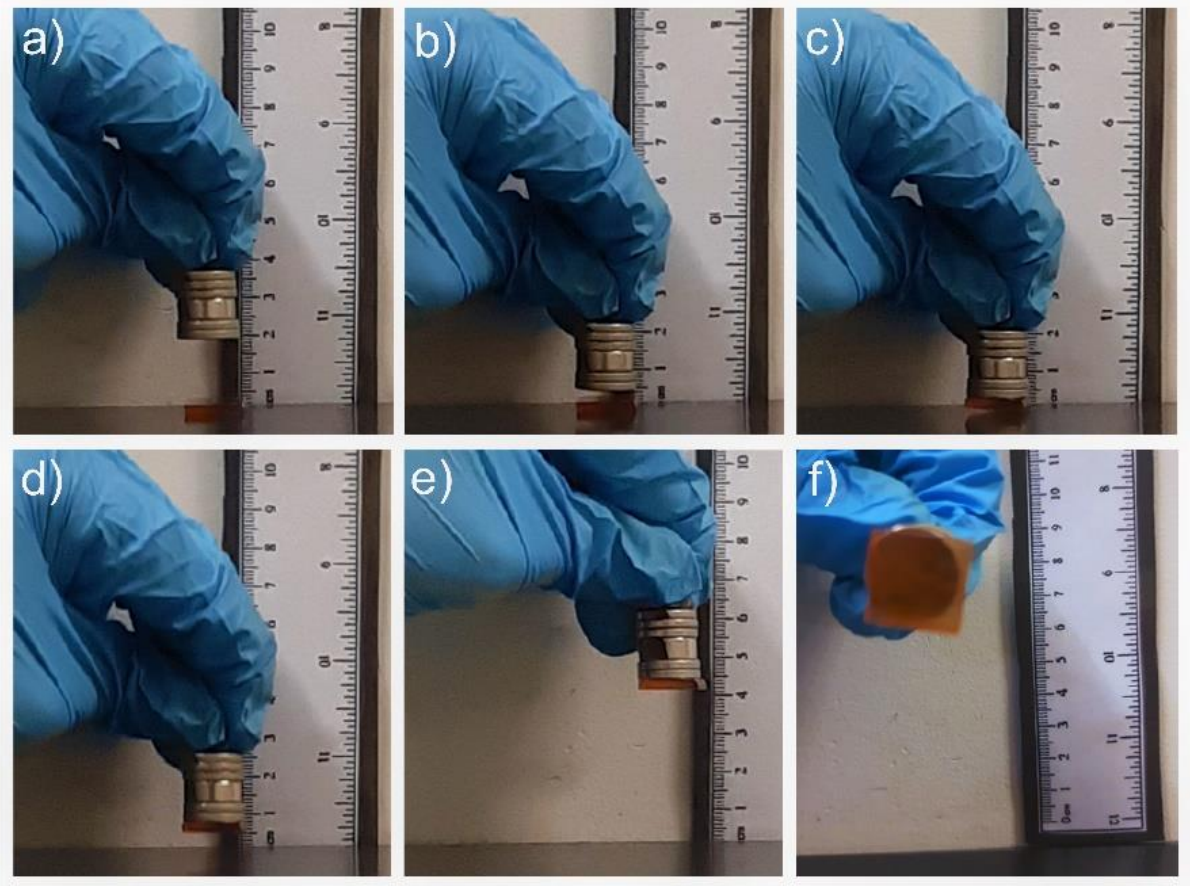

Figure 66. Sequence of photographs showing the attractive response of the glasses to the presence of a Nd-based magnet. a) and b) represent the approximation of the magnet, while the sequence after is related to the suspension of the glass piece (from c to f). (Own authorship).

2. XRD

To confirm the amorphous character of the samples or the presence of crystalline phases in the samples, X-ray diffraction data were obtained from the samples and are shown in Figure 67. As expected, the diffractogram files present only the the halos around 2θ ~30 °, characteristic of amorphous materials and validate the formation of the glassy phase to samples containing up to 30 mol % of MnO.

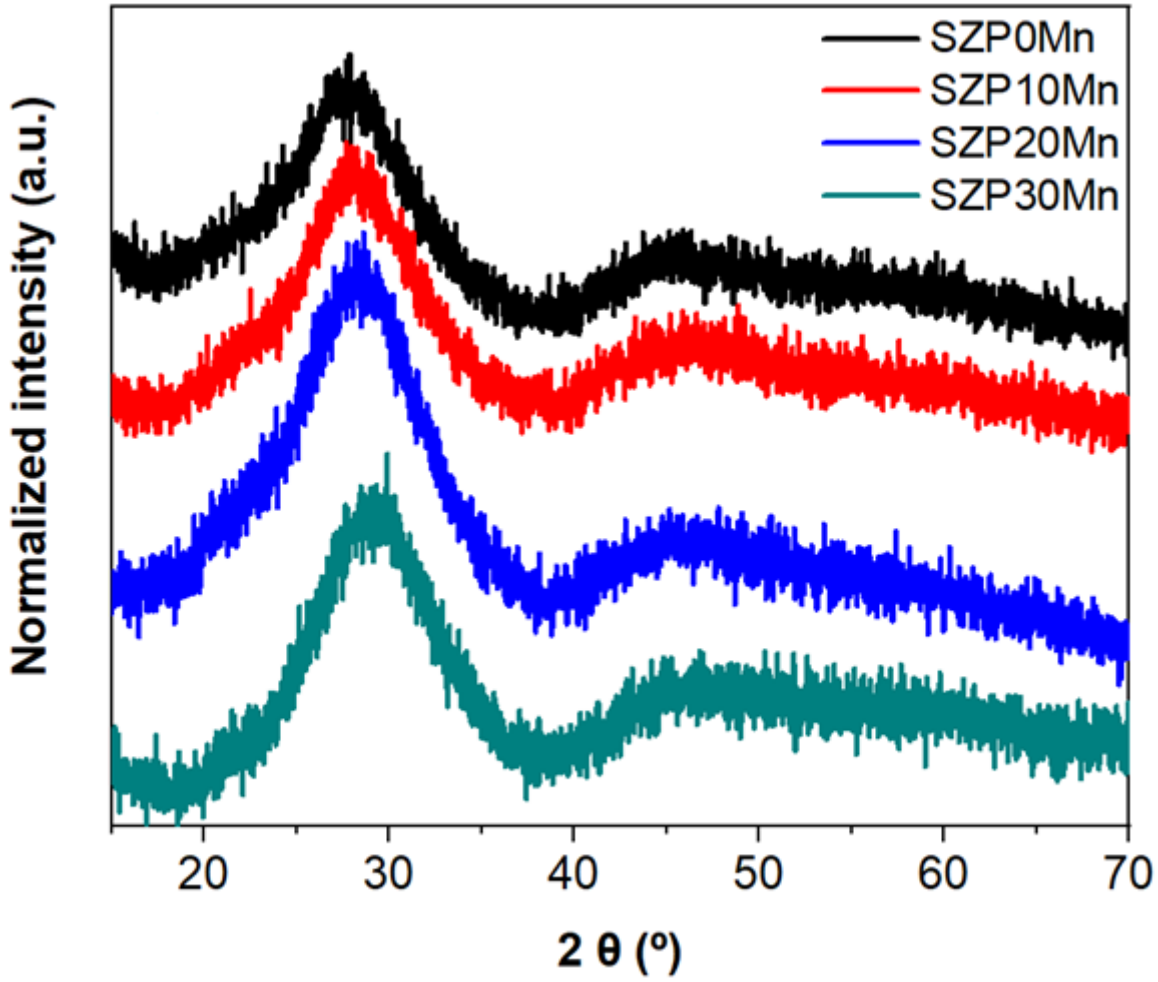

Figure 67. X-ray diffraction data for SZPxMn samples. (Own authorship).

3. Thermal analysis

Figure 64 presented the DSC curves, with the characteristic temperatures of the glasses are summarized in Table 15. Firstly, the addition of MnO increases the glass transition temperatures, Tg, from 371 °C for the sample SZP0Mn to 432 °C for

sample SZP30Mn, suggesting an increase in glass matrix connectivity. In detail, the initial increasing in Tg may be related to formation of a more complex structure by mixing the backbone of the antimony orthophosphate with the octahedral units of MnO6. As observed, the influence of the MnO on Tg is almost linear, however, Tx do not follow the same behavior and, as consequence, the stability parameter initially increases (sample SZP20Mn) and stabilize for sample SZP30Mn. This, linked to the decrease in the width of the crystallization peak, which evolute to sharper and with higher amplitude, indicates that the insertion of Mn in the structure guarantees a better connectivity of the glassy matrix until the point of inducing crystallization, crystallizing the phase simultaneously. The formation of more stable crystalline phases and is directly related to the difficulty of forming a pure glassy matrix for the sample with 40mol% of the MnO. This behavior will be discussed based on the FTIR and Raman spectra for all samples.

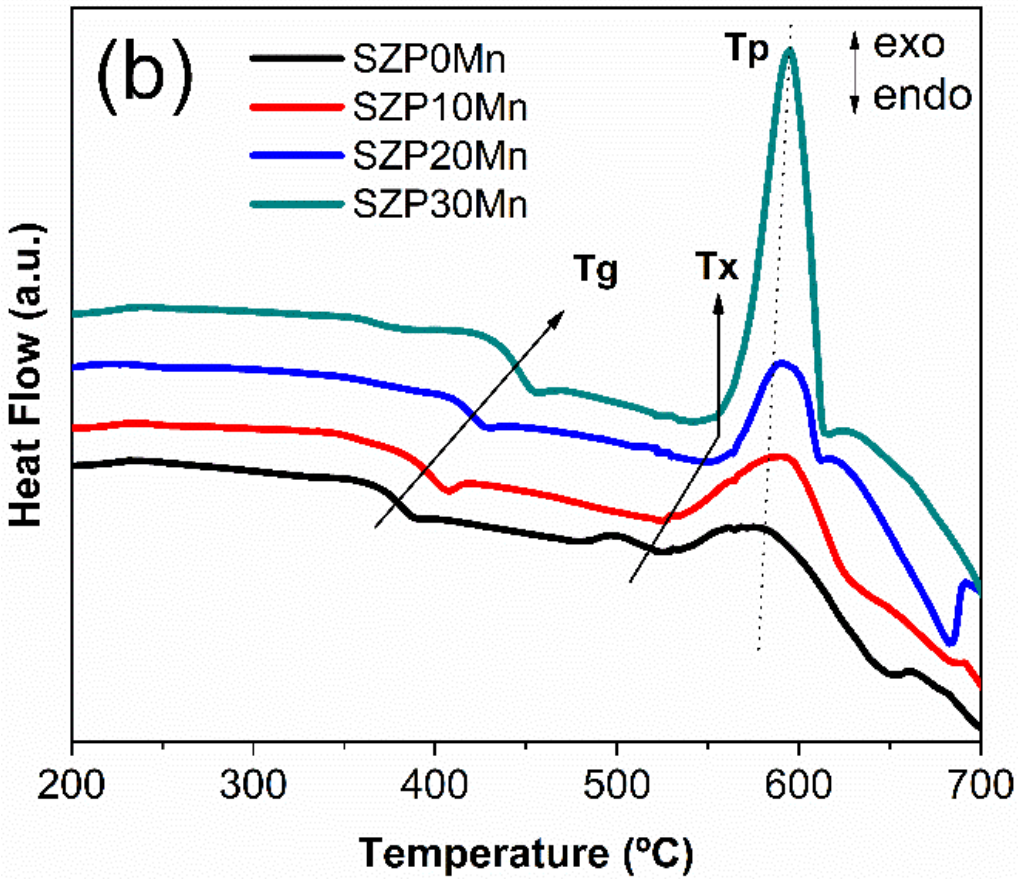

Figure 68. DSC curves for each SZPxMn sample, with arrow indicating the variation of Tg and Tx. (Own authorship).

4. Raman scattering and Infrared spectroscopy

In Figure 69 are shown the Raman spectra of the glasses. Bands at 1135 and 978 cm^{-1} are assigned to asymmetrical stretching (ν_{as}) PO_4 and symmetrical stretching (ν_s) PO_4 (P-O^- (Q^0)), respectively. Bands at 1058, 617, 559, 459 and 404 cm^{-1} are assigned to ν_s P-O^-, ν_{as} Sb–O–P, ν_s Sb–O, symmetrical bending (δ_s) O–P–O and assymetrical bending (δ_{as}) O–Sb–O, respectively. The absorption in the range from 350-200 cm^{-1} was assigned to strong coupling between different bending group modes O–P–O, O–Sb–O, Sb–O–P, [1–4]. As verified in previous works, the band at 850 cm^{-1} (668 nm) is assigned to the Mn^{2+} luminescence in octrahedral sites, referring to the transition $^4T_1 \rightarrow {}^6A_1$ (S)[3,5]. Table 14 shows the main assigned bands, in Raman and IR.

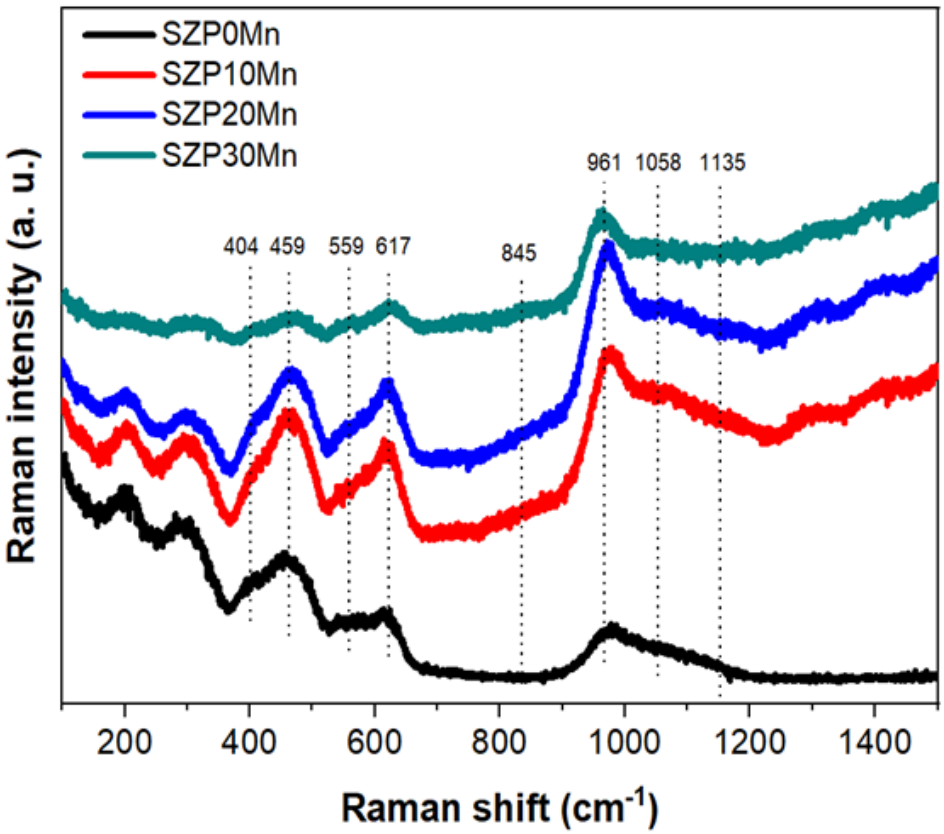

Figure 69. Raman scattering spectra of the samples SZPxMn with the main assignments. (Own authorship).

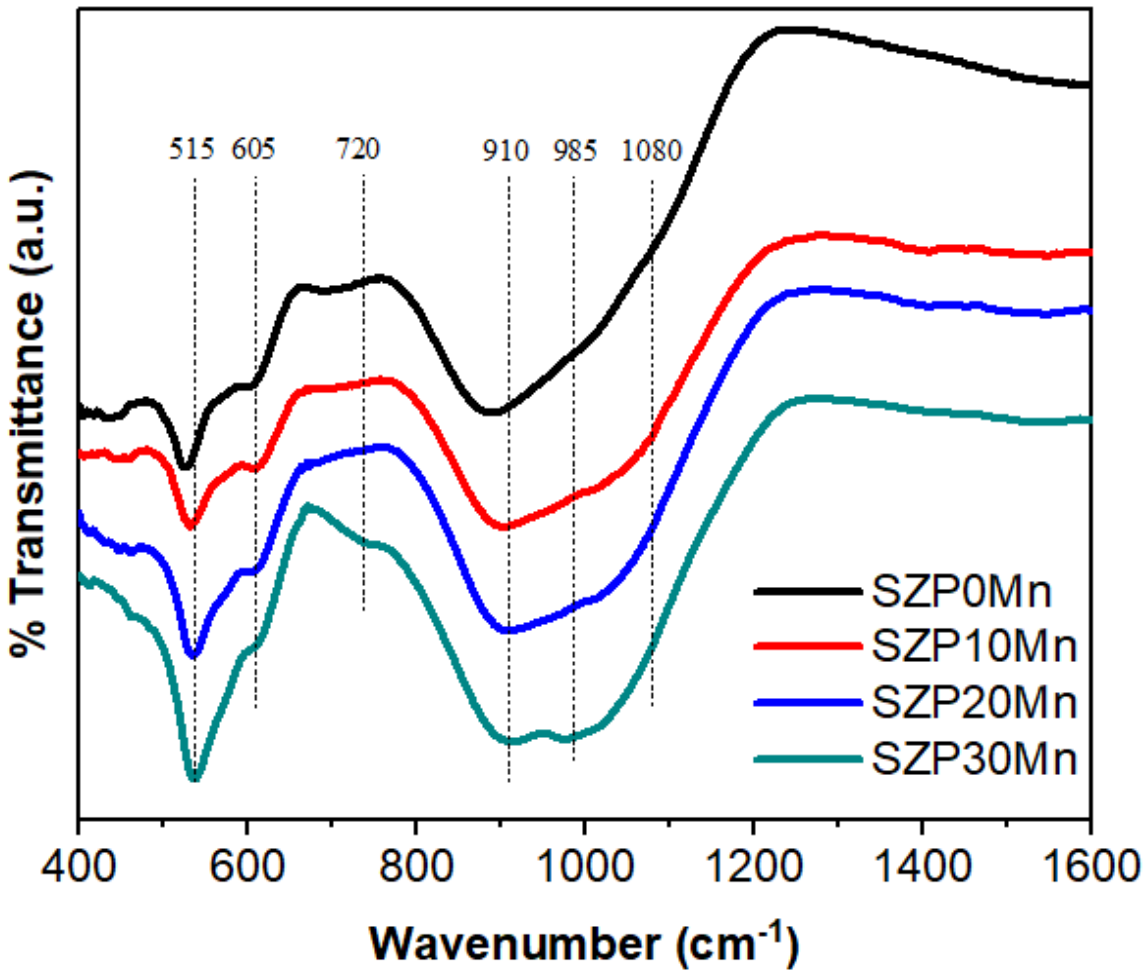

Figure 70. Infrared spectrum for each sample of the SZPxMn system, with the main bands marked. (Own authorship).

Figure 70 presents the infrared spectra of the glass samples in the SZPxMn system. As already observed in previous works, the most prominent bands arise from $SbPO_4$ and the assignments are summarized in Table 15. The bands at 515, 605, 720, 910, 985 and 1080 cm^{-1} can be assigned to δ_s Sb, ν_{as} Sb, ν_s Sb, δ P-O-P, ν_s PO_4 and ν_{as} PO_4, respectively [1,2,6]. Mn-O stretching modes can be observed in the same range of wavenumbers than those of ν_{as} Sb-O [3]. From Figure 70 the band intensity increases along with the content of MnO, however, as the large band envelops both absorptions, it is not possible to distinguish between them.

Table 14. Raman scattering and infrared band assignments for SZPxMn series.

Raman scattering			**Infrared**		
Centered band (cm^{-1})	**Band assignments**	**References**	**Centered band (cm^{-1})**	**Band assignments**	**References**
1135	ν_{as} P-O- (Q0)	[1–5]	1080	ν_{as} PO_4	[1,2,6]
1058	ν_s P-O-		985	ν_s PO_4	
961	ν_s P-O- (Q0)		910	δ P-O-P	
845	luminescence of Mn^{2+} ions present in octahedral sites		720	ν_s Sb-O-P	
617	ν_{as} Sb–O–P				
559	ν_{as} Sb–O				
459	δ_s P-O- (Q0)				
404	δ_{as} Sb–O		605	ν_{as} Sb-O-P	
350-200	Group modes		515	δ_s Sb-O	

(Own authorship).

5. Density.

The densities (ρ), molar volume ($V_M = \rho/M$), ion effective concentration (N_R, R = Mn^{2+}), short wavelength cut-off (λ_{UV}) and refractive index at 532 nm for samples are resumed in Table 15. Analyzing the density of the SZPxMn series, it is observed an increasing as a function of the Mn concentration, which can be related to the increase in the ion concentration and greater matrix connectivity. It is reported that the molar volume (V_M) varies linearly in a decreasing way as the amount of MnO in the glass structure increases, indicating an increasingly smaller packing. Figure 71 shows the molar volume and density variation per effective concentration of Mn^{2+}. No theoretical optical basicity values were found for $SbPO_4$, making it no possible to calculate and forecast NBO for this chapter.

Table 15. Density (ρ), molar volume (V_M), ion effective concentration (N_{Mn2+}), refractive index (n) at 532 nm and short wavelength cut-off (λ_{UV}) for for samples SZPxMn.

Samples	ρ (±0.005 g.cm^{-3})	V_M (mol . cm^{-3})	N_{Mn2+} (10^{21} ion.cm^{-3})	λ_{UV} (nm)	n (532 nm)
SZP0Mn	4.658	43.90	0	384	1.870
SZP10Mn	4.679	40.85	0.42	393	1.863
SZP20Mn	4.690	37.91	0.98	400	1.846
SZP30Mn	4.725	34.80	1.73	402	1.822

(Own authorship).

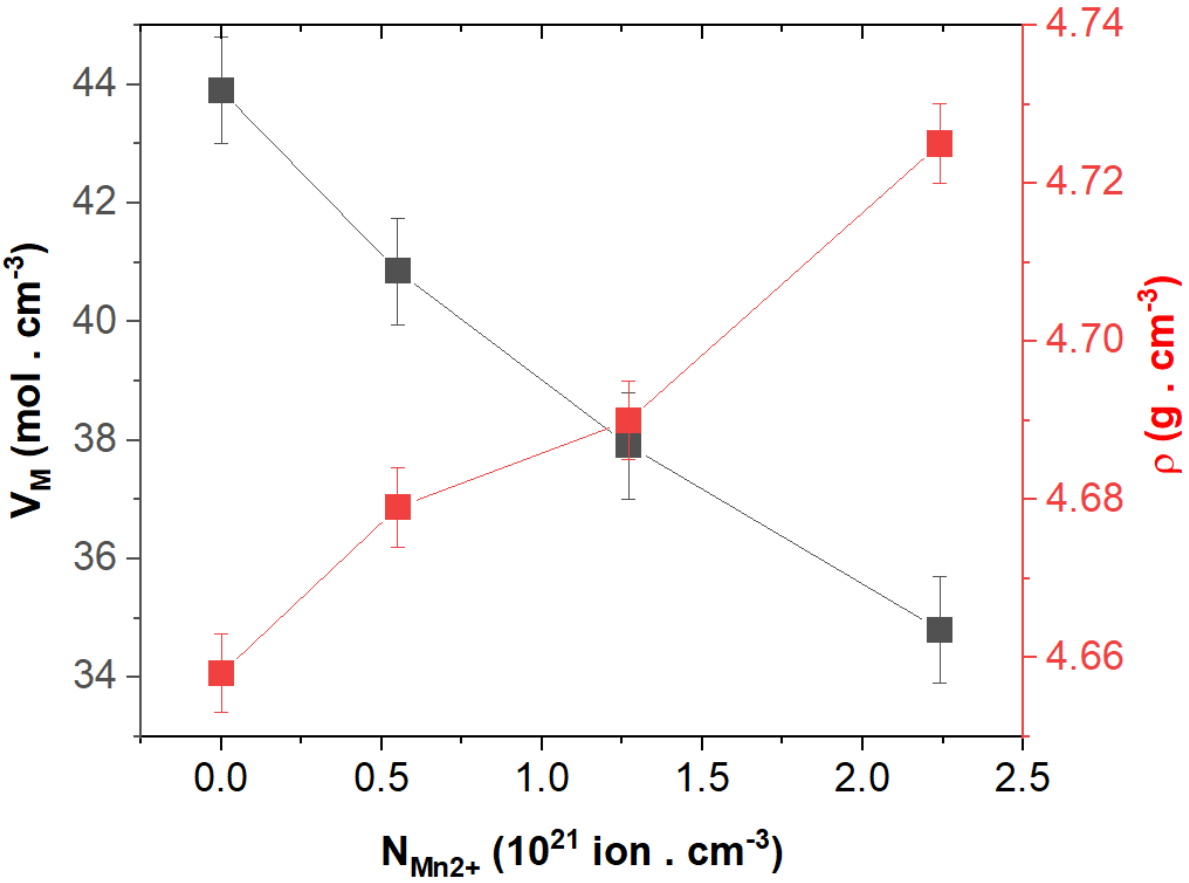

Figure 71. Molar volume (V_M) and density (ρ) variation for ion effective concentration (N_{Mn2+}) of which SZPxMn series samples. (Own authorship).

Analyzing the density of the SZPxMn series, we can observe an increasing as a function of the Mn concentration, which can be related to a better packing, as the concentration of large atoms such as Pb and Sb decreases and Mn, a smaller atom,

increases. As seen earlier, N_{Mn2+} is proportional to density, with values ranging from 0 to 1.73, one order of magnitude when compared to the xTb40W samples. The effective concentration of Mn^{2+} ion is an important factor for magnetic materials once the ion has a high paramagnetic susceptibility.

6. Optical analysis

The transmittance windows for glasses are shown in Figure 72a, with absorption coefficient spectra in 72b. The d-d absorption bands are covered by the absorption at the visible range. The wavelength cut-off of the sample SZP0Mn is around 400 nm and the addition of MnO shifts it to lower energy regions. In the middle infrared region, there is a band at 2.9 μm associated with hydroxyl groups that increases with manganese content and may be related to increased NBO binding. The multiphonon absorption delimits the transparency in the middle infrared region around 4.4 μm. In the UV-Vis region, absorption bands referring to the two oxidation states bivalent (Mn^{2+}) and trivalent (Mn^{3+}) are reported in glasses containing manganese in octahedral environments [3,10–12].

The band at 410 nm corresponds to the overlap of the d-d transitions, $^6A_{1g}(S) \rightarrow {}^4A_{1g}$, ^4E_g (^4G) transition of Mn^{2+} ions and the band that appears as a shoulder at 432 nm is assigned to the $^6A_{1g} \rightarrow {}^4T_{2g}$ (^4G) transition also for Mn^{2+} ions in octahedral environment; in addition, the band at 550 nm which may be due to oxidation of Mn^{2+} towards Mn^{3+} and ($^6A_{1g} \rightarrow {}^4T_{1g}$ (^4G)) transition. This oxidation was previously studied and confirmed for this same matrix by EPR and luminescence data[3]. The Mn^{2+} ion (d^5) has ground level configuration $^6A_{1g}(^6S)$ for both tetrahedral and octahedral coordination, however the excited states are quartets or doublets, $\Delta S \neq 0$, being all transitions not only spin-forbidden, but additionally also Laporte forbidden. Therefore, the absorption bands have low intensity even at high concentrations such as do SZPxMn system.

From the positions of the absorption component bands and their best fit in the Tanabe-Sugano diagram, the values of ligand field splitting (Dq) and the Racah interelectronic repulsion parameter (B) were obtained, being equal to Dq = 842 cm^{-1}, B = 769 cm^{-1}, and Dq/B = 1.09, characteristics for Mn^{2+} (d^5) in octahedral environment for

weak ligand field [10,11]. The trivalent ion Mn^{3+} (d^4) in an environment with weak ligand field suffers Jahn-Teller distortion, with the degeneracy break of the orbitals $^5E_g(^5D)$, into $^5B_{1g}$ and $^5A_{1g}$, and $^5T_{2g}(^5D)$, into $^5B_{2g}$ and ^5E_g. The transition observed at 520 nm corresponds to the $^5B_{1g} \rightarrow {}^5B_{2g}$ transition, which is not prohibited and, even for very low content of Mn^{3+}, it is possible to observe this large absorption band [3,5,10,11].

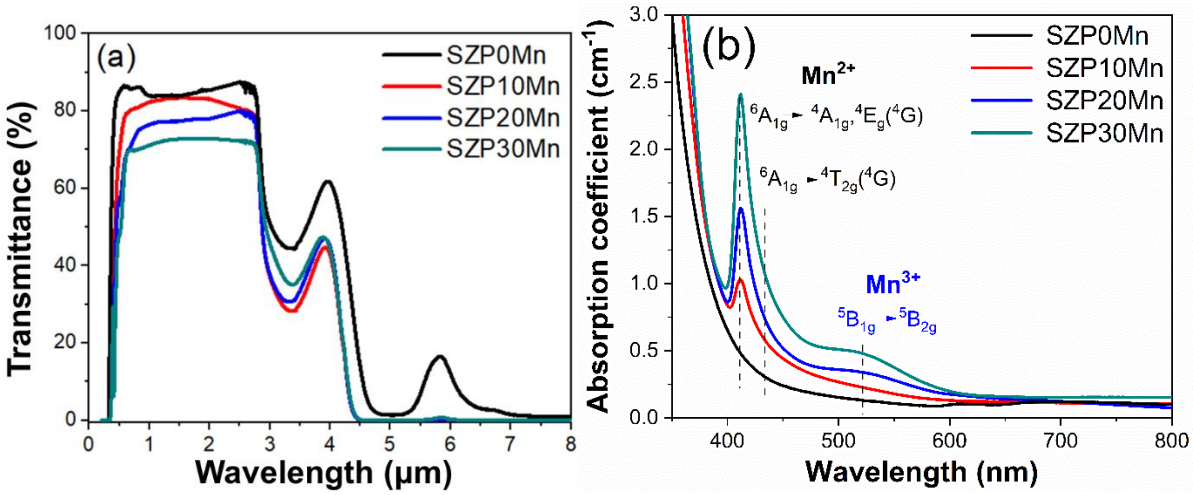

Figure 72. (a) Transmittance windows and (b) absorption coefficient spectra in SZPxMn system, with the mains transitions (Mn^{2+} in black and Mn^{3+} in blue) assigned. (Own authorship).

7. Luminescence analysis

Excitation and emission spectra is shows respectively in Figure 73a and b, with the respective bands of the d-d transitions marked[3,10]. For excitation spectra, six d-d main transitions at 352, 366, 405, 410, and 421 nm are assigned to transitions the fundamental level $^6A_{1g}$ of Mn^{2+} in octahedral environment towards the excited states $^4E_g(^4D)$, $^4T_{2g}(^4D)$, $^4E_g(^4G)$, $^4A_{1g}(^4G)$, and $^4T_{2g}(^4G)$, respectively, and 508 nm correspond to $^5B_{1g} \rightarrow {}^5B_{2g}$ of Mn^{3+} ions. After excitation at 410 nm, a broad emission band was detected, and a redshift of 680-740 nm was observed. This band is attributed to the $^4T_1(G) \rightarrow {}^6A_1(S)$ transition of Mn^{2+} ions in an octahedral environment. The very broad band is indicative of the presence of Mn^{2+} ions at different symmetry sites. Finally, the redshift with the manganese content and a shoulder at ~580 nm (evident for samples SZP20Mn and SZP30Mn) show that the addition of manganese modifies the crystal field

strength due to changing chemical environment around the ion, making it possible to occupy new sites of symmetry and emergence of a new unfolding of energy levels [3,10–12].

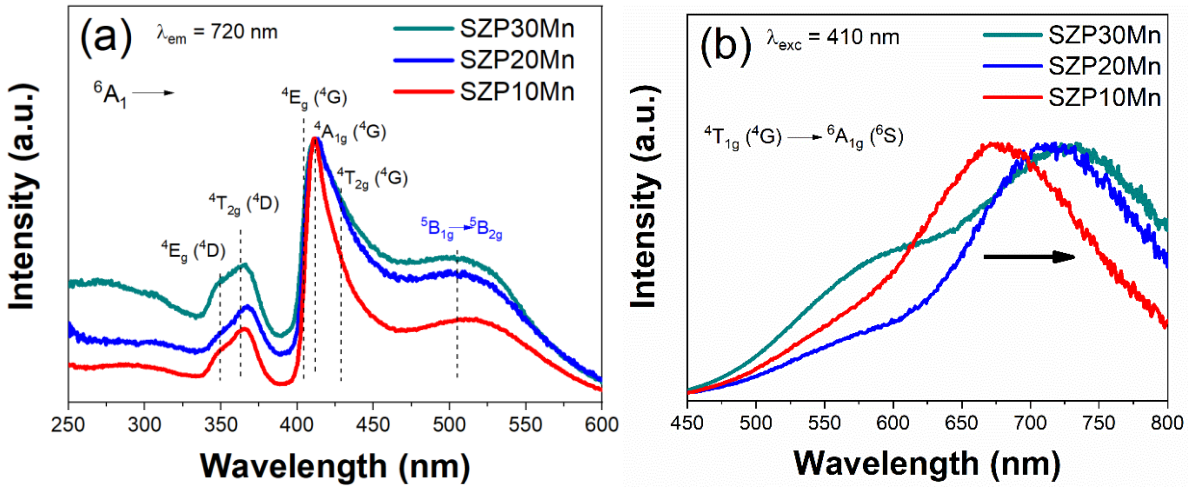

Figure 73. Excitation (a), with λ_{em} = 720 nm, and emission (b), with λ_{exc} = 410 nm, spectra for samples SZPxMn system. (Own authorship).

8. Magnetic analysis

Figure 74a depicts the DC zero-field-cooled (ZFC) and field-cooled (FC) susceptibility (χ_{DC}) curves as a function of temperature for a fixed applied magnetic field of H = 100 Oe of SZPxMn samples, where the 0% MnO content susceptibility curve was included for comparison. The data was collected in emu . g^{-1} . Oe^{-1}.

As observed in Figure 74a., a reversible magnetization between the ZFC and FC was found which suggests no thermal relaxation; also the thermal dependence of the χ_{DC} curves (both ZFC and FC) display a typically paramagnetic behavior. Besides, Figure 74b. shows the ${\chi_{DC}}^{-1}$ vs T for 10, and 30 % of MnO, which exhibits a linear dependence at high temperatures, however, a positive curvature at low temperatures is found, implying that a portion of the sample is thermally independent, which could be associated with the diamagnetism of the host matrix in which the Mn-ions are embedded, as it is suggested in the literature, one adaptation of Curie Weiss law (Eq. 11), With the extra term χ_0 [13].

$$\chi_{DC} = \frac{C}{(T-\theta)} + \chi_0 \qquad (Eq.27)$$

$$\chi_{DC}{}^{-1} = \frac{(T-\theta)}{(\chi_0(T-\theta)+C)} \qquad (Eq.28)$$

where χ_0 is the independent contribution to the magnetic susceptibility, with C, θ and χ_0 are fitting parameters. In order to model the $\chi_{DC}{}^{-1}$ vs T curve the Curie–Weiss law (Figure 74 b) is rewritten to obtain Eq. 28. The results obtained from the fit using Eq. 21 are presented in Table 16.

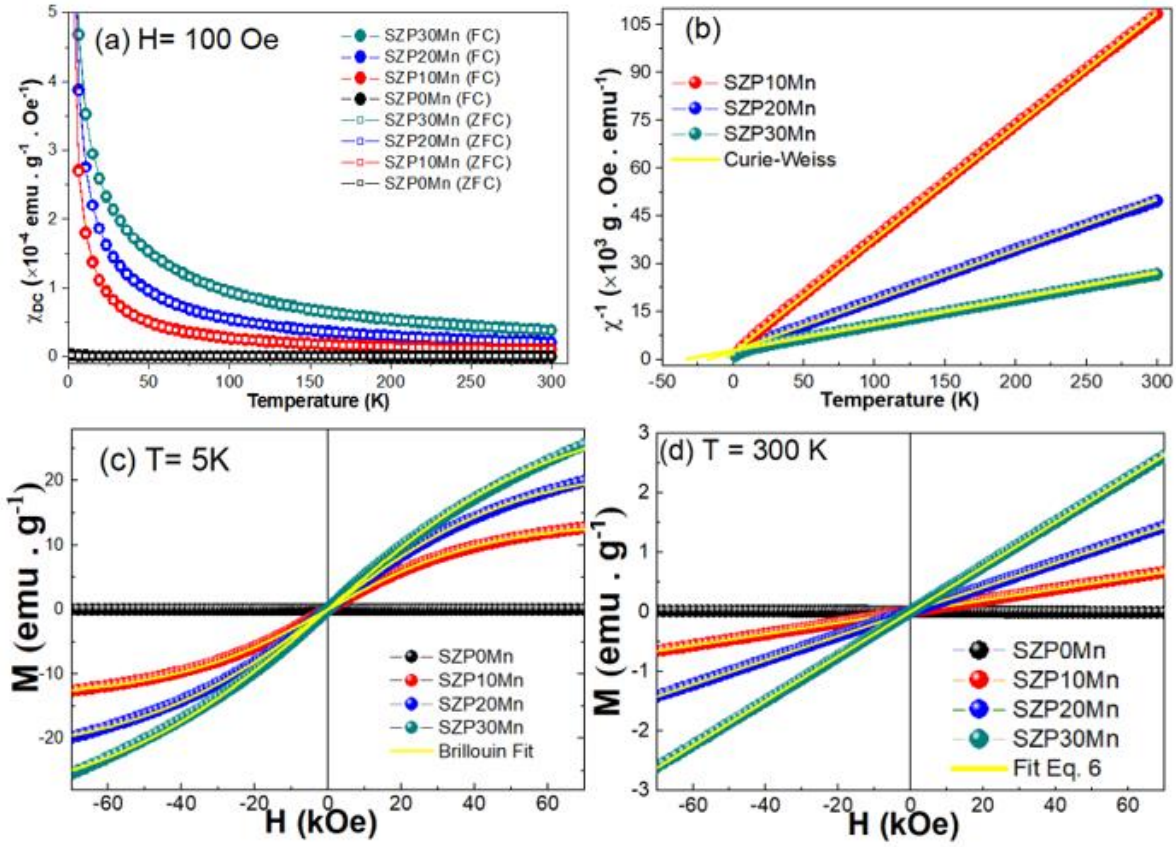

Figure 74. (a) Zero-field-cooled (ZFC) and field-cooled (FC) susceptibility (χ_{DC}) as a function of the temperature (T) for the 1-x($SbPO_4$-ZnO-PbO)-xMnO glass with an applied magnetic field of H = 100 Oe. (b) $\chi_{DC}{}^{-1}$ *vs* T curve for the 30, 20, and 10 MnO containing, where the point represents the experimental data and the blue dashed line represents the fits to the Curie-

Weiss law (Eq. 28). (c) Magnetization as a function of the applied magnetic field (*M vs. H*) loops at 5K (d) and 300 (K). The yellow continue line represents the Brillouin function fit. (Own authorship).

Table 16. Parameters obtained from the fits of the susceptibility (χ_{DC}) versus temperature (T) to the Curie–Weiss law as described in the text.

Sample	χ_{dia} ($x10^{-6}$ emu . mol^{-1})	C (emu . mol^{-1} . Oe^{-1})	χ_0 ($x10^{-5}$ emu . mol^{-1} . Oe^{-1})	θ (K)	μ_{eff} (μ_B)
SZP10Mn	-56.42	0.53	2.1	-6.2	5.02
SZP20Mn	-53.04	1.08	0.7	-14.5	5.14
SZP30Mn	-49.66	1.97	19.4	-29.1	5.75

(Own authorship).

Diamagnetic susceptibility (χ_{dia}), which is independent of field and temperature, was obtained from literature values, showed in Table 1. The calculation was made considering only Mn^{2+}, because, as previously stated, we can consider the amount of Mn^{3+} to be insignificant, if compared to Mn^{2+}. The χ_{dia} decrease in for samples more concentrated in MnO is related to the decrease in concentration of other reagents, which the diamagnetic contribution is higher.

As shown in Table 16, the Curie constant rises as the Mn-content grows, in line with the Mn content, meanwhile, the μ_{eff} estimated for the samples are between 5.02-5.75 μ_B, higher than Mn^{3+} (d^4) = 4.89 μ_B, however, below Mn^{2+} (d^5) = 5.92 μ_B. At this point, it is interesting to note that Mn^{2+} (d^5) is more stable than Mn^{3+} (d^4) due to the stability of the half-filled electronic configuration, especially after thermal annealing at high temperatures performed to produce the samples, also a probable explanation for the elucidation of the oxidized state of manganese ions into the $SbPO_4$-ZnO-PbO glass matrix can be linked to the presence of the negative values of θ_{CW}, that suggest an increase of antiferromagnetic (AF) interaction of neighbor Mn-ions ↑↓, ↑↓↑, which

increase as the Mn content, in concordance with the increase of θ, reducing the observable μ_{eff}, suggesting that manganese ions mostly exist in the Mn^{2+} state.

Figure 74(c) depicts the magnetization as a function of the applied magnetic field (*M vs. H*) loops at a temperature of 5 K for SZPxMn glass system. Main PM behavior is exhibited in all samples, evidenced by the absence of any saturation up to 70 kOe, hysteresis, and remanent magnetization, in good agreement with the ${\chi_{DC}}^{-1}$ *vs T* analysis, displayed in the previous section. Similar behavior is reported in the literature[14]. Figure 70(c) depicts also the fit using the Brillouin function using Eq. 29.

$$M(H) = M_S \times \boldsymbol{B_J}\left(\frac{g\mu_B JH}{k_B(T-T_0)}\right); \qquad \boldsymbol{B_J}(\boldsymbol{x}) = \left[\frac{2J+1}{2J} coth\left(\frac{2J+1x}{2J}\right) - \frac{1}{2J} coth\left(\frac{x}{2J}\right)\right] \qquad \text{(Eq.29)}$$

where M_S is the saturation magnetization, g = 2 (for transition metals), J is the total angular momentum, and T_0 is a phenomenological parameter that represents any magnetic interaction that prevents spins from being completely aligned even in the strongest magnetic field[15].

Using $J = 5/2$ for Mn^{2+} a good correlation between the experimental data and the fit was obtained (see yellow continue line in Figure 74(c)), reinforcing the bivalent oxidized state of the manganese ions. The T_0 obtained from the fit displays a negative, and increase as the Mn content (-2.29, -4.08, and -5.98, for the 10, 20, 30 mol % Mn) which suggests that the antiferromagnetism involves the interaction of Mn^{2+} magnetic moments. Figure 70(d) shows the *M vs. H* loops at room temperature (300 K). To determine the effective magnetic moment of the Mn-ions, from *M vs. H* curve at 300 K the Brillouin function of Eq. 29 can be simplified using the approach of $K_B T \gg g\mu_B JH$, obtained the equation:

$$M = \frac{N\mu_{eff}^2 \mu_B^2}{3K_B T} H \qquad \textit{(Eq. 30)}$$

Eq. 30 predicts a linear behavior of the magnetization as external the magnetic applied field (H), for an isothermal process, which is observed in our sample (see Figure 74d), from it the effective magnetic moment can be calculated, the values of μ_{eff} were Figure 75, which are in good agreement with the obtained from the Curie-Weiss law.

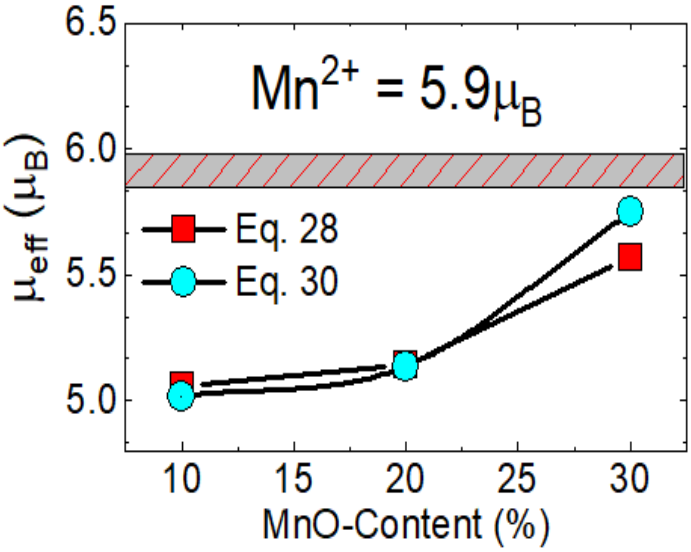

Figure 75. μ_{eff} obtained from the analyses, where also the obtained values using Curie-Weiss law were included for comparison. (Own authorship).

9. Magneto-optical analysis.

Figure 76 shows the graph Verdet constant (V) versus N_{Mn2+} for the SZPxMn series. The average values obtained were +8.7, -13.5, -29.4, and -55.1 (± 3.2) $rad.T^{-1}.m^{-1}$ at 632.8 nm, from the least concentrated sample up to SZP30Mn respectively. It is interesting to observe that for the SZP0Mn sample the Verdet constant value is positive, indicating a greater influence of the diamagnetic behavior part for this sample. As the paramagnetic ion concentration increases, V values go to a maximum for sample SZP30Mn.

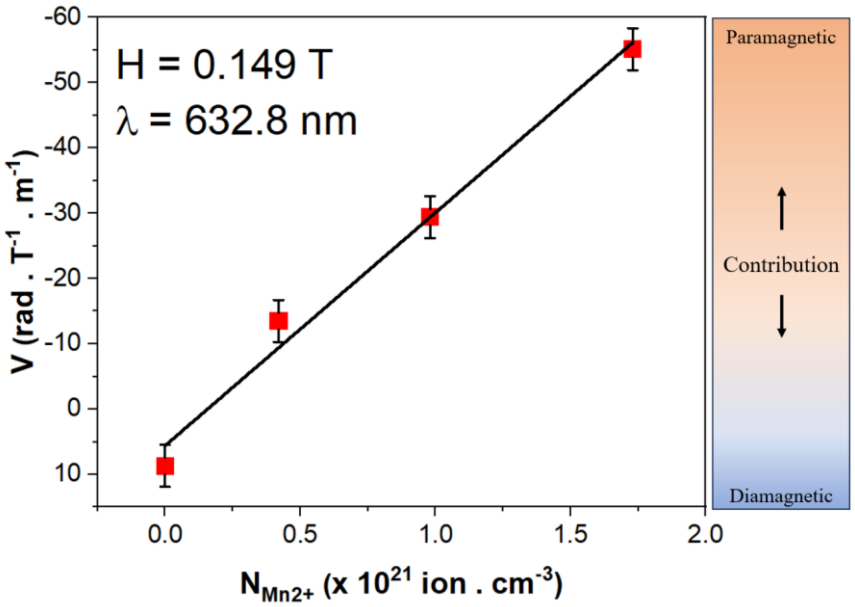

Figure 76. Verdet constant (V) versus effective Mn^{2+} concentration (N_{Mn2+}) for SZPxMn series samples. (Own authorship).

The values of V are proportional to the refractive index and the total magnetic susceptibility of the material, the influence of magnetic susceptibility prevails, because even with the refractive indexes decreasing with the increase in the concentration of Mn in place of Sb and Pb, the paramagnetic susceptibility of Mn is an order of magnitude greater than Sb and Pb. With paramagnetic susceptibility prevailing, the V tends to increase with increasing Mn concentration.

Such Verdet constant values can be compared to some families of glasses containing Tb^{3+}, such as fluorides [16], phosphates[17,18] and fluorophosphates [16,17,19,20] glasses, opening applications for glasses containing manganese for applications in the visible region. It is also interesting to comment that Verdet constant values for glasses with high concentrations of paramagnetic transition metal ions in the visible region is still little studied and explored. These glasses can become alternatives for low-cost magneto-optical materials.

10. Partial Conclusions of this Chapter.

The 100-x(70$SbPO_4$–10ZnO–20PbO)xMnO system was systematically synthesized and investigated by thermal, structural, optical, luminescent, magnetic and magneto-optical techniques. The formation of the glassy phase was confirmed by XRD and DSC, with an increase in Tg from sample SZP0Mn to SZP30Mn, and ΔT ranging from 111-143 ±3 °C from SZP0Mn to SZP20Mn, with a decrease in thermal stability for sample SZP30Mn. The vibrational modes were studied and assigned Raman and FTIR, with some modifications arising regarding the increase in MnO concentration. The density also increases with concentration and the refractive index decreases, due to the decrease in the amount of Sb, Pb, more polarizable atoms than Mn, but remaining high. Theoretical optical basicity increases, indicating a more basic character of the glass, with a greater presence of NBO. By optical analysis, as the concentration increases, it is observed the Mn^{2+} absorptions at 410 nm $^6A_1(S) \rightarrow {}^4A_1$, ^4E (^4G) and also due to possible oxidation of Mn^{2+} towards Mn^{3+} at around 550 nm $^6A_1 \rightarrow {}^4T_1$ (^4G), with a red shift of the short wavelength cut-off. With increasing concentration, an emission band at ~580 nm appears, being likely Mn^{2+} ions in tetrahedral and/or Mn^{3+} environments. There is also a redshift of the emission at 680 nm to 740 nm, attributed to $^4T_1(G) \rightarrow {}^6A_1(S)$ of Mn^{2+} in octahedral environment, due to the increase in the crystal field strength. The susceptibility measurements showed that all samples containing Mn showed paramagnetic behavior, with alignment of antiparallel spins, and the isothermal magnetization measurements confirmed the paramagnetic behavior. Finally, the Verdet constant measurements at 632.8 nm were promising, ranging from +8.7 to -55.1± 3.2 $rad.T^{-1}.m^{-1}$, high and unprecedented values for transition metals, comparable to some families of glasses containing rare earths. The values of thermal stability, optical window, high refractive index, paramagnetic behavior and high Verdet constant, being a low-cost alternative to produce new magneto-optical materials.

References of this Chapter.

[1] M. Nalin, Y. Messaddeq, S.J.L. Ribeiro, M. Poulain, V. Briois, G. Brunklaus, C. Rosenhahn, B.D. Mosel, H. Eckert, Structural organization and thermal properties of the Sb_2O_3-$SbPO_4$ glass system, J. Mater. Chem. 14 (2004) 3398–3405. https://doi.org/10.1039/b406075j.

[2] W. Brockner, L.P. Hoyer, Synthesis and vibrational spectrum of antimony phosphate, $SbPO_4$, Spectrochim. Acta - Part A Mol. Biomol. Spectrosc. 58 (2002) 1911–1914. https://doi.org/10.1016/S1386-1425(01)00639-4.

[3] R.S. Manzan, J.P. Donoso, C.J. Magon, I.D.A.A. Silva, C. Rüssel, M. Nalin, Optical and structural studies of Mn2+ doped SbPO4-ZnO-PbO glasses, J. Braz. Chem. Soc. 26 (2015) 2607–2614. https://doi.org/10.5935/0103-5053.20150289.

[4] A.K. Yadav, P. Singh, A Review of Structure of Oxide Glasses by Raman Spectroscopy, RSC Adv. 5 (2015) 67583–67609. https://doi.org/https://doi.org/10.1039/C5RA13043C.

[5] N. Da, M. Peng, S. Krolikowski, L. Wondraczek, Intense red photoluminescence from Mn^{2+}-doped (Na^+; Zn^{2+}) sulfophosphate glasses and glass ceramics as LED converters, Opt. Express. 18 (2010) 2549. https://doi.org/10.1364/oe.18.002549.

[6] D. Möncke, H. Eckert, Review on the structural analysis of fluoride-phosphate and fluoro-phosphate glasses, J. Non-Crystalline Solids X. 3 (2019) 100026. https://doi.org/10.1016/j.nocx.2019.100026.

[7] V. Dimitrov, S. Sakka, Electronic oxide polarizability and optical basicity of simple oxides. I, J. Appl. Phys. 79 (1996) 1736–1740. https://doi.org/10.1063/1.360962.

[8] D. Möncke, S. Ali, B. Jonson, E.I. Kamitsos, Anion polarizabilities in oxynitride glasses. Establishing a common optical basicity scale, Phys. Chem. Chem. Phys. 22 (2020) 9543–9560. https://doi.org/10.1039/c9cp06930e.

[9] J.A. Duffy, A review of optical basicity and its applications to oxidic systems, Geochim. Cosmochim. Acta. 57 (1993) 3961–3970. https://doi.org/10.1016/0016-7037(93)90346-X.

[10] I. Konidakis, C.P.E. Varsamis, E.I. Kamitsos, D. Möncke, D. Ehrt, Structure and

properties of mixed strontium-manganese metaphosphate glasses, J. Phys. Chem. C. 114 (2010) 9125–9138. https://doi.org/10.1021/jp101750t.

[11] I.E.C. Machado, L. Prado, L. Gomes, J.M. Prison, J.R. Martinelli, Optical properties of manganese in barium phosphate glasses, J. Non. Cryst. Solids. 348 (2004) 113–117. https://doi.org/:10.1016/j.jnoncrysol.2004.08.135.

[12] A. Winterstein, H. Akamatsu, D. Möncke, K. Tanaka, M.A. Schmidt, L. Wondraczek, Magnetic and magneto-optical quenching in (Mn^{2+}, Sr^{2+}) metaphosphate glasses, Opt. Mater. Express. 3 (2013) 184. https://doi.org/10.1364/ome.3.000184.

[13] R. Reisfeld, A. Kisilev, C.K. Jørgensen, Luminescence of manganese(II) in 24 phosphate glasses, Chem. Phys. Lett. 111 (1984) 19–24. https://doi.org/10.1016/0009-2614(84)80430-3.

[14] M. Kawano, H. Takebe, M. Kuwabara, Compositional Dependence of the Luminescence Properties of Mn^{2+}-Doped Metaphosphate Glasses, Opt. Mater. (Amst). 32 (2009) 277–280. https://doi.org/10.1016/j.optmat.2009.08.001.

[15] S. Mugiraneza, A.M. Hallas, Tutorial: a beginner's guide to interpreting magnetic susceptibility data with the Curie-Weiss law, Commun. Phys. 5 (2022). https://doi.org/10.1038/s42005-022-00853-y.

[16] D.F. Franco, R.G. Fernandes, J.F. Felix, V.R. Mastelaro, H. Eckert, C.R.M. Afonso, Y. Messaddeq, S.H. Messaddeq, S. Morency, M. Nalin, Fundamental studies of magneto-optical borogermanate glasses and derived optical fibers containing Tb^{3+}, J. Mater. Res. Technol. 11 (2021) 312–327. https://doi.org/10.1016/j.jmrt.2021.01.010.

[17] F.H. Aragón, J.A.H. Coaquira, P. Hidalgo, S.L.M. Brito, D. Gouvêa, R.H.R. Castro, Structural and magnetic properties of pure and nickel doped SnO2 nanoparticles, J. Phys. Condens. Matter. 22 (2010). https://doi.org/10.1088/0953-8984/22/49/496003.

[18] J. Qiu, K. Tanaka, N. Sugimoto, K. Hirao, Faraday effect in Tb^{3+}-containing borate, fluoride and fluorophosphate glasses, J. Non. Cryst. Solids. 213–214 (1997) 193–198. https://doi.org/10.1016/S0022-3093(97)00101-4.

[19] M. Yamane, Y. Asahara, Glasses for Photonics, Cambridge University Press,

Cambridge, 2000.

[20] A. Babkina, E. Kulpina, Y. Sgibnev, Y. Fedorov, A. Starobor, O. Palashov, N. Nikonorov, A. Ignatiev, K. Zyryanova, K. Oreshkina, E. Zhizhin, D. Pudikov, Terbium concentration effect on magneto-optical properties of ternary phosphate glass, Opt. Mater. (Amst). 100 (2020) 109692. https://doi.org/10.1016/j.optmat.2020.109692.

[21] B. Bellanger, Y. Ledemi, Y. Messaddeq, Fluorophosphate Glasses with High Terbium Content for Magneto-optical Applications, J. Phys. Chem. C. 124 (2020) 5353–5362. https://doi.org/10.1021/acs.jpcc.9b11696.

[22] B. Bellanger, L. Audebert, Y. Ledemi, Y. Messaddeq, Superexchange Interaction Influence on the Faraday Effect in Terbium Fluorophosphate Glasses by Co-doping with Praseodymium, Dysprosium, and Holmium, J. Phys. Chem. C. 125 (2021) 17482–17492. https://doi.org/10.1021/acs.jpcc.1c04713.

CHAPTER VI – Final Conclusion and Perspectives

Chapter VI – Final Conclusion and Perspectives

As general conclusions of this work we can highlight the obtention of two different glass systems presenting magneto optical properties. The borotungstate system showed very high solubility of rare earth ions, which is the pre-requisite to obtain large magneto optical properties and it was demonstrated by the high values of Verdet constant. These glasses present algo good thermal stability allowing to prepare large bulk samples. The system containing manganese also showed good magneto optical properties, but, as expected, due to lower magnetic susceptibility of Mn ions, the Verdet constant is lower than that of borotungstate system. In parallel to the main study of this thesis, a series of samples containing different rare earths were produced and studied, the qualitative results indicates that most of then can be used for more specific magneto optical studies while others do not form glasses. The comprehension of such systems is fundamental to advance towards to chipper and more powerful devices.

Our investigation into the physical principles underlying Faraday effects has shed light on the intricate interaction between magnetic fields and these glassy systems, making correlations between glass composition and desired effects to optimize the magneto-optical performance of these glasses. These insights serve as a foundation for the development of advanced optical devices such as magneto-optical modulators and sensors, leveraging the unique properties of these glasses for real-world applications. Looking to the future, the exploration of magneto-optical glasses in borotungstate systems offers interesting prospects for future research. A cheaper matrix that offers an effect comparable to borogermanates and commercial single crystals. Glasses containing manganese also open doors for the development of this and other matrices with transition metals, since the effect can be compared to certain matrices containing lanthanides. In conclusion, the investigation of magneto-optical glasses within specific vitreous systems revealed a range of possibilities for the advancement of optical technologies. The synthesis, characterization, and manipulation of magneto-optical properties within these glasses provide a strong foundation for future research endeavors that aim to push the boundaries of photonics, catalyze innovation, and shape the landscape of modern optical devices.

Appendix I - Other measurements and experiments carried out.

Appendix I – Other measurements and experiments carried out

Due to the emergence of these new types of magneto-optical materials, with high concentrations of paramagnetic ions that confer other interesting properties to the material, and the possibility of contact with different laboratories, equipment, specialists from other areas, some more tests were carried out during this work, but without deepening due to several reasons. Below are some of these techniques with a brief explanation of the expected and obtained results.

A-I. Photochromism tests.

As already known from the works of Gaël Poirier et al.[1,2], tungstate glasses can present the photochromic property, changing from a yellow color to a dark one. The color change was identified to be due to the reduction of W^{6+} atoms in W^{5+} and/or W^{4+}.

25Tb40W and 25Gd40W samples were exposed to a 410 nm, 10 mW laser, for 40 min, with a 2 mm spot and a distance of 30 cm from the laser. It was expected that the photochromic effect would be observed, but no color change occurred.

For tungsten-based photochromic glasses, the reduction of $W^{6+} \rightarrow W^{5+}$ ions occurs with a subsequent formation of the so-called tungsten bronzes H_xWO_3.

A-II. 3D inscription.

With the collaboration of researchers Prof. doctor Lionel Canioni and Prof. doctor Yannick Petit, at Center lasers intenses et applications (CELIA) in Bordeaux, 3D inscription tests by femtosecond laser irradiation (@1064 nm) were carried out. This technique would allow the creation of waveguides inside the glass with rare earths. with nonlinear, magneto-optical properties, can be employed as isolators, rotating modules, switches and modulators, and high-performance active gain devices[3–5].

A 25Tb40W glass bulk was prepared by cooling inside the crucible, with shock in water at room temperature, to avoid the formation of mechanical stresses. Then some tests were performed using a 40X objective lens, 0.5-0.65 W, at a speed of 0.2 – 2.5 mm/s. Unfortunately for higher powers and lower speeds there is an overlap of

energy, forming holes in the glass surface (Figure A-1a). For lower potencies the inscription was almost nil, weak and discontinuous, as shown in Figure A-1b. New tests need to be performed to carry out the 3D inscription.

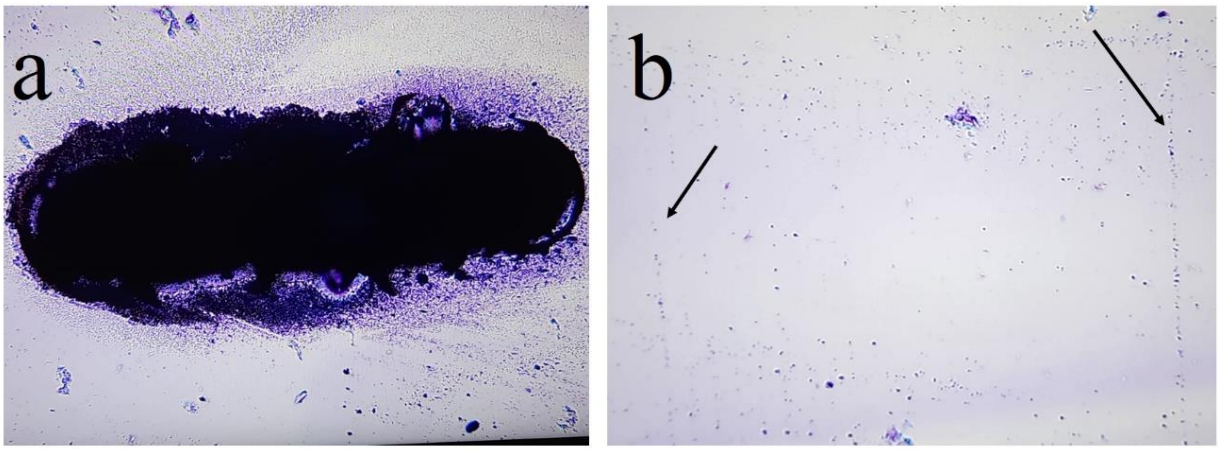

Figure A-1. Photograph of the 3D inscription attempts performed on the 25Tb40W sample, taken with a 40X objective lens. For high powers(A-1a), the formation of holes occurred and for low powers (A-1b), weak and discontinuous markings occurred.

A-III. Optical fiber drawing.

With the guidance and assistance of Dr. Sylvain Danto, Research Scientist – Groupe "Chemistry and photonic of oxide and fluoride materials" Institut de Chimie de la Matière Condensée de Bordeaux (ICMCB), UMR 5026 CNRS Université de Bordeaux optical fiber pulling tests were performed for the 25Tb40W sample.

Cylindrical preforms 7 cm high x 2 cm diameter were prepared in order to obtain optical fibers. The pulling temperature was obtained at 650 °C with the formation of the drop. However, crystallization occurred and it was not possible to wind a fiber, as shown in Figure A-2. The identified phase was the same TbBO3, already assigned in Chapter III.

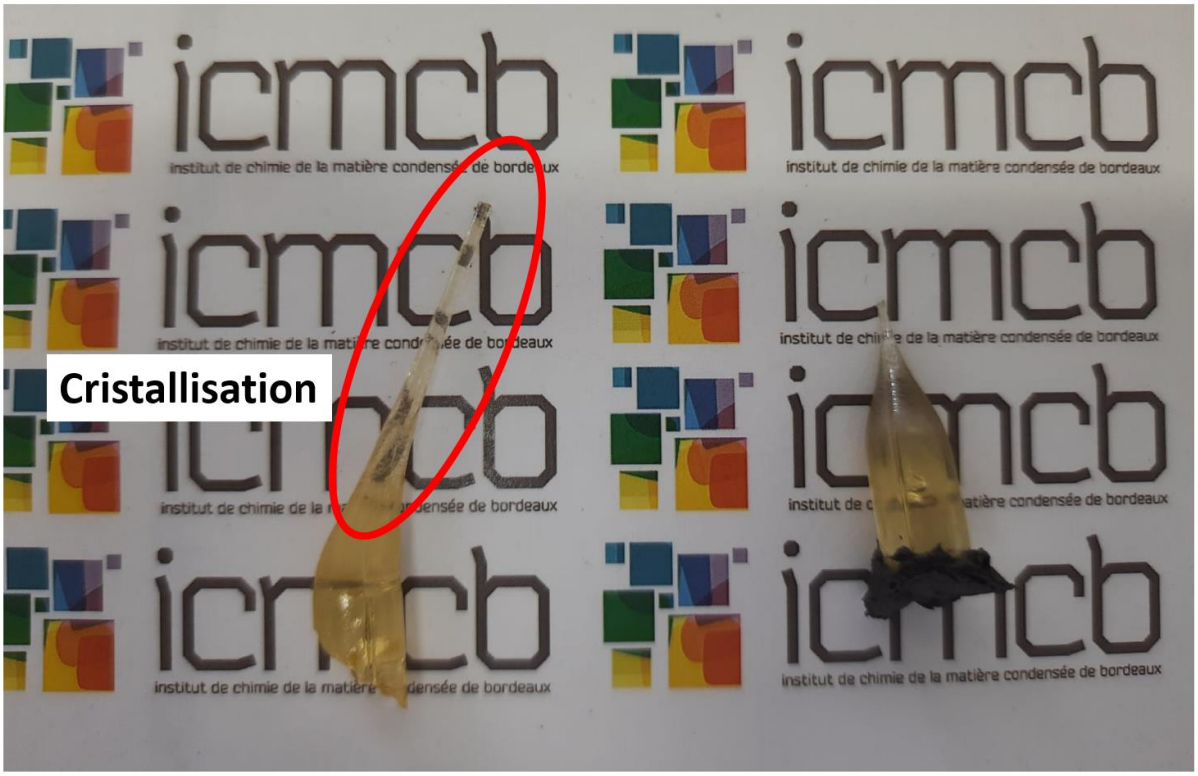

Figure A-2. Preforms after trying to draw the fibers. A crystalline phase is observed in the region where preform heating occurred.

Optical microscopy studies revealed that crystallization occurred preferentially on the glass surface and, therefore, the formation of a core-shell multimode fiber would isolate the 25Tb40W sample from the air and prevent the formation of crystals, allowing fiber drawing.

Three attempts were made to form the core-shell preform (core - 25Tb40W and shell - more stable borogallate glass[6]), using the liquid pouring method, but the samples broke, probably due to the difference between the borogallate and borogallate matrices.

A-IV. Melting-quenching under external magnetic field.

The production of totally amorphous and ferromagnetic materials, that is, spins totally aligned with an external magnetic field, also opens up a wide range of studies and development of new materials.

The high concentration of paramagnetic ions and the magnetic response to neodymium magnets at room temperature suggested that a shedding under an applied field, could lead to an alignment of the spins.

The test was carried out producing a new sample 27.5Tb40W, the highest concentration of Tb_2O_3 without crystallization, with a final mass of 5,0 g. After melting at 1250 °C for one hour and 10 minutes at 1350 °C, to decrease viscosity, the liquidus was poured at room temperature into a steel mold of two neodymium magnets (B = 0.15 T) were attached parallel, one on each side of the mold. After pouring, the magnets were quickly removed and the mold placed in an oven at 550 °C for 6 h, with a cooling ramp of 1 °C/min to room temperature, to reduce the thermal stress on the glass.

However, the glass obtained did not show different properties from the conventional 27.5Tb40W sample, measurements were also performed on the Squid without major changes in the magnetic response, both following the Curie-Weiss Law without showing changes that could represent the formation of ferromagnetic-like phases.

The conclusion reached was that the field of the magnets used did not greatly influence the order or maintenance of these spins during material synthesis. Perhaps a more powerful magnetic field would produce a different response. Also the high temperature of the melt can negatively influence the magnetic field of the Nd magnets, decreasing the strength of the field during the cooling process.

A-V. Inverse Faraday Effect measures.

We had the opportunity to meet and work with Prof. doctor Vincent Rodriguez, at Institut des Sciences Moléculaires, UMR 5255 CNRS, Université de Bordeaux. In their new work[7], Rodriguez et al. leads us to a new measurement approach in magneto-optics, the Inverse Faraday Effect (IFE), method to measure the Faraday rotation angle and determine the Verdet constant, in principle for liquids and solutions. Using a tunable picosecond laser source, the generated IFE enables to reach magnetic flux densities in liquids in the range of 1-100 T, levels which are comparable to or higher than pulsed magnetic fields obtained using electromagnets.

Figure A-3, taken from the article in question, demonstrates the main correlations between the IFE and the conventional Faraday effect.

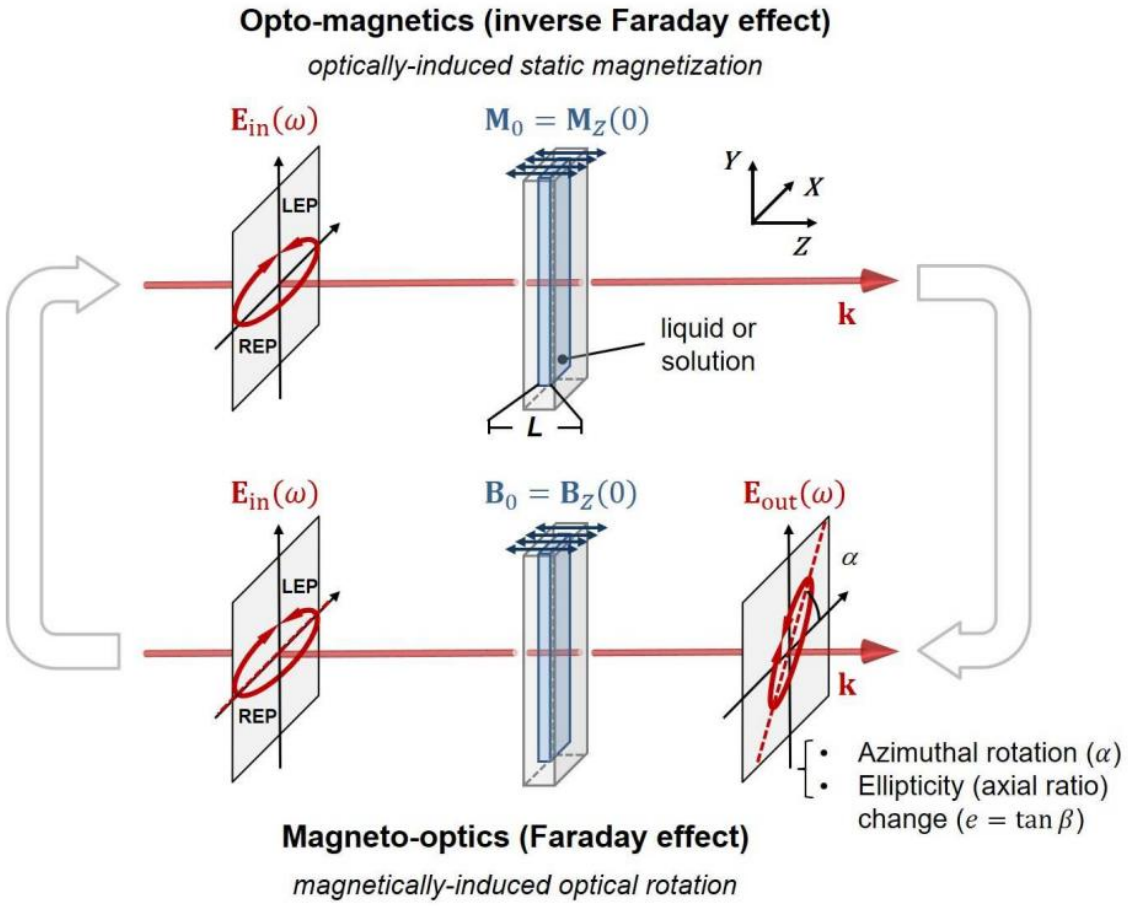

Figure A-3. Schematic illustration of the coupling between the Faraday effect (FE) and the inverse Faraday effect (IFE) in a liquid [7].

The work was done using solutions containing rare earths, and we propose to do the same for glasses highly concentrated with lanthanides. Tests have been performed, but the mathematical treatment is not the same as liquid solutions. Therefore, discussions for these results will be made in the future.

A-VI. Magnetic properties under irradiation at low temperature.

Due to the high concentration of paramagnetic ions in samples of glassy systems, it became interesting to investigate their magnetic behavior irradiated with light

at certain wavelengths under an external magnetic field at low temperature, known as the photomagnetic effect.

Magneto-optical and photomagnetic effects are essentially similar responses observed from different measurement reference points. As explained by C. J. O'Connor[8], while the magneto-optical effects are observed variations in the incident light in the medium under magnetic field, in the photomagnetic effects a magnetic variation is observed as electromagnetic radiation is applied.

The test was carried out at ICMCB, by Groupe 6 - Molécules et Matériaux Commutables and with the help of researcher Patrick Rosa, using a SQUID Quantum Design MPMS-7XL, with 405, 532 and 650 nm laser coupled, at a temperature of 4 K and under field magnetic field of 0.01 T. The 25Ho40W sample was used for the first test, due to the absorptions referring to the 4f-f transitions of Ho^{3+} in these respective wavelengths.

A change in the magnetic response during the experiment would demonstrate the presence of the photomagnetic effect. The biggest challenge, however, was heating the sample under light absorption, which causes measurement inaccuracy.

The 650 nm laser, set at 0.14 V (±1 mW/cm^2), was left to burn for 30 min, with a small decrease of moment corresponding to heating of 3 mK. Measurements were also made at 0.278 V (±2 mW/cm^2), for 30 min, but no difference was noted. 532 nm laser set at 0.608V (±1 mW/cm^2), shutter opened for 25 min. T remains stable, with decrease of moment, slightly smaller than with 650nm. Finally, the 405 nm laser, set at 0.119 V (±1 mW/cm^2), shutter opened for 30 min, with no decrease in moment or change seen.

References in this Appendix

[1] G. Poirier, M. Poulain, Y. Messaddeq, and S. J. L. Ribeiro, “New tungstate fluorophosphate glasses,” *J. Non. Cryst. Solids*, vol. 351, no. 4, pp. 293–298, 2005, doi: 10.1016/j.jnoncrysol.2004.11.017.

[2] G. Poirier, M. Nalin, L. Cescato, Y. Messaddeq, and S. J. L. Ribeiro, “Bulk photochromism in a tungstate-phosphate glass: A new optical memory material?,” *J. Chem. Phys.*, vol. 125, no. 16, pp. 1–4, 2006, doi: 10.1063/1.2364476.

[3] S.-B. . W. W. Liu, C-X.; Li, Y-W.; Fu, L-L.; Zhang L-L.; Guo, H-T.; Zhou, Z-G.; Li, W-N.; Lin, "Optical waveguides in magneto-optical glasses fabricated by proton implantation," *Opt. Laser Technol.*, vol. 85, pp. 55–59, 2016, doi: 10.1016/j.optlastec.2016.05.008.

[4] C.-D. Lai, C-C.; Lo, C-Y.; Huang, J-Z.; Chiang, C-C. F.; Nguyen, D. H.; Chen, Y-P.; Liao, "Architecting a nonlinear hybrid crystal–glass metamaterial fiber for all-optical photonic integration," *J. Mater. Chem. C*, vol. 6, pp. 1659–1669, 2018, doi: 10.1039/C7TC05112C.

[5] C. Bai, J.; Long, X.; Liu, "Ridge waveguides in Yb3+-doped silicate glass fabricated by combination of proton implantation and femtosecond laser ablation," *Mater. Res. Express*, vol. 7, p. 105201, 2020, doi: 10.1088/2053-1591/abc219.

[6] R. Zaiter *et al.*, "Thermal and structural modification in transparent and magnetic gallogermanate glasses induced by Gd_2O_3," *J. Alloys Compd.*, vol. 912, p. 165181, 2022, doi: 10.1016/j.jallcom.2022.165181.

[7] V. Rodriguez, D. Verreault, F. Adamietz, and A. Kalafatis, *All-Optical Measurements of the Verdet Constant in Achiral and Chiral Liquids: Toward All-Optical Magnetic Spectroscopies*, vol. 9, no. 7. 2022. doi: 10.1021/acsphotonics.2c00720.

[8] C. J. O'Connor, "The Photomagnetic and Magneto-Optics Effects," in *Molecular Magnetism: From Molecular Assemblies to the Devices. NATO ASI Series*, Springer, Dordrecht, 1996. doi: https://doi.org/10.1007/978-94-017-2319-0_20.

[9] W. T. Carnall, G. L. Goodman, K. Rajnak, and R. S. Rana, "A systematic analysis of the spectra of the lanthanides doped into single crystal LaF_3," *J. Chem. Phys.*, vol. 90, no. 7, pp. 3443–3457, 1989, doi: 10.1063/1.455853.

Appendix II – Periodic Table of Elements

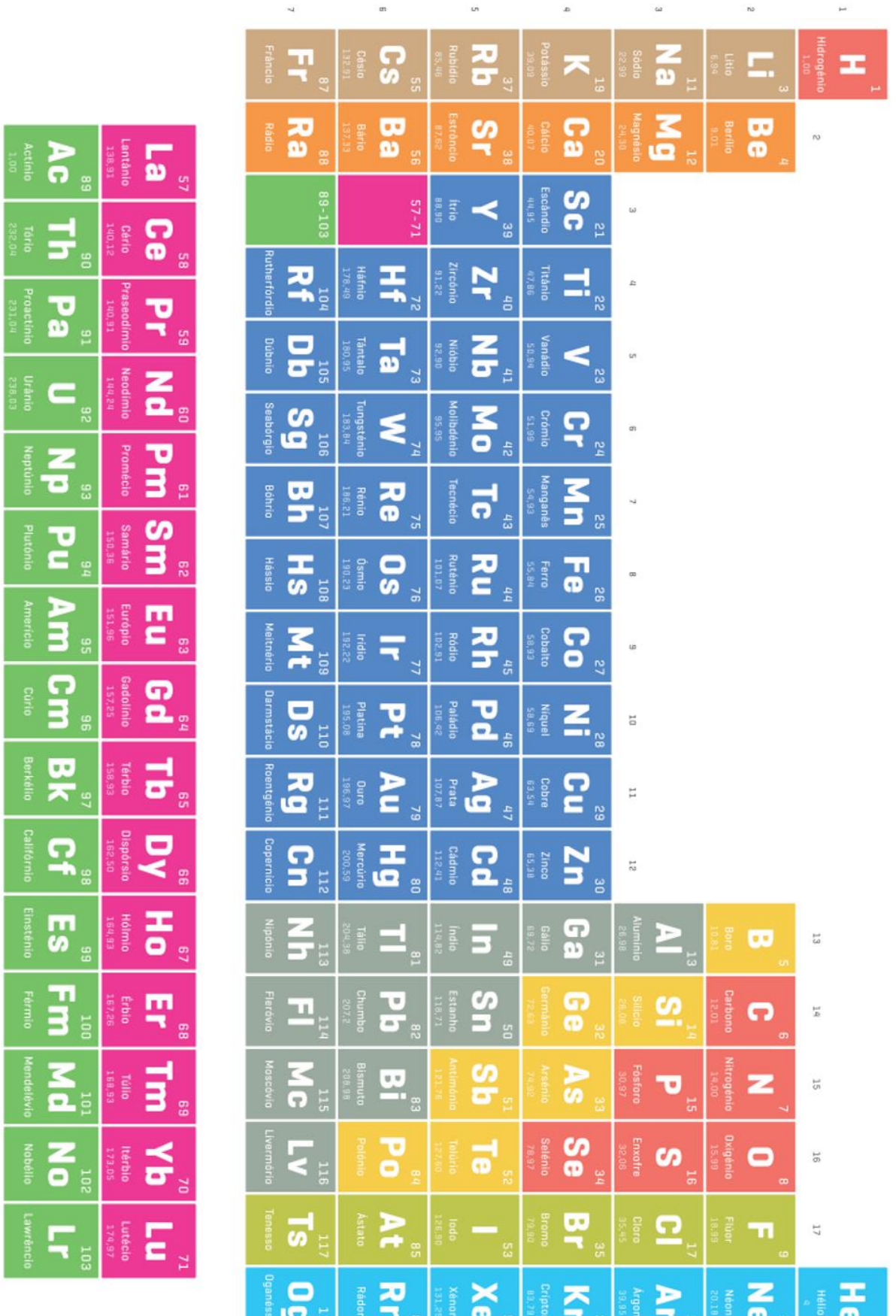

Appendix III – Carnall diagram

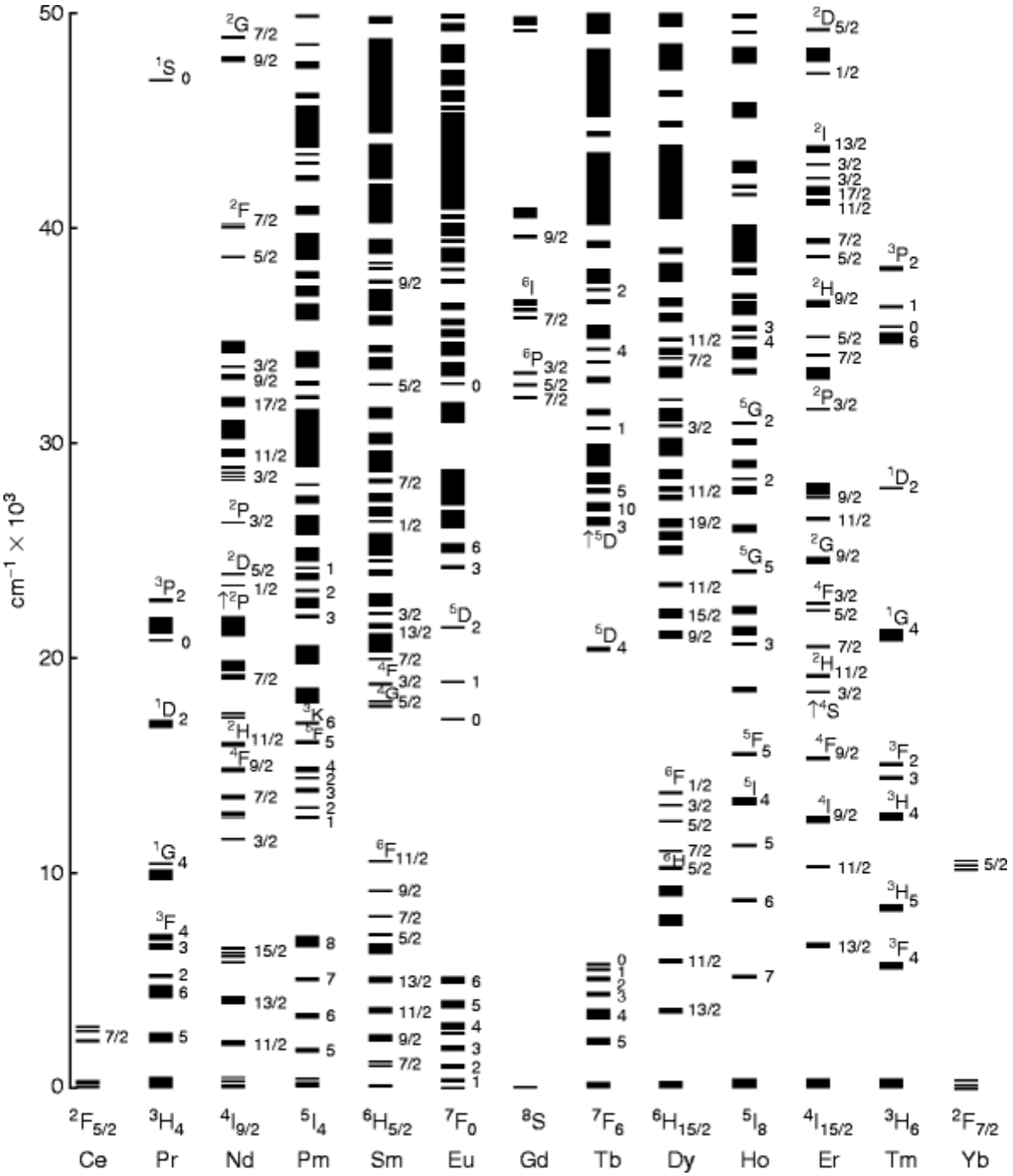

$4f^n$ energy level diagram for Ln^{3+}:LaF_3 based on computed crystal-field in the range 0-50 x10^3 cm^{-1} reported by Carnall [9]

Academic Tree
Leonardo Vieira Albino

Name
(Lifetime) OR (*year of birth)
Thesis – year
Institution of the Thesis

Leonardo Vieira Albino
(*1994)
Thesis – 2023
UNESP/campus Araraquara
Université de Bordeaux

French line

Georges Urbain
(1872 – 1938)
Thesis – 1899
Faculté de Sciences de Paris

Marcellin Berthelot
(1827 – 1907)
Thesis – 1854
Collège de France

André Chrétien
(1899 – 1996)
Thesis – 1929
Université de Paris

Philippe Barbier
(1848 – 1922)
Thesis – 1876
Collège de France

Paul Hagenmuller
(1921 – 2017)
Thesis – 1950
Université de Paris

Raymond Rohmer
(1909 – 1988)
Thesis – 1939
Université de Strasbourg

Jacques Prigent
(1928c. – 1982c.)
Thesis – 1956
Université de Rennes

Victor Grignard
(1871 – 1935)
Thesis – 1901
Université de Lyon

Jacques Lucas
(*1937)
Thesis – 1964
Université de Rennes

Marcel Poulain
(*1945)
Thesis – 1973
Université Rennes-I

Younès Messaddeq
(*1963)
Thesis – 1990
Université Rennes-I

Marcelo Nalin
(*1974)
Thesis – 2002
UNESP/campus Araraquara
Université Rennes-I

German line

Heinrich Limpricht
(1827 – 1909)
Thesis – 1850
Universität Göttingen

Arthur Rudolf Hantzsch
(1857 – 1935)
Thesis – 1880
Universität Würzburg

Hans von Pechmann
(1850 – 1902)
Thesis – 1879
Universität Greifswald

Alfred Werner
(1866 – 1919)
Thesis – 1890
Universität Zürich

Edgar Wedekind
(1870 – 1938)
Thesis – 1895
Universität München

Paul Pfeiffer
(1875 – 1951)
Thesis – 1898
Universität Zürich

Charles Courtot
(1888 – 1955)
Thesis – 1915
Université de Nancy

Jacques V. Metzger
(1921 – 2014)
Thesis – 1948
Université de Nancy

Émile-Jean Vincent
(*1937 – ?)
Thesis – 1966
Université de Aix-Marseille

Evelyne Fargin

Thesis – 1988
Université Aix-Marseille-III

Thierry Cardinal
(*1970)
Thesis – 1997
Université Bordeaux-I

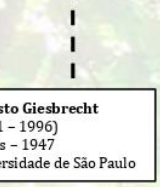

Heinrich Rheinboldt
(1891 – 1955)
Thesis – 1918
Universität Straßburg

Ernesto Giesbrecht
(1921 – 1996)
Thesis – 1947
Universidade de São Paulo

Gilberto Fernandes de Sá
(*1942)
Thesis – 1972
Universidade de São Paulo

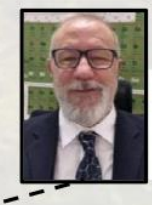

Sidney José Lima Ribeiro
(*1959)
Thesis – 1992
UNESP/campus Araraquara
Universidade Federal de Pernambuco